Clutter Noise Reduction in Ultrafast B-Mode Image

Asraf Mohamed Moubark

School of Electronic and Electrical Engineering

University of Leeds

Submitted in accordance with the requirements for the degree of

Doctor of Philosophy

September 2018

The candidate confirms that the work submitted is their own, except where work which has formed part of jointly authored publications has been included. The contribution of the candidate and the other authors to this work has been explicitly indicated below. The candidate confirms that appropriate credit has been given within the thesis where reference has been made to the work of others.

The work in chapter 4 of the thesis has appeared in publication as follows:

- AM Moubark, Z Alomari, S Harput, DMJ Cowell, S Freear, "Enhancement of contrast and resolution of B-mode plane wave imaging (PWI) with non-linear filtered delay multiply and sum (FDMAS) beamforming", IEEE Int, Ultrasonics Symposium (IUS), 2016, 1-4

I was responsible for the concept, simulation programs, experiments and preparation of the figures and publication. David Cowell was responsible for designing the array excitations. Zainab Alomari, Sevan Harput and Steven Freear were responsible for proofreading the manuscript.

The work in chapter 5 of the thesis has appeared in publication as follows:

- AM Moubark, TM Carpenter, DMJ Cowell, S Harput, S Freear, "New improved unsharp masking methods compatible with ultrasound B-mode imaging", IEEE Int, Ultrasonics Symposium (IUS), 2017 , 1-4

I was responsible for the concept, simulation programs, experiments and preparation of the figures and publication. Thomas Carpenter was responsible for the full design and manufacture of the UARP hardware. David Cowell was responsible for designing the array excitations. Sevan Harput and Steven Freear were responsible for proofreading the manuscript.

This thesis is dedicated to my parents

Acknowledgements

First and foremost, I thank God Almighty for the blessings He has bestowed upon me and for giving me the strength and wisdom to finish my Ph.D. studies. I also would like to express my sincere gratitude to my supervisors Dr. Steven Freear and my co-supervisor Dr. Sevan Harput for their support, patience and guidance. Their advice helped me in all the time of research and writing of this thesis.

Besides my supervisors, I would like to thank my sponsors, Universiti Kebangsaan Malaysia (UKM) and Ministry of Higher Education (MOHE), Malaysia, who have granted my study leave together with the full scholarship.

My special thanks to Mr. Luzhen Nie, my fellow Ultrasound group mate who always supports my research work and writing of this thesis. I could not have imagined having a better commentator and advisor for my Ph.D study than him. Also I would like to thank the rest of Ultrasound group members, Dr. David Cowell, Dr. James R. McLaughlan, Mr. Christopher Adams, Mr. Oscar Knights, Mr. Abdul Rahman, Mrs. Zainal Alomari, Mr. Safeer Hyder, Mr. Jordan Tinkler, Mr. Christopher Cookson, Mr. Chau Vo, Mr. Thomas Carpenter and Mr. Chunqi Li.

Last but not least, I would like to thank my family members, parents Mr. Moubark and Mrs. Fatimah Beevi, spouse Mrs. Siti Zarina and both of our sons, Hariz and Deedat, without their love I won't be here.

Abstract

Ultrafast ultrasound imaging using plane waves has advanced a myriad of novel ultrasound imaging methods such as ultrafast contrast-enhanced imaging and shear wave elastography. However, due to the lack of transmission focusing and the beam steering operation in plane wave imaging (PWI), the presence of clutter noise on the B-mode image is unavoidable. The reduction of clutter noise is expected to increase the image contrast and spatial resolution, the two main criteria in ultrasound medical B-mode imaging for better diagnosis. Researchers have looked into this problem in depth and proposed many solutions. Many of the proposed solutions come with trade-offs. Attenuating the clutter noise may reduce the frame rate (FR), broaden the main lobe or increase the overall computational complexity. Thus, an advanced solution is warranted, with which reducing the clutter noise will not affect the FR and the image quality can be improved with a low computational complexity.

In this thesis, the clutter noise problem has been tackled with various approaches, the first implementing a new filtered delay multiply and sum (FDMAS) beamforming technique, the second being a new compounding method based on autocorrelation and the final being a new version of unsharp masking (UM) filter. In FDMAS, the optimization of the imaging point step in lateral direction has been investigated. By calculating the received echoes with a smaller imaging point in the lateral direction, it helps to lower the side lobe levels and improve the lateral resolution of B-mode images. The proposed compounding method that is based on the autocorrelation process has proved effective to reduce clutter noise even with a very low number of compounding angles. The modified version of the UM filter

suites ultrasound B-mode imaging and it provides promising results granting the improved image contrast and resolution without compromising the FR.

The benefit of reducing clutter noise on the B-mode image was demonstrated with its application to contour segmentation. Attenuating clutter noise not only speeded up the segmentation process but also benefited the measurement accuracy of the intima media thickness, which has the potential to add diagnostic value for the early detection of stokes, among other vascular diseases.

Abbreviations

AR	Axial resolution
B-mode	Brightness Mode
BBR	Black box region
BSAC	Balloon snake active contour
CCA	Common carotid artery
CIRS	Computerized imaging reference systems
DC	Direct current
CC	Computational complexity
CNR	Contrast-to-noise-ratio
CR	Contrast ratio
CPWI	Compound plane wave imaging
DAS	Delay-and-sum
DMAS	Delay-multiply-and-sum
ECA	External carotid artery
FC	Frequency compounding
FDA	Food and drug association
FDMAS	Filtered-delay-multiply-and-sum
FMAS	Filtered-multiply-and-sum
FPGA	Field programmable gate array
FR	Frame rate
HIFU	High-intensity focused ultrasound
HRPWM	Harmonic Reduction Pulse Width Modulation
ICA	Internal carotid artery
IMT	Intima-media thickness
LAI	Linear array imaging
LR	Lateral resolution
LPF	Low pass filter

MACI	Multi angle compound imaging
MI	Mechanical index
MLT	Multi-line-transmission
MV	Minimum variance
OS	Operating system
PAI	Phase array imaging
PCIe	Peripheral component interconnect express
PNP	Peak negative pressure
PSL	Peak side lobe
PWI	Plane wave imaging
RF	Radio frequency
ROI	Region of interest
SNR	Signal-to-noise-ratio
SWE	Shear wave elastography
SAF	Synthetic aperture focusing
SAC	Snake active contour
SC	Spatial compounding
S-G	Savitzky-Golay
SPPA	Spatial pulse peak average
SPTA	Spatial pulse time average
TGC	Time gain compensation
UARP II	Ultrasound array research platform version 2
UM	Unsharp masking

List of Symbols

τ_{tx}	Transmit time
τ_{rx}	Receive time
$\tau_{\mathrm{d}i}$	Time delay for each element
τ_i	Travel time
z_f	Imaging point in lateral direction
x_f	Imaging point in axial direction
y_f	Imaging point in elevation direction
x_i	Element in imaging probe
E	Total number of elements
p	Transducer pitch
c	Speed of Sound
s_i	Received RF signal in each channels
v_i	Aligned RF signal in each channels
r_{DAS}	Beamformed RF signals with DAS
r_{DMAS}	Beamformed RF signals with DMAS
r_{FDMAS}	Beamformed RF signals with FDMAS
N	Total steered plane waves
n	Each plane wave
θ_n	Each steering angles
θ_{max}	Maximum steering angles
θ_{min}	Minimum steering angles
L	Length of aperture
λ	Excitation signal wavelength
λ_{e}	Weithage in UM
F	F-number

d	Non-compounding depth
T_{s}	Receive sampling time
f_{s}	Sampling frequency
f_{o}	Transducer centre frequency
p	Transducer element pitch
m	Signed integer
T_{PRP}	Pulse repetition period
r	Length of signal
p_{m}	peak negative pressure
$a(t)$	Tukey window
α	Tukey window weightage
l	Imaging line
β_{lg}	Imaging line angles
ρ	Correlation
V	Voltage
$m(f)$	Sensitivity of hydrophone
$f_{\mathrm{x_s}}$	Spatial sampling frequency
$f_{\mathrm{x_{max}}}$	Maximum spatial sampling frequency
Com_{MAS}	Multiply-and-sum compounding
Com_{FMAS}	Filtered multiply-and-sum compounding
G	Gaussian filter
σ	Standard deviation
$u_{\mathrm{con}}[a, b]$	Conventional unsharp masking
$u_{\mathrm{new}j}$	New unsharp masking
$h[a, b]$	Original digital B-mode image

a	Distance in horizontal axis
b	Distance in vertical axis
j	Number of iteration
$e_s(t)$	Excitation Signal
T	Excitation signal duration
k	Rate of frequency change
K_e	Kernel size
μ	Mean value
σ^2	Variance
$V(s)$	Snake contour
E_{int}	Snake internal energy
E_{ext}	Snake external energy
$E(V(s))$	Overall snake energy
$\boldsymbol{n}(s)$	Normal vector to the curve
k_1	Amplitude of that force
∇P_s	Stooping point

Contents

List of Figures

Chapter 1

Introduction

In conventional ultrasound medical imaging, the sequential line-by-line scanning mode has been used to produce a B-mode image for clinical use since the 1970s Bradley (2008). With this imaging paradigm, the frame rate (FR) is dependent on the imaging depth, the number of focusing points and the field of view. The unavoidable disadvantage of this conventional image formation method is hence the limited FR. For example, a FR only up to 60 Hz can be achieved for an image with a 5-cm depth and 256 beamformed lines Bercoff (2011). This low FR is the main obstacle for the emerging applications such as ultrafast contrast imaging, shear wave elastography and ultrafast Doppler imaging Montaldo *et al.* (2009); Tanter & Fink (2014). The minimum FR needed for tracking the transient mechanical vibrations is 1000 Hz Tanter & Fink (2014). This is beyond the capability of the conventional line-by-line scanning mode. Another main issue imposed by the conventional focused beam transmission is the high pressure produced at the focal point. Although this will be beneficial to increase the SNR but the downside is that the focused beam can burst the microbubbles in contrast imaging Tanter & Fink (2014). Contrast agents can be disrupted by acoustic wave at low pressures Tanter & Fink (2014). Thus, to solve these issues, researchers have turned to ultrafast imaging. Instead of transmitting focused beams, ultrafast imaging spreads acoustic energy over multiple pulses by using a lower peak negative pressure (PNP) for each transmission. Better image quality can be obtained by preserving the survival rates of microbubbles as PNP is the determinant to microbubble destruction.

In ultrafast imaging, instead of sequential focused beams, a single plane or diverging wave with a lower PNP is transmitted to insonify the entire region of interest (ROI)

Tanter & Fink (2014). With a speed of sound of 1540 m/s, this allows a FR up to 25,000 frames per second at 30 mm depth. In reception, the backscattered echoes from a single transmission are synthetically focused point-by-point to form a B-mode image. Plane wave imaging (PWI) is one of the techniques frequently used in ultrafast imaging. Although ultrafast PWI has been adopted for clinical applications, such for shear wave elastography (SWE) which has been used to measure the tissue elasticity but the main issues that still need attentions are the poor contrast ratio (CR) and low spatial resolution Bercoff (2011). In SWE the resolvable resolution in lateral direction is only 1 mm. High contrast imaging will be beneficial for identifying small anechoic cysts inside the breast tissue region Guo *et al.* (2018). High CR and spatial resolution obtained with CPWI will also be beneficial for measuring more accurately the intima-media thickness inside the common carotid artery. This is because the border between the intima, media and adventitia will be better defined Gaarder & Seierstad (2015). The poor CR and low spatial resolution in PWI originate from several sources. Clutter noise is a general terminology given for a set of noise that is present during imaging and beamforming processes. These include side lobes, grating lobes, axial lobes, edge waves, off-axis scattering and phase aberration Lediju *et al.* (2008); Montaldo *et al.* (2009); Tranquart *et al.* (1999). Due to the lack of transmit focusing, clutter noise is integrated during beamforming, resulting in a low-SNR image in PWI. The two most prominent ways to deal with this problem are applying coherent compounding and advanced beamforming techniques Matrone *et al.* (2016); Zeng *et al.* (2013).

Spatial coherent compounding is a technique where echoes from multiple steered plane waves are summed to form a relatively high-resolution B-mode image compared to that from a single plane wave. By using compounding, speckle noise is smoothened, clutter noise is reduced, and spatial resolution of the final B-mode image is improved. However, the improved image quality comes at the cost of reduced FRs. Another solution proposed to improve the B-mode image quality is by applying advanced beamforming techniques instead of conventional delay-and-sum (DAS). This thesis focuses on the reduction of clutter noise in coherent PWI (CPWI) by using advanced compounding and beamforming techniques, with the aim of improving image contrast and resolution.

1.1 Literature Review

Beamforming is known as one of the most important aspects in ultrasound B-mode imaging. The main objective of beamforming is to spatially focus the reflected signal from the imaged medium. The computation-effective nature of DAS beamforming makes it a popular option for ultrasound medical imaging Zhou *et al.* (2013). However, DAS by its own fails to eliminate clutter noise Lediju *et al.* (2008); Moubark *et al.* (2016). Clutter noise that is inherent with DAS is one of the main reasons that cause the poor CR and low spatial resolution which could negatively affect the diagnostic results. Considerable work has been conducted to overcome the clutter noise issue with DAS by using transmit and receive apodization, F-number and spatial compounding. Both apodization and F-number are known to degrade the lateral resolution (LR) Zhang *et al.* (2016). A number of new beamforming techniques such as Minimum Variance(MV) and short-lag spatial coherence also have been introduced to deal with the clutter noise problem faced by DAS Holfort *et al.* (2009); Zhao *et al.* (2017).

MV is an adaptive beamforming technique which has been widely studied in the ultrasound imaging field. It has been successfully demonstrated that MV outperforms conventional DAS beamforming by producing higher spatial resolution, less clutter noise and improved contrast ratio Chen *et al.* (2013). The working principle of MV is the same as DAS. However, in DAS a fixed weight scale is applied to the predefined apodization windows whereas in MV, the weight scale for the apodization windows is calculated according to received RF signals. The computational complexity (CC) is a major drawback of MV Sakhaei (2015). This is mainly because the received aperture needs to be divided into several smaller overlapping subapertures in order to perform subarray averaging. The high CC is an issue in real-time ultrasound imaging. Many researchers proposed solutions to reduced the CC in MV. Delami *et al.* uses the previously optimized weight vector for one point as the initial weight vector for the new neighboring point Deylami & Asl (2018). By doing this, it can improve the convergence speed and decrease the total CC in MV. On the other hand, embedded GPU computing platforms have been considered by Junying Chen *et al.* for MV beamforming Chen *et al.* (2017).

Jeremy J. Dahl *et al.* introduced an ultrasonic beamforming technique which is capable of forming B-mode images based on the spatial coherence of the backscattered

echoes. The beamforming technique called short-lag spatial coherence (SLSC) is able to reduce clutter noise in ultrasonic imaging. Although the proposed technique is claimed to improve the B-mode image CNR, however, there are no detailed studies have been conducted on the image CR and spatial resolution. The different maximum dynamic ranges (45 dB and 50 dB) used to display the B-mode image make comparisons difficult between those given images. The beamforming technique also shows many flaws and disadvantages. The loss of information in the near field (< 5 mm) is visible whenever the strong echo is present in the B-mode image. This is due to normalization of the spatial coherence factor. Further improvements are needed to facilitate this beamforming technique for ultrasound B-mode imaging Dahl *et al.* (2011).

Recently, Lim *et al.* introduced a novel beamforming technique called delay multiply and sum (DMAS) Lim *et al.* (2008). This technique has been applied to radar microwave imaging for detecting breast cancer where the main priority is to find the tumour with a CR between 2:1 and 10:1 relative to the normal breast tissue Fear *et al.* (2002); Klemm *et al.* (2008, 2009); Lazebnik *et al.* (2007). Thus, this method is unsuitable for ultrasound imaging that comprises several signal levels: hyperechoic, isoechoic, hypoechoic and anechoic. Matrone *et al.* modified and improved the algorithm by introducing new mathematical blocks and named it the filtered DMAS (FDMAS) algorithm Matrone *et al.* (2015). This new beamforming technique provides the higher CR and better lateral resolution with less computational complexity compared to adaptive beamforming techniques Holfort *et al.* (2009). Matrone *et al.* applied FDMAS to linear array imaging (LAI), synthetic aperture focusing (SAF), multi-line transmission (MLT) and PWI Matrone *et al.* (2016, 2017a,b). The application of FDMAS improves the LR and CR in all cases. The axial resolution is retained but the contrast-to-noise ratio is degraded compared with that using DAS. Reduction of crosstalk noise is also demonstrated with MLT.

As an alternative to advanced beamforming techniques, digital image processing techniques have been applied to beamformed images to reduce clutter noise. One of the common filtering techniques used in medical imaging such as mammogram to enhance the image features is Unsharp masking (UM). Conventionally, UM has been applied to improve the digital image details by enhancing the high frequency parts Dutt & Greenleaf (1996). Edge enhancement filters will emphasize the visibility of the diagnostic information. UM has been widely applied in digital mammograms to improve

the microcalcification detection by enhancing the image contrast Akbay (2015); Bhateja *et al.* (2017); Cruz *et al.* (2012). The rationale of microcalcification detection is that the clustered microcalcifications have been associated with the suspicious existence of breast cancer Wilkinson *et al.* (2016). However, the breast tissue and fat always overlay the microcalcification, making it hard to be detected. The UM method has also been exploited to enhance the retinal blood vessel in order to detect multiple eye deceases such as diabetic retinopathy Akram *et al.* (2009). As a result of the disease, the retinal blood vessels show changes in diameter and length. In common, retinal images are acquired with digital fundus cameras. The image suffers from non-uniform illumination Joshi & Sivaswamy (2008). This becomes an obstacle to measure the retinal blood vessel in detail. Enhancing the digital image contrast and details with the UM method could benefit better measurements of retinal blood vessels. UM is not commonly used in ultrasound B-mode image since the properties of the ultrasound image is not the same as that in other medical images. B-mode images are composed of scattering points that is subject to speckle and clutter noise. However, there is a promising future for UM in ultrasound B-mode imaging. By modifying the existing UM algorithm, it could improve the image quality by reducing clutter noise and improve the spatial resolution. Speckle has been considered as one of the dominant noise sources in ultrasound imaging Ahmed & Nordin (2011); Michailovich & Tannenbaum (2006). The speckle noise tends to obscure the diagnosis process by masking the important details of the biological structures Michailovich & Tannenbaum (2006). Speckle will produce constructive and destructive regions when at least two scattering sources are close enough to interact with each other. The main objective of despeckeling is to reduce the speckle noise variations and enhance the anatomical features. Some of the most common despeckling filters that have been used in ultrasound imaging are Gaussian, Weiner, Median, Wavelet and Homomorphic filters Lee (1980); Loizou *et al.* (2005); Westin *et al.* (2000). The despeckling filtering techniques are most commonly used as a pre-processing step for image segmentation Loizou *et al.* (2005) with the aim of suppressing speckle noise. Segmentation is a process of partitioning an image where the intended ROI can be distinguished from the background Jumaat *et al.* (2014). Segmentation can help sonographers analyse the qualitative and quantitative information of the ultrasound images Mahmood *et al.* (2011). It has been used in ultrasound medical imaging for many applications such as automatic left ventricle boundary tracking to assist the assessment

of cardiac dysfunction Noble & Boukerroui (2006a). The most common technique used for segmentation in clinical practice is manual delineation of the borders which is time consuming and prone to operator experience Kuo *et al.* (2013).

1.2 Motivation

Despite a significant amount of research has been reported on FDMAS, no in-depth investigations have been conducted on the effect of varying the lateral beamfoming step size Δx, which is one of the important criteria for determining the B-mode image quality. Probes with a smaller pitch size p ($\leq \lambda/2$) has been favoured in ultrasound imaging since grating lobes can be eliminated during beam steering. But in a study Jensen *et al.* (2016b) using CPWI with DAS, the evaluation of LRs and contrast ratios (CRs) did not exhibit any significant variation, when probes with different pitch sizes (λ or $\lambda/2$) were used. This study also showed that the appearance of grating lobes with a pitch size of λ can be reduced effectively through compounding. This study provides a hypothesis that beamforming in the lateral direction plays an important role in determining the final quality of B-mode images. This finding has motivated us to further explore the effect of varying Δx with the recently proposed FDMAS beamforming technique. The FDMAS algorithm is similar to the autocorrelation process that depends on the time or sample lag among radio-frequency (RF) signals in each channel in the lateral direction. Thus, the minimum requirement for Δx in the lateral direction to determine the B-mode image quality using FDMAS is a subject for investigation.

The conventional compounding technique is performed with coherent arithmetic averaging on spatially obtained signals. Yet it is not the most effective compounding method since the arithmetic averaging fails to eliminate clutter noise which is visible inside the anechoic regions. The side lobe reduction and spatial resolution improvement are also minimal with the conventional compounding technique. Due to the different time delays used for each plane wave, side lobes that occur at different spatial locations are uncorrelated. On the other hand, the main lobe positions do not change much and are highly correlated. Thus, by applying the technique similar to FDMAS on compounding, it is expected to produce better results with reduced clutter noise and side lobes. The technique is based on the correlations between two steering angles and

it is expected that the computational time to produce final results will be the same as that using conventional arithmetic compounding.

The simplicity of the UM method comes with some costs. The high pass filter will enhance not only the image edges but also noise as well Dutt & Greenleaf (1996). Furthermore, the UM technique works better for regions with a high contrast compared to those with a low contrast. One of the most common problems in conventional UM is the overshoot artefact that occurs at the edges Cao *et al.* (2011). It is also known as the ring effect where the transition edge has a higher amplitude than the surrounding regions. This phenomenon is illustrated in Fig. 1.1. In order to overcome the overshoot problem in UM, Polesel *et al.* (2000) has described a new image enhancement technique via adaptive methods. With this method, the digital images were divided into three regions with low, medium and high contrast values. The weightage λ_e, used to scale the high frequency components was assigned according to the different regions. There will be low or no enhancement ($\lambda_e = 0$) in the smooth region, while a maximum weightage ($\lambda_e = 1$) is applied to lower contrast regions and regions with medium contrast values are only moderately enhanced $0 \leq \lambda_e \leq 1$. Another drawback imposed by the conventional UM method is the absolute operation in the algorithm. Any negative values will be sign-inverted when this operation takes place. This leads to additional noise which is not present in the original image, causing false interpretation. In ultrasound B-mode images, clutter noise that is mostly visible in the anechoic regions needs to be attenuated or eliminated. However, the conventional UM technique is unable to address this. This is mainly because the low pass filter (LPF) applied in conventional UM cannot differentiate clutter noise that is present inside the anechoic region. The problem with the conventional UM technique is mainly due to the implementation on the unsigned digital image domain with the single weightage scale. Implementing UM in the RF domain is expected to improve the B-mode image quality in conjunction with the arrangement of different weightage scales for positive and negative errors.

Manual B-mode image segmentation is time consuming and the results are subject to operator errors Khadidos *et al.* (2014). The problem with manual segmentation increases when the ROI is in motion such as the heart. Another conventional segmentation technique is based on the edge detection methods such as canny and sobel Nikolic *et al.* (2016); Zheng *et al.* (2015). The biggest challenge with the segmentation by the edge detection is the false edges detected outside the ROI. This is because the

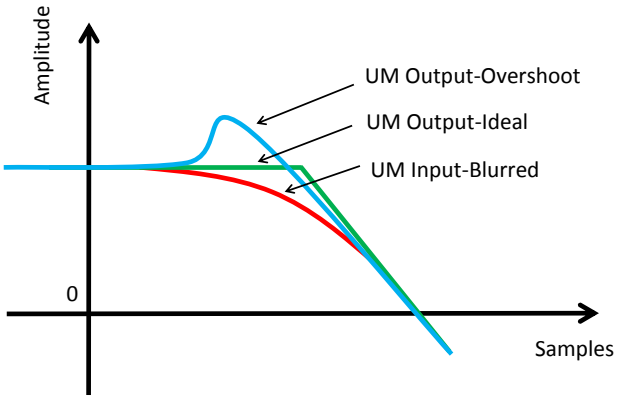

Figure 1.1: UM overshoot phenomenon.

edge detection on canny and sobel is based on a single threshold set to the gradient. Thus, in order to accurately segment the ROI, operators in the medical imaging field turn to semi-automated or automated segmentation techniques. In semi-automated segmentation methods such as snake active contour, a small initial contour will be predefined by the user near to the region that will be segmented. This initial contour acts as the seeded boundary for the whole segmentation process. For the fully automated segmentation process, an initial seeding is not selected manually but assigned by predefined algorithms such as the iterative threshold selection, voting mechanism and deep learning Kumar *et al.* (2018); Yaqub *et al.* (2010). Speckle and clutter noise that are present in the B-mode image also become a challenge for segmentation where the contour fails to converge to the intended boundary Khadidos *et al.* (2014); Slabaugh *et al.* (2009); Zhu *et al.* (2010). Despeckling is thus needed prior to segmentation.

1.3 Objectives of this work and the organization of the thesis

The main objective of this work is to reduce the clutter noise in ultrafast B-mode images. This has been achieved with three different techniques:-

1. Determining the optimal beamforming step in the lateral direction for FDMAS.
2. A new compounding technique based on a process similar to autocorrelation.

3. A new unsharp masking denoising technique which is compatible with ultrasound B-mode imaging.

More about the thesis organization is discussed in this section. In CPWI, clutter noise is associated with off-axis scatterering, side lobes, axial lobes, grating lobes, edge waves, motion artifacts and phase errors Lediju *et al.* (2008); Montaldo *et al.* (2009); Tranquart *et al.* (1999). Those kinds of noise have been studied and analysed with Field II simulations later as reported in detail in chapter 2. The concepts of PWI and spatial compounding have been discussed in the same chapter. Chapter 3 is dedicated to the selection of excitation signals and pressure measurements that suite for in vivo imaging. The main three matrices calculated according to the Food and Drug Association (FDA) are the mechanical index, spatial peak temporal average intensity and spatial peak pulse average intensity. Chapter 4 is dedicated to the new beamforming technique FDMAS. A detailed study has been conducted in order to determine the optimal beamforming step in the lateral direction for FDMAS. An earlier study conducted on FDMAS with coherent compounding techniques has been published in the following papers

- AM Moubark, Z Alomari, S Harput, DMJ Cowell, S Freear, "Enhancement of contrast and resolution of B-mode plane wave imaging (PWI) with non-linear filtered delay multiply and sum (FDMAS) beamforming", IEEE Int, Ultrasonics Symposium (IUS), 2016, 1-4

The conventional compounding technique involving coherent summation and arithmetic averaging could not solve the existing clutter noise problem. This is mainly because the noise pattern has been only averaged with all tilted plane waves. To improve noise cancellation, a new compounding technique is proposed in chapter 4 inspired by the algorithm used in FDMAS. High contrast and spatial resolution acvieved as a results of clutter noise reduction with new compounding but with low computational complexity. The proposed technique takes place between steered plane waves and not during beamforming as in FDMAS. Thus, the proposed compounding technique is much faster and produce better results than those with FDMAS. The contrast ratio and resolution produced with the new compounding technique are better when compared to those with conventional coherent compounding. This has been achieved with low compounding angles hence increasing the FR.

The potential of the conventional UM method has been explored and revived for ultrasound B-mode imaging. Instead of enhancing the high frequency component, a few modifications on the algorithm were made to reduce clutter noise and improve the spatial resolution at the same time. The new UM technique was implemented in the RF domain with non-coherent signals as a LPF and two different weightage schemes for positive and negative errors were used. Chapter 5 discussed the new UM technique in detail when it's implemented on PWI and CPWI. The outcome of this study has been published in the following paper:

- AM Moubark, TM Carpenter, DMJ Cowell, S Harput, S Freear, "New improved unsharp masking methods compatible with ultrasound B-mode imaging", IEEE Int, Ultrasonics Symposium (IUS), 2017 , 1-4

The balloon snake active contour and modified Otsu's segmentation methods were implemented on the B-mode images to study the effect of clutter and speckle noise reduction on despeckling and segmentation. Despeckling is one of the important steps used to reduce clutter and speckle noise variation and improve the contrast-to-noise ratio (CNR). It will benefit the segmentation process Khadidos *et al.* (2014). In chapter 6, various despeckling techniques such as Gaussian, Weiner and Adaptive median filters were with different window sizes after clutter noise reduction with UM. Good despeckling techniques that can retain all the important features were recommended.

Chapter 7 is dedicated to measurements of the intima media thickness (IMT) on the common carotid artery wall. The effect of clutter noise reduction in anechoic regions with UM on the measurements of the IMT was studied. Segmentation process applied on the despeckled B-mode images before the IMT measured. Reducing the side lobes and clutter noise inside the anechoic regions will improve the image contrast and the segmentation process Khadidos *et al.* (2014). The segmentation process is based on identifying the edge or the boundary of the intima and media walls. If any noise is present between those walls, false measurements could occur or more iterations will be needed to complete segmentation. Clutter noise in the intima-media regions was reduced with UM and the associated benefits for segmentation were given.

The research on reducing clutter noise in medical ultrasound imaging contributed to other studies that are not present in this thesis. Four conference papers were published:

- AM Moubark, S Harput, DMJ Cowell, C Adams, S Freear, "Plane wave imaging challenge", IEEE Int. Ultrasonics Symposium (IUS), 2016, pp. 1-4
- AM Moubark, S Harput, DMJ Cowell, S Freear, "Clutter noise reduction in b-mode image through mapping and clustering signal energy for better cyst classification", IEEE Int. Ultrasonics Symposium (IUS), 2016, pp. 1-4
- A Alshaya, S Harput, AM Moubark, DMJ Cowell, J McLaughlan, S Freear, "Spatial resolution and contrast enhancement in photoacoustic imaging with filter delay multiply and sum beamforming technique", IEEE Int. Ultrasonics Symposium (IUS), 2016, pp. 1-4
- AM Moubark, Z Alomari, S Harput, S Freear, "Comparison of spatial and temporal averaging on ultrafast imaging in presence of quantization errors", IEEE Int. Ultrasonics Symposium (IUS), 2015, pp. 1-4

The manuscript related to the work on FDMAS was submitted for review:

- AM Moubark, Z Alomari, David M. J. Cowell, C Adams, L Nie, S Harput, S Freear, "Enhanced Filtered-Delay Multiply and Sum Beamforming to improve Balloon Snake Active Contour Segmentation in Ultrafast Imaging"

Chapter 2

Ultrasonography: Plane Wave Imaging

In this chapter, introduction was given to typical types of noise that impair ultrafast plane wave imaging (PWI) and techniques used to overcome those. Field II simulations were performed in order to discuss the origin of them.

2.1 Plane Wave Imaging

In PWI, all the transducer elements are excited simultaneously without any transmit focusing as shown in Fig. 2.1(a). The created planar wave-fronts will insonify the whole imaging area at once and a whole B-mode image can be created. As opposed to conventional linear array imaging (LAI) and phase array imaging (PAI), where the frame rate (FR) depends on the imaging line density, PWI provides a FR equal to the pulse repetition frequency. Thus, a very high frame rate (FR) up to 20 KHz can be achieved depending on the imaging depth z_f. The travelling time for a plane wave as shown in Fig. 2.1(b) to point (x_f, z_f) is given by

$$\tau_{\text{tx}}(x_f, z_f) = \frac{z_f}{c}. \tag{2.1}$$

Where c is the speed of sound. The heterogenic point will produce an echo signal and the return time to each element, x_i as shown in Fig. 2.1(b) is given by

$$\tau_{\text{rx}}(x_f, z_f) = \frac{\sqrt{z_f^2 + (x_i - x_f)^2}}{c} \tag{2.2}$$

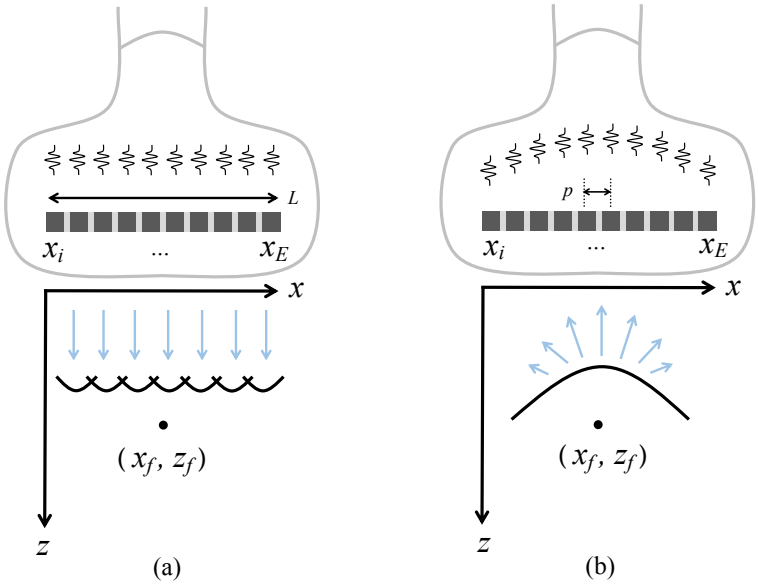

Figure 2.1: Plane wave (a) emission and (b) backscattered echo from a single point located at (x_f, z_f).

Thus, the complete travelling time of the wave to the target point (x_f, z_f) and back to the transducer element x_i is given by

$$\begin{aligned} \tau_i(x_f, z_f) &= \tau_{\text{tx}}(x_f, z_f) + \tau_{\text{rx}}(x_f, z_f) \\ &= \frac{z_f}{c} + \frac{\sqrt{z_f^2 + (x_i - x_f)^2}}{c} \end{aligned} \tag{2.3}$$

The scatter point mainly produces two kinds of information for imaging. One is the location of the point that we can find through the total traveling time and the other is the strength of the signal conveyed by the pressure amplitude. In order to map the scatter point intensities, the received echo signals on all the elements need to be beamformed. Beamforming is a process of applying a specific time delay using equation 2.3 to each echo signal and coherently adding them. The time delay is applied to the RF signal $(s_i(t))$ for each channel, and the aligned RF signal termed v_i is then obtained. v_i is formulated by the following equation:

$$v_i(x_f, z_f) = s_i(t - \tau_i(x_f, z_f)) \tag{2.4}$$

To form a single B-mode imaging point, the aligned RF signals for all channels will be summed according to the following equation:

$$r_{\mathrm{DAS}}(x_f, z_f) = \sum_{i=1}^{N} v_i \tag{2.5}$$

The above calculation is just for a single point but in practice the process will be repeated for whole (x, z) points in the ROI. The process of beamforming in PWI during reception is the same as that in conventional linear array imaging (LAI). But instead of calculating the time delay only for a single focusing point as in LAI, all points of the image are beamformed using the same RF signals with different time delays in PWI.

Even though PWI can produce very high FRs but one significant drawback with this technique is the poor image quality. According to Montaldo *et al.* (2009), the signal to noise ratio (SNR) and contrast obtained for an anechoic object is 0 dB and 12 dB, respectively. The reason behind this downside of PWI is that the transmit focalization is not applied for the pulse transmission. Thus, to improve the image quality without highly sacrificing the FR, the compounding technique was introduced by Cooley and Robinson in 1994 Cooley & Robinson (1994). In Montaldo *et al.* (2009), the concept of coherent summation of plane waves was experimentally demonstrated and this is known as coherent plane wave compounding or compound plane wave imaging (CPWI).

The commonly used compounding techniques are spatial compounding (SC) and frequency compounding (FC) Montaldo *et al.* (2009); Yoon *et al.* (2013). The main advantages of SC are to reduce speckle and clutter noise and improve the lateral resolution Lin *et al.* (2002); Ullom *et al.* (2012). Other improvements from SC can be seen on the image SNR and contrast Montaldo *et al.* (2009). Both metrics for the anechoic object increase gradually when the number of compounding angles increases Montaldo *et al.* (2009). Improvement in lateral resolution has also been reported with SC Montaldo *et al.* (2009). However, after a certain number of compounding angles, the improvement of lateral resolution plateaus and drops with more compounding angles. In Toulemonde *et al.* (2015) and Alomari *et al.* (2014), beyond three coherent compounding angles, the lateral resolution started to degrade. The lateral resolution measured on the main lobe at -6 dB is influenced by the side lobes. Reducing the side lobe level will improve the lateral resolution. The cancellation of side lobes is dependent on the number of compounding and steering angles. The steering angles becomes smaller as the number

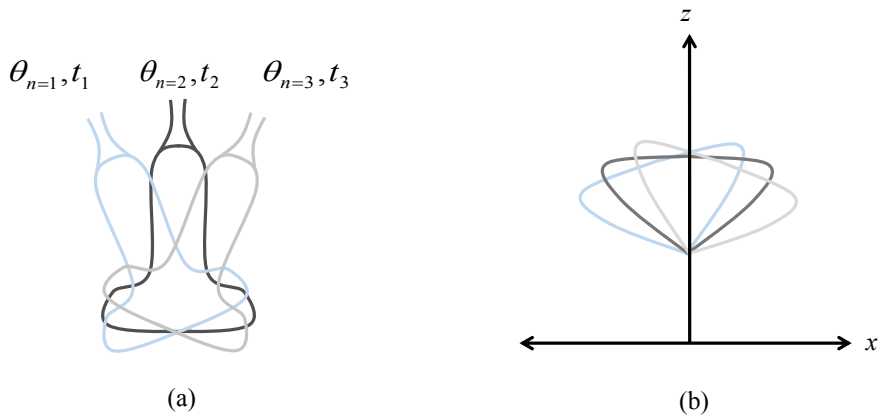

Figure 2.2: Concept of spatial compounding a) beams steered in the same ROI b) shift in x space reflecting decorrelation of the response from steering.

of compounding increases. Thus, the side lobes are no longer far apart but become nearer as the step of steering angles θ_n decreases. The SC technique is also known to reduce clutter noise inside the anechoic region and improve the edge definition. The FC method has been used mainly to reduce the speckle noise variations. This enhances the B-mode image SNR and CNR to improve the visibility of a small anechoic cyst.

In general, both compounding techniques, SC and FC consist of two steps. The first is used to acquire the signals and the second is used to sum the acquired signals.

2.2 Data Acquisition in Compounding

SC or angular compounding is a method of obtaining images by steering the subset or the whole transmit beam to different directions as shown in Fig. 2.2. The compounding operation is effectively a spatial averaging filter that reduces speckle and clutter noise and increases the image contrast and lateral resolution. The signals acquired from the steered beams are summed to reconstruct a single frame. The concept of spatial compounding has been implemented in multi angle compound imaging (MACI) and CPWI. In MACI, a single frame is formed with PAI, while in CPWI a single image is formed with a single plane wave transmission. The fully compounded area is at the center of the field of view where every single frame overlaps.

One of the main aims of SC is to maximize the echoes from all steering angles in the ROI. In general, several decorrelated (more than three) frames are compounded into a single composite B-mode image. In PWI, the received echoes are dependent on the incident angle of the beam. The strongest echoes are generated at the normal incident angle of zero degree. Without SC, the top and bottom boundaries produce the stronger image intensities compared to those on the left and right sides. With the application of SC, the scanning medium will be present on a B-mode image with a more equal intensity distribution benefiting from the beams with different incident angles Jespersen *et al.* (1998).

As mentioned by Burckhardt (1978), if the same object is scanned with different pulse lengths, centre frequencies or incident angles, the speckle patterns are different. In any of these different conditions, the amplitude values at the same point are different for every new scan.

The concepts of FC have been implemented in phase array imaging (PAI) and PWI Magnin *et al.* (1982). In FC, varying the center frequency on transmission or dividing the spectrum of the RF signal on reception is used. The main objective in FC is the same as that in SC, wherein several uncorrelated or partially correlated frames are obtained for compounding. Although FC is able to reduce speckle noise, but the loss in spatial axial resolution is unavoidable Sanchez & Oelze (2009); Ullom *et al.* (2012). This is because that the signal bandwidth has to be divided into smaller sub-bands as shown in Fig. 2.3. No changes in spatial resolution occur on the lateral direction. Applying chirp excitation signals is able to compensate the loss in the axial resolution Sanchez & Oelze (2009). However, this comes with the physical limitation of the probe bandwidth and the heating effect introduced to the imaging medium. Due to the limitation and constraints imposed by FC, SC has been used widely in ultrasound medical imaging. Thus, in this thesis only SC will be investigated for all simulations and experiments.

One of the reasons why SC and FC techniques can improve the image quality is the property of the speckle pattern and clutter noise that change according to the angle of the transmit beam and the bandwidth of the transmitted signal Jespersen *et al.* (1998); Toulemonde *et al.* (2015). Thus, to effectively reduce the speckle and clutter noise each emitted signals should be uncorrelated or partially correlated. The main disadvantage of SC is to lower the FR, while for FC it is the reduction in axial resolution.

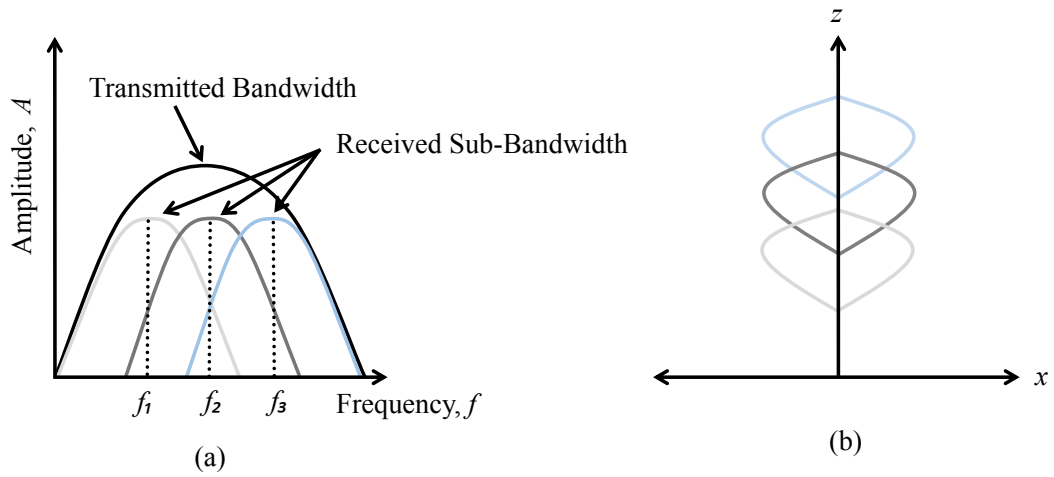

Figure 2.3: Concept of frequency compounding a) transmit and receive frequency bandwidth b) shift in z space reflecting decorrelation of the response from dividing the bandwidth.

2.2.1 Summation of Backscattered RF Signals in Compounding

Several steered PWI frames can be summed either coherently or incoherently to form a single B-mode image. In coherent summation, all the RF signals from each plane wave transmission are added before envelope detection. Coherent plane wave summation was proposed in 2004 by Song & Chang (2004) and has been extensively studied by Montaldo *et al.* (2009). As opposite to coherent summation, in incoherent or non-coherent summation, the envelope of RF signals for each plane wave is detected before summation. Both compounding techniques have advantages and disadvantages. Incoherent summation shows improvement in the transverse motion estimates and the reduction of speckle noise Tanter & Fink (2014). Coherent summation is able to increase the image contrast and resolution Tanter & Fink (2014); Tanter *et al.* (2002). The image spatial resolution with incoherent summation is lower when compared to the coherent technique. This is because that less noise cancellation takes place in incoherent techniques.

2.3 Compound Plane Wave Imaging

To achieve the same image quality as a focused image at a point z_f, f mm deep, N steered plane waves (n) are required Montaldo *et al.* (2009):

$$N = \frac{L}{\lambda F} = \frac{L^2}{\lambda z_f} \tag{2.6}$$

n is defined as:

$$n = \left[-\frac{N-1}{2}, ..., \frac{N-1}{2}\right] \tag{2.7}$$

For each steering angle, θ_n is given by:

$$\theta_n = \arcsin(\frac{n\lambda}{L}) \approx (\frac{n\lambda}{L}) \tag{2.8}$$

where L is length of the aperture, λ is the signal wavelength, F is F-Number defined as $F = z_f/L$.

The time delay $\tau_{\mathrm{d}i}$ associated with each transducer element x_i, for the steering angle θ_n is given by

$$\tau_{\mathrm{d}i} = \frac{px_i}{c}\sin(\theta_n) \tag{2.9}$$

where p is the inter element pitch size in mm. While for a complete travelling time to point (x_f, z_f) and back to the transducer element x_i for the CPWI is given by Korukonda (2012)

$$\begin{aligned}\tau_i(x_f, z_f) &= \tau_{\mathrm{tx}}(x_f, z_f) + \tau_{\mathrm{rx}}(x_f, z_f) \\ &= \frac{z_f\cos(\theta_n) + x_f\sin(\theta_n) + \frac{L}{2}\sin(\theta_n)}{c} + \frac{\sqrt{z_f^2 + (x_i - x_f)^2}}{c}\end{aligned} \tag{2.10}$$

The determination of the proper number of compounding angles is one of the important aspects that will affect the final compound image quality. Detailed studies about the selection of steering angles for CPWI can be found in Alomari *et al.* (2014). In has been mentioned that the steering angles can significantly affect the maximum intensity received by the transducer. This is because in CPWI, the received echoes are dependent on the incident angle of the beam. Moreover, when the imaging depth increases, the steering angle should be small so that the overlapped imaging area is

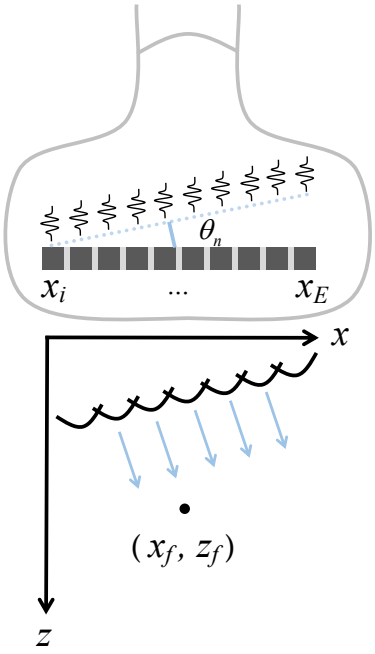

Figure 2.4: Steered plane wave emission.

large. With a fixed angle increment, when the number of steering angles increases, the beam overlapping area will be smaller.

The area which can be fully covered after compounding is determined by the maximum imaging sector angle as given in equations 2.7 and 2.8. Fig. 2.5 shows all four regions where the extent of compounding takes place. Region b is the place where all the steered beams are interfacing together to produce the fully compounded region. While regions a and c are not fully covered areas with compounding. The depth of zero compound region, d in Fig. 2.5 can be computed according to following equation Jespersen *et al.* (1998):

$$d(L, \theta_n, -\theta_n) = \frac{L}{\tan(\theta_n) - \tan(-\theta_n)} \tag{2.11}$$

where L is the length of the aperture, θ_n and $-\theta_n$ represent the maximum steering angles according to equation 2.7.

The general rule of thumb in selecting the number of compounding angles is to minimize it, such that the end results are balanced among the temporal, spatial and

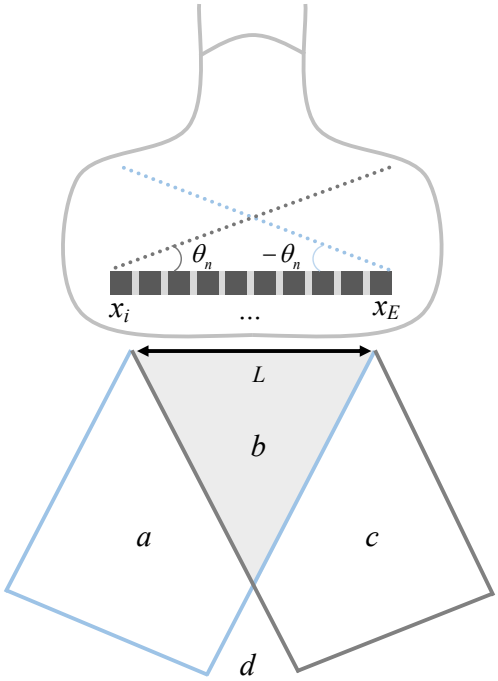

Figure 2.5: Illustration of two steered plane wave emission with maximum and minimum steering angles, θ_n=$-\theta_n$ resulting different compound region.

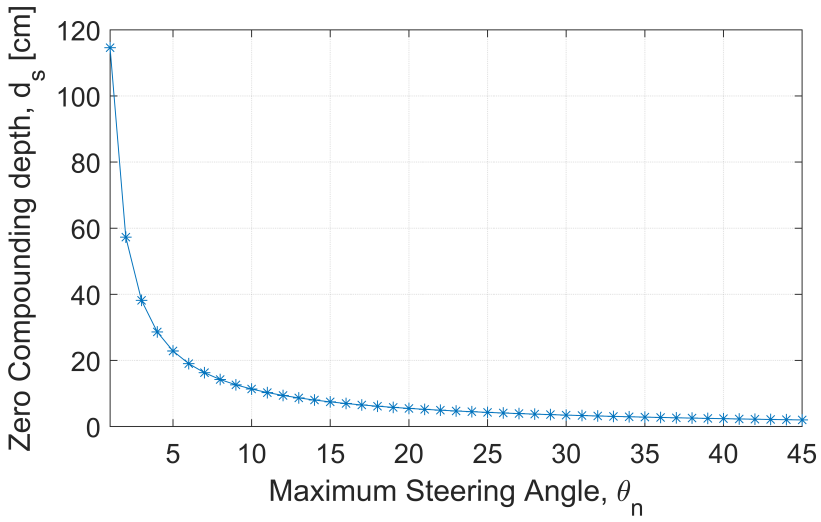

Figure 2.6: Complete compounding region with maximum steering angle.

Table 2.1: Compounding Parameters

Properties	Values						
Number of Compounding, N	1	3	5	7	9	13	25
Angle Increment, $\Delta\theta_n$	0	12	6	4	3	2	1

contrast resolutions. The imaging sector angle should kept as small as possible in order to reduce the appearance of grating lobes in the center of ROI and to maximize the compounding regions. Considering these constraints, the selected number of compounding angles N, and the steering angle increment $\Delta\theta_n$ are shown in Table 2.1. The maximum and minimum steering angles, $[\theta^{\circ}_{max}, \theta^{\circ}_{min}]$, for all compounding setups are set to $\pm 12^{\circ}$.

Ultrasound B-mode Image

The B-mode stands for the brightness mode where the intensity of the received ultrasound signals are represented by the gray color scale. In general, the strength of the echoes can be illustrated as follows

- Anechoic : The imaging medium produces no echoes thus being black in the B-mode image
- Hypoechoic : Produces less amount of echoes when compared to the neighbouring medium thus being varying shades of darker gray in the B-mode image
- Hyperechoic : Strong reflective echo when compared to the neighbouring medium thus being varying shades of lighter gray in the B-mode image
- Isoechoic : The imaging medium produces the same amount of echo within the scanning region
- Echogenic : Medium that produces echoes

Log-compression is used to increase the dynamic range of the received signals Ali *et al.* (2008). The B-mode images are displayed with a range of 40 to 60 dB in the log arithmic scale. In recent years, the manufacturers of ultrasound machines have added a color feature to replace the conventional gray scale. It is known as the Photopic

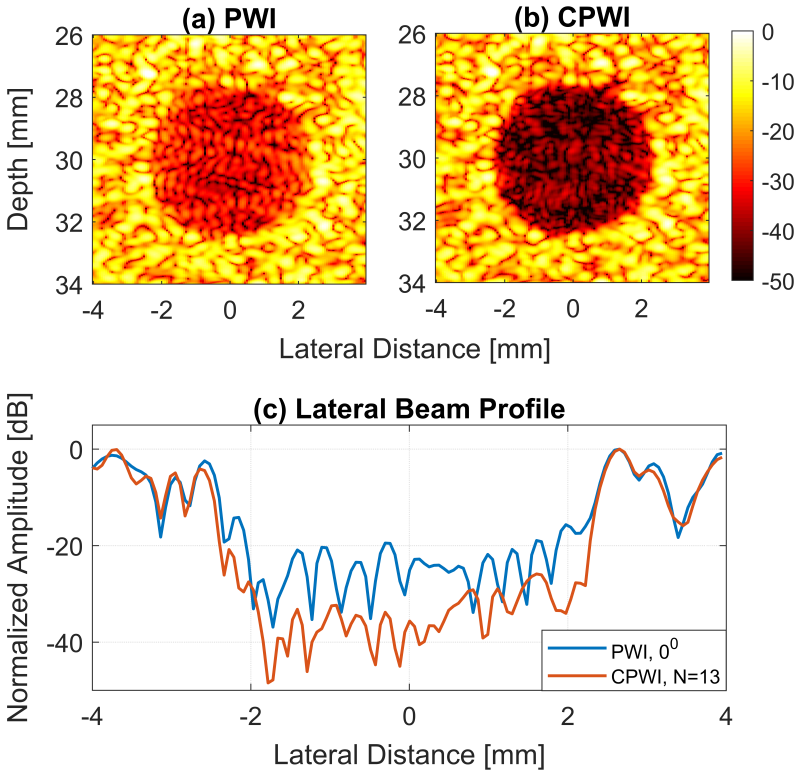

Figure 2.7: A cyst with a 4.0 mm diameter at the 30.0 mm depth imaged with a) PWI and b) CPWI, $N = 13$. The lateral beam profiles for both images are shown in c).

(daytime vision) imaging. The new color map increases both the image contrast and brightness while maintaining overall B-mode image quality. Photopic imaging is a relatively new innovation in ultrasound imaging that has been used to improve the B-mode image contrast by taking advantage of the human eye to distinguish bright colors, as opposed to dark grays Lin *et al.* (2003); Schwiegerling (2004). Before the Photopic imaging implementation, in order to increase the brightness of a B-mode image in deeper tissue regions, sonographers would manipulate the time gain compensation (TGC) to increase the signal strength. This however would increase the background noise and side lobe artifacts. On the other hand, the Photopic imaging would be able to improve the image brightness and contrast without introducing any artifacts.

2.4 Clutter Noise

The term clutter noise has been used as a general term for noise from off-axis scattering, edge waves, side lobes, grating lobes and phase errors Lediju *et al.* (2008); Montaldo *et al.* (2009); Tranquart *et al.* (1999). In general, it reduces the detectability or the CR of the imaging medium. Even though clutter noise is present on the entire B-mode image, it can be easily seen on anechoic or cyst regions such as cysts and blood vessels. The source of the off-axis noise is mainly from scatters located outside the main lobe of the incident beam. In LAI, the off-axis noise is significantly reduced. This is because of two different reasons. Firstly, only a subaperture is used for transmitting and receiving the RF signal where any noise from outside of the imaging line can be reduced. Secondly, the focused-beam mode produces higher SNR. In PWI, all elements in the imaging probe are used to receive the RF signals from the scanning medium. When beamforming takes place to form a single imaging line, all signals from on and off-axis scattering are used. The echo from sub-wavelength scatterers is composed of signal and noise received by all elements. By applying the F-number, the amount of echo received by the aperture can be controlled. This will reduce the clutter noise influence during the beamforming step. When the F-number is fixed, the aperture size keeps increasing according to the imaging depth. Thus, the off-axis noise reduction with a fixed F-number takes place more nearer to the aperture and is not manifest in deep regions. The negative effect of fixing the F-number to reduce the off-axis noise is it will reduce the lateral resolution.

Table 2.2: Field II simulation parameters.

Properties	Equations	Values
Speed of Sound, Water/CISR		1482/1540 m/s
Medium Attenuation,Water/CISR		0.002/0.5 dBcm^{-1} MHz^{-1}
Number of Elements	-	128
Transducer Centre Frequency	-	4.79 MHz
Transducer Bandwidth (−6 dB)	-	57 %
Transducer Element Pitch, p	λ	0.3048 mm
Transducer Element Kerf	$p/20$	15.4 μm
Transducer Element Width	Pitch-Kerf	289.4 μm
Transducer Element Height	-	6 mm
Transducer Elevation Focus	-	20 mm
Sampling Frequency, f_s for Tx/Rx	-	160/80 MHz
Receive Sampling Time, T_s	$1/f_s$	12.5 ns
Excitation Signal	-	2-Cycle Sinusoid
Excitation Signal Window	-	Hanning
Excitation Signal Centre Frequency, f_o	-	5 MHz
Imaging Point Step, x	$\lambda/3$	0.1016 mm
Imaging Point Step, z	$c * Ts/2$	9.625 μm
Spatial Apodization	-	Tukey Window, $\alpha = 0.5$

The appearances of off-axis noise, side lobes, grating lobes and edge waves are dependent on the steering angle. Steering beams at several different angles will locate clutter noise at different positions while maintaining the mainlobes at the same location. Thus, SC can practically reduce clutter noise under a certain level. This is because compounding will enhance the mainlobe intensity while averaging noise Papadacci *et al.* (2014). Applying different types of beamforming such as FDMAS and MV can also eliminate or reduce the off-axis noise. Clutter noise that is present in a B-mode image becomes a challenge for segmentation Slabaugh *et al.* (2009). This is mainly because clutter noise can corrupt the image with missing boundaries.

2.4.1 Grating Lobes, Side Lobes and Axial Lobes

The maximum steering angle for PWI is limited by the occurrence of the grating lobes and the imaging depth. Grating lobes are additional beams emitted from an array transducer and they are stronger than side lobes and can cause artefacts. The positions of grating lobes are dependent on the physical design of the ultrasound array transducer and given by the following equation Ponnle *et al.* (2013):

$$\theta_g = \sin^{-1}(\sin(\theta_n) - \frac{m\lambda}{p}) \tag{2.12}$$

where λ is the wavelength, θ_n is the steering angle and m is the integer order of grating lobes. Grating lobes exist in transmission and reception if the inter-element size or pitch is wider than a signal wavelength equal to $\lambda/2$ and do not exist when the pitch size is smaller than $\lambda/2$.

According to Karunakaran & Oelze (2013), narrowband signals such as the monochromatic sinusoidal excitation signal is also one of the main reasons for grating lobes. Thus, utilizing broadband signals could significantly reduce the grating lobes. Since the grating lobes are dependent on the transmission signal wavelength, applying the chirp signals could steer the grating lobes Karunakaran & Oelze (2013). The chirp excitation will also maintain the intensity at the focusing region. This is vital especially for the high-intensity focused ultrasound (HIFU) where unintended grating lobes can deposit heat at other areas than ROIs. The relative intensity level of the grating lobes can be significantly reduced by combining several beams from multiple transmissions (spatial compounding) De Jong *et al.* (1985); Jensen *et al.* (2015).

The first grating lobe (m = $\pm$1) location for the setup as given in Table 2.2 is given in Table 2.3 according to equation 2.12. To illustrate the effect of grating lobes, Field II simulations have been performed according to the setup in Table 2.2. A linear array probe with a pitch size of λ emits the steered plane wave at 12°, generating grating lobes at approximately 52°. This is shown in Fig. 2.8(a). The grating lobes have intensity around 35 dB relative to the main lobe wavefront. When the same simulation was repeated with the pitch size of $\lambda/2$ the grating lobes disappeared in the imaging field of view. This is shown in Fig. 2.8(b). However, in both simulations, edge waves in circular forms always appear at the edge of the wave front.

In order to remove the grating lobes, the final B-mode image can be displayed in the compressed form. Since we know that the grating lobes always appear towards the end on both sides of the B-mode image, the image width can be reduced. As shown in Fig. 2.17, the grating lobes appear at approximately -16 mm and 16 mm onwards. Thus, by displaying the B-mode image from -15 mm to 15 mm the grating lobes will not appear on the final B-mode display. However, this compression display still depends on the maximum steering angles. Larger steering angles can cause the grating lobes start to affect the center of the imaging medium. It is always desirable to use small steering angles ($\leq \pm 12^{\circ}$) to push away as far as possible the grating lobes from ROI.

Compared to grating and side lobes, axial lobes have not been explored widely in conventional LAI. This is because axial lobes are more synonym with plane and diverging waves. They start to occur during beam steering when the signals from each element do not reach the imaging point simultaneously. The finding about axial lobes has been reported in Jensen *et al.* (2015); Rodriguez-Molares *et al.* (2015). The wavefronts of each element reach the intended location or point at the same time but it's not the case for the wave tails. Thus, the wave tails interact with each other constructively and destructively. One of the solutions proposed by Rodriguez-Molares *et al.* (2016a) is to use angle dependent transmit apodization to reduce the number of elements that affects axial lobes. The proposed method is able to reduce the axial lobes by 40 dB. However, no spatial resolution and contrast information are provided. It is known that llimiting the number of transmitting elements by applying apodization will reduced the spatial resolution. In another work to reduce the axial lobes, Zhang *et al.* (2018) has combined the plane and spherical waves. The signals from a single plane wave and two spherical waves are both utilized to suppress the side lobes and reduce the axial artifact for the improvement of image contrast.

Motion Artifacts

The motion artifacts can occur for the moving imaging medium. The CPWI technique is based on the coherent summation of the RF signals from several PWs. However, human organs such as the heart and carotid artery are constantly moving at a certain speed. Thus, there is a high possibility that those moving mediums will create a smearing or blurring effect on the final B-mode images. In order to analyse the motion artifact, it is important to know the FR. By assuming the maximum imaging point is located at

Table 2.3: Grating lobes angles for $p = \lambda$

Steering Angles, θ_n	Grating Lobes Angles, θ_g
0	± 90.0
± 5	± 65.9
± 10	± 55.7
± 15	± 47.8
± 20	± 41.1
± 25	± 35.2
± 30	± 30.0
± 35	± 25.2
± 45	± 17.0

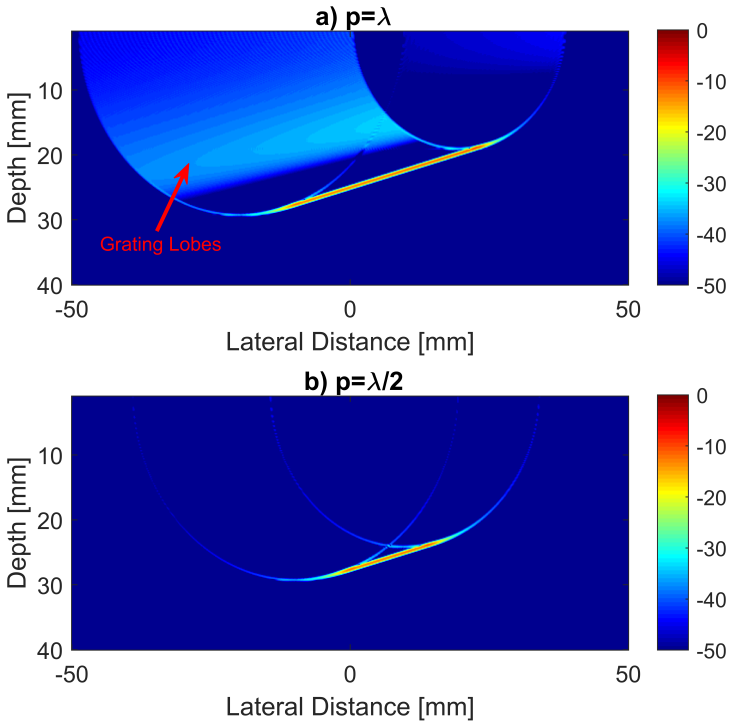

Figure 2.8: Results from the Field II simulation for the plane wave steered at $+12°$ for a) pitch $= \lambda$ and b) pitch $= \lambda/2$. The grating lobes start to emerge at approximately $-52°$ back of the wavefront for pitch $= \lambda$ and no grating lobes are visible for pitch $= \lambda/2$. The simulation setup is according to Table 2.2 but without apodization.

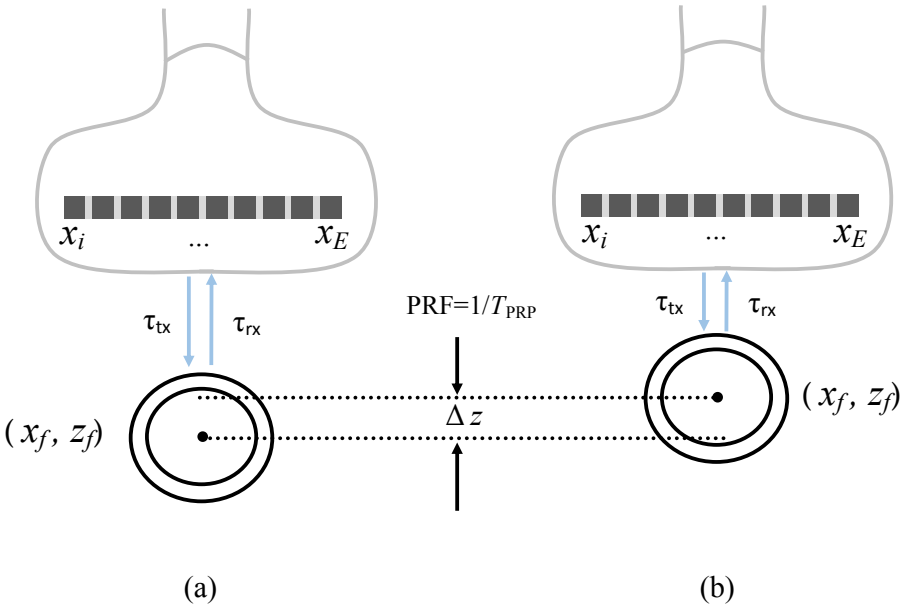

Figure 2.9: Illustration of moving artefact in PWI.

depth of $z_{\max}$, total number of plane waves N with θ_n, the required travelling time can be represented by the following

$$T_{\text{PRP}} = \sum_{n=1}^{N} \frac{1}{\cos(\theta_n)} \frac{2z_{\max}}{c} \tag{2.13}$$

Correspondingly, the pulse transmission rate or the FR can be represented by the pulse repetition frequency, PRF $= 1/T_{\text{PRP}}$. For the imaging point at (0, 15) cm, the required round trip time, T_{PRP} is 0.195 ms or the FR is approximately 5133 Hz for $N = 1$. The speed of sound sets a physical limit to the maximum FR achievable.

As illustrated in the Fig. 2.9, the motion of the organs in between the imaging process will cause, Δz movement in axial direction. By knowing the organs speed and the PRF, Δz can be estimated. The average speed of healthy human heart tissue and carotid artery wall are approximately 10 cm/s and 5 cm/s respectively (Hoskins *et al.* (2010); Kanai *et al.* (1999)). For the PRF of 5133 Hz, the tissue and wall displacements Δz between two consecutive transmissions will be 19.5 μm and 9.75 μm away or towards the transducer surface. The displacement is too small and won't significantly affect PWI, since each frame is displayed independently without the influences from other

Table 2.4: Moving artifacts.

N	1		13		25	
	50 mm	150 mm	50 mm	150 mm	50 mm	150 mm
FR [Hz]	15400	5133	1184	394	616	205
T_{PRP} [ms]	0.065	0.195	0.84	2.5	1.62	4.88
Heart Tissue, Δz [μm]	6.25	19.5	84	250	162	488
Carotid Artery, Δz [μm]	3.13	9.75	42	125	81	244

frames. This is however, not the case for CPWI where several frames are compounded to form a single frame. Any fast movement can significantly affect the final compounding result. This can be reduced by minimizing the number of steering angles and by applying incoherent compounding Øvland (2012). A detailed calculation made for heart tissue motion at speed of 10 cm/s for different number of compounding angles is shown in Table 2.4.

With 25 steering angles, the maximum displacement by the heart tissue and carotid artery wall will be 488 μm and 244 μm. This error needs to be corrected when determining the exact location of the moving objects.

2.5 Apodization

Apodization or windowing is a technique used to attenuate side lobes and edge waves in ultrasound B-mode imaging. Apodization can be applied to the excitation signal in time domain or frequency domain. It can be also applied in the spatial domain, by varying the amplitude across the aperture. Applying window functions on the excitation and aperture is a process to reduce the spectral leakage which is one of the main causes for the side lobes. Although apodization will not influence the spatial resolution in axial direction, it will affect the lateral resolution. Axial resolution is determined by the number of cycles and wavelength (λ) in the excitation signal. While lateral resolution is determined by several factors such as the wavelength (λ) and F-number. Applying apodization to the aperture will cause the main lobes broadened and reduce the lateral resolution. The most commonly used windows for apodization are Gaussian, Hanning, Hamming, Blackman and Tukey.

Unlike most of other windows, the Tukey window has an advantage. By applying different weightages between 0 and 1, the amount of side lobes reduction and main lobe expansion can be controlled. The Tukey window $a(t)$ is given as

$$a(t) = \begin{cases} \frac{1}{2}\{1 + \cos(\frac{2\pi}{r}[t - \alpha/2])\}, & 0 \leq t < \alpha/2 \\ 1, & \alpha/2 \leq t < 1 - \alpha/2 \\ \frac{1}{2}\{1 + \cos(\frac{2\pi}{r}[t - 1 + \alpha/2])\}, & 1 - \alpha/2 \leq t \leq 1 \end{cases} \tag{2.14}$$

where r is the length of the signal and $\alpha \in (0,1)$. When $\alpha = 0$, it is a rectangular window, and when $\alpha = 1$, it is a Hanning window. Fig. 2.10 shows three different weightages, $\alpha = 0$, 0.5 and 1 applied to the 2-cycle sinusoidal signal. As the weightage α increases, the spectral leakage starts to decrease and the main lobe bandwidth broadens around the -6 dB level. However, in the time domain the excitation signal amplitude which is responsible for the signal energy also starts to decrease. Thus, in order to balance the amount of energy transmitted into the imaging medium and the spectral leakage, $\alpha = 0.5$ has been chosen.

The effect of applying apodization technique on B-mode image was studied by performing Field II simulations with the setup given in Table 2.1 and 2.2. A Tukey window with $\alpha = 0.5$ has been applied to all excitation signals and the aperture. Fig. 2.11 shows the effect of apodization on plane waves steered at $+12^\circ$ for pitch $= \lambda$ and pitch $= \lambda/2$. With apodization, the edge waves produced by the most outer elements are completely attenuated. However, the appearance of grating lobes still the same as no apodization applied for pitch $= \lambda$. Results from the Field II simulation performed on point targets are given in Fig. 2.12. The side lobes of point targets from 10 mm to 50 mm depth with PWI have been significantly reduced with apodization. The beam profiles along lateral and axial directions for PWI are shown in Fig. 2.13. Along the lateral direction, the side lobes have been attenuated and the main lobes have been broadened when apodization applied. While the beam patterns in the axial direction did not show any significant changes. Results obtained from applying apodization together with compounding on point targets are shown in Fig. 2.12(c) and (d). Compounding is able to attenuate side lobes along the lateral direction. Thus the reduction of side lobes with apodization is minimal with CPWI. The beam profiles along the lateral direction at 50 mm depth and axial direction along $x = 0$ mm are shown in Fig. 2.14. Fig. 2.15 shows the point target at 10 mm depth when no apodization applied. The minimal

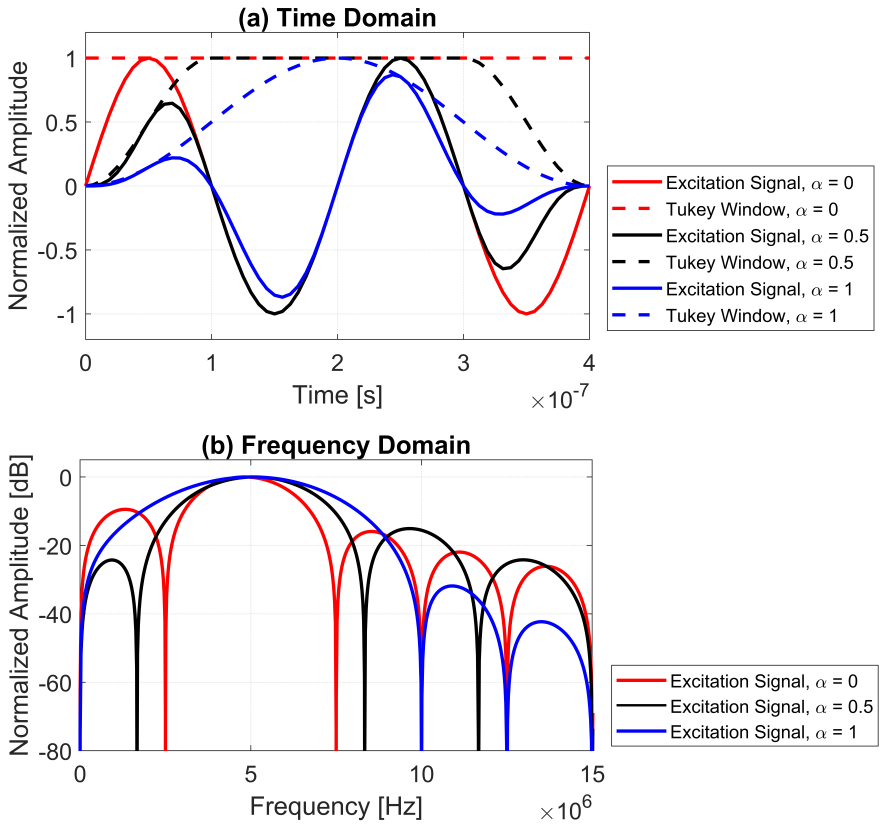

Figure 2.10: Excitation signal with different Tukey window weightages a) time domain and b) frequency domain.

side lobes reduction on each steered plane waves compensated when compounding takes place. The beam profiles for the point target along lateral and axial directions are given in Fig. 2.16.

The final B-mode image Fig. 2.17 composed of 13 compounding angles shows a significant improvement in attenuating the grating lobes and the side lobes. The lateral and axial beam profiles for the point target are also shown in Fig. 2.18. Almost more than 15 dB of the grating lobe intensity has been reduced with CPWI. Spatial compounding is also able to reduce the axial lobe by almost 10 dB. The axial lobes which tend to appear after the main lobes in the axial direction also have been reduced from -38 to -53 dB. This can be seen in Fig. 2.18(b) from 9.5 to 12.5 mm. The axial lobes have been described as an artefact similar to grating lobes which appear when the pitch size of λ is used for steering Rodriguez-Molares *et al.* (2016b). Imaging with a

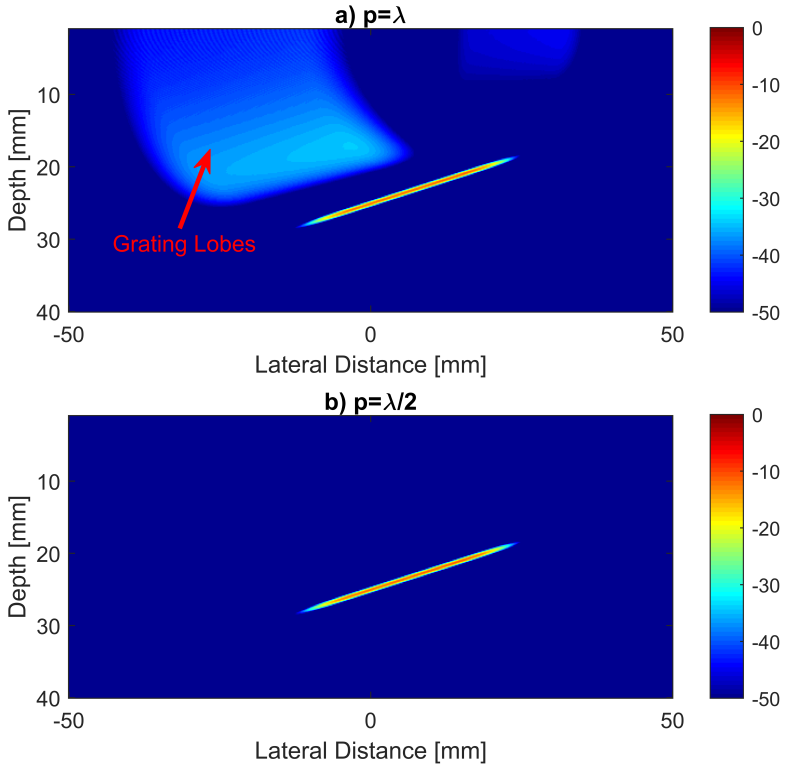

Figure 2.11: Results from the Field II simulation when Tukey apodization is applied to the plane wane steered at $+12°$ for a) pitch $= \lambda$ and b) pitch $= \lambda/2$. Appearance of the grating lobes for pitch $= \lambda$ is still visible, while the edge waves have been attenuated for both the pitch sizes of λ and $\lambda/2$. The simulation setup is given in Table 2.2.

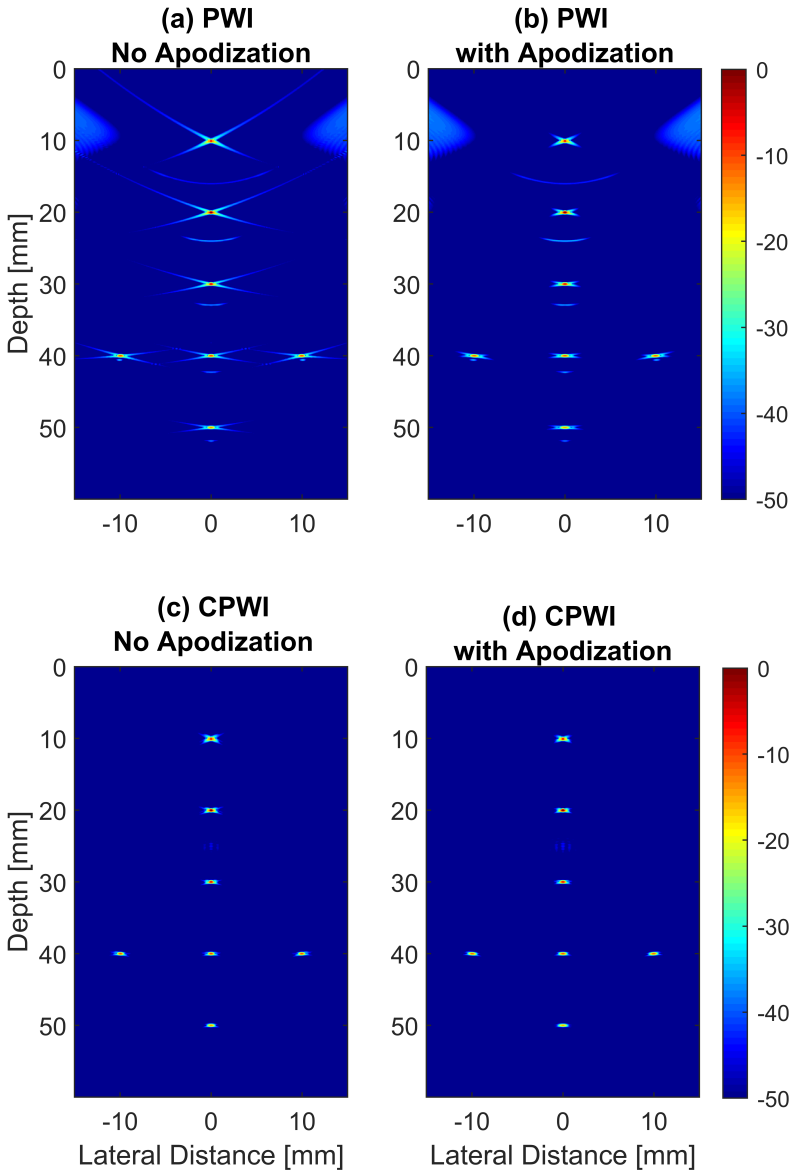

Figure 2.12: Results from the Field II simulation performed on point targets. a) PWI with no apodization, b) PWI apodized with a Tukey window ($\alpha = 0.5$), c) CPWI, $N = 13$ with no apodization, d) CPWI, $N = 13$ apodized with a Tukey window ($\alpha = 0.5$). Side lobes attenuation is more visible with PWI (b) when compared to (d). The setup for all simulations is according to Table 2.2 for the pitch size of λ.

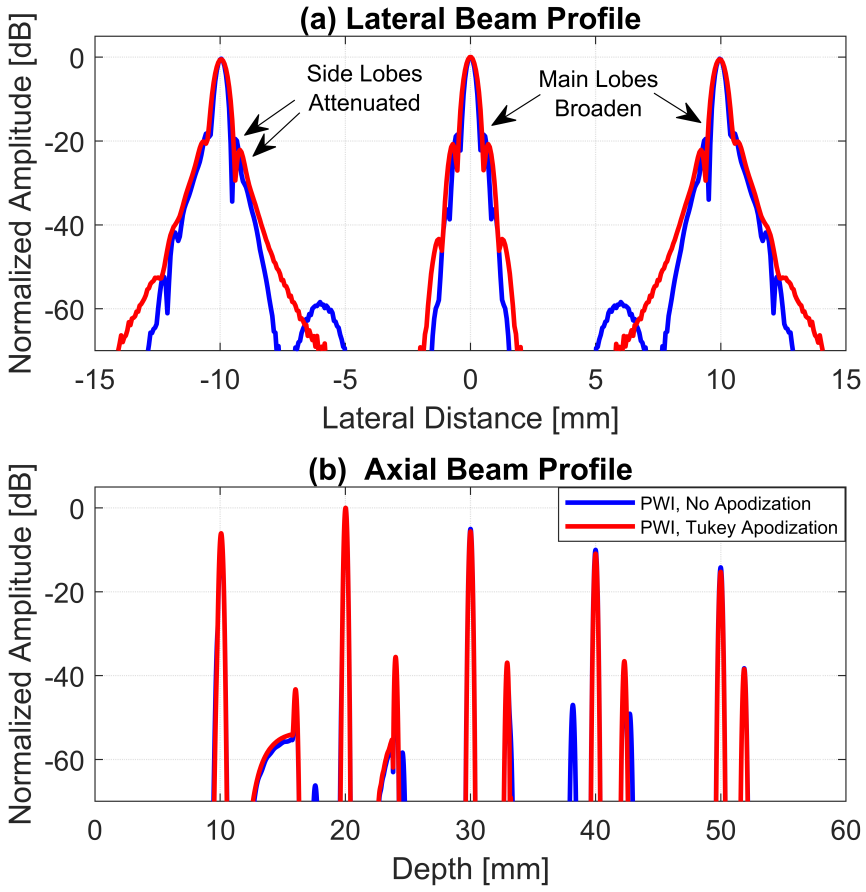

Figure 2.13: Beam profiles for PWI a) in the lateral direction at the 50 mm depth and b) in the axial direction along $x = 0$ mm with and without the Tukey ($\alpha = 0.5$) apodization window.

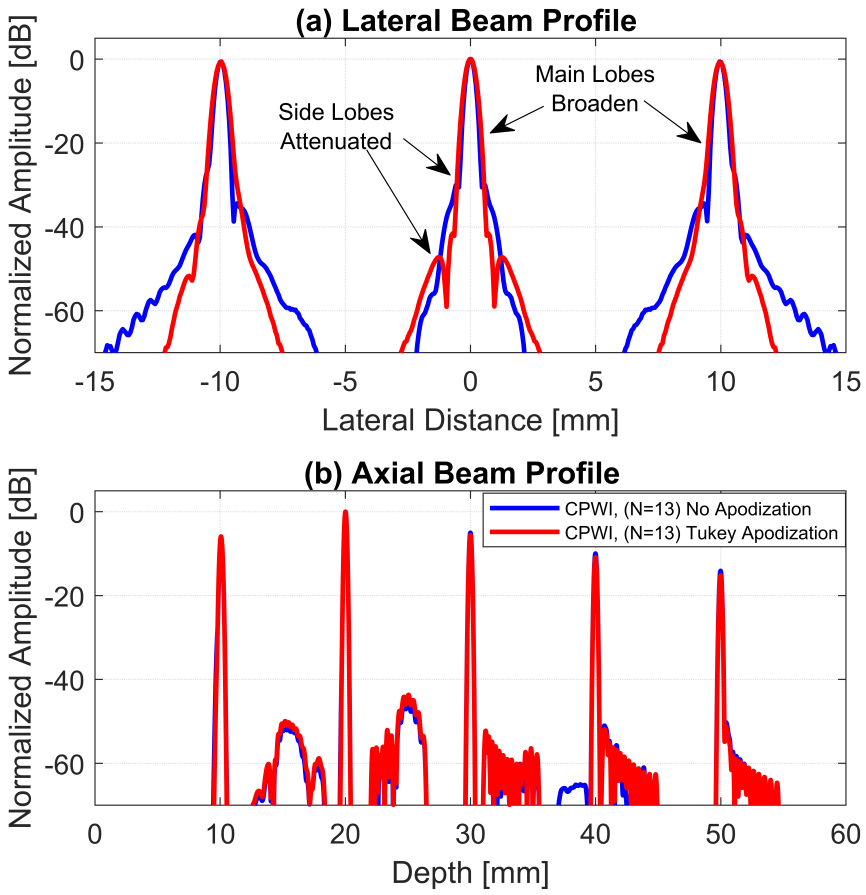

Figure 2.14: Beam profiles for CPWI, $N = 13$, a) in the lateral direction at the 50 mm depth and b) in the axial direction along $x = 0$ mm with and without the Tukey ($\alpha = 0.5$) apodization window.

pitch size of $\lambda/2$ can reduce the appearance of the axial lobes as well. The appearance of the grating and axial lobes can be reduced significantly when the B-mode image displayed within a 50 dB dynamic range.

Phase Error

Phase error is a terminology used to describe the deviation between the aligned RF echo in each element. This happens mainly due to two reasons. Firstly, it is because of the non-ideal physical transducer characteristics and the second reason is the non-uniform speed of sound in the imaging medium Hemmsen *et al.* (2010); Karaman *et al.* (1993). The characteristics of each transducer are defined by a fixed central frequency, limited bandwidth, damping and sensitivity. Each transducer is unique and none of them are same Cowell & Freear (2008a). At the same time, not all elements in a transducer respond or vibrate equally and there is a deviation in between of them Hansen & Jensen (2012).

In this thesis, only the phase error caused by the non-ideal physical transducer characteristics will be discussed. But the proposed solutions, adding a sign-reversed lag to the RF signals can be applied to correct the phase errors caused by the speed of sound as well.

In an ideal case, it is expected the calculated time delays added to the received RF signals will align those RF signals before coherent summation. However, in a real scenario the aligned RF signals are not always in phase due to the above reasons. Many techniques have been proposed to estimate the phase error in ultrasound B-mode imaging. Some of the estimation techniques are the speckle brightness method Nock *et al.* (1989); Trahey *et al.* (1990) and the autocorrelation technique Hansen & Jensen (2012).

In order to analyse the effect of the phase error on PWI, a study was conducted on the wire targets located inside the degassed and deionized water. Performing ultrasound imaging in water is an advantage since the medium attenuation is very low and no other scattering except that from the wire point targets. The experiments were conducted with the parameters shown in Table 2.2 except that the speed of sound inside the water was 1482 m/s at the room temperature of 22° C. The wire targets were imaged with PWI and beamformed with DAS. The B-mode image was log-compressed and displayed with a dynamic range of 50 dB as shown in Fig. 2.19.

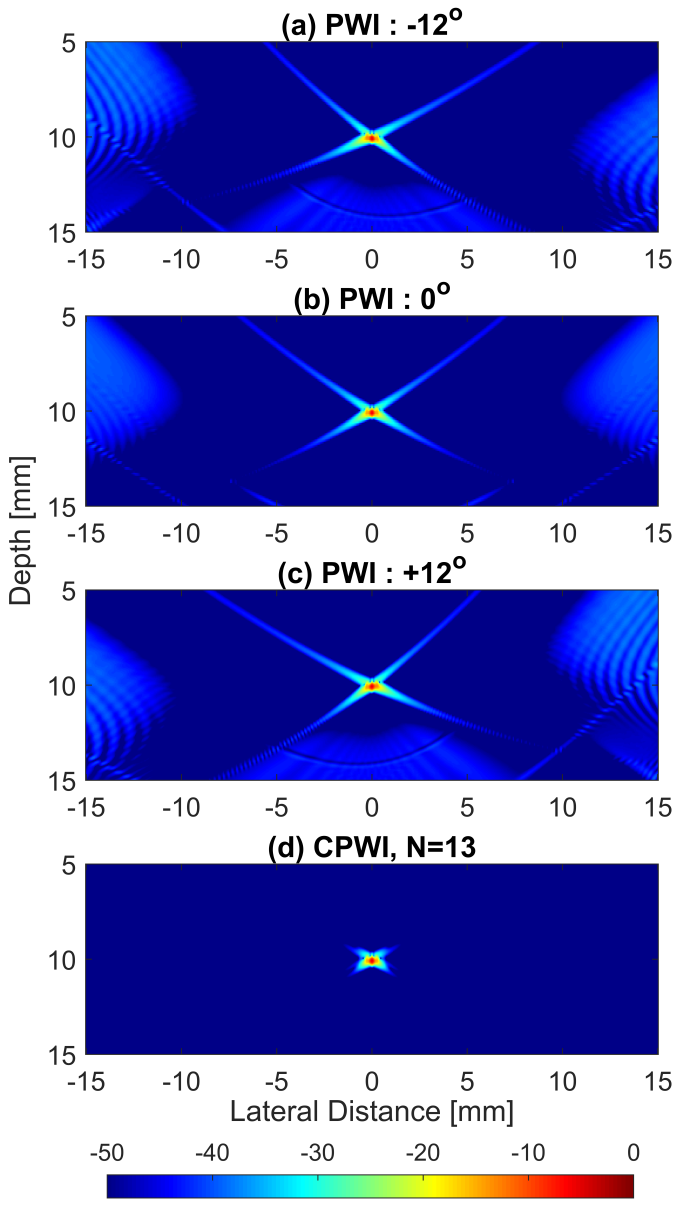

Figure 2.15: Results from the Field II simulation performed on a point target located at the 10 mm depth. No apodization was applied to any of the PWs steered at a) $-12°$, b) $0°$, c) $+12°$, d) CPWI, $N = 13$. The grating lobes are no longer visible with compounding. The simulation setup is given in Table 2.2 for the pitch size of λ.

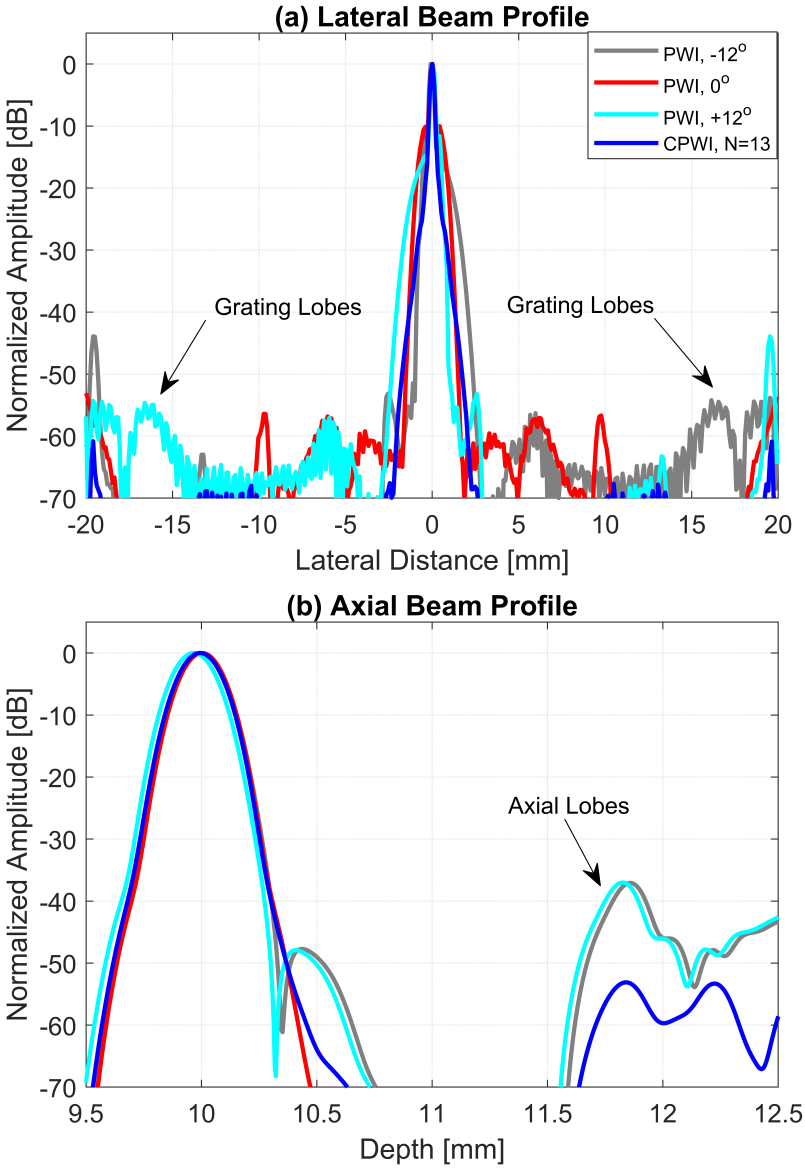

Figure 2.16: a) Lateral beam profile and b) axial beam profile for Fig. 2.15.

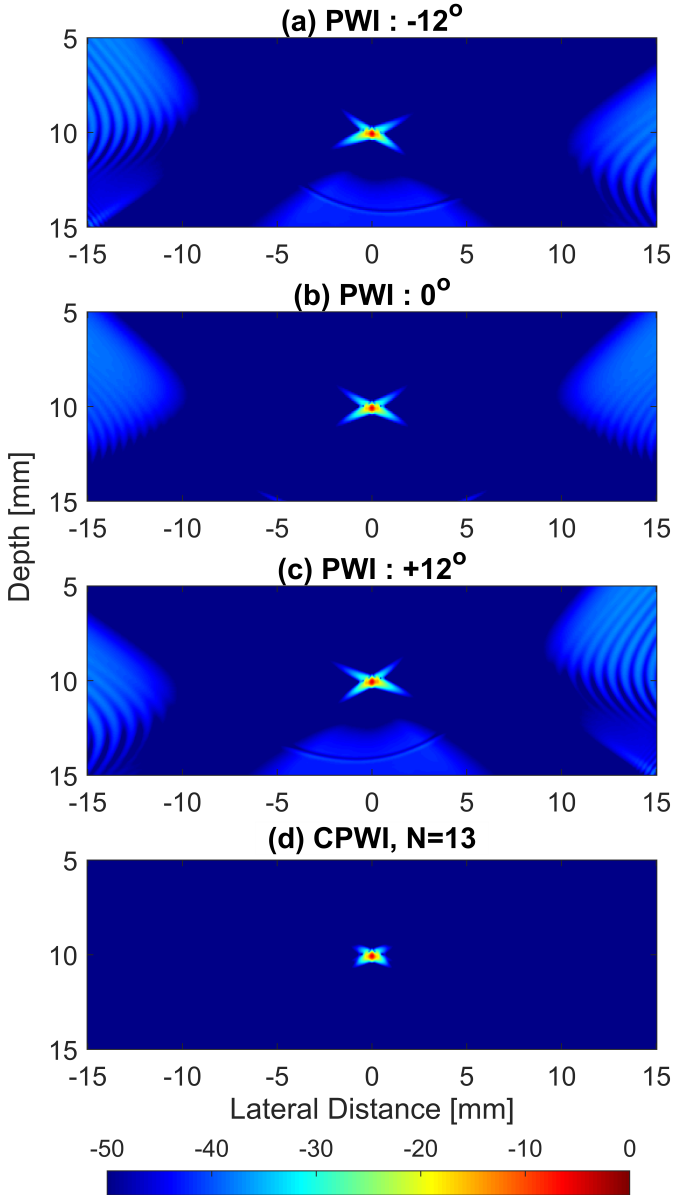

Figure 2.17: Results from the Field II simulation performed on a point target located at the 10 mm depth. Tukey apodization with $\alpha = 0.5$ was applied to PWs steered at a) $-12°$, b) $0°$, c) $+12°$, d) CPWI, $N = 13$. The grating lobes are no longer visible with spatial compounding. The simulation setup is given in Table 2.2 for the pitch size of λ.

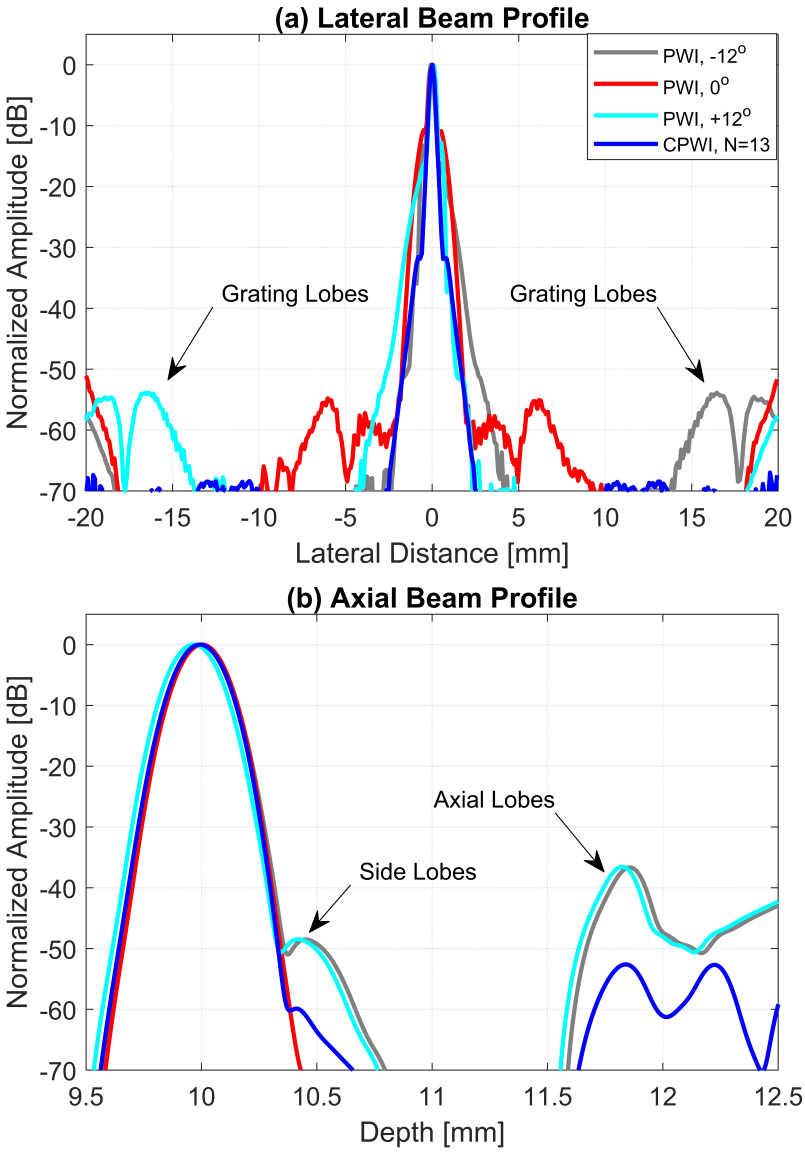

Figure 2.18: a) Lateral beam profile and b) axial beam profile for Fig. 2.17.

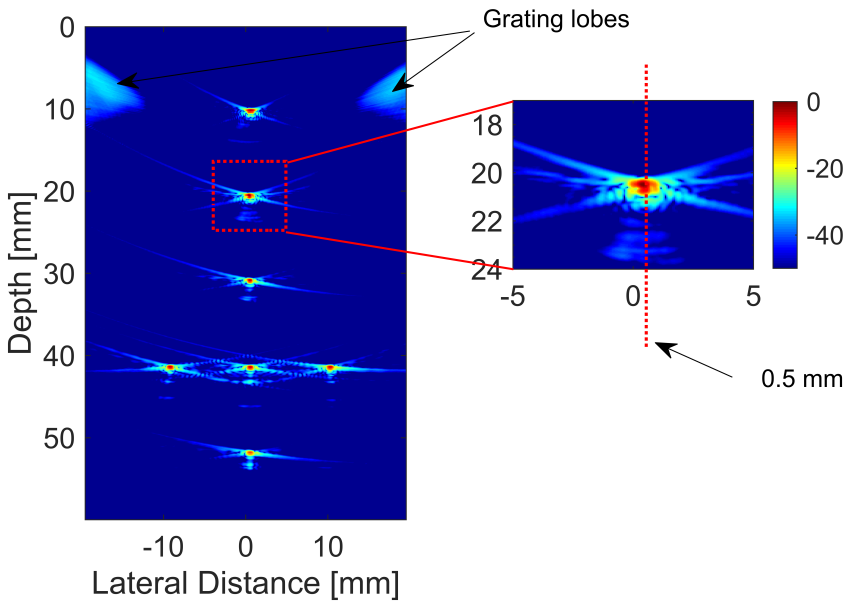

Figure 2.19: The B-mode image of point targets beamformed with DAS obtained with PWI. The red dashed line marked on the point target at 20 mm depth to show the imaging line chosen for phase error analysis.

The B-mode image was formed line by line with different sets of time delays assigned to the same received RF signals according to equation 2.10. The computed time delays were added to the received RF signal $s_i(t)$, giving the aligned RF signal $v_i(t)$ which can be represented by the following equation:

$$v_i(t) = s_i(t - \tau_i(x, z)) \tag{2.15}$$

The aligned RF signals for the imaging line located at $x_f = 0.5$ mm for the wire target at the 20 mm depth have been used to analyse the effect of phase error. In an ideal case, aligning the RF signals for the central imaging line, for a wire target located at the centre of the imaging medium, is expected to produce a set of RF signals in a straight line form parallel to the face of the transducer. Thus, any deviation in the aligned RF signals can be considered as the result of phase error. A portion of the aligned RF signals obtained for the wire target at the 30 mm depth is shown in Fig. 2.20(a). It can be seen that the signals were not perfectly straight (aligned) and still maintained the parabolic shape of the Rx echo signal. Fig. 2.20(b) shows the RF

Table 2.5: Phase error.

	80 MHz		1600 MHz	
	Time, ns	Distance, μm	Time, ns	Distance, μm
Max. Phase Error	50	37	53.13	39.37
Total Phase Error	3450	2560	3462.5	2565.7

signals from the elements 1, 64 and 128. Qualitatively, it can be seen that all of the RF signals on those elements were not in-phase with each other.

The phase deviation between the aligned RF signals, $v_i(t)$ on all the elements were calculated by applying cross-correlation techniques relative to the RF signal from element 1, $v_1(t)$. The lags between the RF signals peaks , determine the phase deviation in between the RF signals. The RF signals between elements 1 and 64 have a phase shift of approximately 76° and 38° between elements 1 and 128. The phase error was computed with two different sampling frequencies. The first is the UARP II hardware Rx sampling frequency of 80 MHz and the second is a higher sampling frequency of 1600 MHz produced by up-sampling the time domain signal $v_i(t)$ using the linear interpolation technique. The results obtained with the higher sampling frequency provided more details on the phase error compared to that with the lower sampling frequency. The accurate estimated phase error helps to determine more precisely the number of samples needed to align the RF signals. The result is shown in Fig. 2.21.

The maximum and total phase errors for a single imaging line calculated for 128 elements with the sampling frequencies of 80 MHz and 1600 MHz are given in Table 2.5. The higher sampling frequency provides more accurate results than the lower sampling frequency. The time calculated with a higher frequency shows an increase of 6.26% from 50 to 53.13 ns, while the distance shows an increase of 6.4% from 37 to 39.37 μm. This is because the interpolation function is able to increase the accuracy by adding the missing data Mahmoudzadeh & Kashou (2013).

Once the phase error represented by the lag values was calculated, an sign-reversed lag value was applied to the aligned RF signals in order to compensate for the aberration. The main lobes in the lateral direction have been improved when the aligned RF signals are compensated with both lower and higher frequencies. A significant improvement in main lobes along the lateral direction can be seen on -10 dB and -20 dB

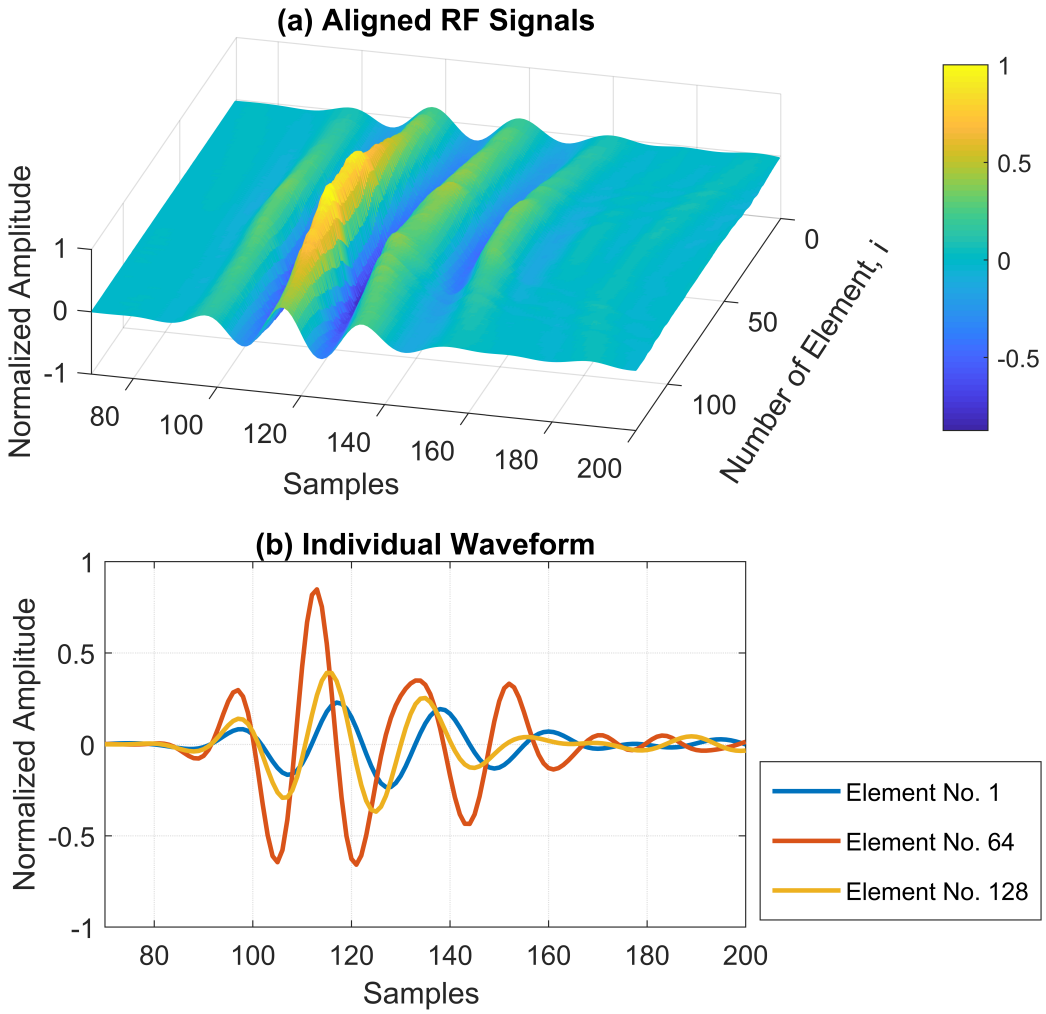

Figure 2.20: a) The aligned RF signals for the imaging line at $x_f = 0.5$ mm at the 20 mm depth and b) the individual waveform for the elements 1, 64 and 128.

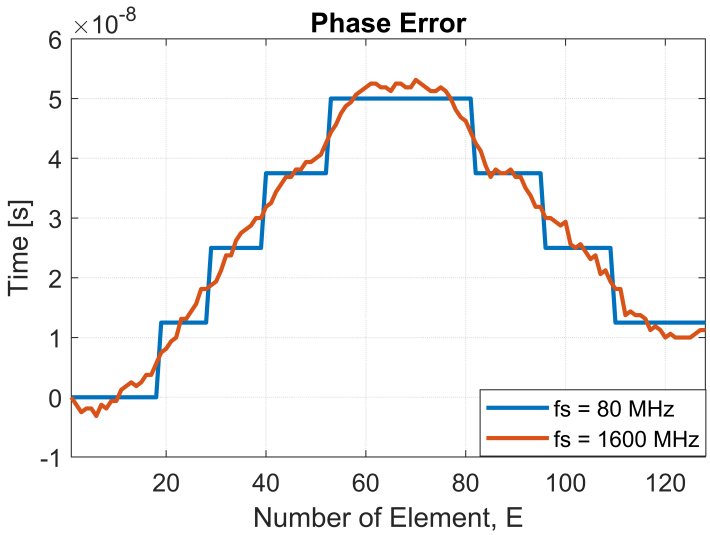

Figure 2.21: Phase error measured on the aligned RF signals relative to the first element for the imaging line of 0.5 mm in the lateral direction as shown in Fig. 2.19.

levels as shown in Fig. 2.23. However, the peak side lobes (PSLs) have increased from −30 dB to −20 dB after the correction. The small amount of PSL increment (from −26 dB to −24 dB) can be also seen in the axial direction. In general, increasing the sampling rate to correct for the phase error does not show any change on the main lobes in the axial direction. It can be seen in Fig. 2.22(b) as highlighted in region A, more side lobes and clutter noise are produced on both sides of the wire target. Correcting the phase aberration with both low and high sampling frequencies is able to reduce noise in the lateral direction. This has been highlighted in region B in Fig. 2.22. As a conclusion, the phase corrected signal is able to improve the signal resolution in the lateral direction and reduce the noise level. On the other hand, the side lobes are not totally eliminated and are still visible within the imaging region and the PSL has increased.

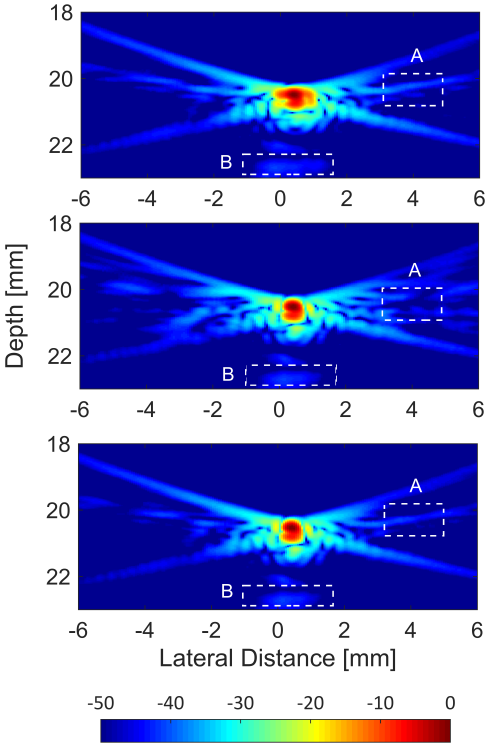

Figure 2.22: B-mode image of the wire target at the 20 mm depth with phase error (Top), after phase error correction with the sampling rate of 80 MHz (Middle) and after phase error correction with the sampling rate of 1600 MHz (Bottom). The dashed box marked with A and B shows the effect of phase correction on noisy regions.

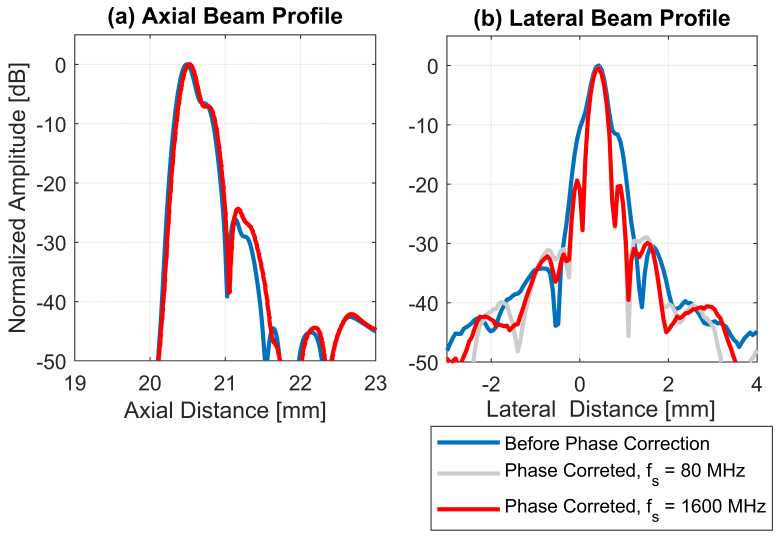

Figure 2.23: Beam profiles of the wire target at the 20 mm depth in the a) axial direction and b) lateral direction before and after correction of phase error.

2.6 Conclusion

A general background study was conducted in this chapter about beamforming, PWI and CPWI. More detailed studies on typical types of noise that impair ultrafast PWI and techniques used to overcome those noise were conducted in this chapter with Field II simulations and experiments. Spatial and frequency compounding techniques are found to be the main method used to obtained images in ultrafast PWI. Those images summed either coherently or non-coherently to form a single B-mode image. Clutter noise is a general terminology used to describe noise from off-axis scattering, edge waves, side lobes, grating lobes and phase errors. Apodization or windowing can be applied on excitation signals or on the aperture to reduce spectral leakage, side lobes and edge waves. The phase error that occurs due to the non-ideal transducer characteristic can be overcome by adding a sign-reversed lag to the aligned RF signals. In general, the proposed solution used to overcome the clutter noise effect in ultrafast PWI involves some trade-offs. Either the spatial resolution or the FR will be reduced during the clutter noise reduction in ultrafast PWI.

Chapter 3

Selection of Excitation Signals and Acoustic Pressure Measurement

In this chapter, the introduction to the ultrasound research platform which was used in this thesis for all experimental measurements was given. The selection of excitation signals and pressure measurements are important since they play major roles when imaging in vivo medium. The advantages and disadvantages of different excitation signals have been discussed.

3.1 Ultrasound Research Array Platform version II (UARP II)

The UARP II is a custom ultrasound imaging system developed by the Ultrasonics and Instrumentation Group at the University of Leeds Cowell & Freear (2008b); Smith *et al.* (2012). It contains a 8-field programmable gate array (FPGA) backplane which connects to a computer running any 64 bit version of the Windows operating system (OS) via a peripheral component interconnect express (PCIe) link. Each FPGA card consists of 16 channels and there are total of 128 channels in the current UARP II. However, the design of this system is highly flexible, and the system can be easily scaled to have more channels. All excitation signals except the square pulse are designed in the Matlab software (The MathWorks Inc., Natick, MA, USA) by using a harmonic re-

duction pulse width modulation (HRPWM) method Smith *et al.* (2013). The sampling rate for Tx is 160 MHz. Those signals are then uploaded to UARP II which excites the connected probe by using a five level switched mode excitation scheme Cowell & Freear (2008a). The received radio frequency (RF) data are acquired at a 80 MHz sampling rate and processed off line using MATLAB. The maximum sampling depth for a single firing can be more than 32768 samples per channel, which equates to a round trip in water of approximately 61 cm with the speed of sound of 1482 m/s at 22° C.

3.2 Selection of Excitation Signals

Three different excitation signals have been explored in order to find the most suitable for in vivo imaging. Each of the excitation signals except the square pulse were uploaded to the UARP II utilizing a five level switching mode with the driving voltages upto ±100, ±50 and 0 Volts. The maximum amplitude for all excitation signals have been fixed to ±100 volts in order to generate maximum pressure values at the elevation focus. The first excitation was a broadband square pulse signal $e_{s1}(t)$ with a 50 ns duration and can be expressed in the analytical form as

$$e_{s1}(t) = \begin{cases} 1, & 0 \leq t \leq T \\ 0, & \text{otherwise} \end{cases} \tag{3.1}$$

where T is the time duration. The Tukey window was applied to the excitation with a weightage of 0.5. Fig. 3.1 shows the square pulse in time and frequency domain. The output of the transducer is known as the result of convolution between the excitation signal and the transducer impulse response. While the echo is a convolution result between the acoustic response and the transducer's impulse response.

Next the 2-cycle sinusoidal signal $e_{s2}(t)$ tapered in the time domain using a Tukey window $a(t)$ with a factor of 0.5 was applied. The signal can be expressed as follows:

$$e_{s2}(t) = \begin{cases} a(t)\sin(2\pi f_o t), & 0 \leq t \leq 2/f_o \\ 0, & \text{otherwise} \end{cases} \tag{3.2}$$

Fig. 3.2 shows the 2-cycle sinusoidal signal in time and frequency domain. Finally, the linear frequency modulated excitation signal $e_{s3}(t)$ with a 10 μs duration, 57%

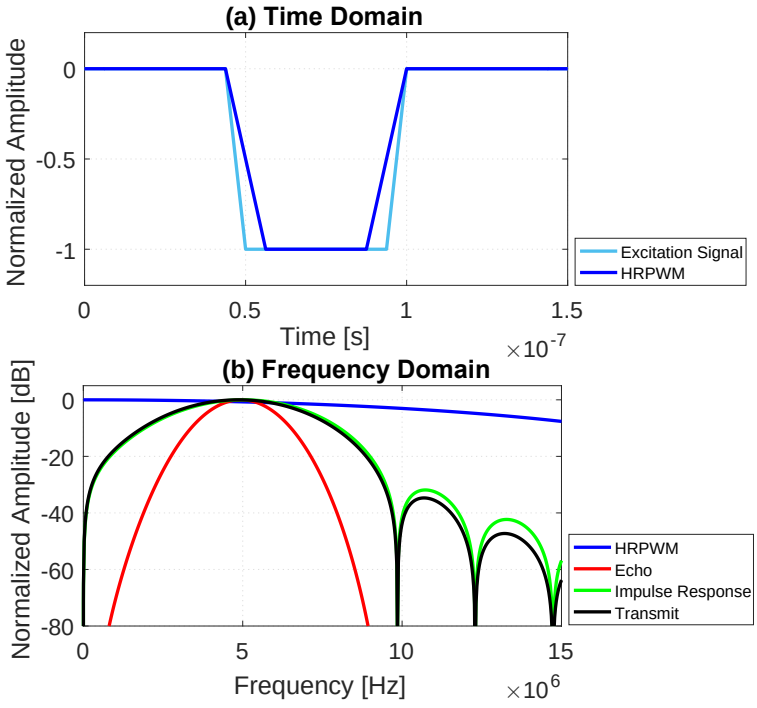

Figure 3.1: Square pulse signal properties shown in a) time domain and b) frequency domain.

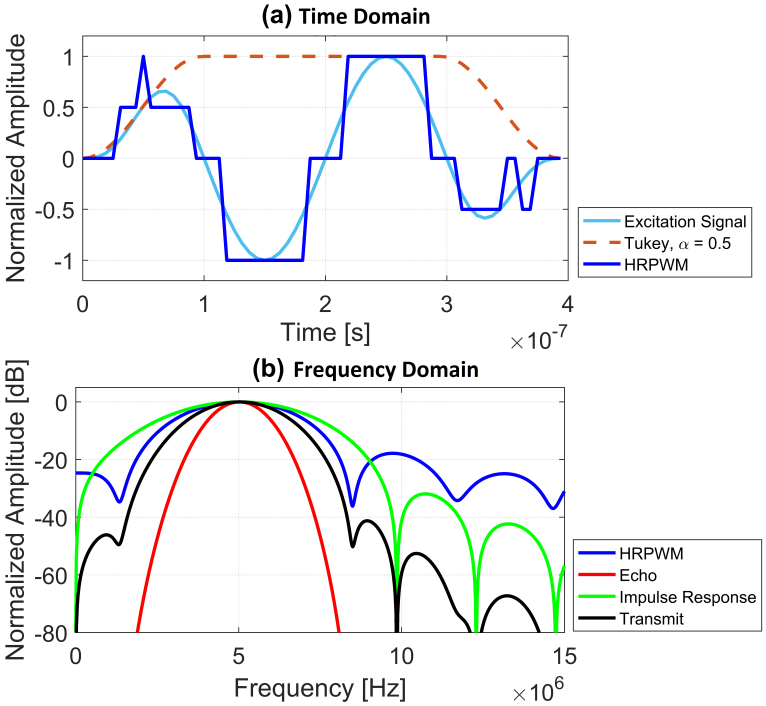

Figure 3.2: Tukey windowed ($\alpha = 0.5$) 2-cycle sinusoidal signal shown in a) time domain and b) frequency domain.

Table 3.1: Excitation signals.

Excitation Signals	Duration	Fractional Bandwidth	Windowing
Square Pulse	50 ns	57%	None
Sinusoidal	0.4 μs	57%	Tukey, $\alpha = 0.5$
Chirp	10 μs	57%	Tukey, $\alpha = 0.5$

bandwidth and tapered with a Tukey window $a(t)$ ($\alpha = 0.50$) was employed in the experiments. The signal can be expressed as follows:

$$e_{s3}(t) = \begin{cases} a(t)\sin(2\pi t(f_o + kt/2)), & 0 \leq t \leq T \\ 0, & \text{otherwise} \end{cases} \tag{3.3}$$

where T is the signal duration, f_o is the centre frequency and k is the rate of the frequency change as given by

$$k = \frac{f_2 - f_1}{T} \tag{3.4}$$

where f_1 is the starting frequency of the sweep and f_2 is the frequency at the end of the time duration T. The chirp signal can be pulse compressed to produce a short pulse by applying matched or mismathed filtering techniques Chun *et al.* (2015); Harput *et al.* (2013). The output of the matched filter has a narrow main lobe with side lobes Cowell & Freear (2008a). In the matched filtering technique, the received signal is cross correlated with the same excitation signal as shown in Fig. 3.3(a). The frequency domain of the mathched filtering output is shown in Fig. 3.3(c).

The summary of all the excitation signals is given in Table II. It should be noted that the convolution model used to form B-mode images is only an approximates of the real excitation signal-tissue interaction Michailovich & Tannenbaum (2006). Real models can be more complex when considering the hard surface condition which can produce strong reflections. However, considering the fact that the regions occupied by strong reflectors are not common in regular ultrasound images, the convolution model is known to approximate very closely the real image formation process. The approximation convolution model has been widely used in numerous methods for ultrasound image reconstructions by Jensen (1991); Taxt (1995).

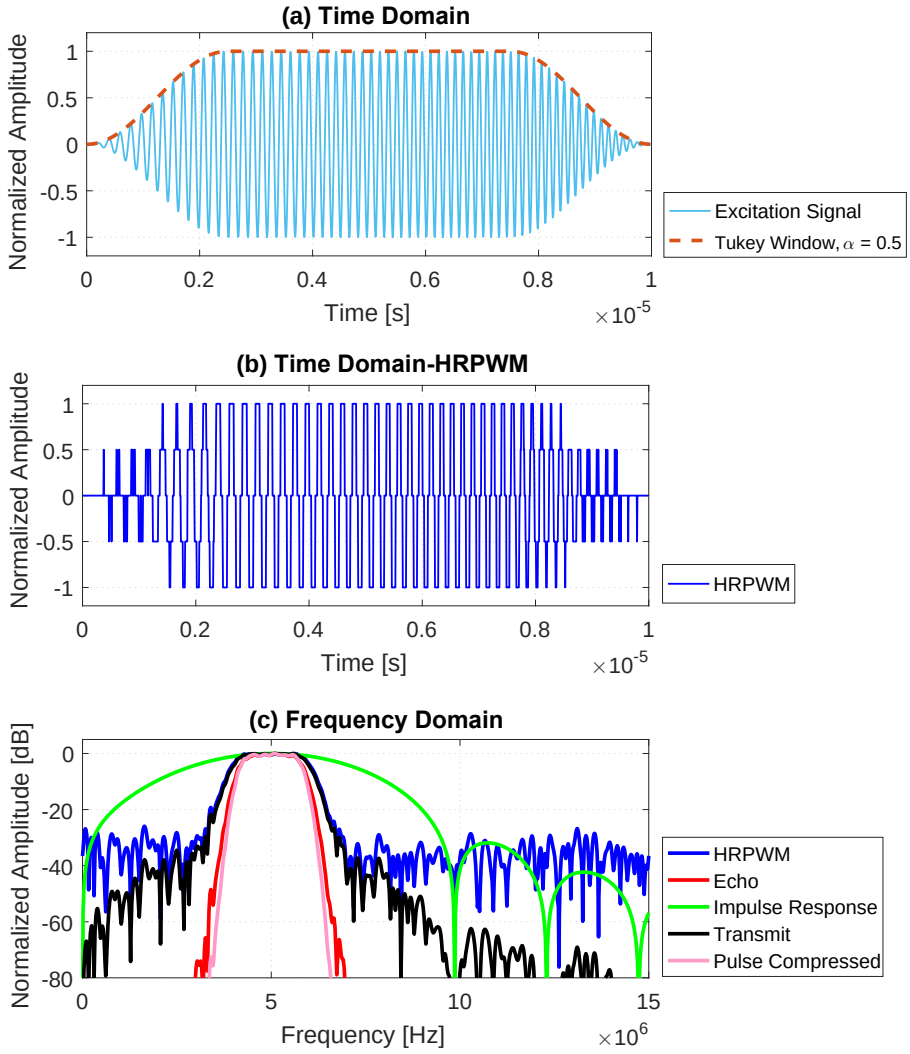

Figure 3.3: Tukey windowed ($\alpha = 0.5$) chirp signal shown in a) time domain b) after modulated with HRPWM and c) frequency domain.

3.3 Pressure Measurement

Before conducting in-vivo experiments, the acoustic pressures need to be measured. The measured parameters need to be within the limits set by the food and drug administrations (FDA) Ter Haar (2011). This is to ensure that the acoustic beam intensities do not cause any thermal damage and cavitation. The most important three parameters that need to be monitored according to the FDA are the mechanical index $MI \leq 1.9$, the spatial peak pulse average intensity $I_{\text{SPPA}} \leq 190\text{W/cm}^2$ and the spatial peak temporal average intensity $I_{\text{SPTA}} \leq 720\text{mW/cm}^2$ Fowlkes (2008); Nelson *et al.* (2009). The MI is a metric used to avoid cavitation and it is unit-less. It is defined as:

$$MI = \frac{p_m}{\sqrt{f_o}} \qquad \leq 1.9 \tag{3.5}$$

where p_m is the peak negative pressure (PNP). I_{SPPA} is the maximum intensity in the beam averaged divided by the pulse duration.

$$I_{\text{SPPA}} = \frac{p_m^2}{2\rho c} \qquad \leq 190\text{W/cm}^2 \tag{3.6}$$

where ρ is the density and c is the speed of sound in the propagating medium. As the measurements were performed inside the degassed and deinonized water, ρ is set to 1000 kg/m^3. The speed of sound c inside the water measured at room temperature 22^o C was 1482 m/s Laugier & Haïat (2011). I_{SPTA} is the maximum intensity divided by the pulse repetition period. It indicates the thermal deposition and is related to the likelihood of cavitation due to the rise of the tissue temperature.

$$I_{\text{SPTA}} = I_{\text{SPPA}} \frac{T}{T_{PRP}} \qquad \leq 720\text{mW/cm}^2 \tag{3.7}$$

The pressure reading of all the three excitation signals with the signal properties as shown in Table. 3.1 have been recorded at the centre of the transducer along the elevation direction as shown in Fig. 3.4. The pressure waveform emitted by the transducer was measured by using a 0.2 mm needle hydrophone (Model 1574, Precision Acoustic, Dorchester, UK). The needle hydrophone was attached to the submersible preamplifier (Model PA07093, Precision Acoustic, Dorchester, UK). The submersible preamplifier was connected to a DC coupler (Model 692, Precision Acoustic, Dorchester, UK) and the signal output was displayed and recorded with a oscilloscope (Model MSO-S 104A,

Agilent Technologies, California, United States) with the sampling rate of 10 GS/s. The complete setup for the pressure measurements is shown in Fig. 3.5.

The measurement was performed at the 20 mm depth where the maximum PNP occurs at the elevation focus. The raw data recorded from the hydrophone in voltage formats were converted into acoustic pressures by using the following equation:

$$p_m = \frac{V}{m(f)} \tag{3.8}$$

where V is the measured voltage in mV, and $m(f)$ is the sensitivity of the hydrophone as a function of frequency in mV/MPa. The uncertainty of this 0.2 mm needle hydrophone was 14%. The water attenuation coefficient value is far smaller than any other tissue or material which falls in between 0.15 to 20 dB cm^{-1} MHz^{-1} Azhari (2010). The in situ pressures were then estimated with a derating factor of 0.3 dB cm^{-1} MHz^{-1}, corresponding to a linear factor as given by Fowlkes (2008); Nightingale *et al.* (2015):

$$p_d = \exp(-0.069 f_c z_f) p_m \tag{3.9}$$

The MI measured for all the three excitation signals are below the recommendation value of 1.9 set by the FDA. The highest MI value is 0.55 for the 10 μs chirp signals while the lowest is 0.22 for the square pulse signal. The I_{SPTA} value for the 10 μs chirp signal is 3778 mW/cm^2, which is far more than the maximum value of 720 mW/cm^2. There are two reasons for this high value. The first reason is the longer pulse duration of 10 μs within a single PRP and the second reason is the high FR of 37000 Hz (at 20 mm depth, c = 1480 m/s). In order to comply the FDA requirements, either the pulse duration or the FR shall be reduced if the pressure has been fixed. Other FDA limitsd are given in Table 3.2.

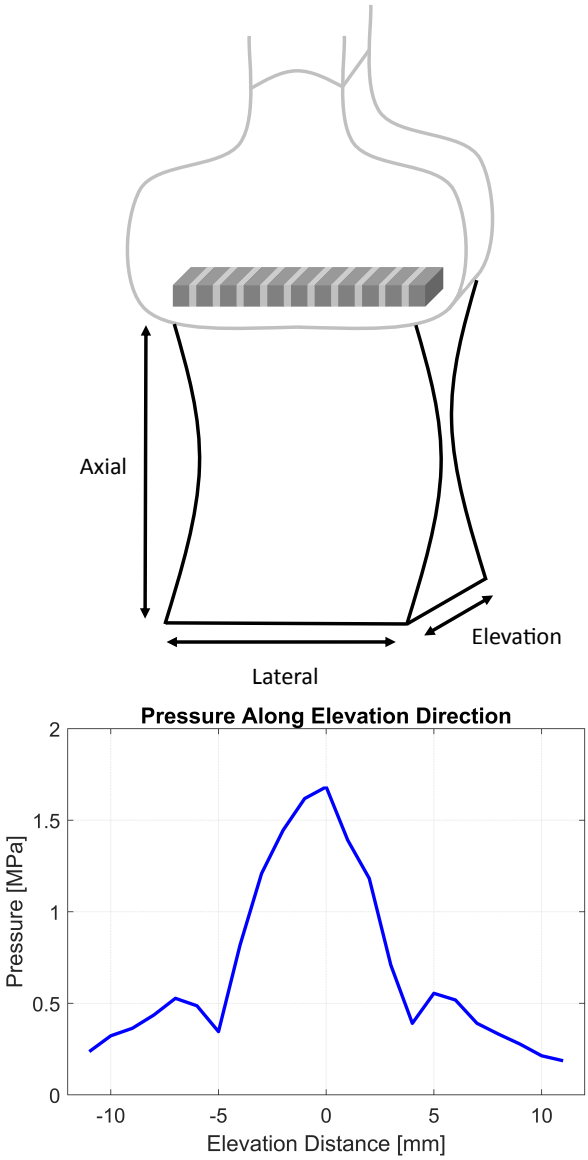

Figure 3.4: Maximum pressure points along the elevation, y_f direction at the 20 mm depth has been measured and used as reference points along the elevation direction in order to measure the PNP for all the excitation signals. The pressure in the elevation direction measured for with a step of 0.1 mm.

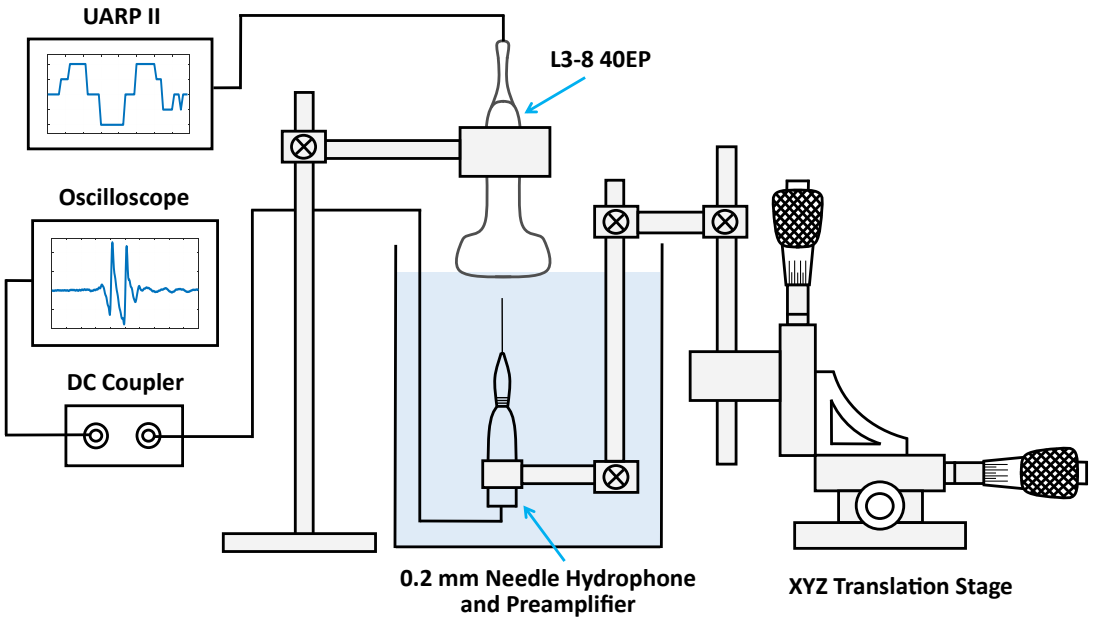

Figure 3.5: Pressure measurement setup.

Table 3.2: FDA Standard for Safety Consideration

Metrics	p_m, MPa	p_d, MPa	MI, -	I_{SPPA}, W/cm^2	I_{SPTA}, mW/cm^2
Square Pulse	0.98	0.49	0.22	1.63	3
2-Cycle Sinusoidal	1.55	0.78	0.35	4.13	61.1
10 μs Chirp	2.43	1.22	0.55	10.2	3778
FDA Standard	-	-	1.9	190	720

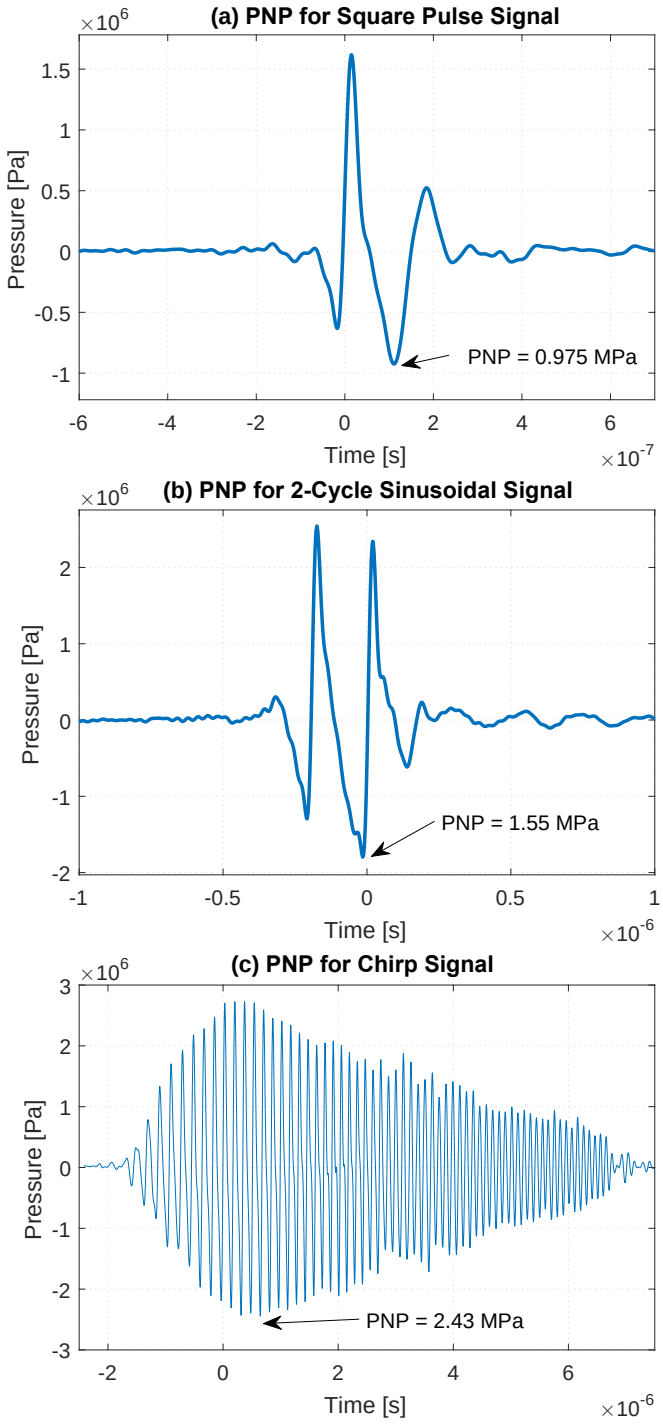

Figure 3.6: Peak negative pressures at 20 mm depth measured at the maximum elevation focusing point for square pulse, 2-cycle sinusoidal and chirp excitation signals.

3.4 Discussion and Conclusion

Three different types of excitation signals, square pulse, 2-cycle sinusoidal and chirp have been investigated in this chapter. Each of the excitation signals has their own advantages and disadvantages. Square pulse with shortest duration is able to produce high axial resolution but the pressure is relatively low compared to the sinusoid and chirp. The sinusoid on the other hand has the higher energy than the square pulse and is able to penetrate deeper in the scanning medium with a compressed axial resolution Tole *et al.* (2005). Chirp excitation signals are well known for its ability to improve the image SNR and penetration depth whilst retaining the axial resolution Harput *et al.* (2015). The biggest challenge in chirp coded imaging is to design its matching filter. This is because the non-linearity in the imaging medium causes shifts in frequency on the echoes which will directly affect the design of the matched filter Harput *et al.* (2015). Chirps also produce the highest amount of MI, SPPA and SPTA intensities among all investigated signals. Those values can be lowered by reducing the transmitted voltage, FR and pulse duration.

It is found that the excitation signal duration can influence the pressure measurements and SPPA. The FR can influence the SPTA. A high PNP can be hazardous because it can produce cavitation and thermal heating. Thus, by considering advantages and disadvantages of all investigated excitation signals, the 2-cycle sinusoidal signal has been selected for all simulations and experiments in this thesis.

Chapter 4

Filter Delay Multiply and Sum Beamforming

In this chapter, the new filtered delay multiply and sum (FDMAS) beamforming technique has been discussed in detail. The effect of altering the imaging point step size in the lateral direction on FDMAS was studied. The performance of FDMAS was evaluated in this chapter by fine-tuning the lateral step size to find its optimal value. To demostrate the effect of altering the lateral steps in the lateral direction on FDMAS, measurments were performed on point targets, anechoic and human *in-vivo*. All results obtained from FDMAS have been compared with those from DAS.

4.1 Introduction

As an alternative to delay-and-sum DAS beamforming, a novel beamforming technique called FDMAS was introduced recently to improve ultrasound B-mode image quality. The initial process in FDMAS is the same as that in DAS. However, unlike in DAS, the aligned RF signals will undergo a process similar to the autocorrelation function, which can be represented by the following equation Matrone *et al.* (2015):

$$r_{\mathrm{DMAS}} = \sum_{i=1}^{E-1} \sum_{m=i+1}^{E} \mathrm{sgn}\{v_i(t)v_m(t)\} \times \sqrt{|v_i(t)v_m(t)|}, \tag{4.1}$$

where $v_i(t)$ is the aligned RF signal on the i-th element, E is the total number of elements on the imaging probe and $m = i + 1$ is the aligned RF signal at the m-th element. The multiplication of two RF signals with the same frequency content will

eventually produce second harmonics ($f_o + f_o$) and direct current components ($f_o - f_o$). Thus, a band-pass filter is applied to r_{DMAS} to extract its second harmonics ($2f_o$), and finally, r_{FDMAS} is obtained.

4.1.1 Simulation and Experimental Setup

To validate the FDMAS beamforming technique, Field II simulations and laboratory experiments were performed on points targets, anechoic cysts and human *in-vivo*. The setup for both simulations and experiments are the same as given by Table 2.2. Data were collected from seven different point targets as shown in Fig. 4.1(b). The simulated cyst phantom had cysts located at 30 mm, 40 mm and 50 mm with diameters of 2 mm, 4 mm, and 6 mm, respectively. 100,000 scatters (20 scatterers/mm^3) were distributed randomly as shown in Fig. 4.7(a). As for experimental work, several measurements were performed on nylon wire targets with a diameter of 120 μm, a tissue-mimicking phantom (040GSE, CIRS, Virginia, USA) and *in-vivo*. The anechoic sections of the tissue-mimicking phantom (depth: from 10 mm to 50 mm) as shown in Fig. 4.2 and the wire target (depth: from 10 mm to 50 mm) as shown in Fig. 4.1 were imaged. *In-vivo* data were collected from the cross section of the right common carotid artery of a healthy volunteer as shown in Fig. 4.3. A 128-element linear array transducer (L3-8/40EP, Prosonics Co. Ltd., South Korea) with a centre frequency of 4.79 MHz and a 57 % bandwidth at -6 dB was used to collect all the data. A two-cycle sinusoidal excitation signal with a centre frequency of 5 MHz was digitised with the ultrasound array research platform II (University of Leeds, UK) Cowell & Freear (2008b); Cowell *et al.* (2016); Smith *et al.* (2012). The received signals were sampled at 80 MHz. The complete experimental parameters are provided in Table 2.2. No apodization is applied on the elements along the lateral direction during transmission and reception for simulations and experiments.

4.1.2 Performance Evaluation

The performance of the final B-mode images produced using the DAS and FDMAS beamforming techniques can be described by: spatial resolution in axial and lateral directions, peak side lobe (PSL), contrast-to-noise-ratio (CNR) and contrast ratio (CR). To determine the image axial resolution (AR), lateral resolution (LR) and PSL, the main lobes of the point target represented by the nylon wire in degassed and deionized

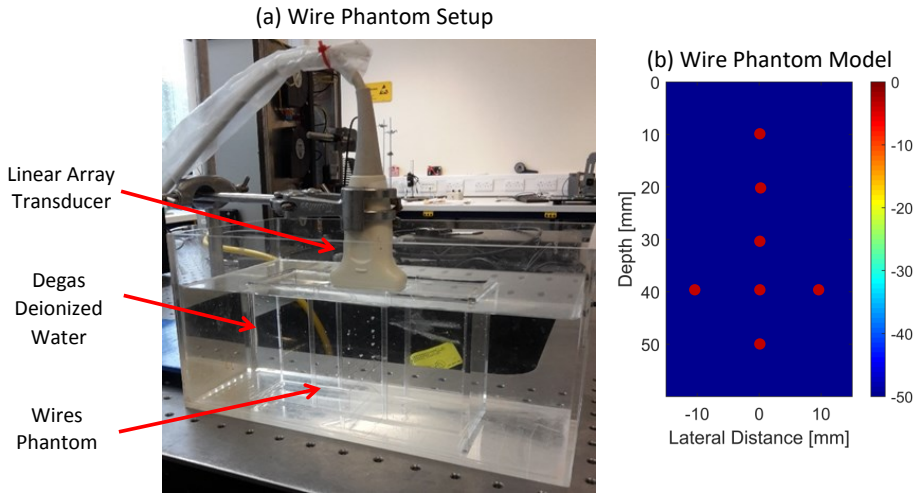

Figure 4.1: a) Experimental setup to scan wires phantom inside the degassed and deionized water and (b) the model of the wire phantom.

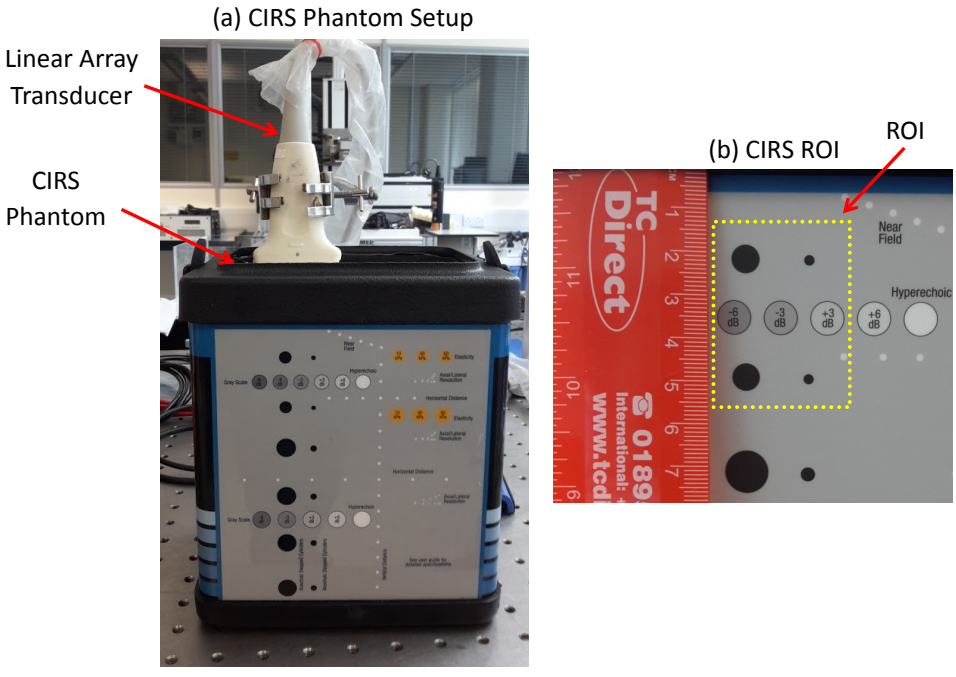

Figure 4.2: a) Experimental setup to scan the cyst region inside the tissue-mimicking CIRS phantom and (b) the region of interest (ROI) in close-up.

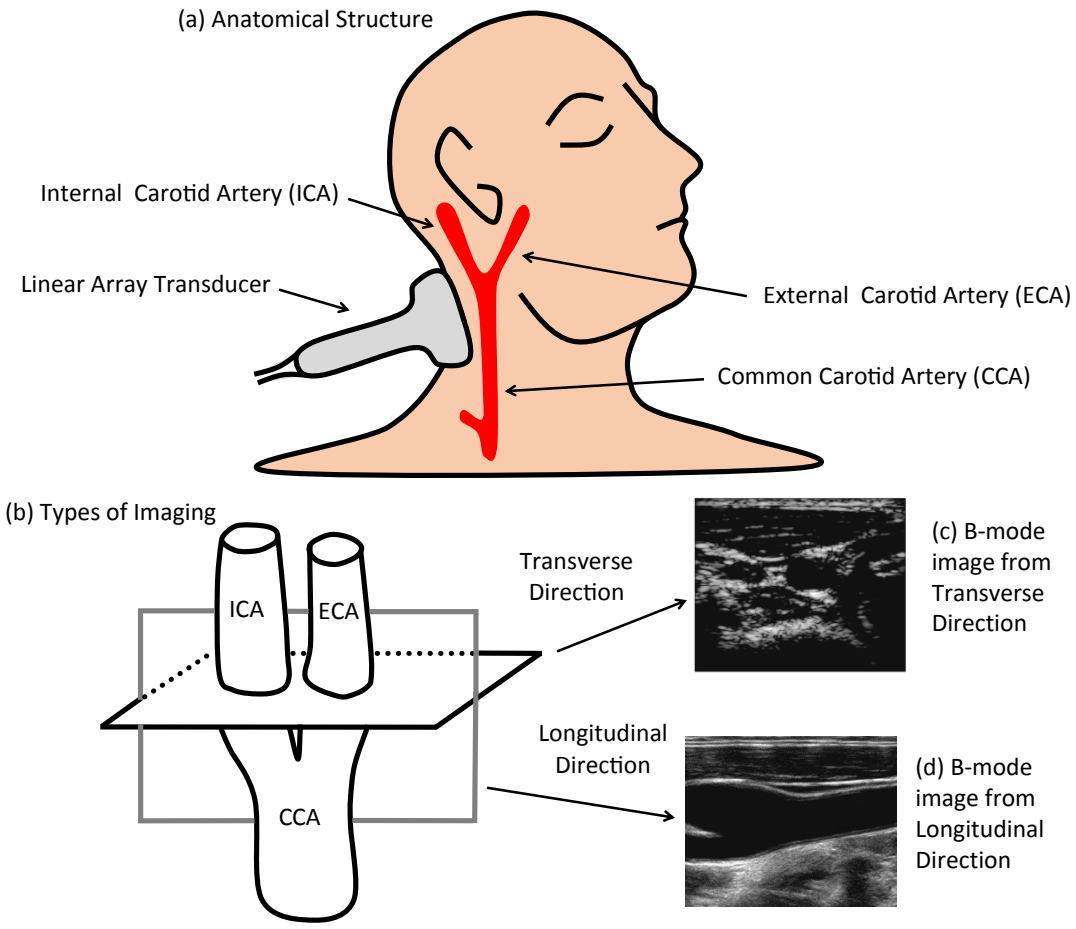

Figure 4.3: a) General anatomical structure of the common carotid artery, internal carotid artery and external carotid artery located on the right side of the neck, b) Two different ways on positioning the transducer face, transverse and longitudinal direction for imaging the carotid artery, c) The B-mode image obtained from the transverse direction Jensen *et al.* (2016a) while d) obtained from the longitudinal direction Tegeler *et al.* (2005).

water were measured at −6 dB and −20 dB using the function developed in Harput *et al.* (2014). The measurement was performed on a wire with a diameter of 120 um at a depth of 30 mm as shown in Fig. 4.1(b). PSL is defined as first side lobes peaks in axial and lateral directions. CR is used to express the detectability of the object contrast between the ROI inside the cyst and its background. The image CR of the anechoic cyst was computed on the CIRS phantom at a depth of 15 mm by creating two different regions with the same dimensions as shown in Fig. 4.2(b). The first region is located inside the cyst, whereas the second region is located outside the cyst at the same depth. This condition ensures that the attenuation caused by depth does not affect the measurements. A high CNR value means that the cyst can be visualized easily and there is less variation on acoustic noise. Both CR and CNR equations are given by Matrone *et al.* (2015); Ullom *et al.* (2012)

$$\mathrm{CR(dB)} = 20\log_{10}\left(\frac{\mu_{\mathrm{cyst}}}{\mu_{\mathrm{back}}}\right), \tag{4.2}$$

$$\mathrm{CNR(dB)} = 20\log_{10}\left(\frac{|\mu_{\mathrm{cyst}} - \mu_{\mathrm{Back}}|}{\sqrt{({\sigma_{\mathrm{cyst}}}^2 + {\sigma_{\mathrm{Back}}}^2)}}\right) \tag{4.3}$$

where μ_{cyst} and μ_{back} are the mean image intensities inside and outside of the cyst, respectively.

4.1.3 Result and Discussion

In this section, only the FDMAS results from simulations for PWI ($N = 1$, $0°$) are presented qualitatively without any numerical values. This is mainly to avoid redundancy or repetition with FDMAS results. The B-mode images for the point target bemaformed with DAS and FDMAS are presented in Fig. 4.4(a) and (b), respectively. Grating lobes at approximate −40 dB level that appears at the 10 mm depth as shown in Fig. 4.4(a) with DAS are no longer visible in Fig. 4.4(b) when beamformed with FDMAS. All the side lobes in the lateral direction that appear on the point targets also have been significantly reduced with FDMAS. This can be seen from lateral beam profiles plotted for point targets located at the 40 mm depth presented in Fig. 4.4(c). The

main lobes along the lateral direction are also narrowed using FDMAS when compared to DAS. In the axial direction, the beam profiles as shown in Fig. 4.4(d) for FDMAS shows the same pattern as that using DAS. However, with FDMAS, the signal intensity drops gradually with depth. This can be associated with FDMAS signals obtained from 2nd harmonic components that have lower amplitude levels when compared to DC components as shown in Fig. 4.5. Once equation 4.1 was performed on the DAS signals, the DC component and 2nd harmonic have been produced and a band pass filter between 8.5 to 11.5 MHz was applied to extract the 2nd harmonic component.

A single point target at the 30 mm depth as shown in Fig. 4.6 has been chosen to show in detail the effects of FDMAS on B-mode imaging. It can be seen that the axial side lobes are higher with FDMAS. The PSL starts to appear at approximately -50 dB and there is no significant change on the main lobes in the axial direction. The PSL along the lateral direction is attenuated from -19 dB with DAS to -37 dB with FDMAS.

The B-mode images for the cysts using DAS and FDMAS are presented in Fig. 4.7 (a) and (b). The contrast for all cysts is improved with FDMAS compared to DAS. This is mainly due to the attenuation of clutter noise inside the cyst anechoic region. The sidelobes that leak into the anechoic regions along the lateral direction mainly reduce the contrast using DAS. The border definition for all cysts with FDMAS has been improved as the edge becomes steeper. This can be seen in Fig. 4.7 (c) and (d).

4.2 Optimal Imaging Point Step Size

Despite the significant amount of research were reported on FDMAS, no in-depth investigation has been conducted on the effect of varying imaging point step size, Δx, in the lateral direction, which is one of the important criteria for determining B-mode image quality. In a previous study Jensen *et al.* (2016b) on compound PWI (CPWI) with spacings or pitch sizes, p (λ or $\lambda/2$), of imaging probes were used whilst maintaining other experimental parameters. The LR measured on the wire targets at full width at half maximum (-6 dB) from a depth of 10 mm to 60 mm obtained using imaging probes with pitch sizes of λ and $\lambda/2$ are nearly the same. Moreover the CR values measured using probes with pitch sizes of λ and $\lambda/2$ on a cyst with a depth ranging from 20 mm to 60 mm do not exhibit any significant difference between them. This previous study

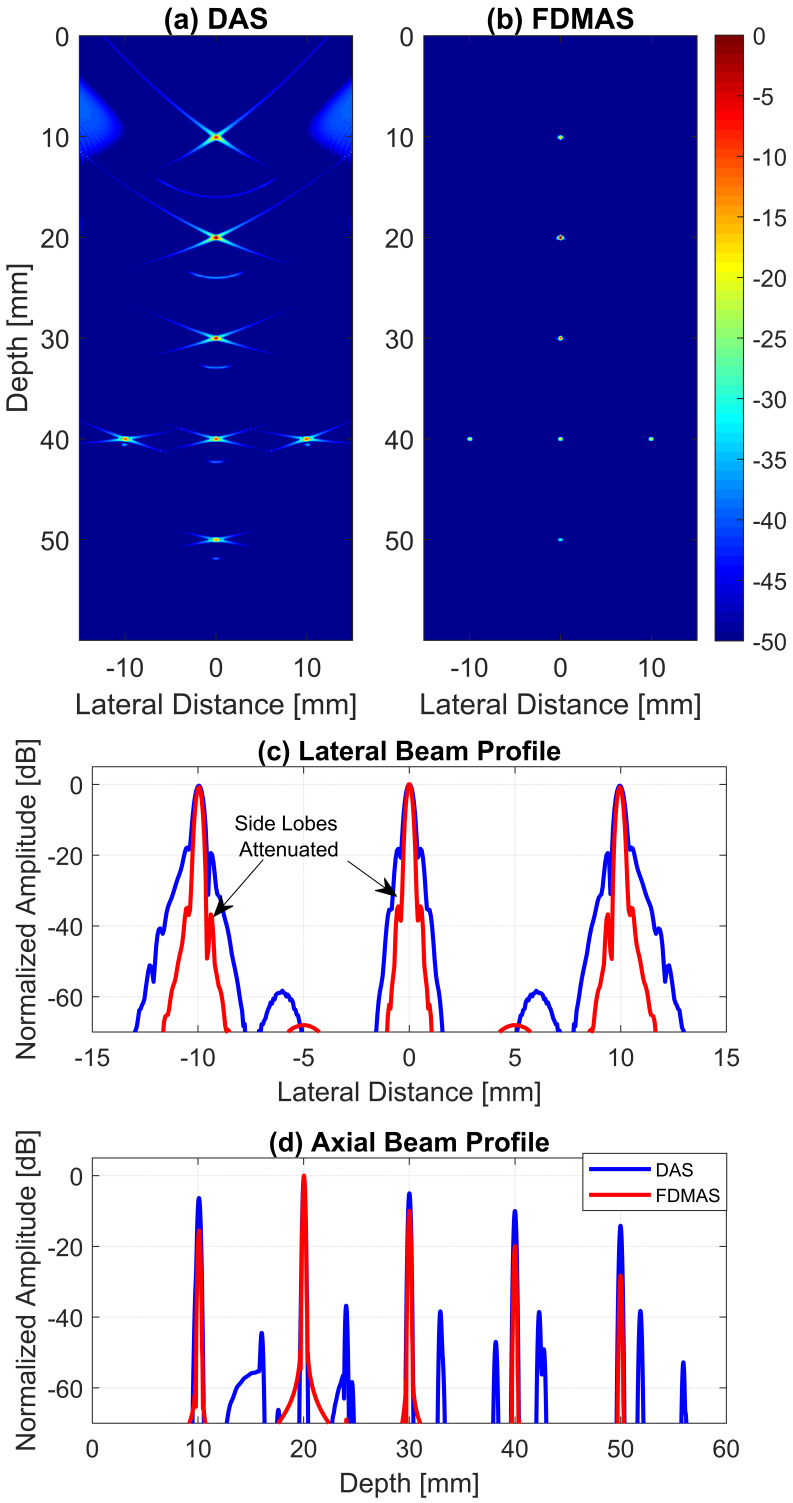

Figure 4.4: Field II simulated PWI for a point target beamformed with a) DAS and b) FDMAS. c) Lateral and d) axial beam profiles with DAS and FDMAS.

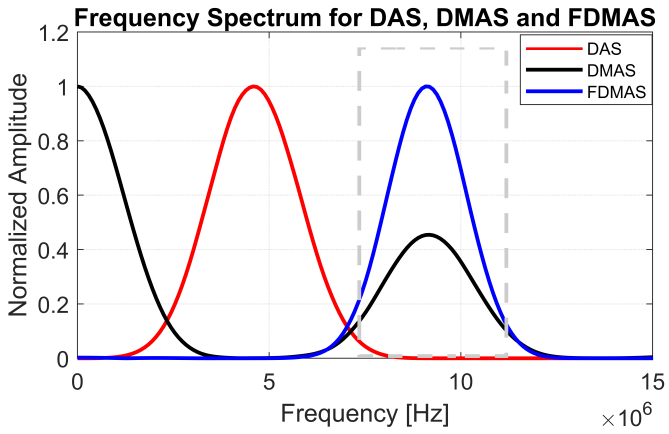

Figure 4.5: The normalized amplitude for the frequency spectrum obtained using DAS, DMAS and FDMAS. The frequency spectrum was performed on a single point target located at the 30 mm depth as shown in Fig. 4.6. The dashed gray color box represents a band pass filter between 8.5 to 11.5 MHz to extract the 2nd harmonic component from DMAS.

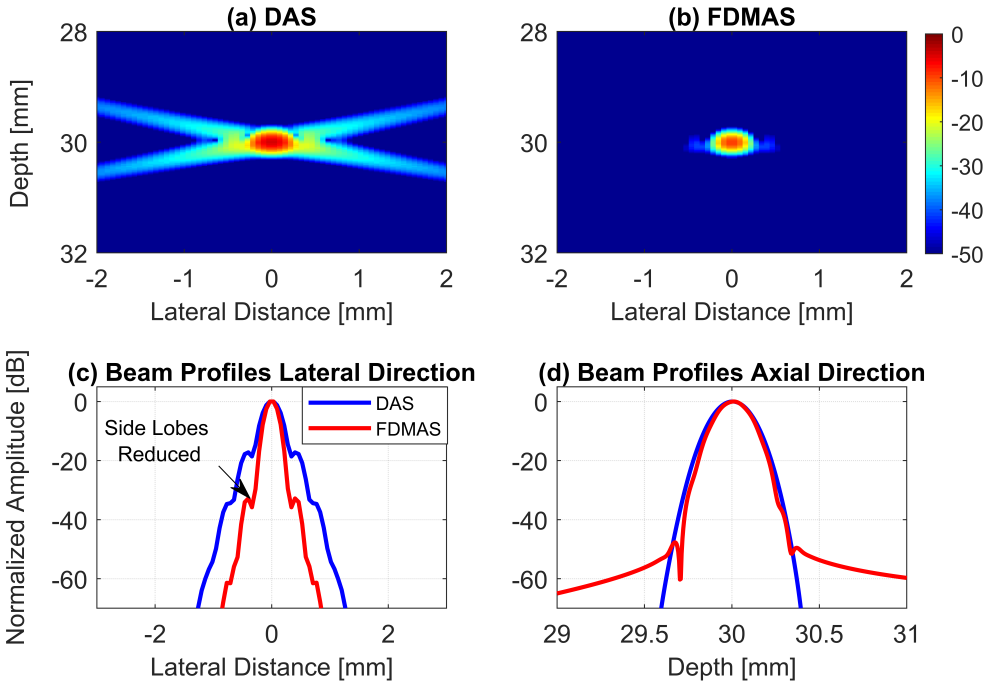

Figure 4.6: PWI for a point target located at the 30 mm depth beamformed with a) DAS and b) FDMAS. c) Lateral and d) axial beam profile with DAS and FDMAS.

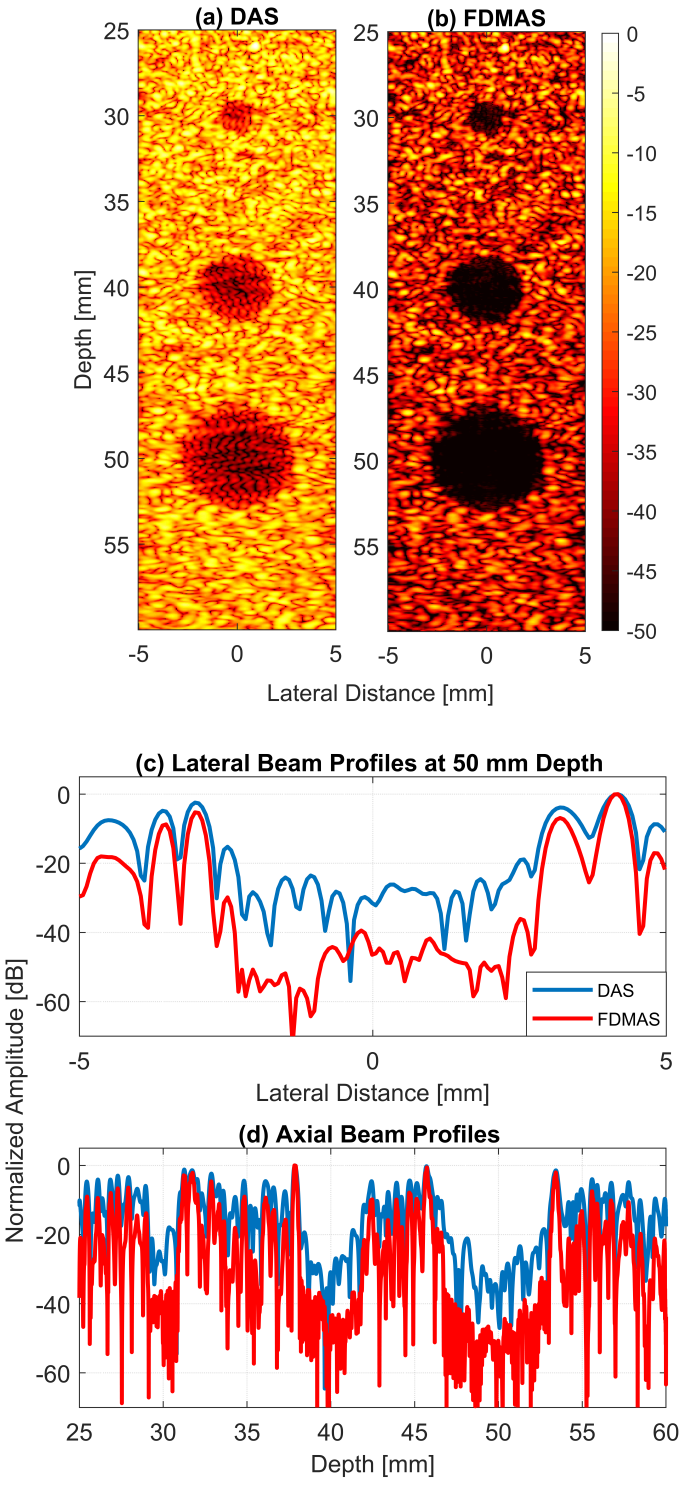

Figure 4.7: Field II simulation with PWI for the cysts located at 30 mm, 40 mm and 50 mm deep using a) DAS and b) FDMAS. c) lateral beam profile for cyst at the 50 mm depth with a 6 mm diameter and b) axial beam profile along $x = 0$ mm.

also showed that the appearance of grating lobes on the imaging medium with a pitch size of λ whilst steering the probes can be reduced effectively through compounding. Furthermore, grating lobes mainly appear in the near-field regions ($\leq$ 10 mm). The final outcome of Jensen *et al.* (2016b) provides a strong hypothesis that beamforming Δx in the lateral direction plays an important role in determining the final quality of B-mode images. This finding has motivated us to further explore the effect of varying Δx in the lateral direction with the recently proposed FDMAS beamforming techniques primarily because the FDMAS algorithm is similar to the autocorrelation process that depends on the lag among radio-frequency (RF) signals in each channel in the lateral direction. Thus, the minimum requirement for Δx in the lateral direction for FDMAS is a subject for discussion. In this study we investigated the effect of varying the imaging point step size on CPWI with the following point targets, a tissue-mimicking phantom and a human carotid artery *in-vivo*. This study is expected to propose the optimised Δx in the lateral direction for FDMAS to improve the B-mode image quality.

The main objective of this work is to evaluate the effect of varying imaging point step size, Δx, in the lateral direction on any number of compounding parameters with the DAS and FDMAS beamforming techniques and not to find the optimum number of compounding parameters in CPWI. Many studies, including Alomari *et al.* (2014); Jensen *et al.* (2016b); Montaldo *et al.* (2009); Toulemonde *et al.* (2015), have proposed a unique number of compounding parameters that provide the best image quality according to their experimental setup. Thus, a particular compounding parameter that will provide the best end results for all image quality indices is impossible to propose. The general rule of thumb in selecting the number of compounding parameters is to minimise it, such that the end results are balanced among the optimum temporal, spatial and contrast resolutions. Several studies, such as Montaldo *et al.* (2009) and Alomari *et al.* (2014), have mentioned that after a certain number of compounding angles, image resolution will no longer improve but will deteriorate instead due to reduced noise cancellation near the main lobe. In consideration of these constraints, the selected number of compounding, N, and the steering angle increments, $\Delta\theta_n$, are shown in Table 2.1 to validate the effect of varying imaging point step size, Δx, on DAS and FDMAS. The sector angles, $[\theta^{\circ}_{max}, \theta^{\circ}_{min}]$, for all compounding are set to $\pm 12^{\circ}$.

4.2.1 Imaging Point Step Size, Δx

The effect of varying Δx during beamforming on B-mode image quality was studied by first calculating the difference in the imaging line angles and then calculating the correlation coefficient between two adjacent aligned RF signals for the second imaging line. Δx is also referred to as the lateral step, λ/g, in this work, where $g = 1$, 2, 3, 4 and 5. The imaging line angle is denoted by $\beta^o_{l_g}$, and the imaging lines are denoted by l.

The angle formed between a set of aligned RF signals and the surface of the transducer is known as the imaging line angle (Fig. 4.8(a)). The $\Delta\beta$ between the imaging lines, $l = 1$ and 2, for the lateral steps, λ and $\lambda/4$, are given by

$$\begin{aligned} \Delta\beta_1 &= \beta^o_{2_1} - \beta^o_{1_1}, \quad \text{for} \quad \lambda; \\ \Delta\beta_4 &= \beta^o_{2_4} - \beta^o_{1_4}, \quad \text{for} \quad \lambda/4; \\ \Delta\beta_1 &> \Delta\beta_4; \end{aligned} \tag{4.4}$$

where $\beta^o_{1_1}$ and $\beta^o_{2_1}$ are the imaging line angles for the aligned RF signals according to equation 2.15 for the first imaging line calculated with $x = -15$ mm and the second imaging line calculated with $x = -15{+}\lambda$ mm for the lateral step of λ. $\beta^o_{1_4}$ and $\beta^o_{2_4}$ are the imaging line angles for the aligned RF signals for the first imaging line calculated with $x = -15$ mm and the second imaging line calculated with $x = -15{+}\lambda/4$ mm for the lateral step of $\lambda/4$.

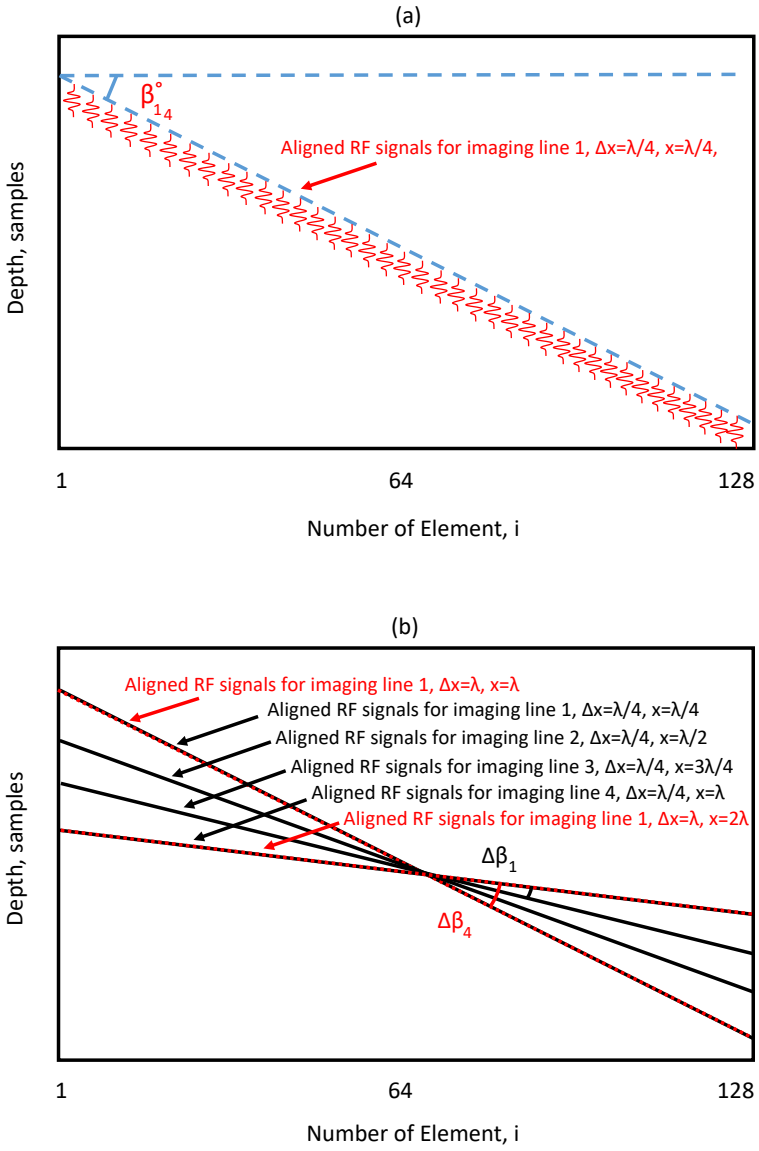

Figure 4.8: Aligned RF signals with different lateral steps are illustrated to show the formation of imaging line angle and difference between the imaging line angles. a) Aligned received RF signals for $E = 128$ elements according to equation 2.15 for imaging line 1 for the lateral step of $\lambda/4$. The imaging line angles formed between the face of the imaging probe and the aligned RF signals highlighted. b) The aligned RF signals for imaging lines 1 and 2 for the lateral steps of λ and aligned RF signals for imaging lines 1, 2, 3 and 4 for the lateral steps of $\lambda/4$ are shown together with difference between the imaging line angles.

The aligned RF signals in Fig. 4.8(a) for first imaging line with the lateral step of $\lambda/4$ illustrated as originated from the echo of a single wire target located at $x = 0$, $z = 40$ mm. The z coordinates for all the three imaging lines is located from the start to the end of the imaging field.

The correlation coefficient, ρ, between two adjacent aligned RF signals is computed on the second imaging line according to the following equation Ruchkin (1965)

$$\rho = \frac{v_1(t)v_2(t)}{\sqrt{v_1(t)^2 v_2(t)^2}}, \tag{4.5}$$

where $v_1(t)$ and $v_2(t)$ are the RF signals from the first ($i = 1$) and second ($i = 2$) elements as given by equation 2.15. The correlation between the two RF signals, as given by equation 4.5, was not calculated on the first imaging line because no change occurred on the RF signals for the imaging line angles for every lateral step. As shown in Fig. 4.8, $\beta^{\circ}_{1_1}$ and $\beta^{\circ}_{1_4}$ are the same for the lateral steps of λ and $\lambda/4$ or any other lateral step as the starting imaging point, in this case, x for all lateral step will always be -15 mm.

In digital signal processing, the autocorrelation between two signals is calculated with a lag that is relative to the starting point of one of the signals. Lag refers to the distance or difference between two points. The multiplication of two RF signals and then summing them at a specific lag is known as short-time autocorrelation Harrington & Cassidy (2012). Lag is commonly represented by the sample numbers. In this work, however lag is assigned to the difference in angles, $\Delta\beta$, between two imaging line angles. The lag between adjacent RF signals along the lateral direction depends on Δx. Instead of aligning all the RF signals of all the elements at one time with the lateral step of λ, all the RF signals will now be aligned with twice the lateral step of $\lambda/2$. Simultaneously, instead of assigning a single grey colour intensity on a particular imaging point, two different grey colour intensities will be assigned with the lateral step of $\lambda/2$ on two different imaging points. The length of an imaging point with the lateral step of λ is equal to two imaging points with the lateral step of $\lambda/2$.

4.2.2 Spatial Sampling Frequency

The temporal sampling theorem states that a signal must be sampled at a minimum sampling frequency of f_s (of period T_s) to avoid aliasing as given by

$$f_s = \frac{1}{T_s} \geq 2f_{s_{max}}, \tag{4.6}$$

where $f_{s_{max}}$ is the maximum incoming signal frequency. Similarly, for the minimum spatial sampling frequency to avoid aliasing or grating lobes as given by Mccowan (2018)

$$f_{x_s} = \frac{1}{p} \geq 2f_{x_{max}}, \tag{4.7}$$

where f_{x_s} is the spatial sampling frequency in samples per meter, and $f_{x_{max}}$ is the highest spatial frequency that can be represented by

$$f_{x_{max}} = \frac{1}{\lambda_{min}}, \tag{4.8}$$

When equation 4.8 is substituted to equation 4.7, we will get

$$p \leq \frac{\lambda_{min}}{2}, \tag{4.9}$$

where λ_{min} is the minimum wavelength of the signal. The occurrence angle of the grating lobe is given by the following equation Ponnle *et al.* (2013):

$$\theta_g = \sin^{-1}(\sin(\theta_n) - \frac{m\lambda}{p}) \tag{4.10}$$

The disadvantage of using a small pitch size is the increment in computational time to produce a B-mode image.

4.3 Results and Discussion

4.3.1 Simulation Results

The difference between the first and second imaging line angle $\Delta\beta$ and the correlation calculated on the second imaging lines between the RF signals in the first ($i = 1$) and second ($i = 2$) elements for the lateral step Δx from λ to $\lambda/5$ for the pitch size of λ and $\lambda/2$ are illustrated in Fig. 4.9. The lag $\Delta\beta$ begins to decrease when reducing the

lateral step from λ to $\lambda/5$. For the pitch size λ and the lateral step λ, the $\Delta\beta$ is 0.8°. The lateral step is reduced to $\lambda/5$, and thus $\Delta\beta$ becomes 0.21°. When $\Delta\beta$ starts to decrease, the correlation coefficient ρ will also decrease Harrington & Cassidy (2012). This situation shows that the two RF signals on adjacent elements are moving further apart. In accordance with equation 4.1, this condition will produce the precise grey colour intensity at particular imaging points. FDMAS uses a nearly similar process to autocorrelation to compute the beamformed signals from the aligned RF signals. The reduction of lateral steps will enable FDMAS to beamform the received RF signals accurately. Thus, instead of assigning approximate grey colour intensity values on imaging points with less imaging lines, assigning more imaging lines with smaller imaging points will help define the exact or accurate intensity values.

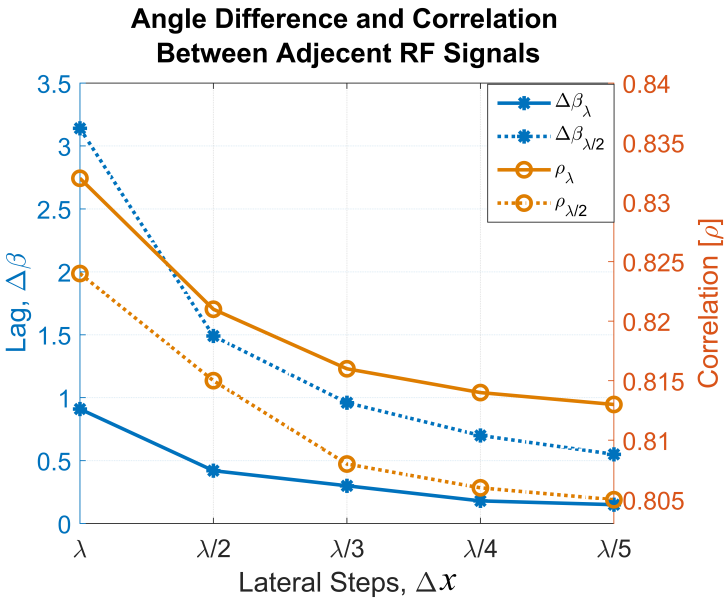

Figure 4.9: Effect of reducing lateral step was evaluated on probe with pitch sizes of λ and $\lambda/2$ by measuring the angle difference and correlation between adjacent RF signals according to equations 4.4 and 4.5.

The results of the Field II simulation with the parameters listed in Table 2.2 are presented in Fig. 4.10. Fig. 4.10 shows the B-mode images for the wire target located at $x = 0$, z= 30 mm beamformed with a) DAS, $p = \lambda$, $E = 128$; b) FDMAS, $p = \lambda$, $E = 128$; c) DAS, $p = \lambda/2$, $E = 256$ and d) FDMAS, $p = \lambda/2$, $E = 256$. The beam

Table 4.1: Specification of transducers.

Properties	Prosonics	Verasonics	Verasonics
Model	L3-8/40EP	L3-12-D	L11-4v
Centre Frequency, MHz	4.79	6.5	7.55
Bandwidth (−6 dB), %	57	85	90.8
Element Pitch, mm	λ	λ	1.46λ-1.48λ

profiles of Fig. 4.10 are shown in the lateral direction in Fig. 4.11. Regardless of the pitch size p, the B-mode images and the beam pattern exhibit the same outcomes when the beamforming lateral step is set to $\lambda/2$. This important finding shows that the step size of imaging points plays an extremely important role in determining final image quality. Even with a larger pitch size p of λ, good quality B-mode images can be produced with less number of elements and shorter computational time compared with probes with the pitch size of $\lambda/2$. Some linear array transducers available in the market are provided in Table 4.1. They are used for research purposes and have a pitch size that is equal to or higher than the λ values. The optimisation of beamforming lateral steps for such probes is expected to improve the B-mode image quality.

4.3.2 Effect of Imaging Point Step Size Δx on FDMAS

The B-mode images of the wire target and cyst phantom beamformed with DAS and FDMAS, $N = 9$, the lateral steps of λ and $\lambda/5$ are shown in Fig. 4.12 and Fig. 4.13. All the images are presented with a dynamic range of 50 dB. The wire targets beamformed with FDMAS achieve better results than those beamformed with DAS due to reduced side lobes produced with FDMAS. The cysts located at a depth of 15 mm and 45 mm obtain higher CRs with FDMAS than that with DAS.

The advantages or gains of reducing the lateral step lies in the transducer with a larger pitch size starting from λ and above. However, this approach is inapplicable to a smaller pitch size ($\lambda/2$ or lower). In Fig. 4.9 no significant difference is observed if the RF signals obtained from the transducer with the pitch size of $\lambda/2$ are beamformed with a lower lateral step, such as $\lambda/3$, $\lambda/4$ or $\lambda/5$. This is because the correlation between adjacent RF lines is already low. The low correlation is an indication that the aligned RF signals for the second imaging line, become further apart. This is a good

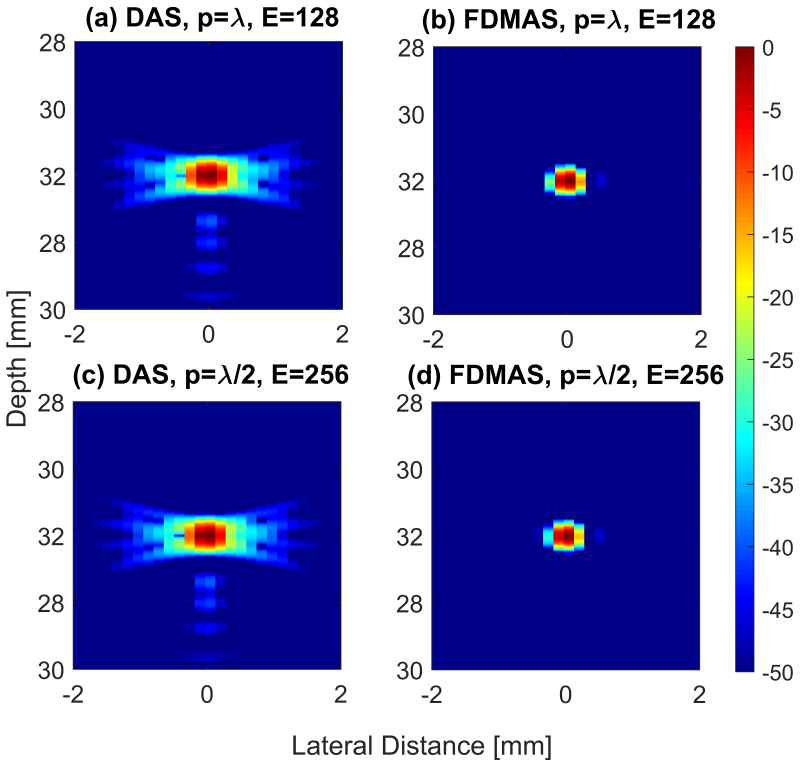

Figure 4.10: B-mode images from CPWI, $N = 9$ for a point target located at $x = 0$, $z = 30$ mm with the lateral step of $\lambda/2$: a) DAS, $p = \lambda$, $E = 128$; b) FDMAS, $p = \lambda$, $E = 128$; c) DAS, $p = \lambda/2$, $E = 256$ and d) FDMAS, $p = \lambda/2$, $E = 256$.

indication such that when the process similar to autocorrelation takes place on the RF signals with a lower correlation value, the noise cancellation will be higher on those particular imaging lines.

AR results at −6 dB and −20 dB levels for DAS and FDMAS measured on wire phantom at the 30 mm depth are given in Fig. 4.14(a–d). In general, there is not any significant change on the AR for DAS at −6 dB and −20 dB levels. Average ARs are 0.37 mm and 0.68 mm at −6 dB and −20 dB levels, respectively. There is a variation on AR for FDMAS when compounding takes place. The lateral steps have been reduced in the lateral direction thus the expectation on the spatial improvement is on the lateral direction. The PSL in the axial direction for DAS is not significantly affected by the reduction of lateral steps. The average PSL in the axial direction using DAS is −25.4 dB. The PSL in the axial direction using FDMAS shows improvement

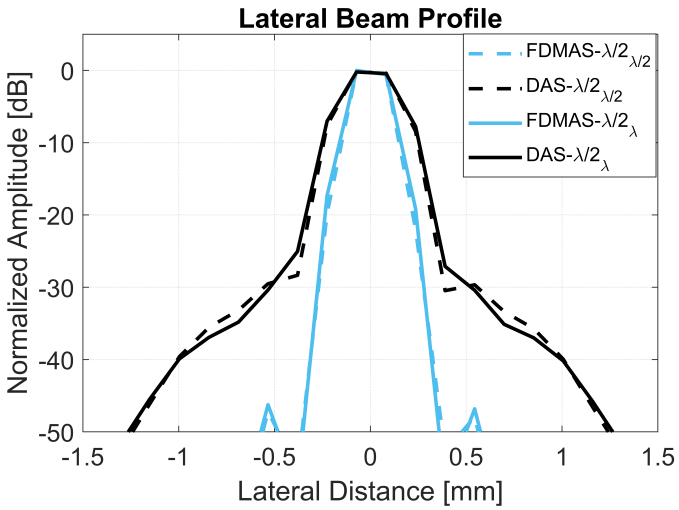

Figure 4.11: Lateral beam profile of a wire target at a depth of 30 mm simulated using Field II using the pitch sizes of λ and $\lambda/2$ beamformed with the lateral step of $\lambda/2$. The Field II simulation parameters are the same as that provided in Table 2.2. Regardless of pitch size, both beamforming techniques produced nearly similar results when beamformed with the same lateral step. The legend represents the beamforming techniques-lateral step-pitch size.

at a low number of compounding angles ($N = 3$ to $N = 9$) when the lateral steps are reduced from λ to $\lambda/5$. However, the PSL for $N = 3$ shows much smaller values for all lateral steps compared to other compounding angles. A low PSL is due to less noise cancellation. This is because of a low number of compounding angles and the large steering angle induce grating lobes. At $N = 9$, the PSL in the axial direction has only decreased by 1.0 dB from λ to $\lambda/5$.

LR results at −6 dB and −20 dB levels for DAS and FDMAS measured on the wire phantom at the 30 mm depth are given in Fig. 4.15(a–d). The LRs for DAS and FDMAS keep improving as the lateral step is reduced from λ to $\lambda/5$ for all numbers of compounding angles from $N = 1$ to $N = 25$. With $N = 9$, when the lateral step is reduced from λ to $\lambda/5$, the LR using FDMAS achieves 67.9% and 81.2% improvements at −6 dB and −20 dB, respectively. With the same lateral step reduction, DAS achieves 54.8% and 67.4% improvements at −6 dB and −20 dB, respectively. However, most of the changes in LR for DAS only occur from λ to $\lambda/2$, whereas those for FDMAS occur

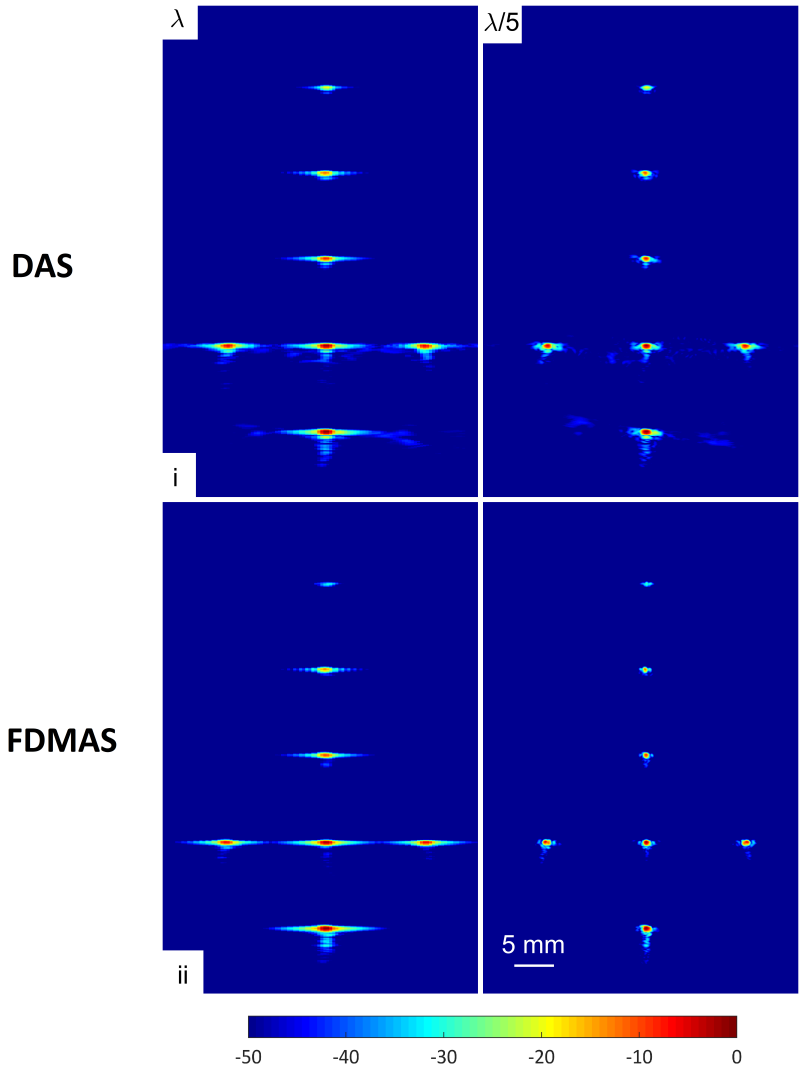

Figure 4.12: B-Mode images of point targets beamformed with row (i) DAS and row (ii) FDMAS, $N = 9$ with the lateral steps of λ and $\lambda/5$.

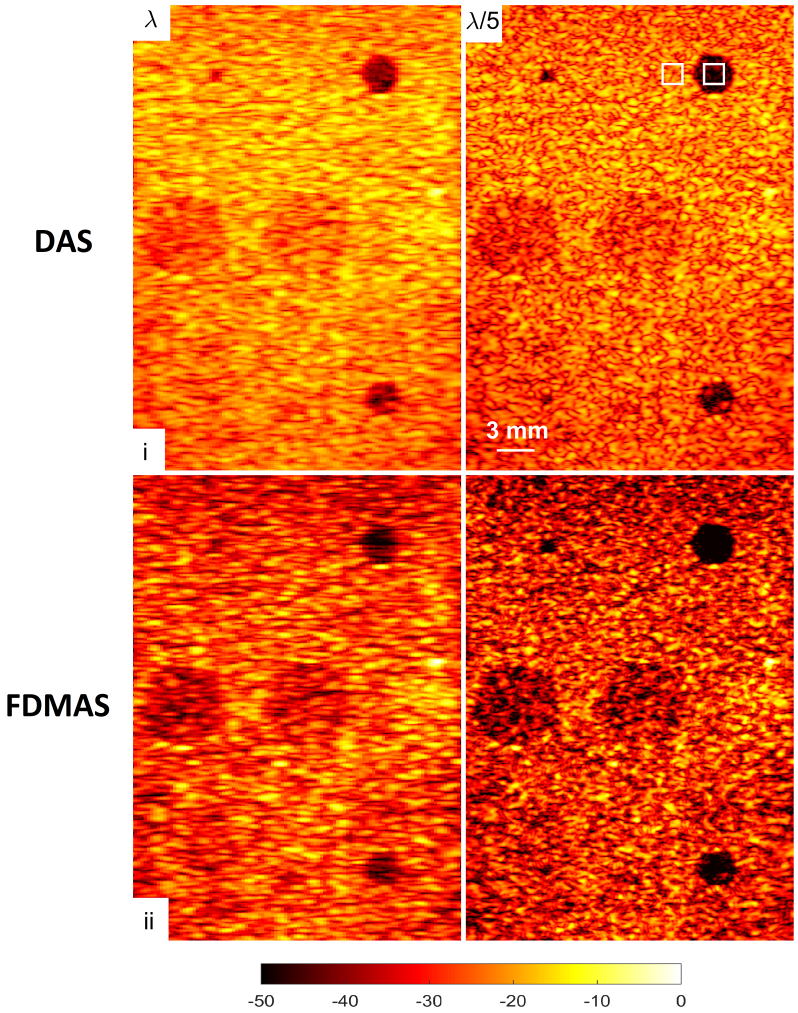

Figure 4.13: B-mode images of cysts beamformed with row i, DAS and row ii, FDMAS, $N = 9$ with the lateral steps of λ and $\lambda/5$. Two regions with the same size are selected to measure image CR and CNR.

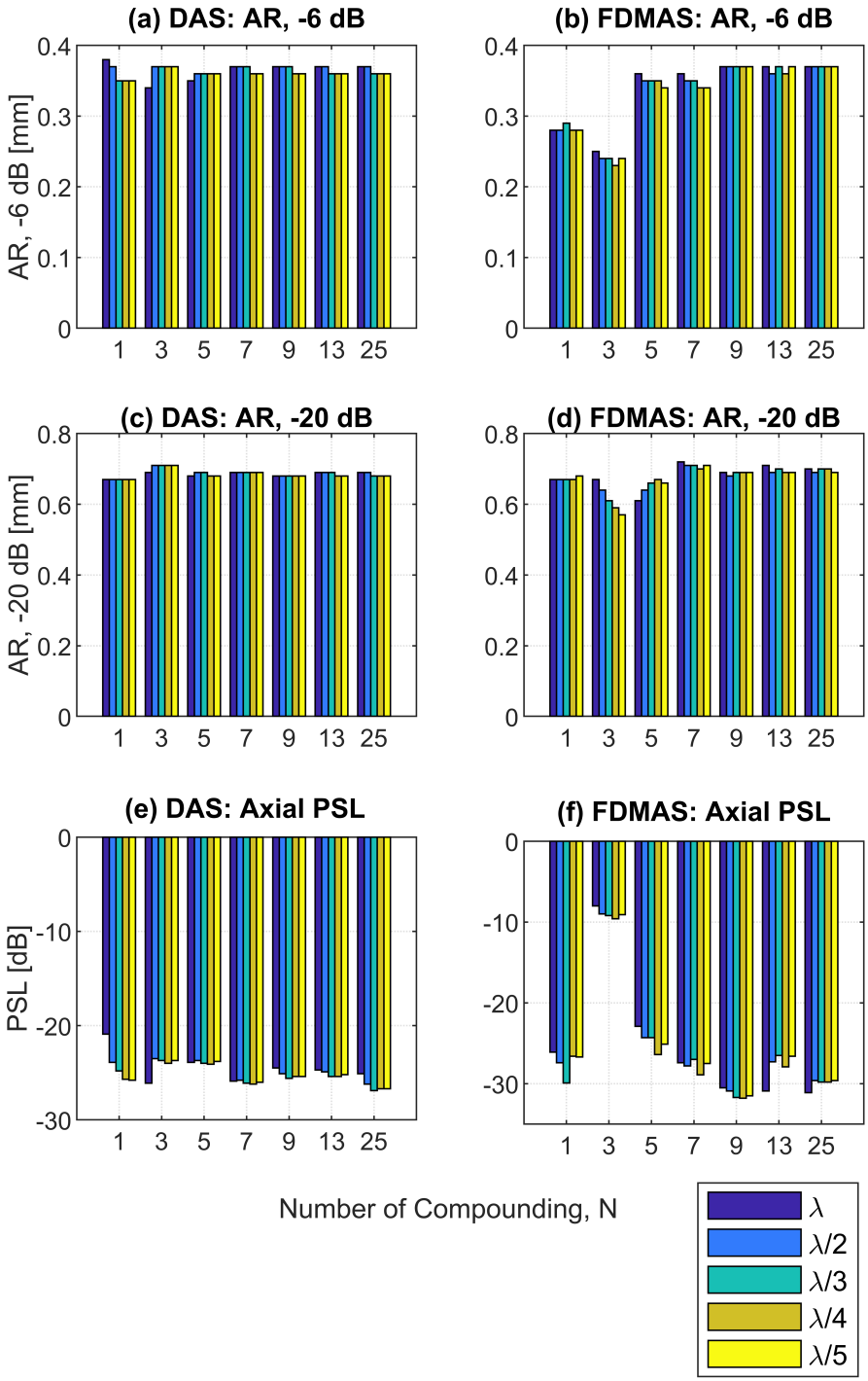

Figure 4.14: AR performance at −6 dB: a) DAS and b) FDMAS, AR at −20 dB; c) DAS and d) FDMAS, PSL; e) DAS and f) FDMAS for CPWI ($N = 1$ to $N = 25$) as the lateral step is reduced from λ to $\lambda/5$.

from λ to $\lambda/3$. Beyond these values, improvements plateau. The concept behind this approach is clearly illustrated through the beam profile pattern in the lateral direction shown in Fig. 4.18 for point targets located at 30 mm depth, respectively.

CR and CNR results for DAS and FDMAS measured on the 3.0 mm diameter cyst located at the 15 mm depth are presented in Fig. 4.16. Improvements in CR and CNR are shown when the lateral step is reduced from λ to $\lambda/5$ for both DAS and FDMAS. The CRs are improved by 4.18 dB and 10.38 dB for DAS and FDMAS, respectively. The B-mode images of the point target shown in Fig. 4.17 exhibit a noise reduction in the lateral direction as the lateral step is reduced from λ to $\lambda/5$. The energy in the side lobes regions is the main factor that affects the image contrast level Matrone *et al.* (2015); Misaridis & Jensen (2005). Thus, attenuating side lobes more frequently through a process similar to autocorrelation with smaller $\Delta\beta$ helps improve the image CR. Side lobes are known to interfere with LR Lawrence (2007). Thus, the CR is improved by attenuating the side lobes along the lateral direction. The significant effect of side lobes reduction along the lateral direction with FDMAS is illustrated in Fig. 4.17, row ii. This however is not the case for CNR. The side lobes reduction as the lateral step is reduced from λ to $\lambda/5$ is the main reason for the CNR to decrease for both DAS and FDMAS. The attenuation of clutter noise due to side lobes reduction makes speckle regions initially covered by clutter noise visible. This condition produces high variations in speckle regions, leading to low CNRs there.

The leaking of the side lobes into the anechoic region is reduced as the lateral step is reduced from λ to $\lambda/5$. This phenomenon is illustrated in Fig. 4.19. The lateral profile of the 3.0 mm diameter cysts is also shown in Fig. 4.20 for DAS and FDMAS. As the lateral step is reduced from λ to $\lambda/3$, the cyst edges become steeper due to side lobes reduction. In general, the definition of the cyst boundary is improved with both DAS and FDMAS from the lateral step of $\lambda/2$.

The low-quality B-mode image produced with the lateral step of λ can be associated with beamforming that does not occur at the right location where the point target is located. A pixel length in the x direction is equal to λ, which is comparably longer than the exact length of the point target diameter of 120 μm. Thus, a single grey colour intensity will be assigned through the λ length. One of the solutions for this problem is reducing the lateral step used for beamforming.

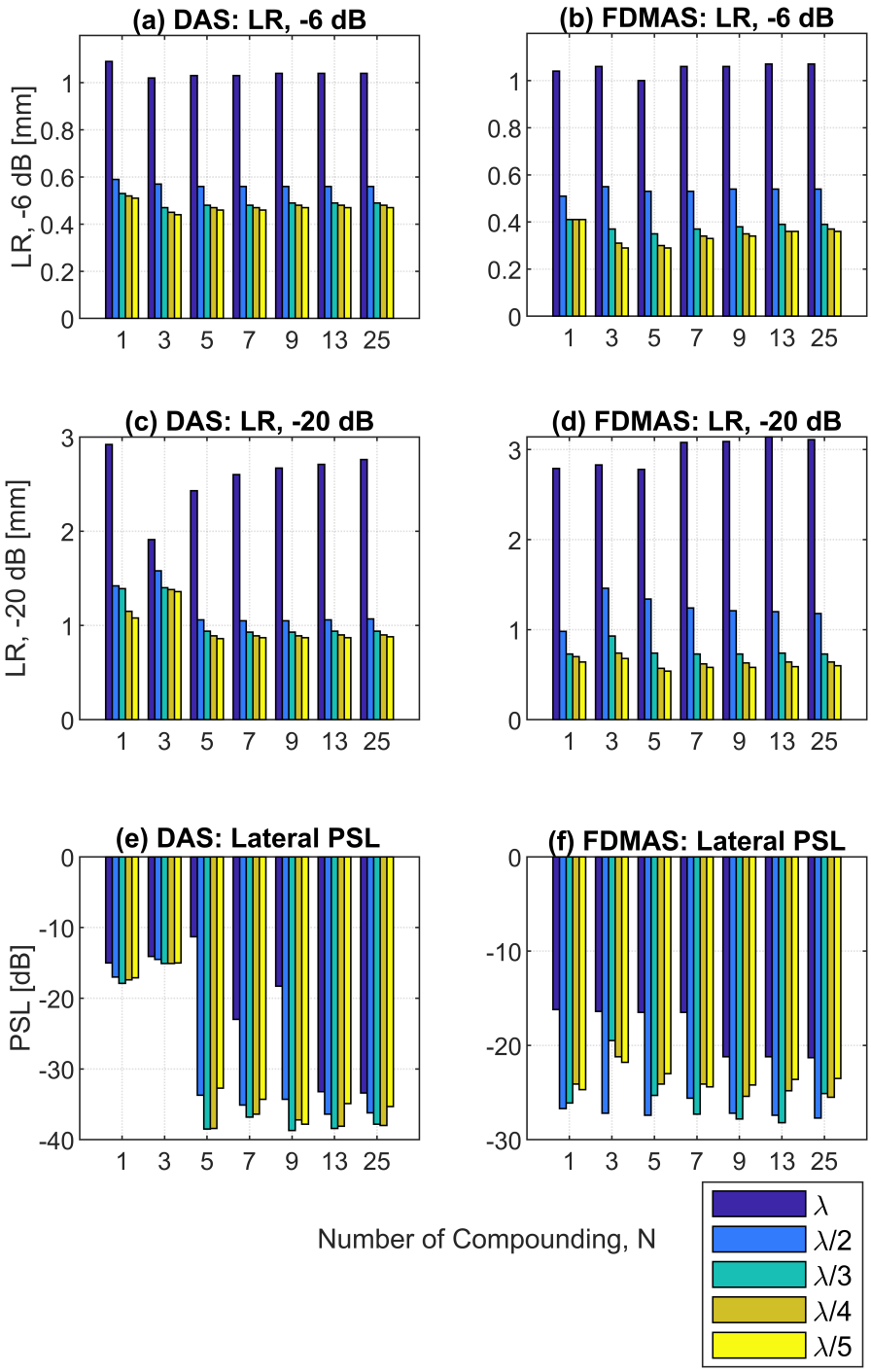

Figure 4.15: LR performance at −6 dB: a) DAS and b) FDMAS, LR at −20 dB; c) DAS and d) FDMAS, CR; e) DAS and f) FDMAS for CPWI ($N = 1$ to $N = 25$) as the lateral step is reduced from λ to $\lambda/5$.

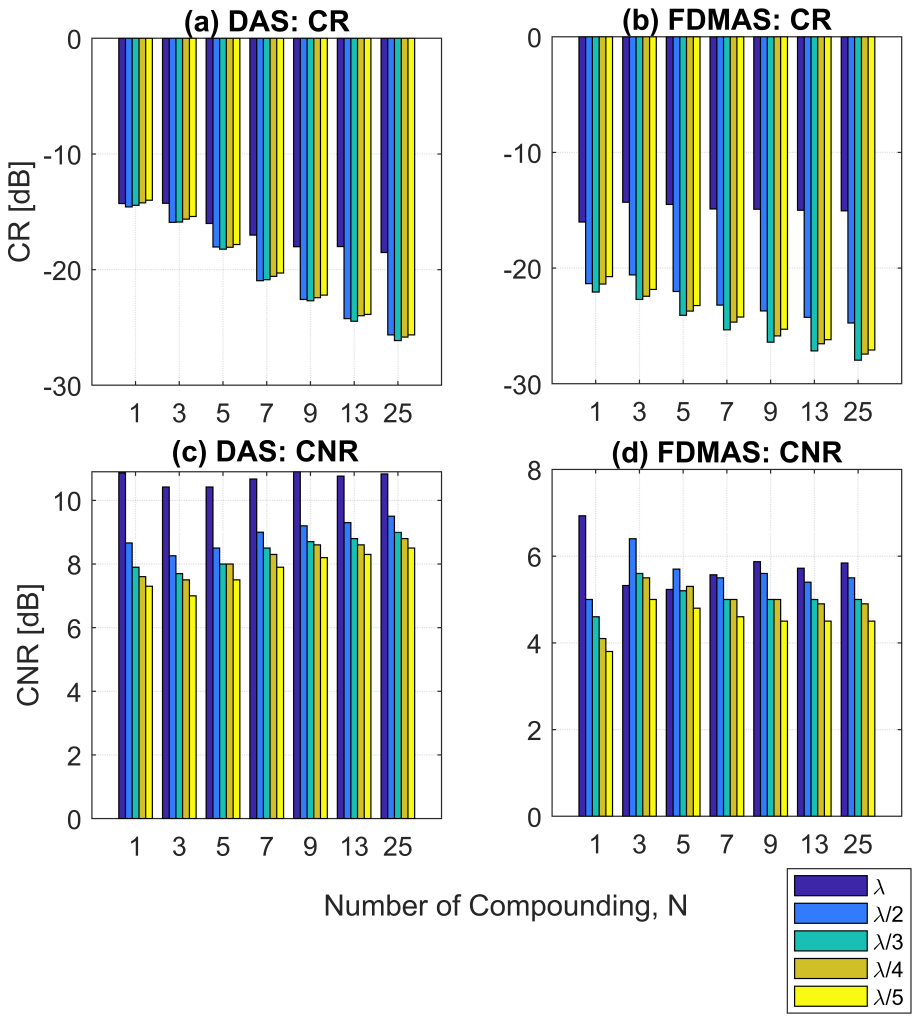

Figure 4.16: LR performance at −6 dB: a) DAS and b) FDMAS, LR at −20 dB; c) DAS and d) FDMAS, CR; e) DAS and f) FDMAS for CPWI ($N = 1$ to $N = 25$) as the lateral step is reduced from λ to $\lambda/5$.

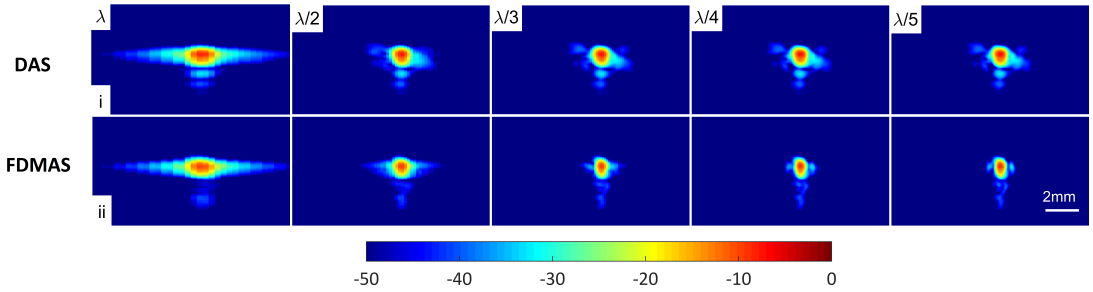

Figure 4.17: B-mode images of point targets at the 30 mm depth beamformed with DAS (row i) and FDMAS (row ii) using different lateral steps ranging from λ to $\lambda/5$ and CPWI, $N = 9$. The colour map for the figure is the same as the one presented in Fig. 4.12. All the images are shown within a dynamic range of 50 dB.

4.3.3 Clinical Images

The performance of DAS and FDMAS with *in-vivo* data was evaluated on the right side of one male carotid artery. The reduction in clutter noise and side lobes as the lateral step is reduced from λ to $\lambda/5$ facilitates enhancement of spatial and contrast resolutions with the FDMAS beamforming technique, as shown in Fig. 4.21, row ii. The side lobe leaking into the carotid artery anechoic regions is similar to that observed in the cyst region shown in Fig. 4.19. However, the medium that surrounds the cyst border is uniformly composed of hypoechoic regions. Thus, the amount of side lobes signal leaking from the hypoechoic region to the anechoic region is less observable although such leaking also exists. However, the carotid artery presents a different case. The side lobes that are leaking into the carotid anechoic regions are caused by an extremely strong hyperechoic medium. Thus, such leaking becomes an obstacle to get the contour formation on the carotid boundary during the segmentation process. The speckle and clutter noise in B-mode images pose a challenge to the segmentation process which BSAC fails to converge to the intended boundary Khadidos *et al.* (2014); Slabaugh *et al.* (2009); Zhu *et al.* (2010). Thus, the reduction of clutter and side lobes in the carotid regions improves the segmentation process Kumar *et al.* (2016).

Segmenting the carotid artery wall is the one of the first procedures before any measurement can be performed. This process can either involve measuring the diameter of the common carotid artery (CCA) or the intima-media thickness. The 3D recon-

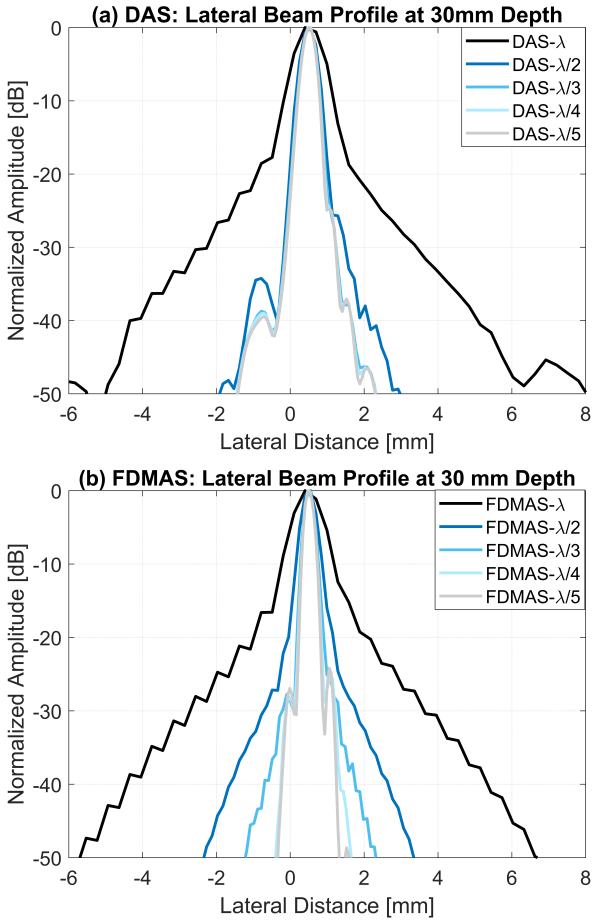

Figure 4.18: Lateral beam profiles of the wire targets located at the 30 mm depth using a) DAS and b) FDMAS beamforming techniques with the lateral step from λ to $\lambda/5$ for CPWI, $N = 9$.

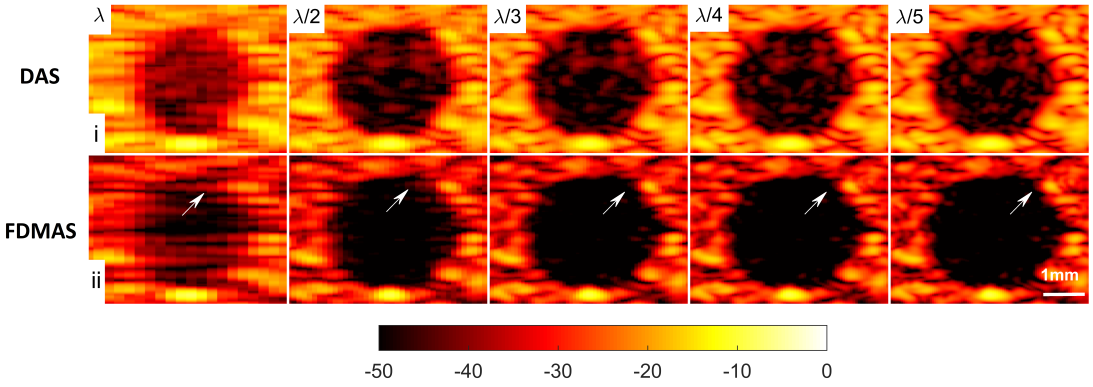

Figure 4.19: B-mode images (CPWI, $N = 9$) of a 3 mm-diameter cyst located at a depth of 15 mm beamformed with a lateral step from λ to $\lambda/5$ using (i) DAS and (ii) FDMAS. The colour map for the figure is the same as that in Fig. 4.13. All the images are shown with a dynamic range of 50 dB.

struction of the carotid artery from the 2D transversal imaging also depends on a good segmentation output Yeom *et al.* (2014). Thus, applying the segmentation output from FDMAS with a smaller lateral step is expected to produce a good 3D carotid image.

4.4 Parameter Optimisation

To form a single B-mode image line using DAS, w for the lateral step is equal to λ, and the total computational complexity (CC) is E, i.e the total number of elements. However, to form the same single imaging line for FDMAS, l is given as follows

$$l = \frac{E^2 - E}{2}, \tag{4.11}$$

As the lateral step is reduced, the total number of imaging lines increases along with CC. Table 4.2 shows the CC for FDMAS as the lateral step is reduced. As shown in the table, CC increases linearly as the lateral step is reduced for FDMAS.

A summary of the performance indices measured for FDMAS with CPWI, $N = 9$ is shown in Fig. 4.22. The increment is indicated by the CC in linear form but is not reflected on the overall performance. Beyond the lateral step of $\lambda/3$, a slight jump is observed in the performance improvement. As the lateral step is reduced from $\lambda/3$ to $\lambda/5$, the improvement in LR at -6 dB and -20 dB are only 10.5% and

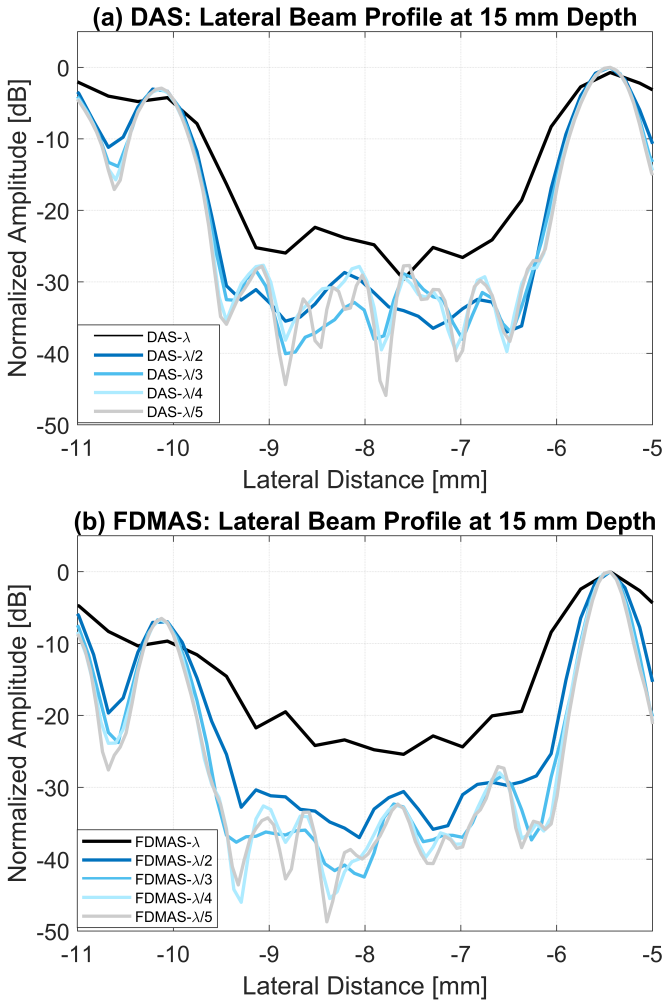

Figure 4.20: Normalized lateral beam profiles of the 3.0 mm-diameter cyst at a depth of 15 mm with a) DAS and b) FDMAS from the lateral step from λ to $\lambda/5$ for CPWI, $N = 9$.

Table 4.2: Computational complexity for FDMAS.

Properties	Values				
Lateral Step	λ	$\lambda/2$	$\lambda/3$	$\lambda/4$	$\lambda/5$
Total Imaging Lines	E	$2E$	$3E$	$4E$	$5E$
Computational Complexity, CC	El	$2El$	$3El$	$4El$	$5El$

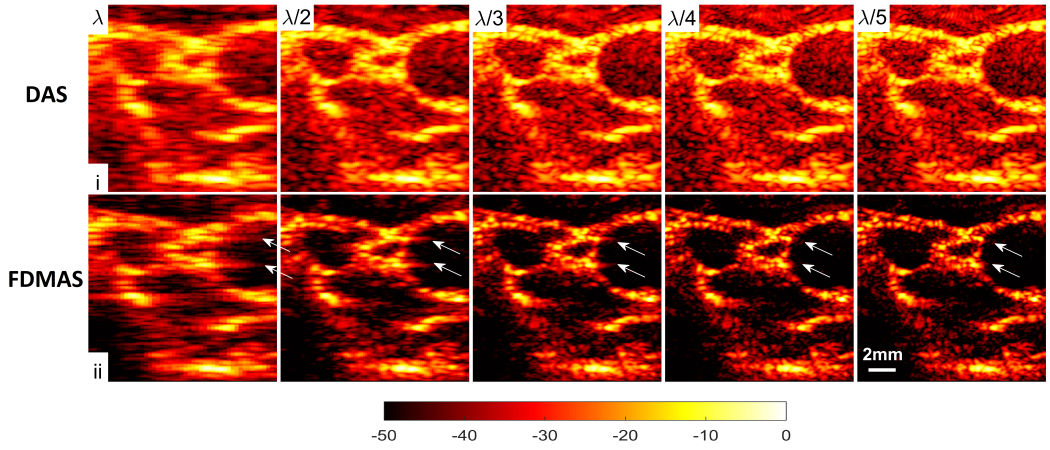

Figure 4.21: Carotid artery B-mode images obtained with a two-cycle sinusoidal excitation signal and nine compounding angles beamformed with the lateral step from λ to $\lambda/5$ using DAS (row i) and FDMAS (row ii). The arrows shown on the 2nd row indicate the side lobes reduction in the lateral direction as the lateral step is reduced. This improves the boundary definition. The colour map in the figure is the same as the one presented in Fig. 4.13. All the images are shown within a dynamic range of 50 dB.

20.5%, respectively, compared with 64.1% and 76.4% from λ to $\lambda/3$. Meanwhile the improvement for CR as the lateral step is reduced from λ to $\lambda/3$ is 11.49 dB. The CR result for FDMAS from $\lambda/3$ to $\lambda/5$ does not exhibit any improvement; instead, it decreases by 1.22 dB. Thus, to balance CC and performance gains, the received RF signal is suggested to be beamformed with FDMAS using the lateral step of $\lambda/3$. One drawback of FDMAS methods is the longer processing time to produce an image compared with DAS. Although FDMAS is slower than DAS, it is still relatively faster than other adaptive beamforming techniques.

Table 4.3 presents the results obtained from a two-cycle sinusoidal excitation signal with $N = 9$ and $N = 25$ for the lateral step of $\lambda/2$ and $\lambda/3$. Only the values obtained with the two lateral steps were compared in this study because both values produced comparably good image quality with low CC. Moreover, only these values were compared to demonstrate that performance can be improved with less compounding angles when beamformed with a smaller lateral step whilst considering CC. All spatial and contrast performance indicators produce better results with FDMAS, CPWI, $N = 9$ and the lateral step of $\lambda/3$ instead of with FDMAS, CPWI, $N = 25$, and the lateral

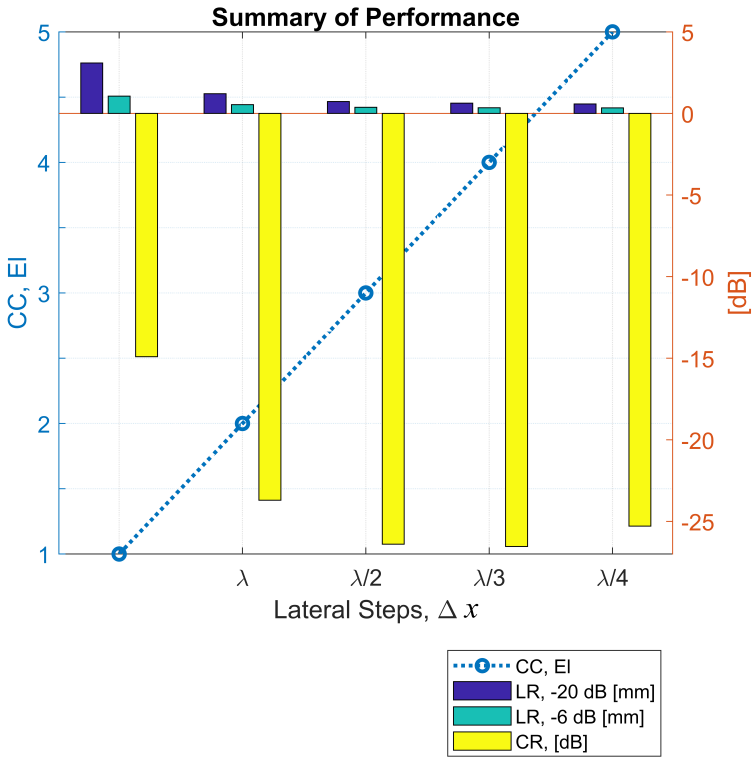

Figure 4.22: Summary of performance, LR and CR with CC for FDMAS beamforming when the lateral step is varied from λ to $\lambda/5$ for CPWI, $N = 9$.

Table 4.3: LR and CR for DAS and FDMAS.

CPWI, N		LR, -6 dB [mm]		LR, -20 dB [mm]		CR [dB]	
		$\lambda/2$	$\lambda/3$	$\lambda/2$	$\lambda/3$	$\lambda/2$	$\lambda/3$
9	DAS	0.56	0.49	1.05	0.93	-22.58	-22.69
	FDMAS	0.54	**0.38**	1.21	**0.73**	-23.70	**-26.40**
25	DAS	0.56	0.49	1.07	0.94	-25.65	-26.14
	FDMAS	**0.54**	0.39	**1.18**	0.73	**-24.74**	-27.96

step of $\lambda/2$. All the values that compare the compounding and lateral step are highlighted in Table 4.3 in bold typeface. From the results, a conclusion can be drawn that FDMAS generally has lower compounding angles with a lower lateral step, which can improve the temporal resolution of B-mode imaging. The reduction of the number of compounding angles from $N = 25$ to $N = 9$ results in a 64% improvement in temporal resolution.

4.5 Conclusion

In this study, the performance of DAS and FDMAS has been evaluated with CPWI, various pitch sizes and various imaging point steps in the lateral direction. The results clearly show that FDMAS produces better image quality than DAS when the beamforming lateral step is smaller than $\lambda/2$. The main observation from reducing the lateral step is that the performance of FDMAS is improved when the process similar to autocorrelation occurs with a smaller step. The multiplication and addition of RF signals with a smaller lateral step further attenuated clutter noise, which can increase the image CR. Although reducing the lateral step from λ to $\lambda/5$ improves the image quality, the most significant improvement occurs between λ and $\lambda/3$. Thus, $\lambda/3$ is selected for FDMAS to optimise beamforming processing time. There is no any significant change in the axial direction when the lateral step is reduced. The CNR tends to get lower as the lateral step is reduced. This work found that a high number of frame rates can be achieved without sacrificing image spatial and contrast resolutions when the received RF signal is beamformed with FDMAS at a lower lateral step.

Chapter 5

Filter Multiply and Sum

Inspired by the filter delay multiply and sum (FDMAS) beamforming technique, a new compounding method has been proposed in this chapter. The proposed technique is similar to autocorrelation where it can provide better results by finding the correlation between steered plane waves. In this method, low-correlated side lobes will be attenuated while the main lobe will be preserved. The new proposed compounding is named as filtered multiply and sum (FMAS) compounding technique. The main advantage of this new compounding technique is the ability to produce better contrast and spatial resolutions than conventional FDMAS but with higher FR and less computational complexity.

5.1 Introduction

Compounding techniques have been used in ultrafast ultrasound imaging to improve the B-mode image quality by reducing the clutter noise and smoothing the speckle variation Montaldo *et al.* (2009); Toulemonde *et al.* (2015). However, the conventional compounding technique with coherent arithmetic averaging is not the most effective method since the reduction of clutter noise inside the anechoic regions is minimal. The side lobes reduction is also ineffective. A high number of steered plane waves are thus needed to achieve good spatial resolution which in return reduces the FR. The poor performance of conventional compounding is because that the side lobes that occur at different spatial locations are loosely correlated. This happens due to the different time delays used for each plane wave transmission. On the other hand, the main

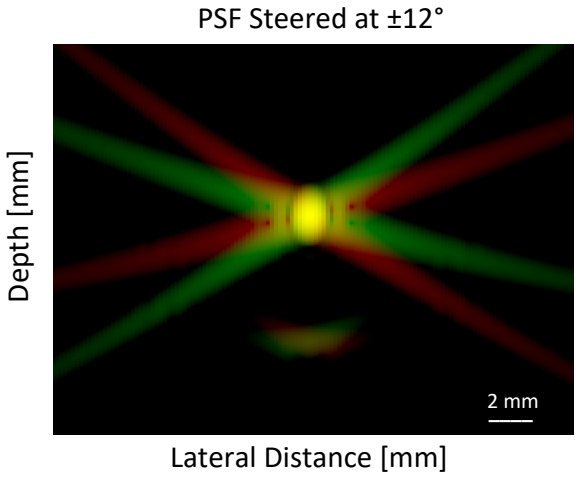

Figure 5.1: Field II simulation of a point target located at the 30 mm depth beamformed from two plane waves steered at $+12^{o}$ and -12^{o}. The yellow color highlights the main lobes for both plane waves. It can be noticed that the position of axial lobes for both steering plane waves also appears slightly at different locations.

lobe position does not change and highly correlate between steered plane waves. This concept is illustrated in Fig. 5.1. The point target at the 30 mm depth was simulated with Field II with the setup given in Table 2.2. The B-mode images obtained with two plane waves steered at $+12^{o}$ (green color) and -12^{o} (red color) are given. The received RF data was beamformed with DAS and the B-mode image is displayed with a 50 dB dynamic range. It can be seen that the side lobes for both plane waves are at different locations, while the main lobe highlighted in yellow remains at the same location. This is the fundamental of the proposed compounding technique.

5.1.1 Methods

The proposed compounding technique takes place after receiving echoes from multiple steered plane waves beamformed with DAS. Unlike the conventional compounding technique where all the steered plane waves are added and averaged after beamforming, the beamformed RF frames are multiplied to form the multiply-and-sum (MAS)

frames. The MAS equation is given as follows

$$Com_{\mathrm{MAS}} = \sum_{n=1}^{N-1} \sum_{k=n+1}^{N} \mathrm{sgn}\{V_n(t)V_k(t)\} \times \sqrt{|V_n(t)V_k(t)|}, \tag{5.1}$$

where $V(t)$ represents a set of aligned RF signals $v_i(t)$ ($i = 1$ to 128) for each steered plane wave. The process is similar to the autocorrelation function. Instead of finding correlations between all channel RF signals to form an imaging line as in FDMAS, the proposed technique is faster due to the number of times of multiplication B involved in autocorrelation for FMAS is equal to number of compounding angles of N as given by :

$$B = \frac{N^2 - N}{2}, . \tag{5.2}$$

The RF signals obtained from Com_{MAS} need to be band pass filtered to produce filtered multiply-and-sum, Com_{FMAS}. The reason is the same as that in FDMAS where two different frequency spectrums (DC and 2nd harmonics) are produced when two RF signals with the same frequency multiplied. The frequency components are illustrated in the Fig. 4.5. Once filtered, the RF signals are Hilbert transformed for envelope detection and then log-compressed to form the B-mode image.

5.2 Simulation and Experimental Setup

The performance of FMAS has been compared to that using DAS and FDMAS with both simulations and experiments by using the point targets, cyst phantom and *in-vivo* data. The setup for experiments is the same as given in Section 4.1.1. The setup for the simulation environment is given in Table 2.2, and no transmit and receive apodization were employed.

5.3 Results

5.3.1 Simulation Results

The B-mode images obtained from Field II simulations were obtained on seven point targets located from the 10 mm to 50 mm depth for DAS, FDMAS and DAS-FMAS, and they are shown in Fig. 5.2(a), (b) and (c). The beam pattern along the lateral

direction at $z = 40$ mm depth and the axial direction at $x = 0$ mm for DAS, FDMAS and DAS-FMAS are shown in the Fig. 5.2(d) and (e), respectively. The proposed new compounding technique, DAS-FMAS is able to eliminate the grating lobes that appear at the 10 mm depth, on both lateral directions, -10 mm and 10 mm when beamformed with DAS as shown in Fig. 5.2(a). Side lobes and axial lobes along lateral and axial directions also have been reduced with the new compounding technique. This is shown in Fig. 5.2 (d) and (e). Up to 7 dB of PSL along the lateral direction has been reduced with the new compounding technique when compared to FDMAS. Although both techniques, FDMAS and DAS-FMAS use the same mathematical theorem, a process similar to autocorrelation.

The beam pattern produced along the axial direction with DAS-FMAS is almost the same as that using FDMAS. The signal intensity level with DAS-FMAS is lower than that with DAS except at the depth of elevation focus. This is because all signals have been normalized to their maximum value. The explanation for this phenomenon is the same for what happened with FDMAS. When RF signals with almost the identical frequency component from two steering angles are multiplied, the DC and second harmonic components are produced. The second harmonic component as shown in Fig. 4.5 with a lower amplitude level has been used to form all images in DAS-FMAS. Thus, the signal has a lower intensity level. The low signal intensities at a deeper location can be amplified by applying TGC.

Axial lobes that occur when plane waves are steered are visible below the point targets located at the depth of 10 mm and 20 mm, as shown in Fig. 5.2(a). Both FDMAS and DAS-FMAS are able to reduce these axial lobes. The spatial distribution of axial lobes for different steering angles are different, thus, when the process similar to autocorrelation taking place, the decorrelation between the axial lobes is higher. The axial lobes mainly occur at around the -45 dB level with DAS and are attenuated below -70 dB with FDMAS and DAS-FMAS as shown in Fig. 5.2(e).

To analyse in detail the effect of the proposed technique on a point target, B-mode images and beam profiles along the axial and lateral directions are plotted for a point target at the depth of 30 mm as shown in Fig. 5.3. It can be seen in Fig. 5.3(c) that the side lobes along the lateral direction have been nearly fully suppressed for a imaging dynamic range 50 dB. But this is not the case for DAS. The noise cancellation does not effectively take place with three compounding angles. The axial lobes are still

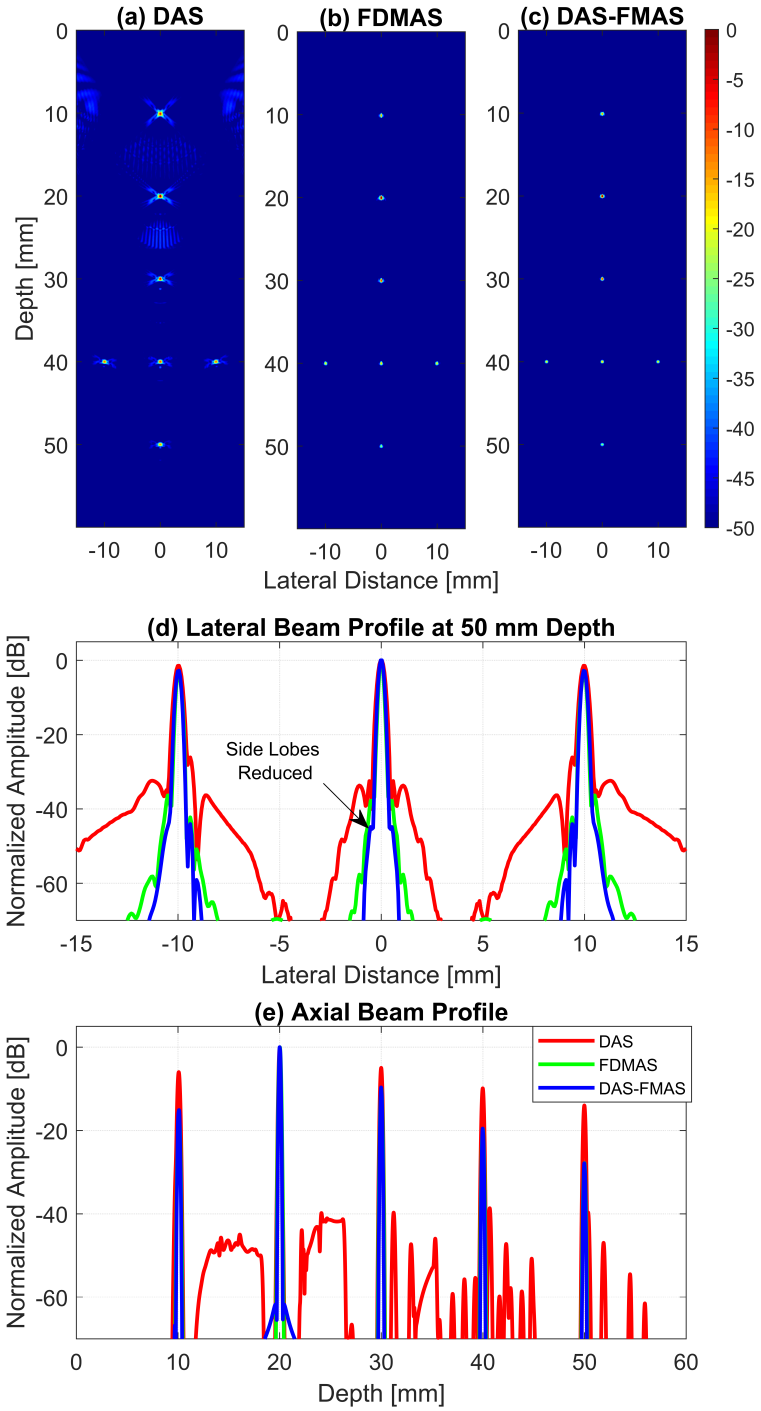

Figure 5.2: Plane wave B-mode images for point targets beamformed with a) DAS, b) FDMAS and c) DAS-FMAS, $N = 3$ $(-12,\ 0,\ +12)$. The lateral beam profile at the depth of 40 mm and the axial beam profile at $x = 0$ mm are shown in d) and e) for all three beamforming techniques (DAS, FDMAS and DAS-FMAS).

visible at approximately 31 mm depth with DAS as shown in Fig. 5.3(a). Although FDMAS is able to tackle the noise problem along the axial and lateral directions, the PSL produced along the lateral direction is higher than that with DAS which can be seen in Fig. 5.3(d). The PSL along the lateral direction at the depth of 30 mm for DAS is −32.9 dB, while for FDMAS it is −32.7 dB. For DAS-FMAS, the PSL along the lateral direction has been reduced to −68 dB.

As can be seen from the axial beam profile, the side lobes with DAS-FMAS is higher than DAS and FDMAS. However, the side lobes occur below −60 dB and all the images are displayed with a 50 dB range. Thus, the side lobes will not occur on the B-mode image even if displayed with a 60 dB dynamic range. The proposed technique DAS-FMAS produced the narrower main lobes along the axial direction compared to DAS and FDMAS. This can be seen in Fig. 5.3(e). It is hard to observe the same improvement along the axial direction in Fig. 5.2(e) although the improvement is significant. Complete axial resolution measurements on the wire target at the 30 mm depth for DAS, FDMAS and DAS-FMAS ($N = 1$ to $N = 25$) are presented in Fig. 5.9.

Measurements were then performed on three difference cysts with diameters of 2 mm, 4 mm and 6 mm located at the depths of 30 mm, 40 mm and 50 mm as shown in Fig. 5.4. The number of steering angles was $N = 3$ (-12^0, 0^0 and $+12^0$). The CR for the cyst located at the 30 mm depth is significantly improved with DAS-FMAS. Although FDMAS is able to improve the CR, yet the clutter noise inside the anechoic region is still visible and not fully eliminated. The border definition for all cysts is improved with FDMAS but more improvement is obtained with DAS-FMAS due to the further reduced clutter noise. This can be seen clearly from the lateral beam profile for the cyst at the 50 mm depth as shown in Fig. 5.4(d). The attenuation of clutter noise because of lateral side lobes leaking into the anechoic region makes the edge steeper and hence improves the border definition.

5.3.2 Experimental Results and Discussion

The experimental results on seven wire targets are presented in Fig. 5.5. Thirteen steered plane waves as given by Table 2.1 were used. High number of compounding able to eliminate the grating lobes in DAS which tends to appear at low number of compounding angle ($N = 3$ or less). The most significant improvement can be seen

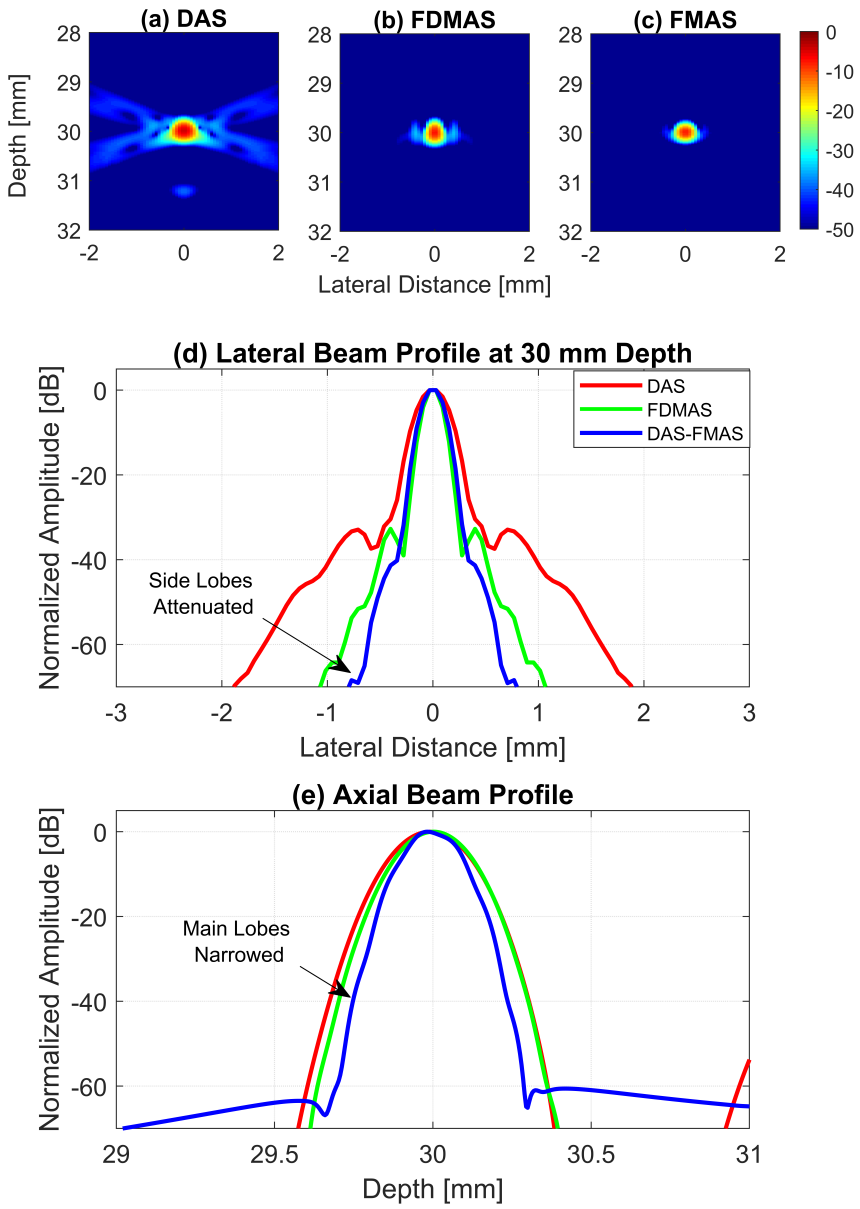

Figure 5.3: Plane wave B-mode images ($N = 3$) for the point target at the depth of 40 mm beamformed with a) DAS, b) FDMAS and c) DAS-FMAS with a 50 dB dynamic range.

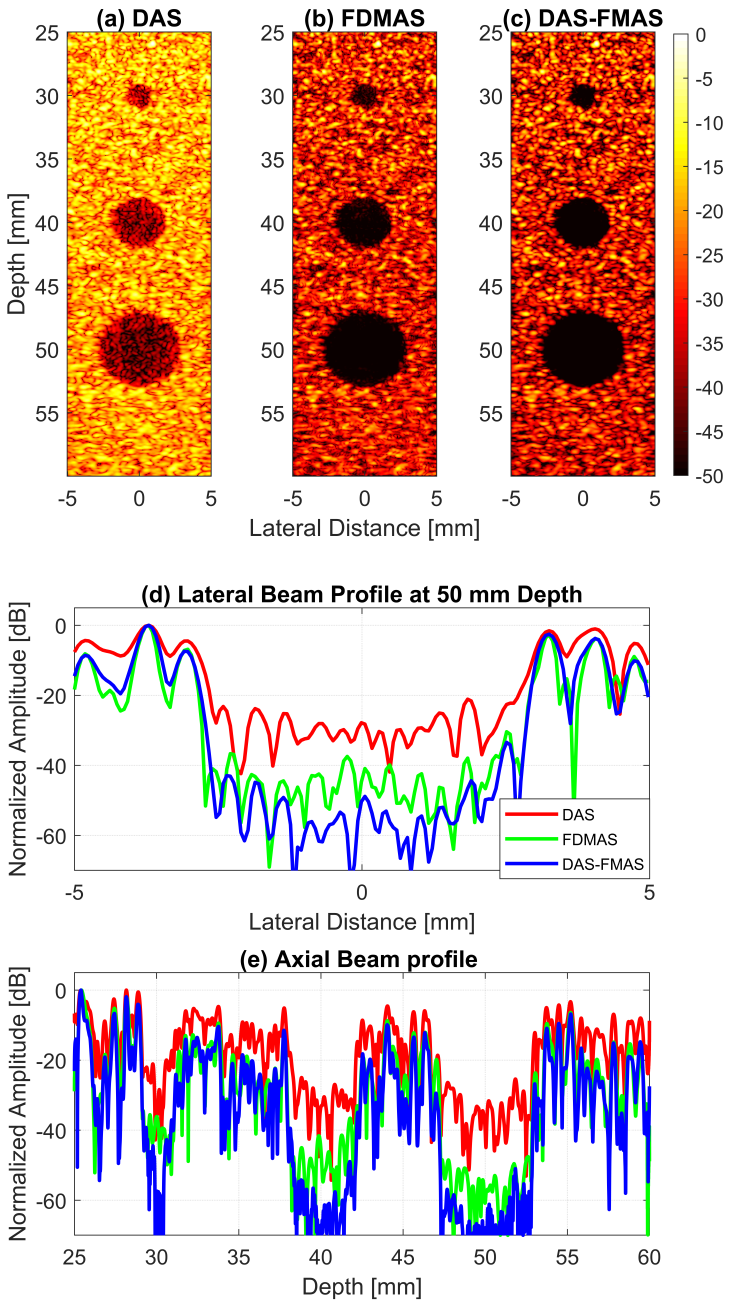

Figure 5.4: Field II simulations performed on cysts located at the depths of 30 mm, 40 mm and 50 mm with diameters of 2 mm, 4 mm and 6 mm with a) DAS, b) FDMAS and c) DAS-FMAS. The number of steering angles is $N = 3$ $(-12, 0, +12)$. d) Lateral beam profiles for the 6-mm cyst at the 50 mm depth and e) axial beam profiles along $x = 0$ mm.

with DAS-FMAS as the side lobes along the lateral and axial directions have been reduced significantly.

In order to measure the spatial resolution for the proposed compounding technique DAS-FMAS and compared it to conventional approaches with a wire target at the 30 mm depth, the B-mode images for the wire target with 3 to 25 compounding angles with DAS, FDMAS and DAS-FMAS are presented in Fig. 5.6. The corresponding axial and lateral beam profiles for the wire target are given in Fig. 5.7 and Fig. 5.8, respectively.

Axial resolution (AR) results at the −6 dB level for DAS, FDMAS and DAS-FMAS are becoming stable as the number of compounding angles increases from $N = 3$ to $N = 25$. The AR improves significantly with DAS-FMAS compared to DAS and FDMAS. At $N = 3$, the AR with DAS-FMAS is improved by 43% and 12.5% compared to DAS and FDMAS, respectively. While with 25 compounding angles, the AR is improved by 44% and 47% compared to DAS and FDMAS. The ARs for DAS and FDMAS do not show any significant differences from $N = 5$ to $N = 25$ except for $N = 3$. With $N = 25$, the AR at −6 dB are 0.36 mm and 0.37 mm for DAS and FDMAS, respectively. All results for AR at −6 dB for different numbers of compounding angles are shown in Fig. 5.9(a). It is unexpected to have any improvement in AR for DAS and FDMAS through spatial compounding since it is in the lateral direction. This can be seen from the beam profile along the axial direction as shown in Fig. 5.7 for the wire target at the 30 mm depth for all investigated techniques.

AR results at −20 dB level for DAS, FDMAS and DAS-FMAS shows almost the same pattern at −6 dB. At $N = 3$, the AR with DAS-FMAS improved by 32% from DAS and 31% from FDMAS. While with 25 number of compounding angles, the AR improved by 26% from DAS and 28.5% from FDMAS. Complete results for AR at −20 dB with all compounding angles is shown in Fig. 5.9(b).

The PSL in the axial direction is attenuated by 33 dB and 48 dB more with DAS-FMAS when compared to DAS and FDMAS for $N = 3$. With 25 compounding angles, DAS-FMAS is able to reduce more PSL by 28 dB and 25 dB than DAS and FDMAS. All results for PSLs in the axial direction for different numbers of angles are shown in Fig. 5.9(c).

Lateral resolution (LR) results at the −6 dB level for DAS, FDMAS and DAS-FMAS are given in Fig. 5.10(a). High LR is achieved with a lower number of

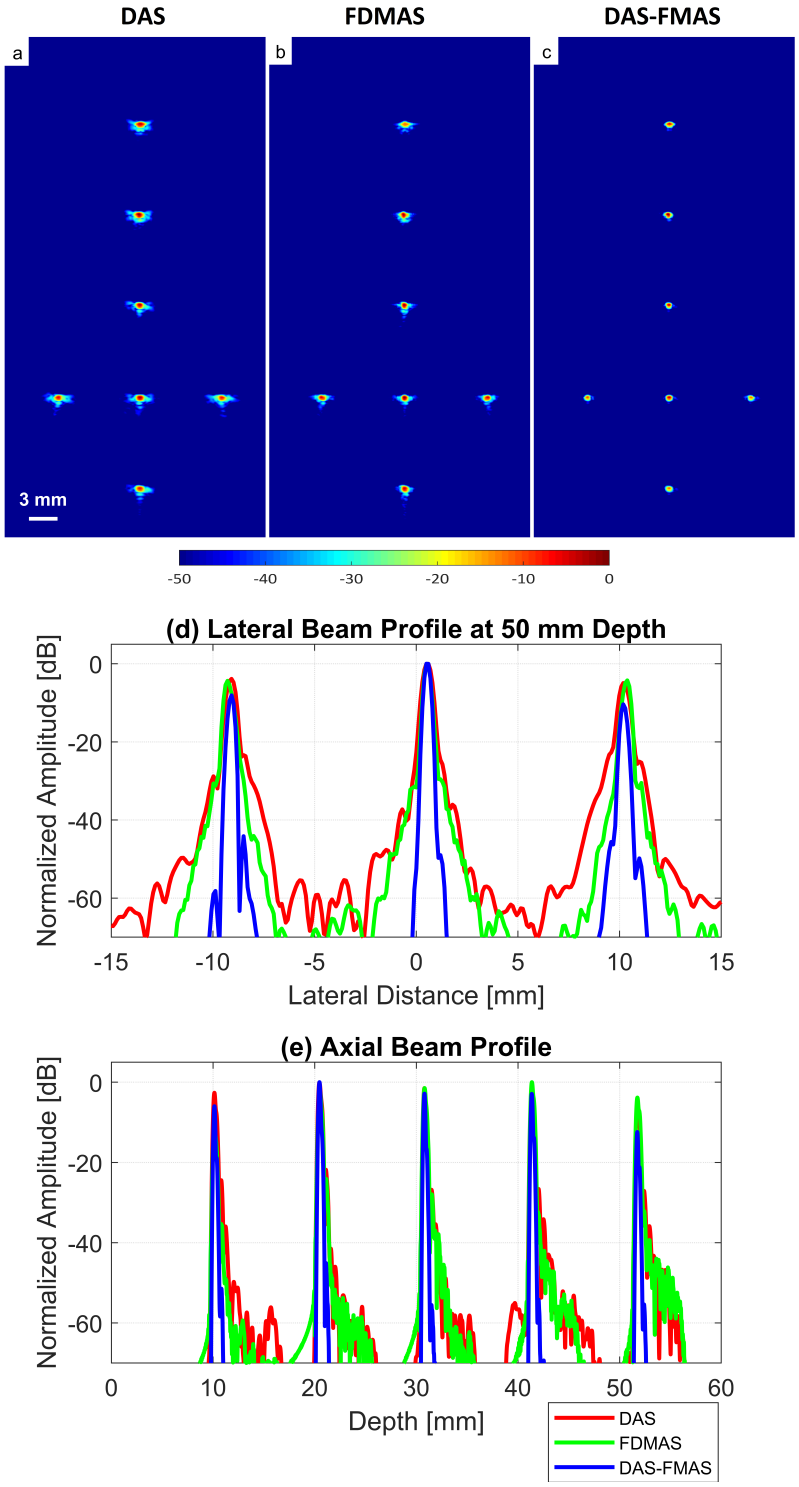

Figure 5.5: B-mode images of wire phantoms for a) DAS, b) FDMAS and c) DAS-FMAS formed with 13 plane waves. d) Beam profile along the lateral direction at the 45 mm depth.

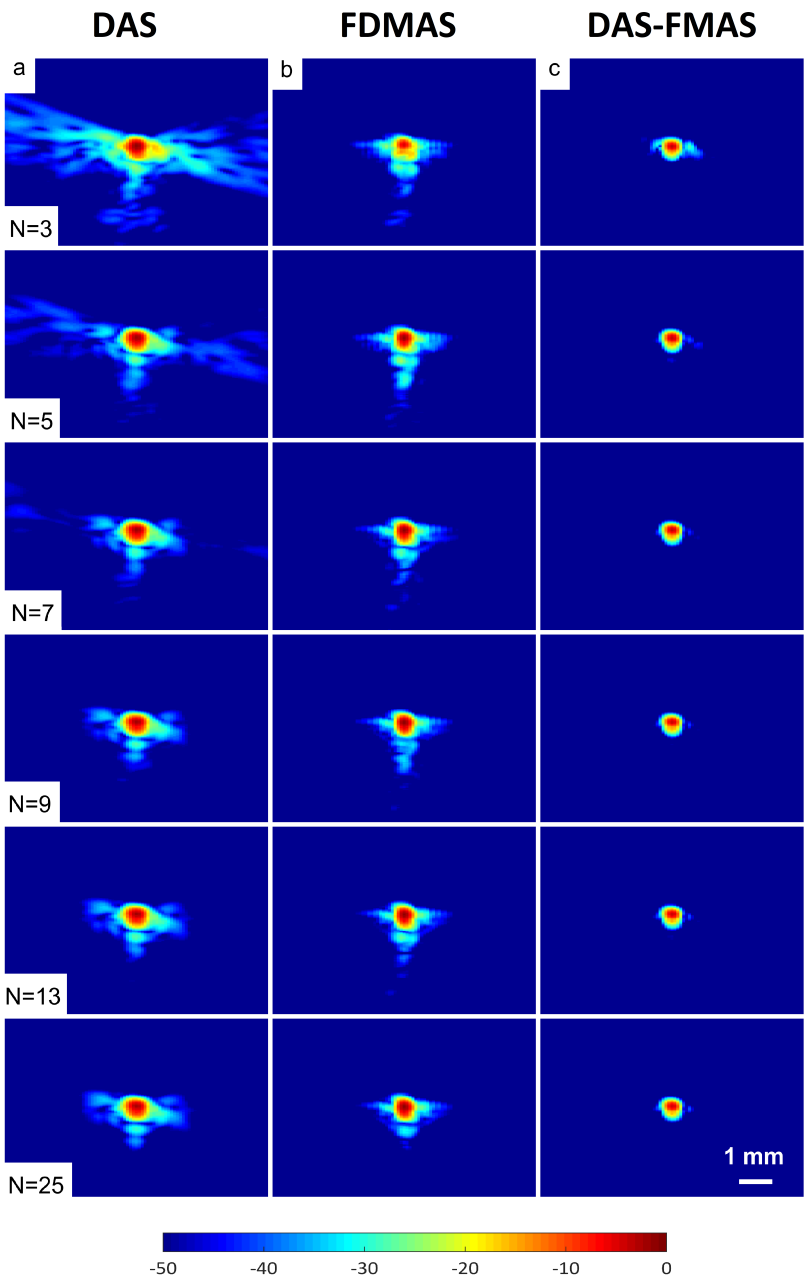

Figure 5.6: B-mode images with plane waves ($N = 3$ to $N = 25$) for the wire target at the 30 mm depth with a) DAS, b) FDMAS and c) DAS-FMAS. The side lobes reduction in the lateral direction starts to improve with DAS-FMAS from $N = 3$.

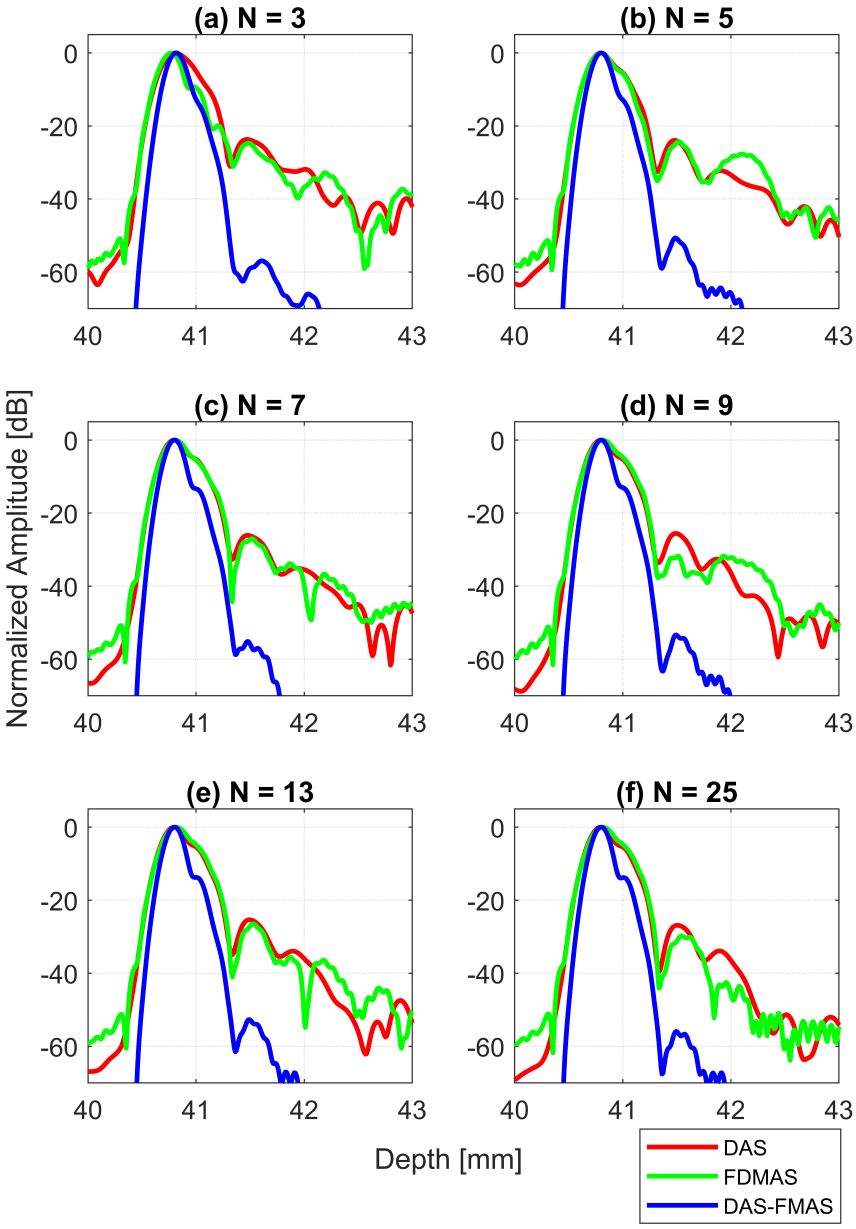

Figure 5.7: Axial beam profile for the wire target at the 30 mm depth with DAS, FDMAS and DAS-FMAS using a) $N = 3$, b) $N = 5$, c) $N = 7$, d) $N = 9$, e) $N = 13$ and f) $N = 25$. There are no significant changes in axial lobes between DAS and FDMAS for all numbers of compounding angles, whereas for DAS-FMAS the main lobes are narrowed and the side lobes are attenuated by average 25 dB.

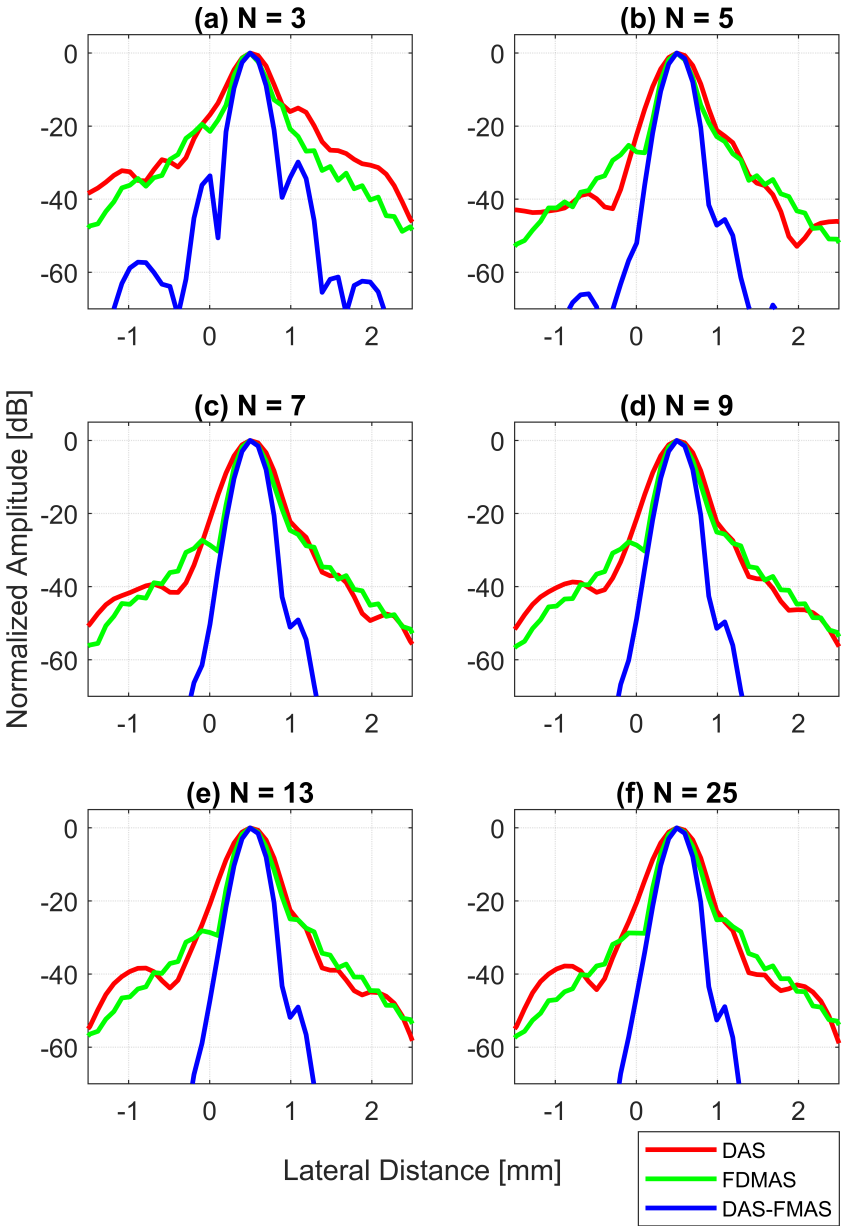

Figure 5.8: Lateral beam profile for the wire target at the 30 mm depth with DAS, FDMAS and DAS-FMAS using a) $N = 3$, b) $N = 5$, c) $N = 7$, d) $N = 9$, e) $N = 13$ and f) $N = 25$. The main lobes are narrower and the side lobes are attenuated more with DAS-FMAS compared to DAS and FDMAS.

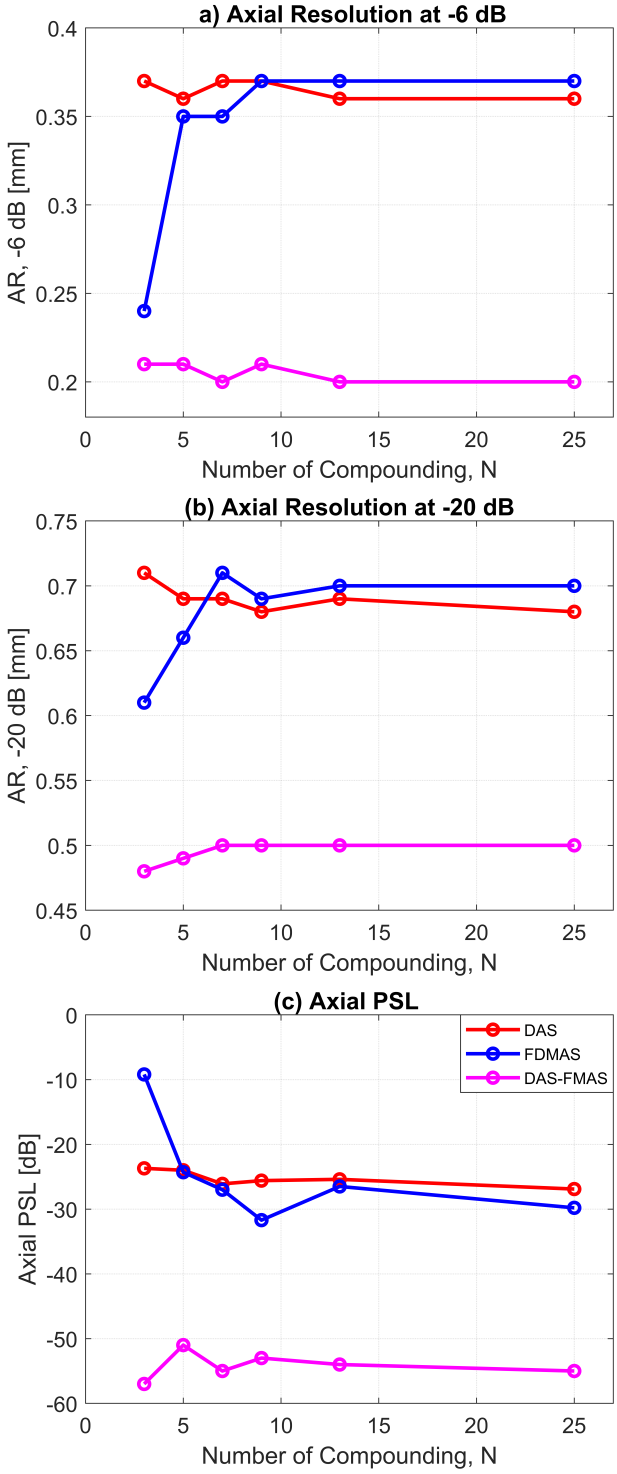

Figure 5.9: The AR for DAS, FDMAS and DAS-FMAS at a) −6 dB and b) −20 dB levels measured at the 30 mm depth on the wire target. The PSL along the axial direction is presented in (c).

compounding angles for all investigated techniques and DAS-FMAS produces the best results among them. At $N = 3$, the LR for DAS-FMAS is improved by 36% and 19% compared to DAS and FDMAS. As the number of compounding angles increases to $N = 25$, DAS-FMAS shows improvement by 37% and 20% compared to DAS and FDMAS. The LR for all techniques does not show any changes beyond $N = 13$.

LR results at −20 dB level for DAS, FDMAS and DAS-FMAS are given in Fig. 5.10(b). The LR at -20 dB with $N = 3$ for DAS, FDMAS and DAS-FMAS are 1.4 mm, 0.93 mm and 0.57 mm. The DAS-FMAS shows improvement by 59% and 38% when compared to DAS and FDMAS. With $N = 25$, the LR with DAS-FMAS shows improvement by 38% and 20% compared to DAS and FDMAS. Beyond $N = 5$, there is no any changes on the LR at -20 dB for all techniques investigated.

The PSLs in the lateral direction for DAS, FDMAS and DAS-FMAS are given in Fig. 5.10(c). All investigated techniques show improvement in reducing the PSL as the number of compounding angles increases from $N = 3$ to $N = 25$. DAS-FMAS gives the best results when compared to DAS and FMAS. At $N = 3$, the PSL with DAS-FMAS has been reduced by 14.7 dB and 10.3 dB more than that using DAS and FDMAS, respectively. For $N = 25$, the PSL has been reduced by 11.1 dB and 23 dB more with DAS-FMAS when compared to that using DAS and FDMAS.

The experimental results on cysts with diameters of 1.3 mm and 3.0 mm at the depths of 15 mm and 45 mm with 13 compounding angles as given in Table 2.1 are shown in Fig. 5.11(a), (b) and (c). The CRs for all cysts in the circles i, ii, iii and iv, have been improved with FDMAS and DAS-FMAS compared to DAS. Qualitatively, it can be seen the reduction of clutter noise levels is more significant with DAS-FMAS compared to DAS and FDMAS. This can be seen on the B-mode image of the 1.3 mm diameter cyst (marked as circle iii) which is barely visible with DAS and FDMAS but the contrast has been improved with DAS-FDMAS. The lateral beam profiles at 15 mm and 45 mm are shown in Fig. 5.11(d) and (e), respectively.

A cyst with a 3 mm diameter located at the 15 mm depth as marked by circle ii in Fig. 5.11 is chosen to measure the image CR and CNR. The B-mode images for the cyst with DAS, FDMAS and DAS-FMAS are shown in Fig. 5.12 (a), (b) and (c), respectively. All images are displayed with a 50 dB dynamic range. In general, FDMAS and DAS-FMAS perform better than DAS where more clutter noise has been reduced inside the anechoic region. The beam profile along the lateral direction at the 15 mm

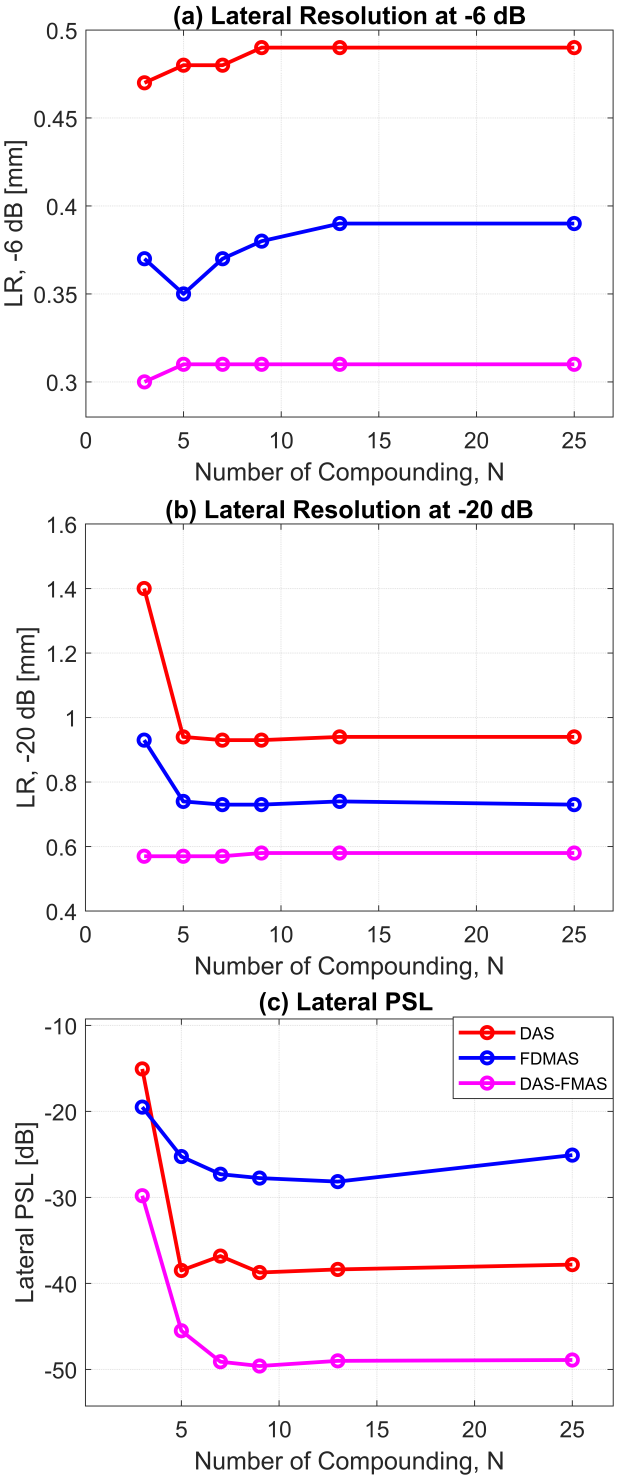

Figure 5.10: The LR for DAS, FDMAS and DAS-FMAS at a) −6 dB and b) −20 dB levels measured at the 30 mm depth on the wire target. The PSL along the lateral direction is presented in (c).

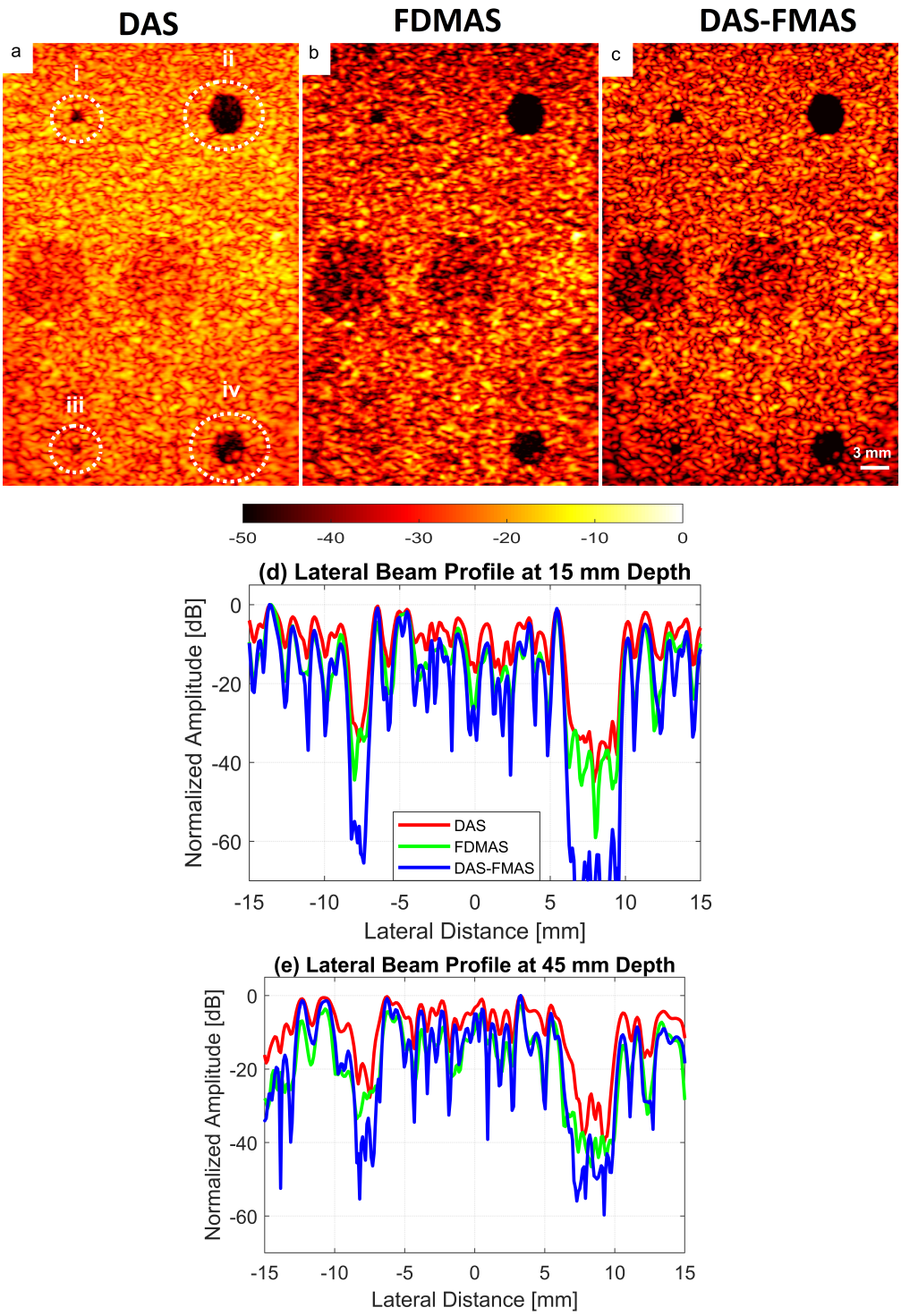

Figure 5.11: B-mode images ($N = 13$) for a) DAS, b) FDMAS and c) DAS-FMAS. Beam profiles along the lateral direction at the d) 15 mm and e) 45 mm depth. The CRs for all four cysts are improved with DAS-FMAS.

depth is given in Fig. 5.13. The clutter noise is keeping reduced as the number of compounding angles increases from $N = 3$ to $N = 25$ for both the 1.3 mm and 3.0 mm diameter cysts.

The CR for the 3.0 mm diameter cyst at the 15 mm depth is given in Fig. 5.14(a). The CRs for all techniques keep improving as the number of compounding angles increases. DAS-FMAS provides improvements of 14.1 dB and 7.29 dB in CR than DAS and FDMAS with $N = 3$. With $N = 25$ the CR for DAS-FMAS is -49.8 dB which is the highest when compared to that using DAS (-26.1 dB) and FDMAS (-27.9 dB). No clutter noise is present inside the anechoic regions with DAS-FMAS, as it has been attenuated below the -60 dB range as shown in Fig. 5.13(f).

The CNR for the 3.0 mm diameter cyst at the 15 mm depth is given in Fig. 5.14(b). As opposed to all other performance indexes, the CNR for DAS-FMAS is the lowest compared to that using DAS and FDMAS. The CNR does not show significant variations for DAS-FMAS from $N = 3$, 2.9 dB to $N = 25$, 2.8 dB. The CNRs for FDMAS keep reducing for the same compounding range from $N = 3$ to $N = 25$, while for DAS the CNRs keep increasing. The reduction of clutter noise outside of the cyst reduces the CNR value for DAS-FMAS. The destructive speckle regions in DAS are filled by clutter noise. Once clutter noise is reduced, the destructive region becomes more visible as the dark spot. This can be seen from the beam profile shown in Fig. 5.13. Outside of the cyst regions, the speckle variation is higher with FDMAS and DAS-FMAS. This can be seen when dark spots caused by the speckle destructive regions start to appear outside the cysts with FDMAS and DAS-FDMAS. One of the ways to solve the low CNR problem is by using despeckeling which reduces the speckle fluctuation.

The clutter noise reduction at the 45 mm depth for all techniques is less than that at the 15 mm depth. This is mainly due to the low SNR at deeper locations. DAS-FMAS still performs better than the other two techniques even at the deeper location. Clutter noise inside the 3.0 mm diameter cyst keeps reducing as the number of compounding angles increases from $N = 3$ to $N = 25$.

The B-mode images for *in-vivo* obtained from DAS, FDMAS and DAS-FMAS are presented in Fig. 5.15. All the images are shown with a 50 dB dynamic range. Clutter noise reduction with FDMAS and DAS-FMAS can be seen on the B-mode images starting from $N = 3$. As the number of compounding angles increases to $N = 25$,

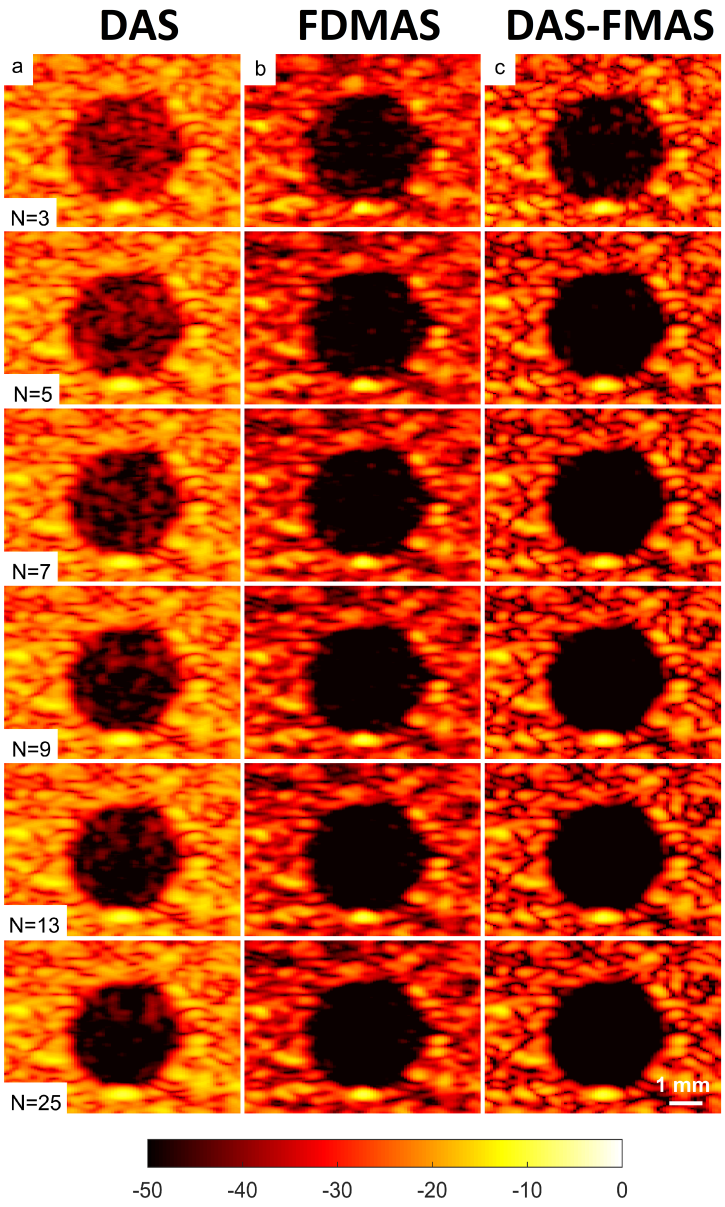

Figure 5.12: B-mode images for the 3.0 mm diameter cyst located at the 15 mm depth using (a) DAS, (b) FDMAS and (c) DAS-FMAS with 3 to 25 compounding angles.

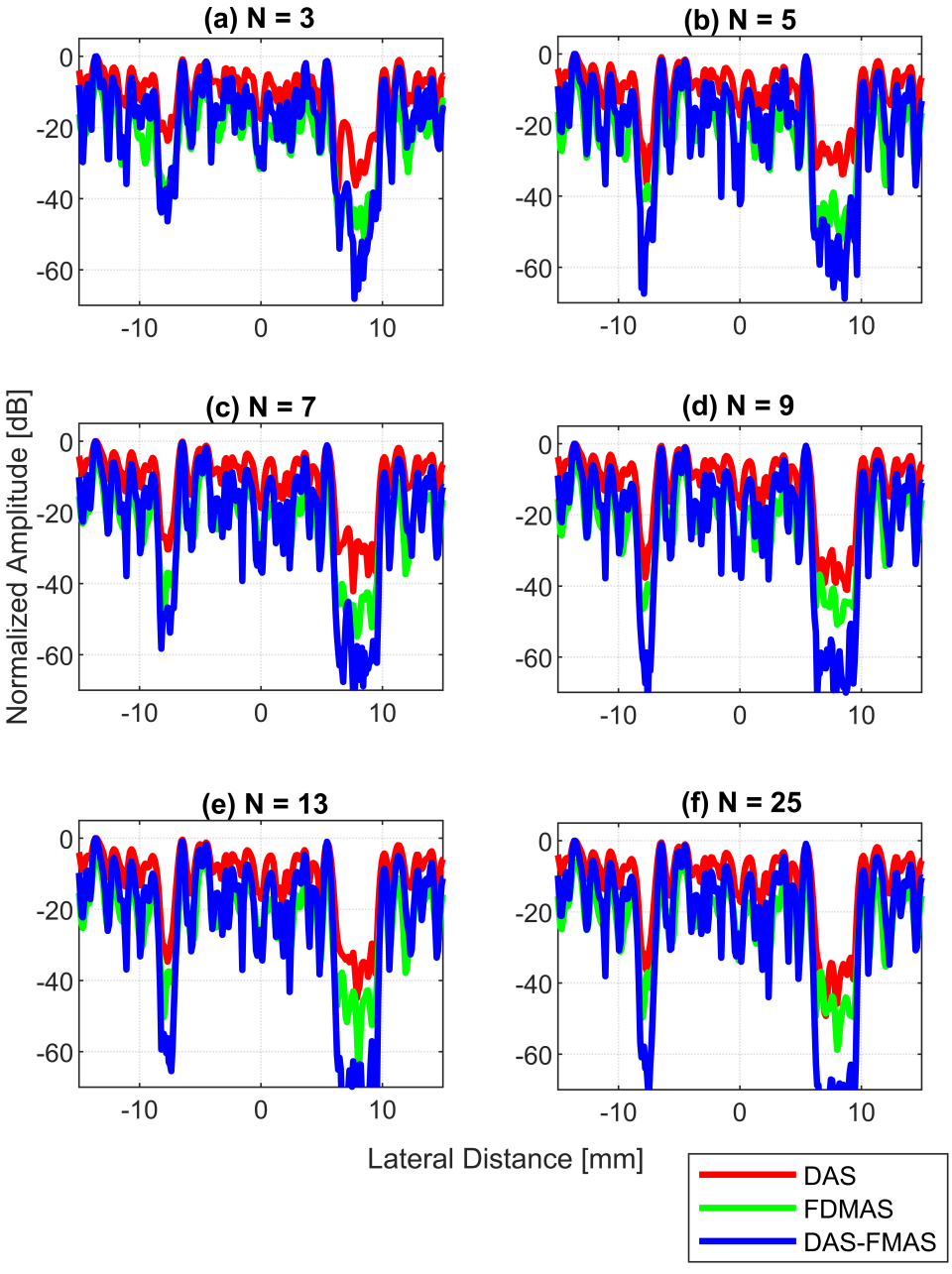

Figure 5.13: Lateral beam profile for the 1.3 mm and 3.0 mm diameter cysts at the 15 mm depth from a) $N = 3$, b) $N = 5$, c) $N = 7$, d) $N = 9$, e) $N = 13$ and f) $N = 25$.

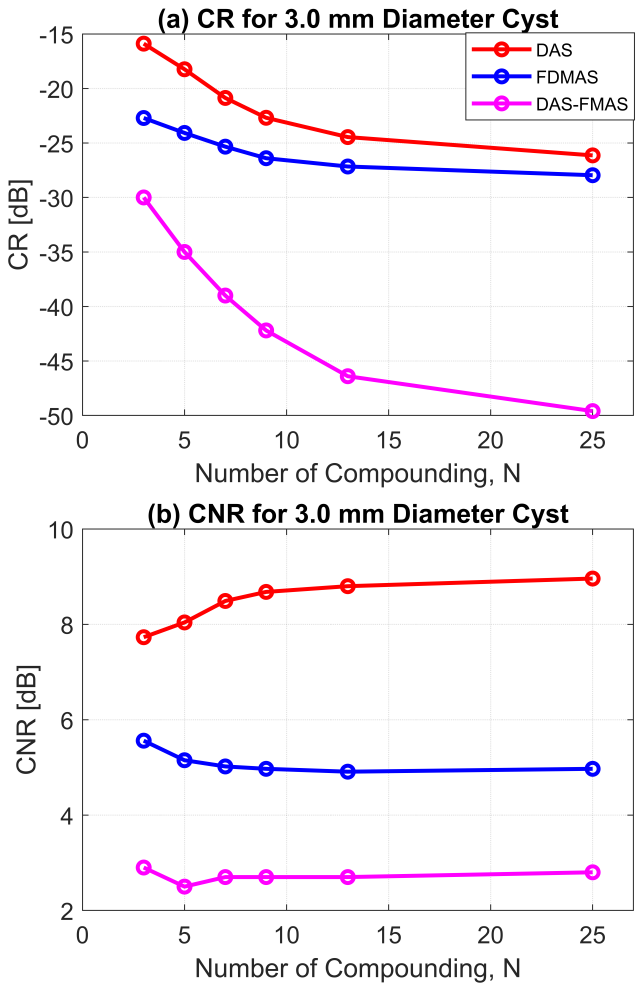

Figure 5.14: The a) CR and (b) CNR using DAS, FDMAS and DAS-FMAS for the 3.0 mm diameter cyst located at the 15 mm depth.

the common carotid artery and the near field regions are free of clutter noise with DAS-FMAS. With FDMAS, the side lobes in the lateral direction are still visible in the common carotid artery. Whereas with DAS clutter noise is still dominating most of the imaging regions.

It is expected with spatial compounding, the lateral resolution will be improved. This is due to noise cancellation between side lobes in the lateral direction. With both DAS and FDMAS, the LR increases with the number of compounding angles but there are only small changes in axial resolution. This is because the axial resolution is mainly determined by the bandwidth of the excitation signal regardless the beamforming techniques or the number of compounding angles. However, with the proposed compounding technique, the axial resolution is improved significantly when compared to that with DAS and FDMAS. The theory behind this is related to the beam directivity which determines the object appearance and shape in the compound image. The intensity distributions of steered plane waves are different for different angles. As the angle increases or decreases, the beam pattern and its intensity distribution are shifted accordingly. This phenomenon is mainly observable on the side lobes along the lateral direction and the axial lobes in the axial direction where they appear at different locations according to the steering angles. In order to analyse this phenomenon in detail, Field II simulations have been performed to obtain the emitted pressure fields for different steering angles at the 30 mm depth. The setup for the simulation is given in Table 2.2. The emitted pressure fields simulated for steering angles $-12°$, $0°$ and $+12°$, are shown in Fig. 5.16. The normalized pressure fields at $x = 0$ mm as highlighted by the dashed line in Fig. 5.16 are shown in Fig. 5.17 for the three steering angles. The variations between pressure fields steered at $\pm 12^0$ and 0^0 in the axial direction are clearly visible. There is a phase shift of 0.02 mm between peak pressure points in between different steering angles. While the shift is invisible between plane waves steered at $-12°$ and $+12°$.

The simulation to measure the phase shift between the pressure points was repeated on the point target located at the 30 mm depth. The 0.02 mm shift between RF peaks are also found in the axial direction for the point target between steering angles of $-12°$ and $0°$. This is shown in Fig. 5.18(a). While this shift is 0.06 mm for the experimental point target between steering angles of $12°$ and $0°$. This is shown in Fig. 5.18(b) and Fig. 5.19. Even though the variation is too small to be considered

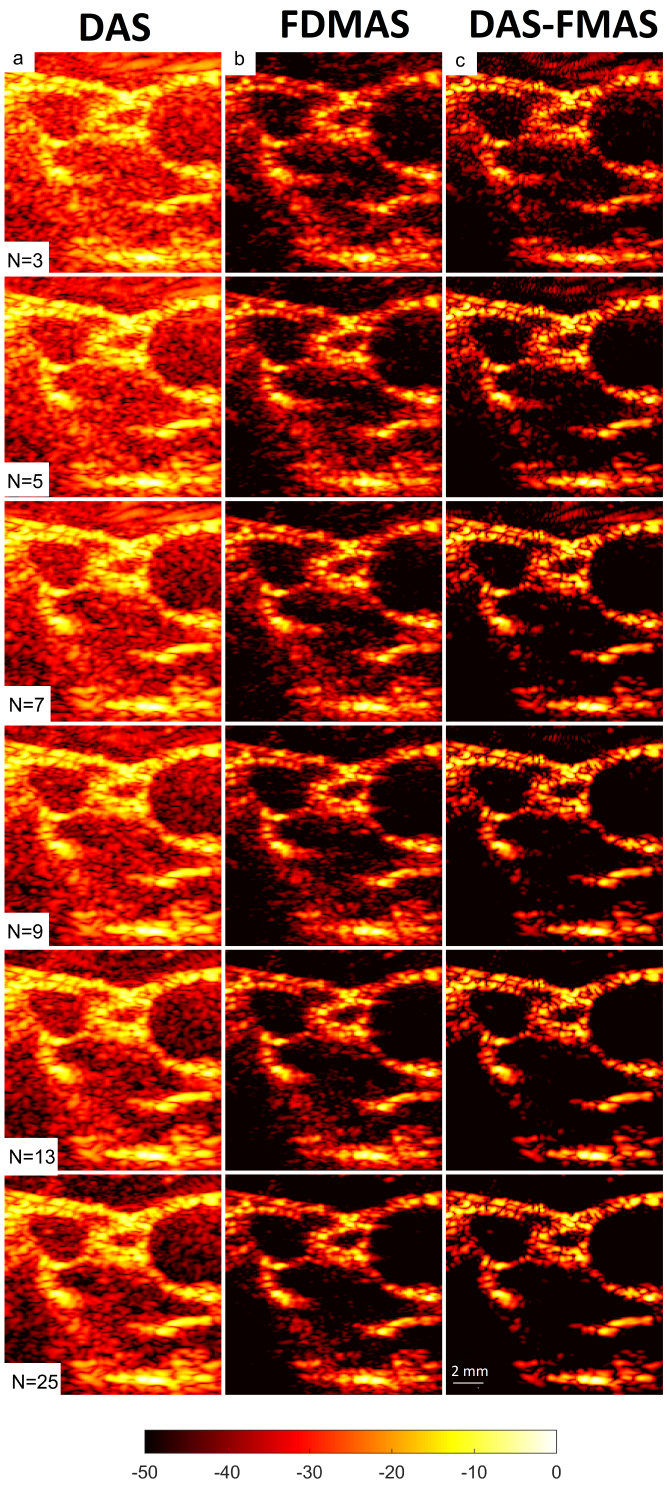

Figure 5.15: The right side CCA B-mode images ($N = 3$ to $N = 25$) formed with (a) DAS, (b) FDMAS and (c) DAS-FMAS, column (c).

in conventional compounding techniques which apply averaging between the steered plane waves, this is not the case when the procedure similar to autocorrelation is used in the proposed technique. For example, when averaging three points as shown in Fig. 5.19(a), it will produce an amplitude value of 0.74. While applying the procedure similar to autocorrelation as given by equation 5.1 for the same three points, it will produce an amplitude value of 1.39. Even a 0.02 mm variation between the aligned RF signals will produce a significant difference on the main lobe values in the axial direction when FMAS compounding is applied. Further implications of phase shift in the RF signals in the axial direction can be seen from the experimental result. Different with simulations, due to many other factors such as phase aberration, the variation between the RF signals further increases up to 0.06 mm. Now as shown in Fig. 5.19(b), the steering effect causes the RF signals appearing at $x = 30.77$ mm have the amplitude values of 1 and -0.4522 for steering angles ± 12 and for $0°$.

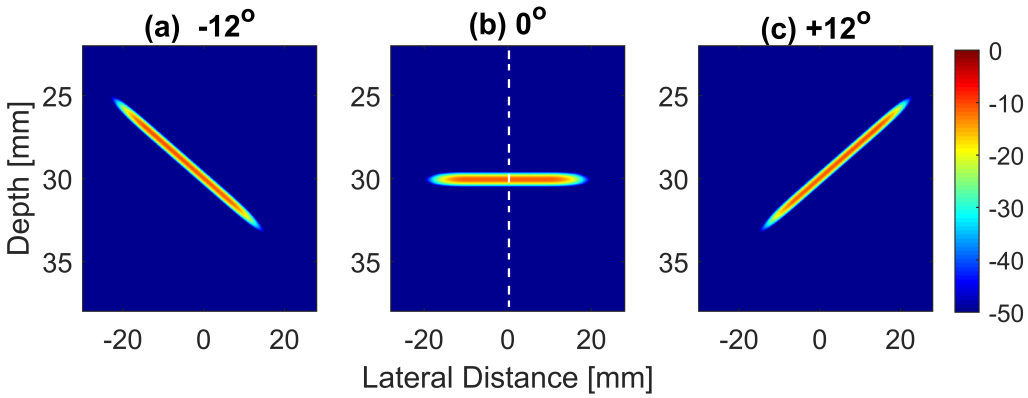

Figure 5.16: Normalized and log compressed pressure fields from plane waves steered at a) $-12°$, b) $0°$ and c) $+12°$. A transmit apodization with a Tukey window ($\alpha = 0.5$) was applied to all emitted pressure fields in order to eliminate edge waves.

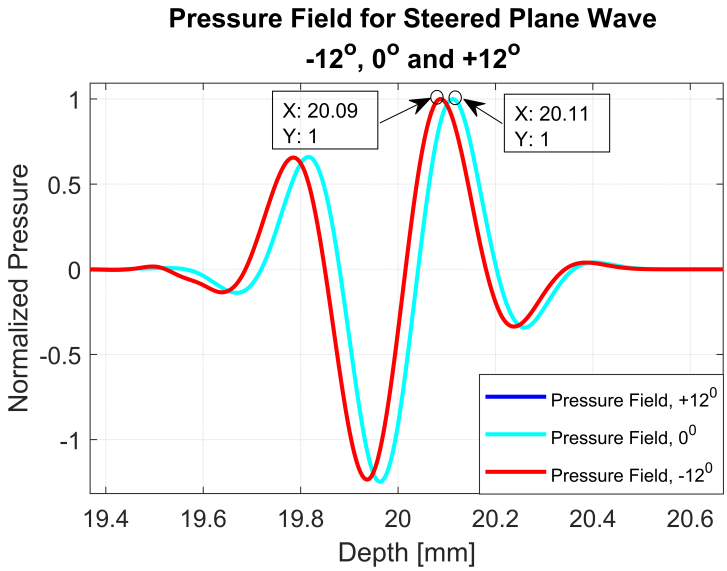

Figure 5.17: Normalized pressure fields at the position of the dashed line as shown in Fig. 5.16 from plane waves steered at a) −12°, b) 0° and c) +12°.

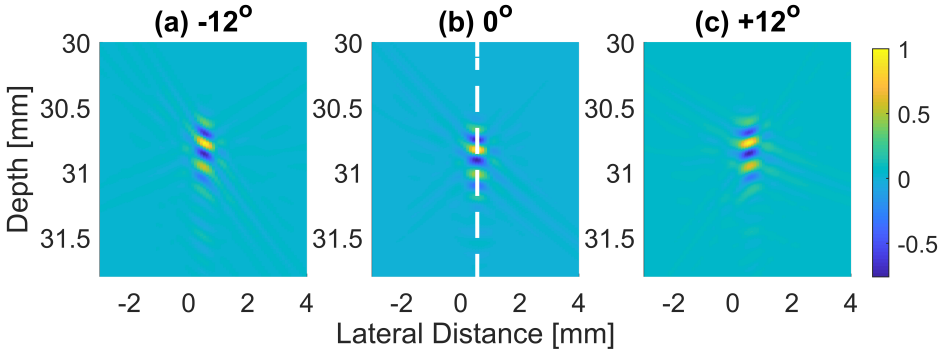

Figure 5.18: The received RF signals beamformed with DAS (before envelope detection and log compression) for a wire target with plane waves steered at a) −12°, b) 0° and c) +12°.

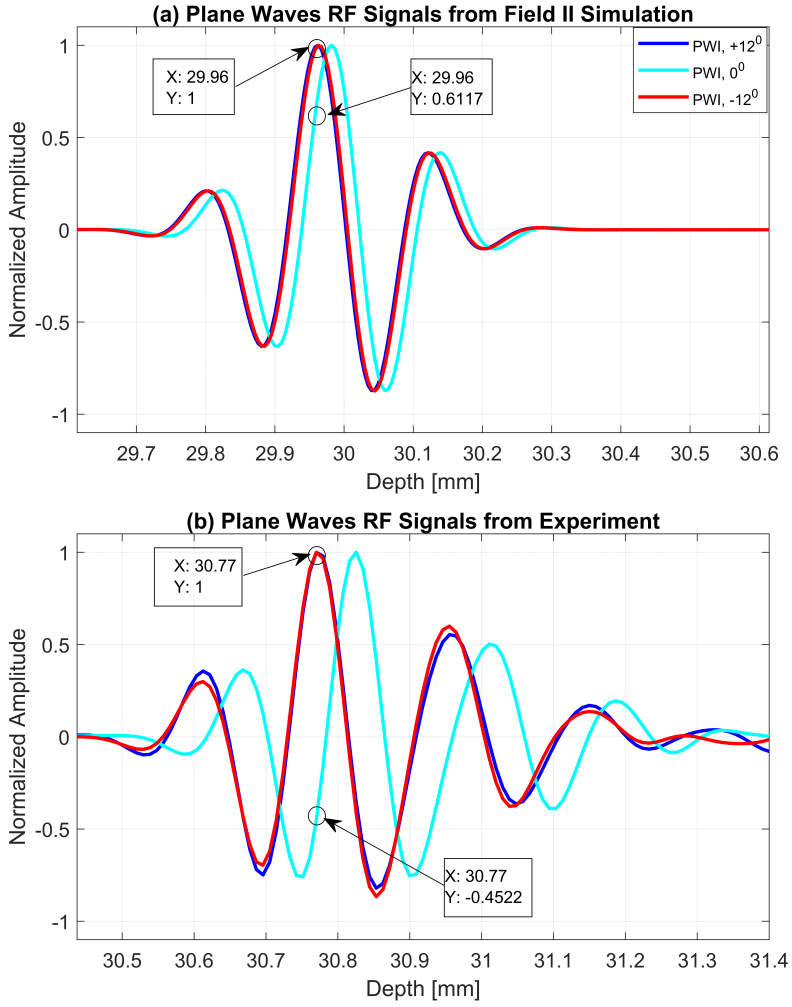

Figure 5.19: RF signals for the dashed line as shown in Fig. 5.18(b) from plane waves steered at $-12°$, $0°$ and $+12°$ with a) Field II simulations and b) experiments.

The computational time with DAS, FDMAS and DAS-FMAS for the setup in Fig. 4.1 is given in Fig. 5.20. The computer operating system used to calculate the processing time is Windows 7 enterprise 64-bit. The computer specification is as follows: CPU (CORE i5-4460, Intel Corporation Co., Ltd., Santa Clara, CA, USA), 3.20-GHz clock speed, 4 cores and 16-GB DDR3 RAM. The imaging point step in the lateral direction for DAS and FDMAS is set to $\lambda/3$=0.1 mm and for the axial direction it is c*T_s/2=9.625 μm. The width and depth of the imaging field are 60 mm and 39 mm. It can be seen that the computational time for DAS with conventional compound-

ing is almost the same with that using DAS-FMAS. There is no significant difference between the processing time using DAS and DAS-FMAS. Whereas for FDMAS the computational time is 7 times more than that with DAS and DAS-FMAS for $N = 25$.

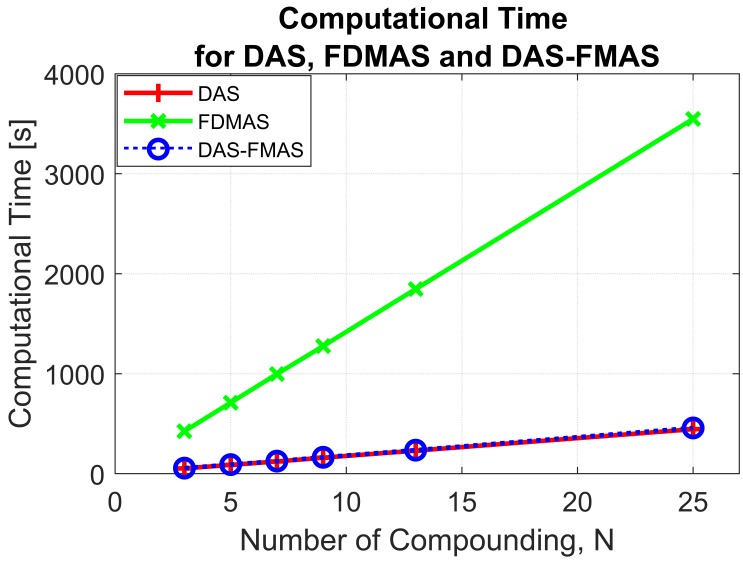

Figure 5.20: Computational time measured for DAS, FDMAS and FMAS with different number of compounding.

5.4 Conclusion

The proposed compounding technique FMAS is able to improve the B-mode image spatial resolution and CR compared to DAS and FDMAS. The CC of FDMAS is significantly higher than DAS and lower than other adaptive beamforming techniques such as minimum variance. However, keeping lowering the CC in FDMAS will be beneficial for real time imaging and reducing the processing power. Thus, instead of applying FDMAS during beamforming, implementing FDMAS during compounding will not only reduce the CC, but also improve the overall B-mode image quality. There are several rooms for improvements on the present method. The clutter noise reduction at deeper locations, beyond 40 mm, tends to produce small dark-spot artifacts as found in Eigenspace-based beamformer Aliabadi *et al.* (2016); Zeng *et al.* (2013). One of the methods to solve this problem is by displaying the B-mode image with a higher dynamic range such as more than 70 dB. The downside of increasing the dynamic range is that

it may make clutter noise visible. Thus, more work is needed to deal with the dark-spot artifacts that are present with DAS-FMAS.

Chapter 6

New Unsharp Masking Method Compatible with Ultrasound B-mode Imaging

In this chapter, the conventional and new improved unsharp masking (UM) techniques were discussed and analysed in detail. In the first section, the implementation of conventional UM on the ultrasound B-mode images were discussed. As for the second section, the improved version of UM was implemented and its contribution of improving the ultrasound B-mode image quality was explored in detail. The advantages and disadvantages of the new proposed UM have been highlighted.

6.1 Conventional Unsharp Masking

The conventional UM technique, $u_{\text{con}}[a, b]$ can be represented by the following equation:

$$u_{\text{con}}[a, b] = h[a, b] + \lambda_e |h[a, b] - G[a, b] * h[a, b]| \tag{6.1}$$

where a is the distance in the horizontal axis (columns) while b is the distance in the vertical direction (rows), $h[a, b]$ is the original digital B-mode image, λ_e is the weightage or positive scaling factor and $G[a, b]$ is the low pass filter (LPF). Most commonly employed LPF in UM is the 2-D Gaussian smoothing kernel as given by Cao *et al.*

(2011); Ueng *et al.* (2014):

$$G[a,b] = \frac{1}{2\pi\sigma^2} e^{-\frac{a^2+b^2}{2\sigma^2}} \tag{6.2}$$

where σ is the standard deviation of the Gaussian pixel intensity distribution. UM starts blurring the original digital image with the 2-D Gaussian kernel which will remove the high but retain the low frequency components of the original signal. The blurred image will be subtracted from the original image which contains both high and low frequency components. As a result from the subtraction process, only the high frequency signal of the original image will be preserved. This high frequency signal will be scaled by the weightage λ_e before it is added back to the original image. The weithage is between 0.1 and 0.9 Kwok *et al.* (2013). Implementing a low weightage of 0.1 or less will not produce any significantly change on the final image while a high weightage of 0.9 or more will introduce overshot phenomena. Now the new image will have additional amplitudes on its high-frequency component when compared to the original image. In the ideal case, the visual appearance of the new image sharpness will be significantly improved since its high-frequency contents or the edges have been boosted.

6.2 Use of Unsharp Masking on Ultrasound B-Mode Images

In this section, the effects of UM on ultrasound B-mode images have been investigated. The conventional UM technique has been excessively employed in many medical imaging modalities to enhance the image contrast and details Akbay (2015); Bhateja *et al.* (2017); Cruz *et al.* (2012). However, in ultrasound B-mode imaging, the expected outcome is not the same as that for other kinds of medical images. For B-mode images, it is expected that not only the image contrast and resolution, but also the level of clutter noise is low. Clutter noise has become an obstacle for the radiographer and physician to interpret the scanning results accurately.

To evaluate the influences of the conventional UM technique on the B-mode image, anechoic cysts with a 3.0 mm diameter located at the 15 mm depth were chosen. The anechoic regions consist of water or fluid produce a very low level of echoes. Thus, the

region is highlighted in black in B-mode images. Fig. 6.1 shows the B-mode image used to evaluate the effects of UM.

The steps involved in the implementation of UM on the B-mode image is the same as that in equation 6.1. From equation 6.1 it is known that either the weightage λ_e or the standard deviation σ of the 2-D Gaussian blurring kernel will influence the final image quality. Thus, in this section only the standard deviation of the 2-D Gaussian kernel has been varied between 1, 3 and 5 with the fixed λ_e of 0.6. Fig. 6.1 shows the B-mode of the 3.0 mm diameter cyst when the UM taking place with different standard deviations. As expected, increasing the standard deviation by 1, 3 and 5, magnifies the errors between the original and the blurred images. The changes can be seen in Fig. 6.1(c) to (f) and (i). The errors become more apparent and stronger as the standard deviation σ increases. The errors that are added back to the original B-mode image don't reduce clutter noise that is present inside the cyst, instead, it has increased the noise level. This is shown in Fig. 6.1 (j) and Fig. 6.2(c).

The normalized amplitudes in the dB scale have been quantized to their corresponding unsigned 8-bit (0-255) counterparts. The adjacent normalized amplitudes in the lateral direction have relatively bigger differences. This is because the B-mode image as shown in Fig. 6.1 has been beamformed with the spatial sampling period of $\lambda/3$. Since the sampling period is determinant to the smoothness level of transition of the digital image pixel values in the lateral direction, reducing the sampling period will produce smoother signal transition. This can be seen in Fig. 6.2. This unpleasant sharp overshoot phenomenon starts to exist with the low standard deviation of $\sigma = 1$. When σ for the Gaussian kernel increases, the sharp overshot also keeps increasing.

The conventional UM technique is performed in the quantized digital domain. Thus, saving the B-mode image with different dynamic ranges will affect the final UM outcome Dutt & Greenleaf (1996). A lower dynamic range may produce better output with UM compared with that using a higher dynamic range. Even though a low dynamic range qualitatively improves the image contrast ratio, there are no changes on the image resolution in the axial and lateral directions.

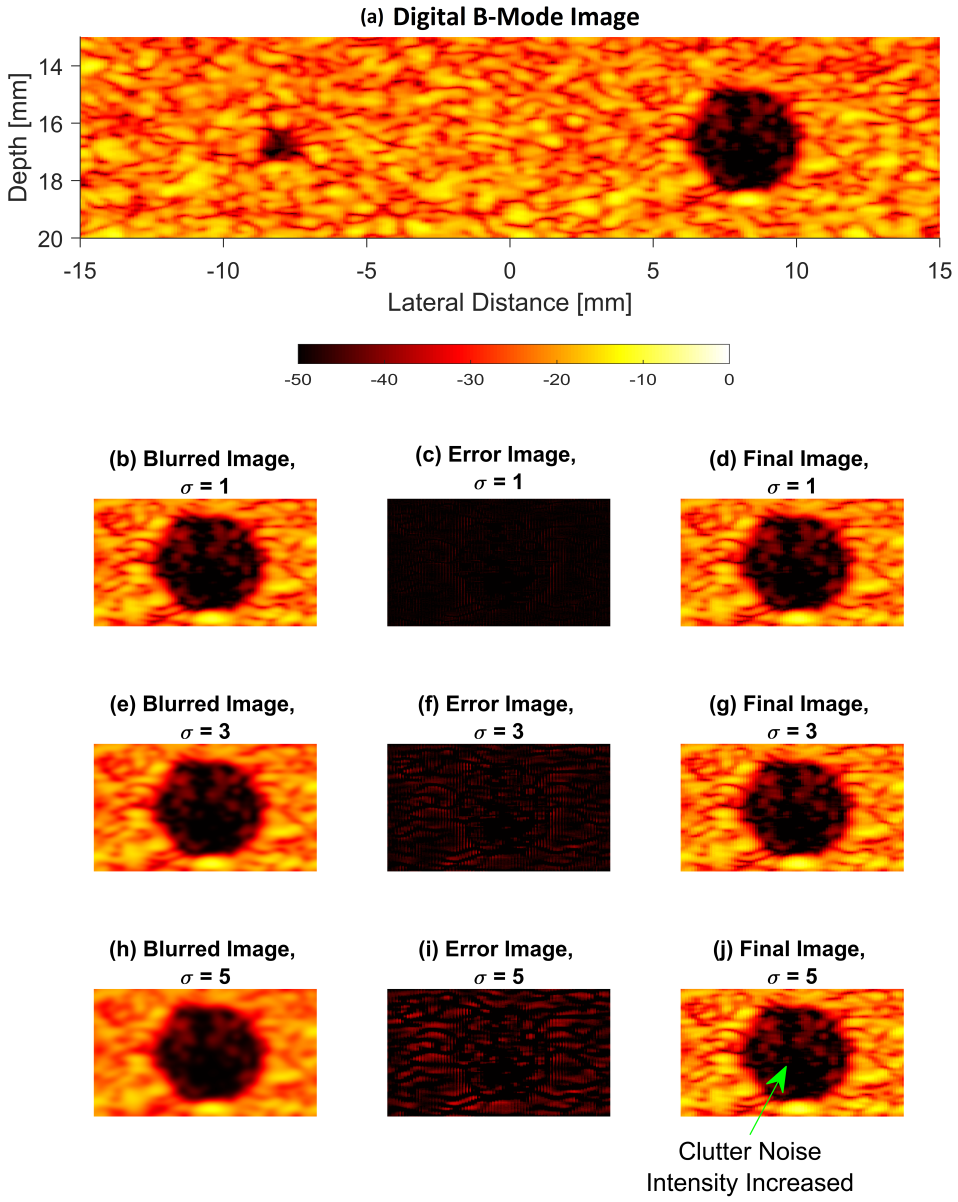

Figure 6.1: a) B-mode image of the 3.0 mm and 1.3 mm diameter cysts beamformed with DAS located at the 15 mm depth for $N = 13$. The B-mode images of the 3.0 mm diameter cyst blurred with different standard deviations ($\sigma = 1$, 3 and 5 for b, e and h). The error images produced between the original and the blurred images prior to scaling are shown in c, f and i. The final B-mode images produced from UM are given in d, g and j. The arrows on (j) indicate the increased level of clutter noise. The B-mode image displayed within dynamic range of 50 dB.

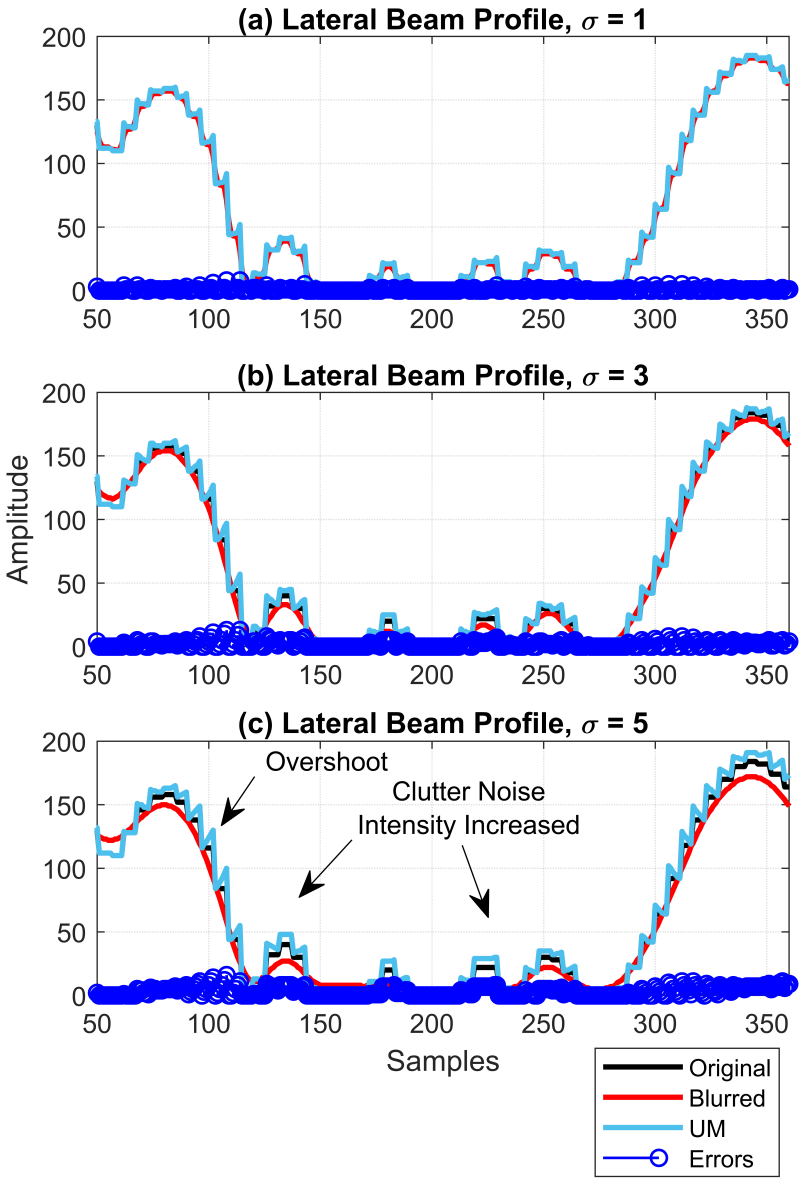

Figure 6.2: The lateral beam profile of the 3.0 mm diameter cyst when blurred with different standard deviations (a) $\sigma = 1$, b) $\sigma = 3$ and c) $\sigma = 5$ for b, e and h shown in Fig. 6.1. The arrows highlight the increased level of clutter noise.

6.3 Improved Unsharp Masking Method

In this thesis, the UM method is implemented on the ultrasound B-mode image on the RF signal envelope prior to log-compression, with three iterations and unique weightages for positive and negative errors that are produced between the original and blurred signals. We begin with the review of conventional UM implemented on digital images in order to lay the foundation for our improved UM technique based on coherent and non-coherent CPWI techniques. In this work, the proposed UM method acts as a denoising tool to reduce clutter noise and at the same time enhance the spatial resolution of the B-mode image.

Instead of applying the conventional UM method to the ultrasound B-mode image, a new application has been found to reduce clutter noise and improve the image resolution. The conventional UM equation has been modified to adapt the CPWI B-mode imaging criteria. The new improved UM equation no longer enhances the high-frequency components but increases the image contrast.

The new proposed UM method taking place on the envelope of the beamformed RF signal has an iterative scheme that computes the successive new improved envelope signal as given by:

$$u_{\mathrm{new}j}(x,z) = \begin{cases} u_{\mathrm{new}j-1} + \lambda_{\mathrm{e}1}(u_{\mathrm{new}j-1} - u^{*}_{\mathrm{new}j-1}), & u_{\mathrm{new}j-1} - u^{*}_{\mathrm{new}j-1} \geq 0 \\ u_{\mathrm{new}j-1} + \lambda_{\mathrm{e}2}(u_{\mathrm{new}j-1} - u^{*}_{\mathrm{new}j-1}), & u_{\mathrm{new}j-1} - u^{*}_{\mathrm{new}j-1} < 0 \end{cases} \tag{6.3}$$

where j is the number of iterations, $u_{\mathrm{new}j}(x,z)$ is the unsharp masked image, $u^{*}_{\mathrm{new}j}(x,z)$ is the original image, λ_{e1} and λ_{e2} indicate two different weightages for positive and negative errors. Two different weightage schemes have been used in the proposed UM method to selectively control the amount of intensity attenuation or amplification in ROIs. The UM technique was applied to PWI and CPWI with different blurring methods, Savitzky-Golay as LPF for PWI and non-coherent CPWI for CPWI. Since there is no non-coherent portion for PWI, a LPF as used in conventional methods has been used to blur the original PWI signal $u^{*}_{\mathrm{new}j}(x,z)$. While for CPWI, the non-coherent CPWI signals have been assigned as the blurring signals. Thus, the evaluation of the proposed UM method was divided into two sections detailing its implementation on PWI and CPWI.

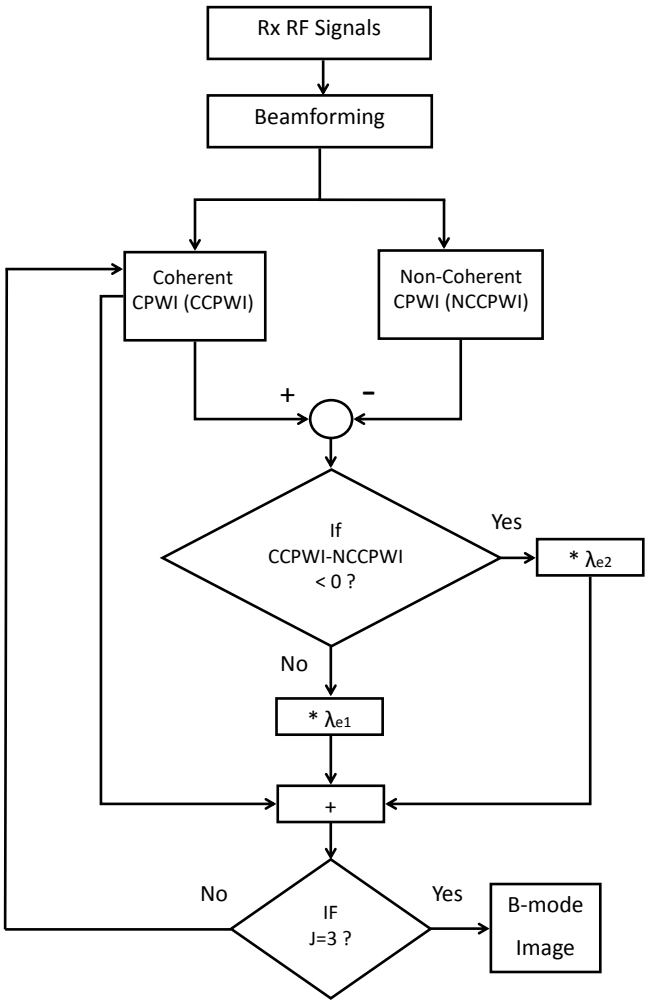

Figure 6.3: Flow chart for the proposed UM technique.

6.3.1 Implementation of UM on PWI

In PWI, there are no non-coherent signals. The digital filtering technique known as Savitzky-Golay (S-G) has been used as the smoothing kernel in equation 6.3 Schafer (2011). It was chosen since this filter performs better than other standard averaging finite impulse response (FIR) filters which tend to filter high frequency components along with noise. The filter operation is based on the polynomial order and the frame length.

The implementation of UM on PWI gives mixed results where the weak clutter noise was attenuated while the strong clutter noise was amplified. This is because that filtered PWI acts as the blurring kernel in the UM process. Whenever clutter noise appears above the filtered PWI signals, it will be amplified and vice versa. As can be seen in Fig. 6.4, when the PWI signals are smaller than the filtered PWI signals (from the 3rd to 15th order), that particular portion is amplified in the UM process as shown in Fig. 6.5. Enhancing clutter noise is undesired. As an alternative to the conventional filtering technique, the Non-coherent CPWI signals have been used as the blurring kernel.

All the results for PWI with UM are present together with those for CPWI with UM.

6.3.2 Implementation of UM on CPWI

The two main objectives for the proposed UM method are to improve the B-mode image lateral resolution and reduce clutter noise mainly inside the anechoic region (cyst). This has been done by evaluating the error polarities produced between the coherent and non-coherent signals. There is a possibility to apply filtered coherent CPWI as the blurring signals in the proposed UM method. But the tricky part is to identify the correct filtering order for coherent CPWI. Applying a high filter order on coherent CPWI signals will produce the almost flat output. Thus, when the over filtered coherent CPWI signals appear below the original coherent CPWI ones, the errors are always positive. This is wrong since the blurring signal is supposed to differentiate constructive speckle regions from destructive ones. Whereas, the counterparts of coherent CPWI signals, non-coherent CPWI signals, are always above clutter noise. Thus, there is no need to determine the filtering order manually with the non-coherent CPWI signals

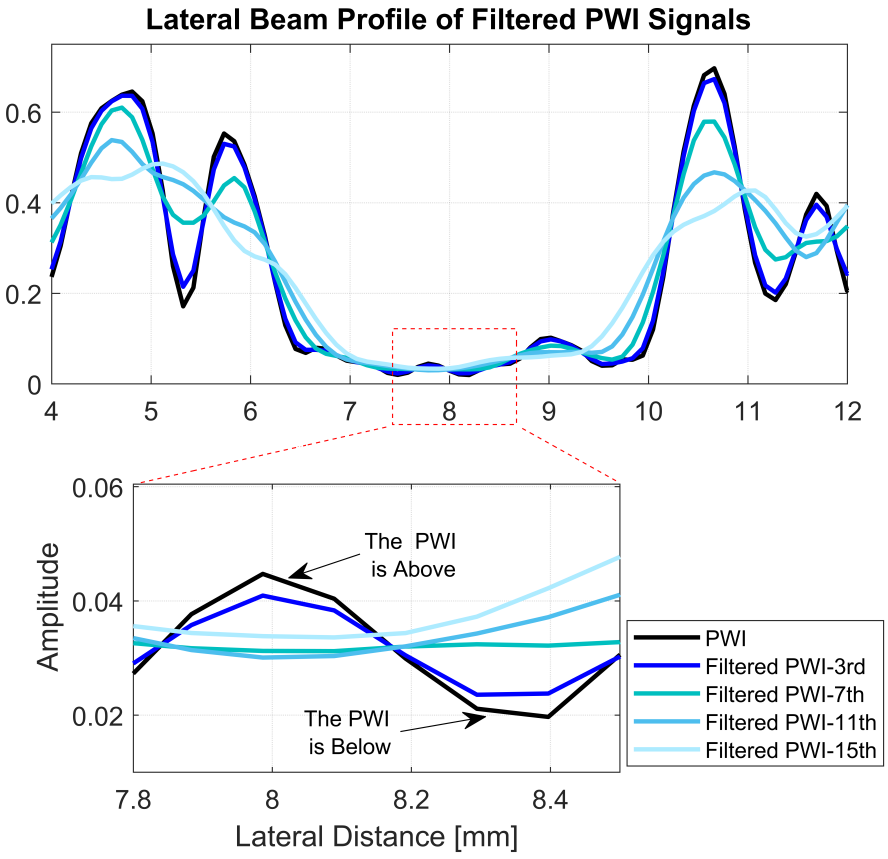

Figure 6.4: The PWI signals filtered with S-G LPF by different numbers of filtering orders. The zoomed portion shows that the PWI signals keep appearing below and above the filtered PWI signal. The beam profile in the lateral direction is shown for the 3.0 mm diameter cyst beamformed with DAS and $N = 9$.

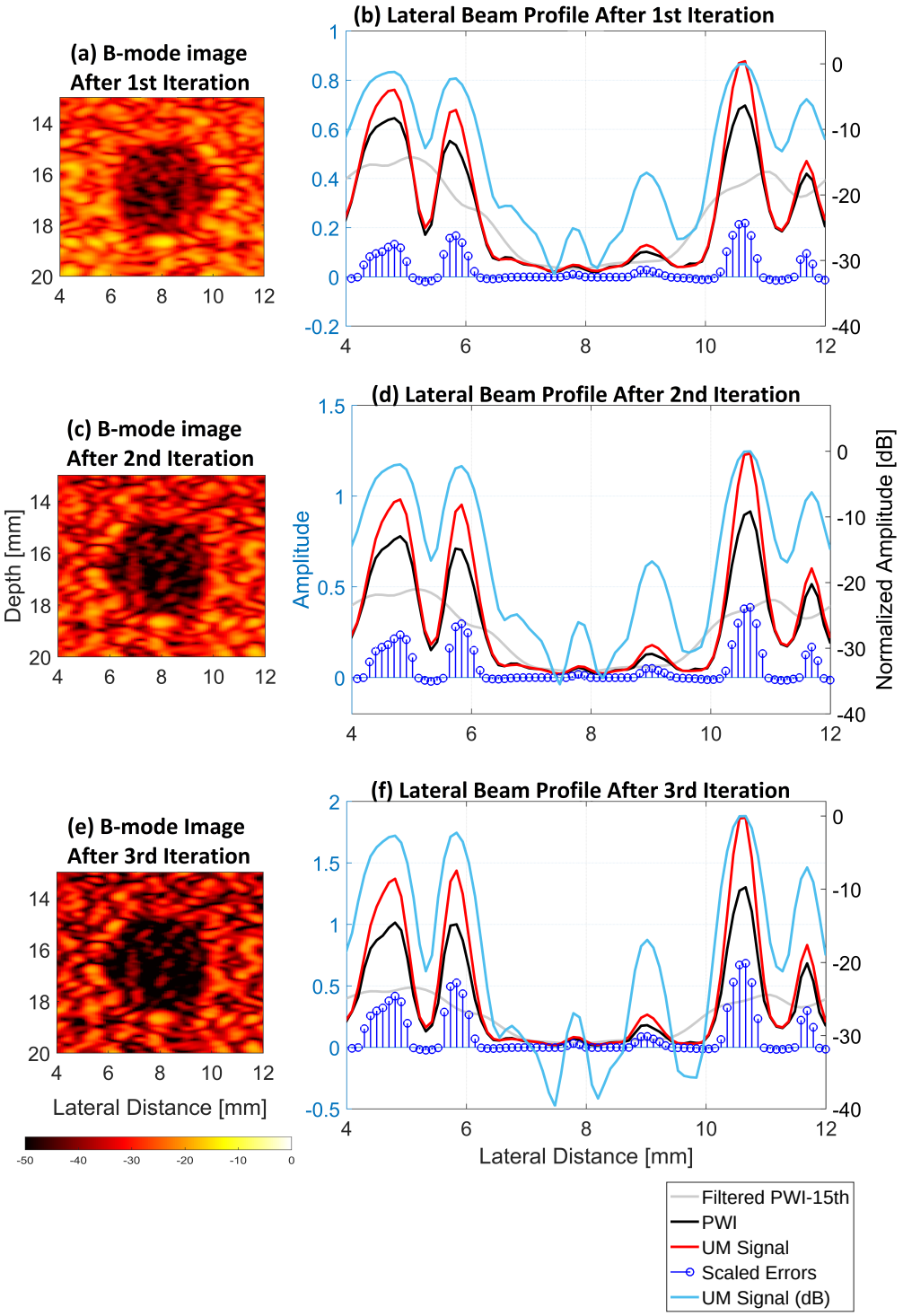

Figure 6.5: The UM technique implemented on PWI. B-mode image and beam profiles for the 1st (a and b), 2nd (c and d) and 3rd (e and f) iteration are shown.

acting as the ideal LPF for the proposed UM method. Clutter noise can be easily identified inside the cyst where the regions are supposed to be anechoic. As opposed to the filtered coherent CPWI signals, non-coherent CPWI signals don't have low-level signals that have a similar amplitude with clutter noise. One of the main reasons is that the phase of the non-coherent CPWI signal has been removed. With this advantage, all signals inside the cyst can be treated as clutter noise and attenuated.

The UM process starts with subtracting the coherent CPWI signal with non-coherent CPWI signal before log compression. The errors are then multiplied with different weightages according to their polarities. The weightages $\lambda_1 = 0.77$ and $\lambda_2 = 0.07$ were determined empirically. This arrangement of weightages is to control the attenuation level of clutter noise. Applying same weightages for both positive and negative errors will lead to a higher dynamic range and turn the grey speckle parts to black regions. This can be misidentified as anechoic regions. The value of 0.07 was assigned for the negative errors because the difference between the non-coherent CPWI and CPWI signals was huge. This small scale was enough to attenuate the noise level. The scaled errors were added back to coherent CPWI signals and all the procedures were repeated for three times. Beyond three iterations, the quality of the B-mode image was worse with a very low level of CNR.

6.4 Experimental Setup

To validate the performance of the proposed UM method, experiments were performed on point targets, anechoic cysts and human *in vivo*. A B-mode imaging sequence was implemented on the UARP II according to the setup shown in Table 2.2 and 2.1. The experimental setup for the point targets, tissue-mimicking phantom and common carotid artery are given in Section 4.1.1. The received RF echoes were sampled at 80 MHz and beamformed with DAS and FDMAS.

6.5 Performance Evaluation

To measure the spatial resolution with the new improved UM technique, a point target at the 30 mm depth was chosen. The axial and lateral resolutions were measured at -6 dB and -20 dB levels. The PSLs on both axial and lateral directions were measured

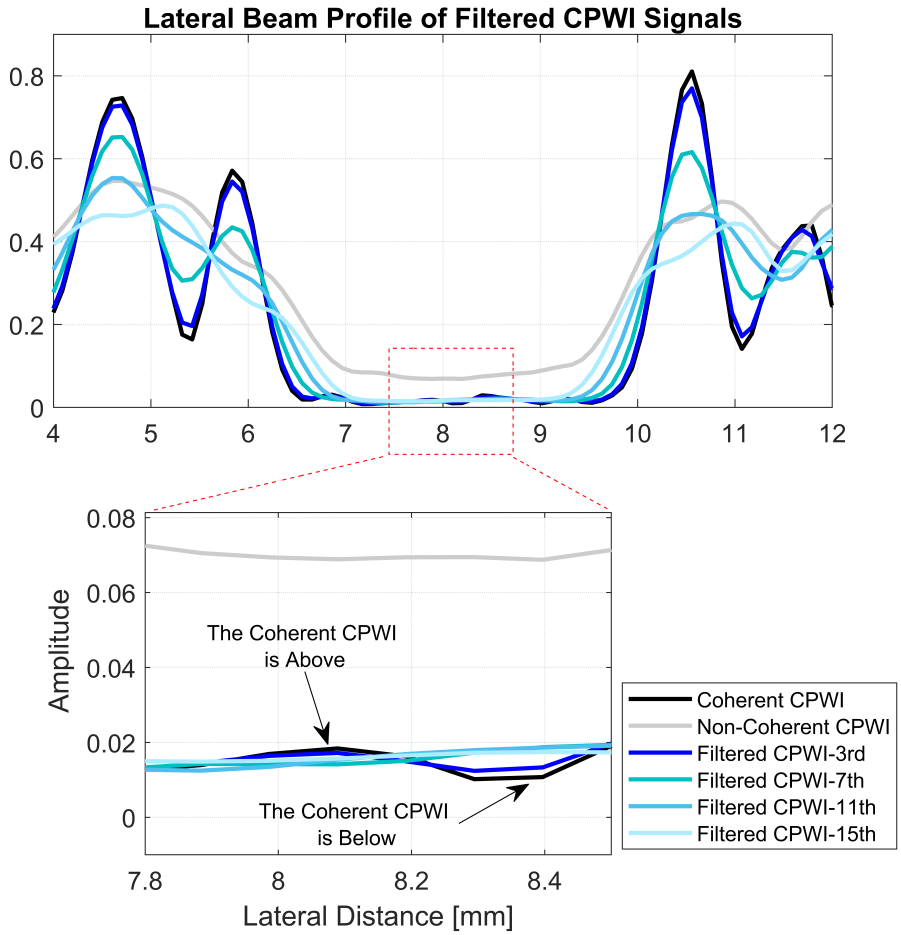

Figure 6.6: The CPWI signals filtered with S-G by different numbers of filtering orders. The zoomed in portion is showing that the CPWI signals keep appearing below and above the filtered CPWI signal, while the Non-coherent CPWI signals are always above the coherent CPWI signals. The lateral beam profile is shown for the 3.0 mm diameter cyst beamformed with the DAS and $N = 9$.

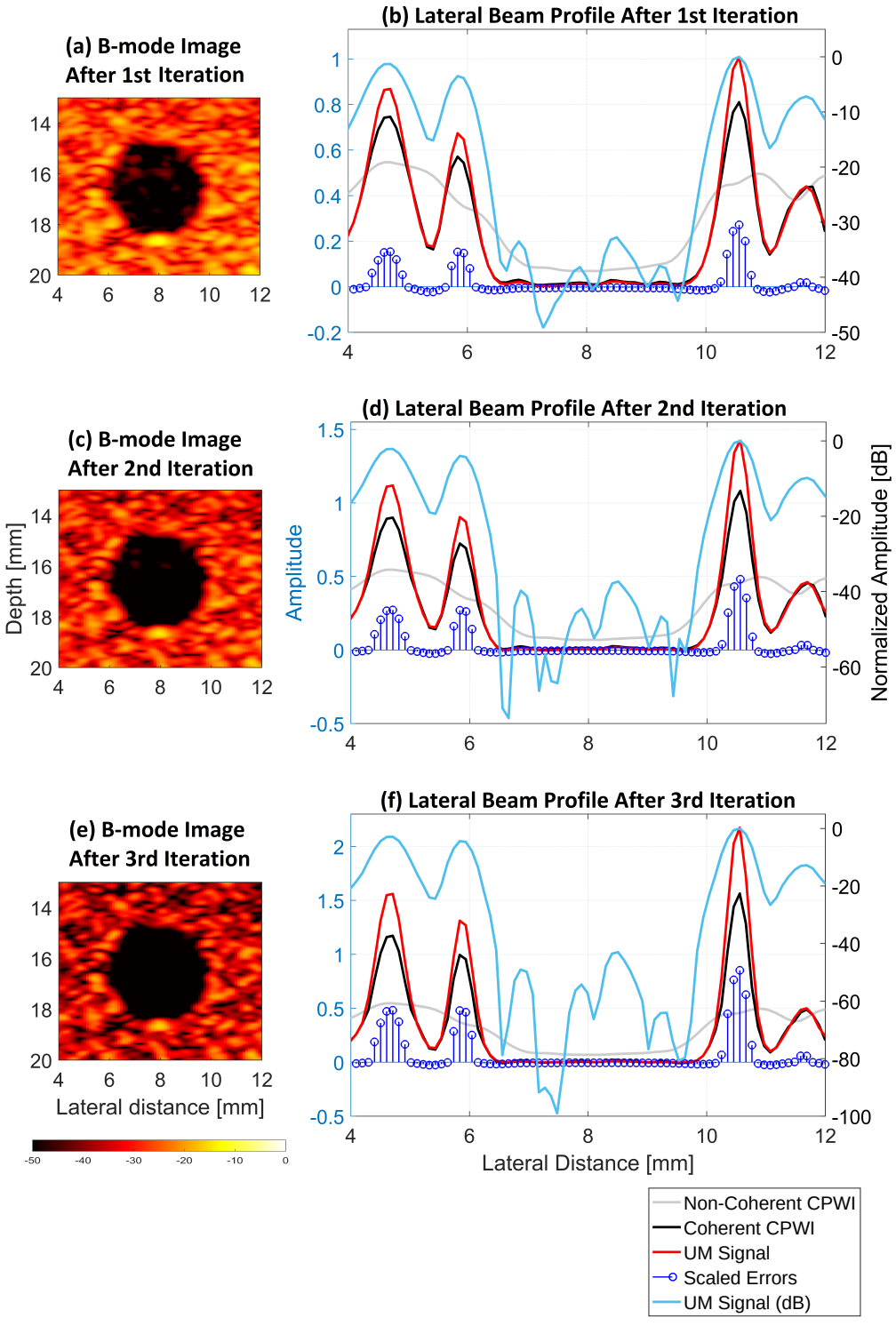

Figure 6.7: The UM technique implemented on CPWI ($N = 9$). The beam profiles for the 1st (a and b), 2nd (c and d) and 3rd (e and f) iteration are shown.

on the same point target. The CRs and CNRs were measured on the 3.0 mm diameter cyst located at the 15 mm depth. The formula for both CR and CNR are given in Section 4.1.2.

6.6 Result and Discussion

The performance of UM on the point target is presented in Fig. 6.8. The UM denoising method is able to reduce the side lobes levels when used with DAS and FDMAS. The corresponding lateral and axial beam profiles at $z = 40$ mm and along $x = 0$ mm are shown in Fig. 6.9. The reduction of lateral side lobes is observed for DAS and FDMAS. However, there is no significant change on the main lobes in the axial direction. This is somehow expected since the UM process takes place along the lateral direction.

The B-mode images for the wire phantom from $N = 1$ until $N = 25$ using DAS, UM-DAS, FDMAS and UM-FMAS are presented in Fig. 6.10. The corresponding axial and lateral beam profiles for the wire phantom are given in Fig. 6.11 and Fig. 6.12, respectively.

Axial resolution (AR) results at the −6 dB and −20 dB level using DAS, UM-DAS, FDMAS and UM-FDMAS are shown in Fig. 6.13(a) and (b). The variations on the AR between all techniques are less than 0.1 mm. There is no significant changes occurring on the axial main lobes at the −6 dB level.

The PSLs in the axial direction with different numbers of compounding angles are shown in Fig. 6.13(c). The patterns for the PSLs do not exhibit any significant change when UM takes place on both beamforming techniques with the same setup of steering angles. From $N = 3$ to $N = 25$, there is PSL reduction for DAS and FDMAS. At $N = 3$, the PSLs for DAS and UM-DAS are −23.5 dB and −23.4 dB. As the number of compounding angles increases to $N = 25$, the PSLs are reduced to −26.2 dB for both DAS and UM-DAS. As for FDMAS and UM-FDMAS, at $N = 3$, the PSLs are −9.8 dB and −9.6 dB. For $N = 25$, the PSLs are reduced to −29.5 dB for both FDMAS and UM-FDMAS.

The LR results at −6 dB using DAS, UM-DAS, FDMAS and UM-FDMAS are shown in Fig. 6.14(a). UM is able to enchance the LR resolution for DAS and FDMAS. The best LRs using DAS and UM-DAS are 0.47 mm and 0.39 mm with $N = 3$, and 17% of improvement is achieved with UM. While for FDMAS and UM-FDMAS, they are

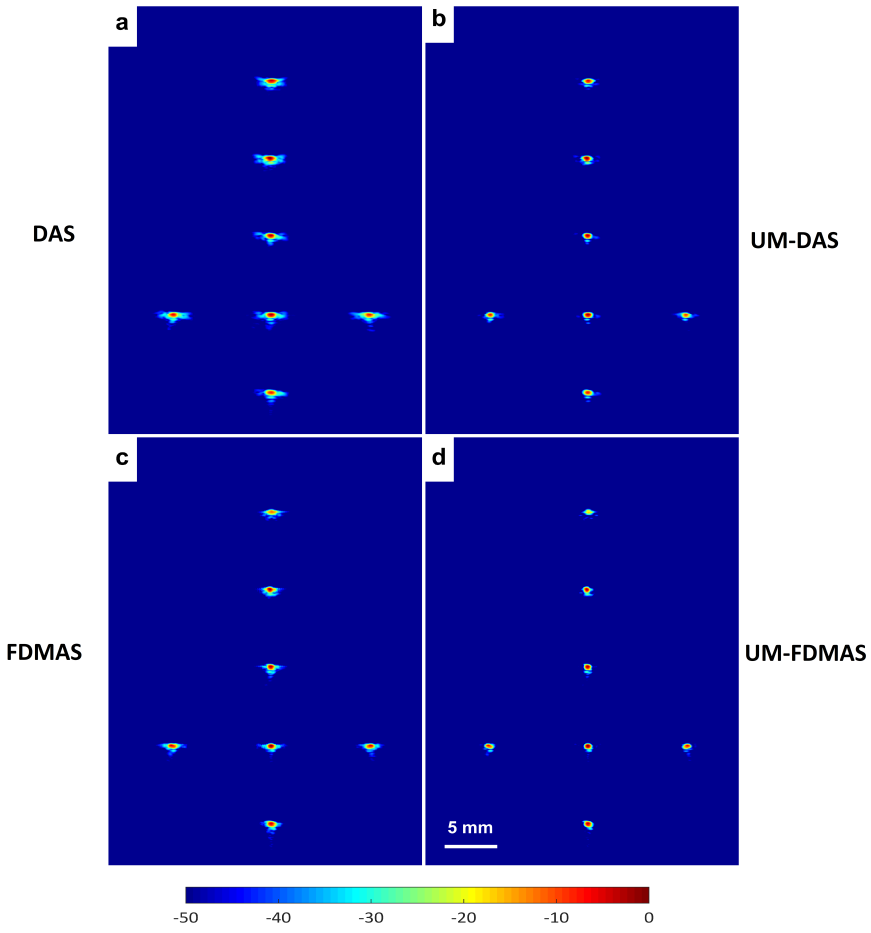

Figure 6.8: B-mode images of wire targets beamformed with a) DAS, b) UM-DAS, c) FDMAS and d) UM-FDMAS with $N = 13$.

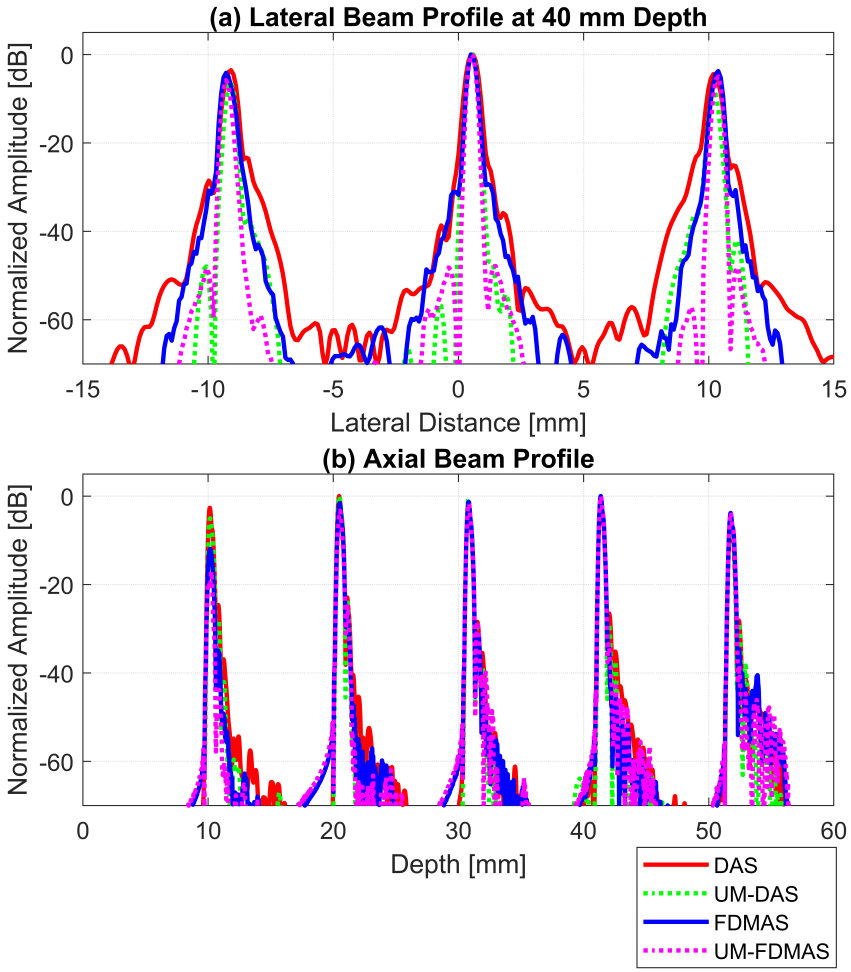

Figure 6.9: a) Lateral beam profiles for wire targets and b) axial beam profiles for wire targets along $x = 0$ mm for B-mode images shown in Fig. 6.8.

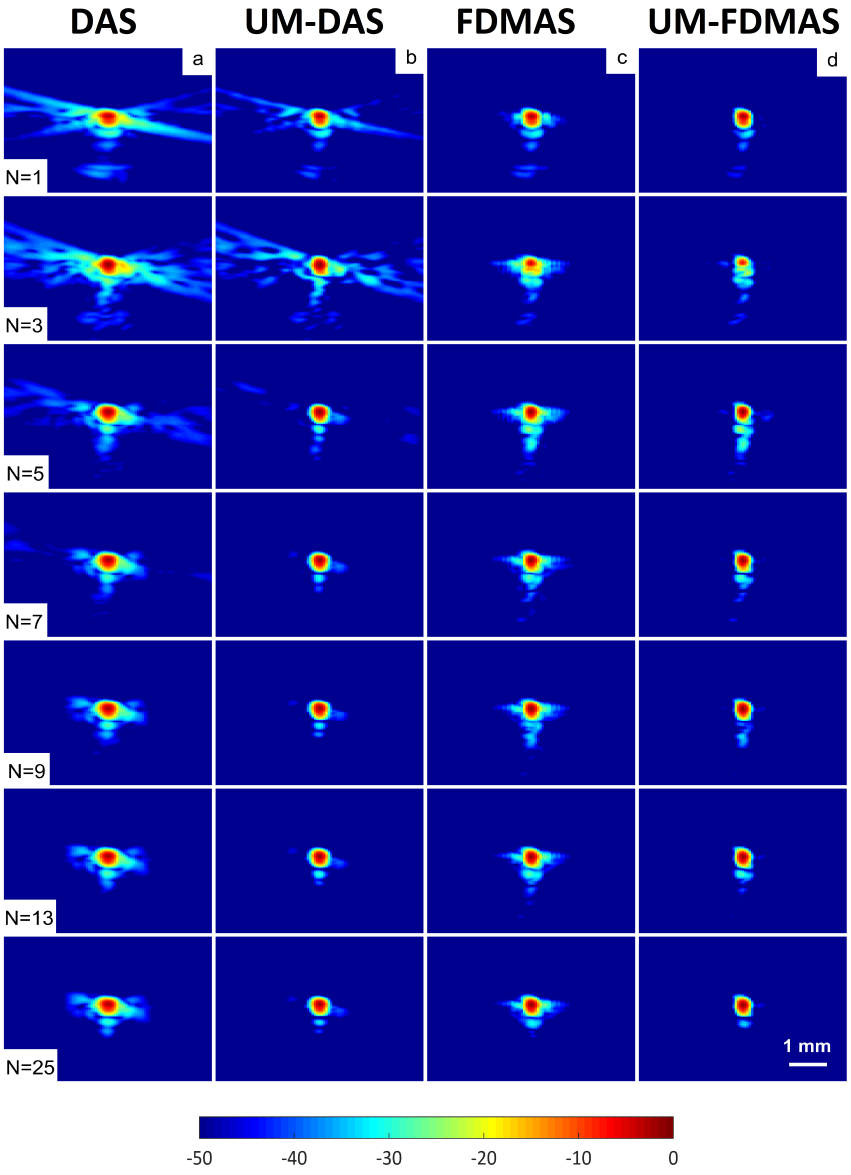

Figure 6.10: The PSFs (30 mm deep) from $N = 1$ to $N = 25$ using a) DAS, b) UM-DAS, c) FDMAS and d) UM-FDMAS.

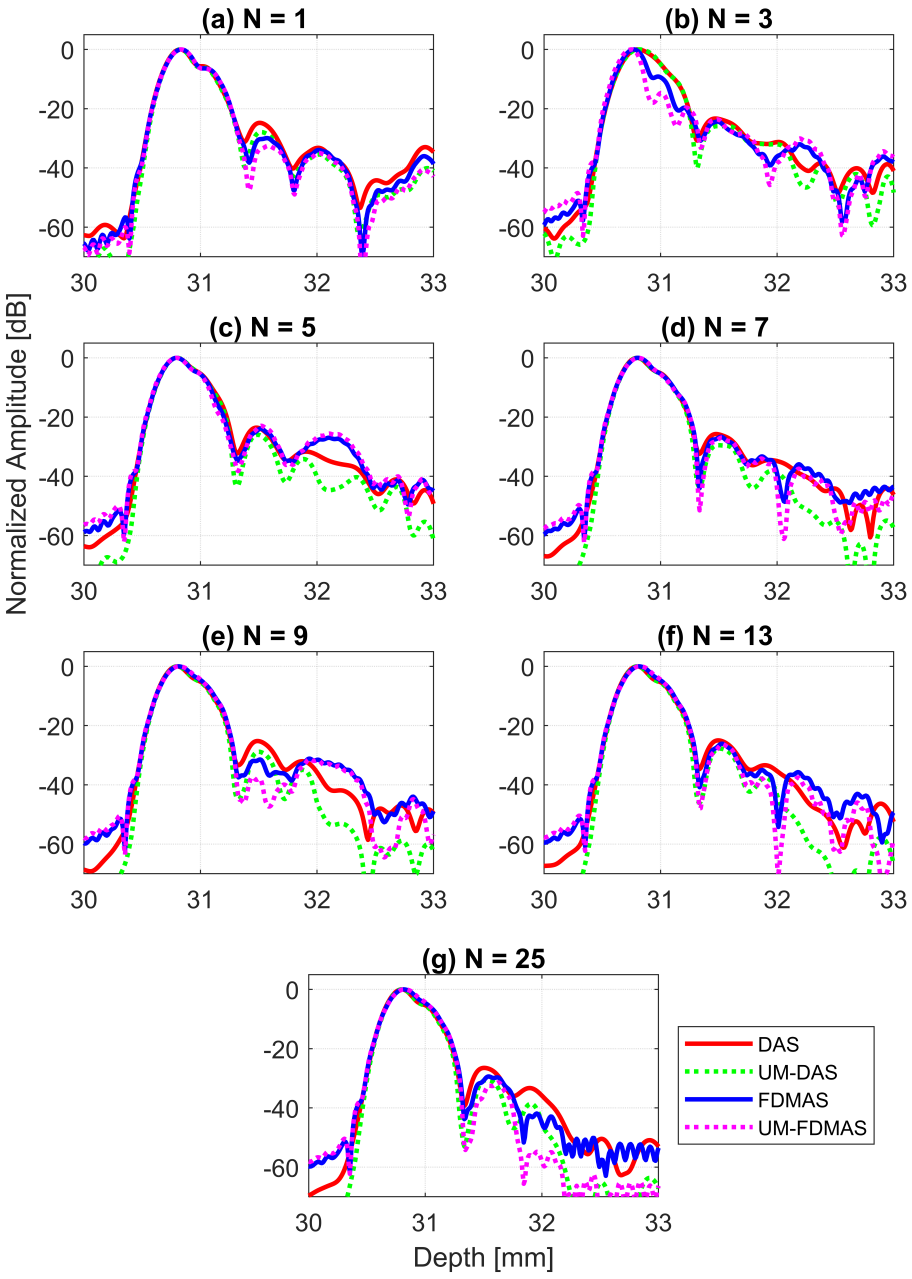

Figure 6.11: The axial beam profiles for the point target located at the 40 mm depth with a) $N = 1$, b) $N = 3$, c) $N = 5$, d) $N = 7$, e) $N = 9$, f) $N = 13$ and g) $N = 25$ using DAS, UM-DAS, FDMAS and UM-FDMAS.

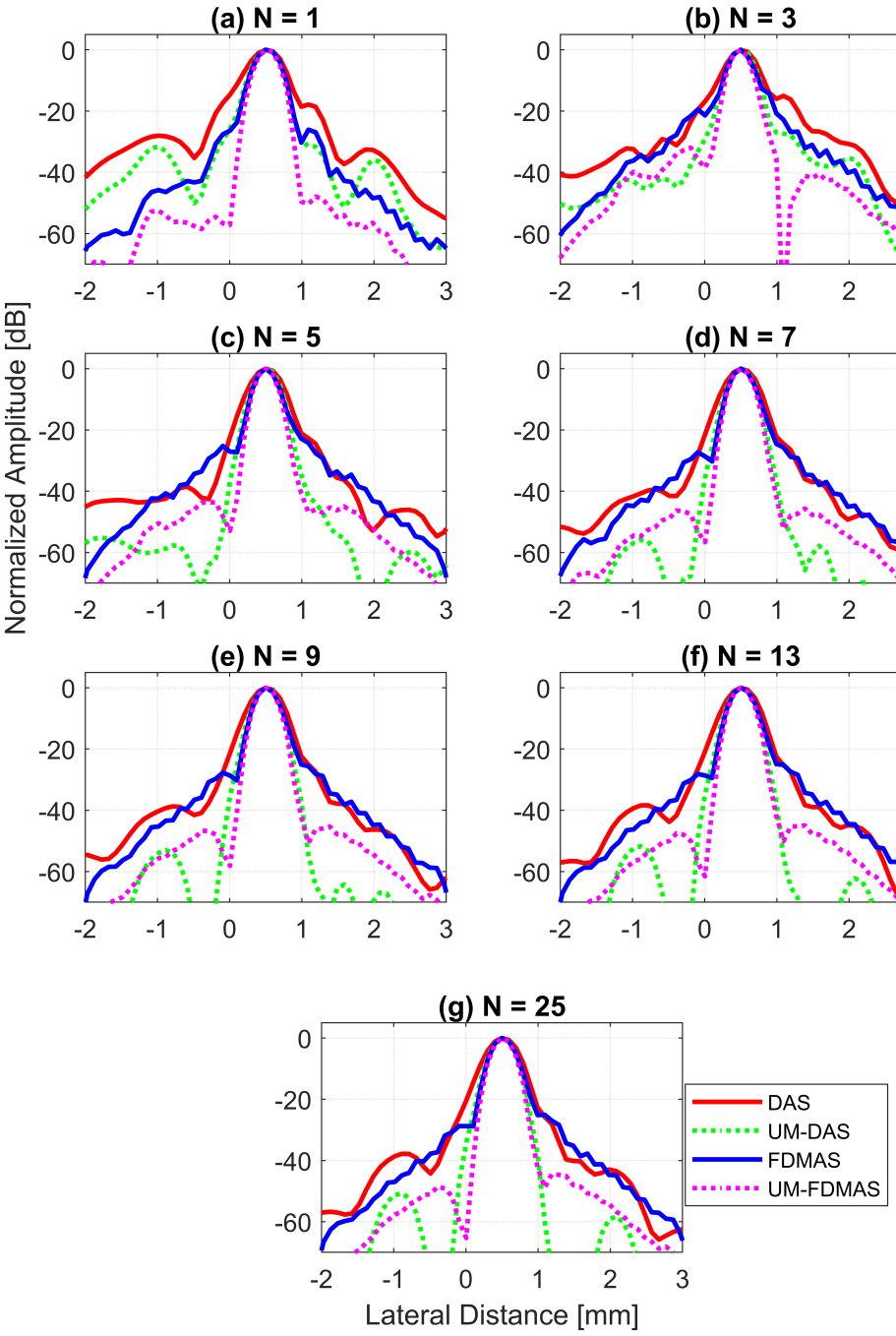

Figure 6.12: The lateral beam profiles for the point target located at the 40 mm depth with a) $N = 1$, b) $N = 3$, c) $N = 5$, d) $N = 7$, e) $N = 9$, f) $N = 13$ and g) $N = 25$ using DAS, UM-DAS, FDMAS and UM-FDMAS.

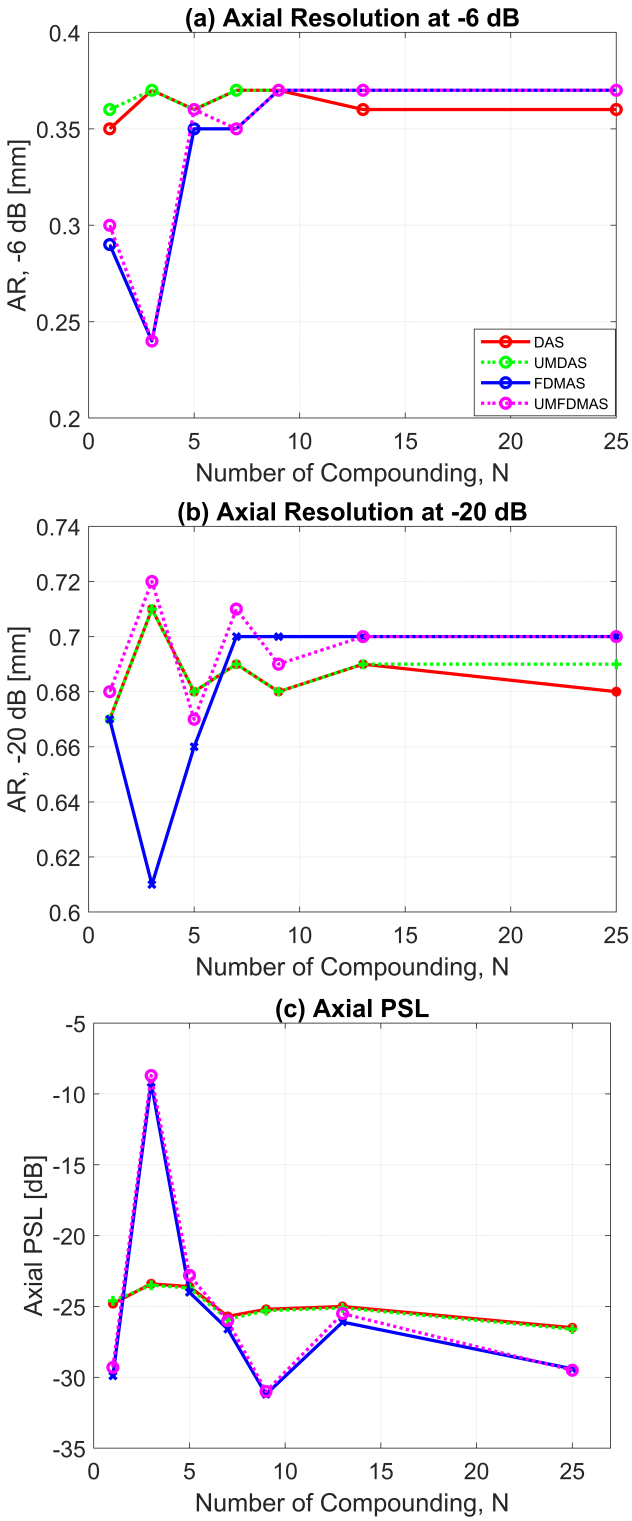

Figure 6.13: Results for a) AR at −6 dB, b) AR at −20 dB and b) PSL using DAS, UM-DAS, FDMAS and UM-FDMAS.

0.35 mm and 0.32 mm with $N = 5$, and the improvement of 8.6% is achieved with UM. As the number of compounding angles increases to $N = 25$, the LRs at -6 dB using all beamforming techniques are deteriorated. This is because the region of the intersection of main lobes in the lateral direction keeps increasing as the number of compounding angles increases, broadening the lateral main lobes. Whereas with a small number of compounding angles and a larger angle sector, the interaction between those main lobes in each steering angles is small, producing narrower lateral main lobes.

LR results at -20 dB for DAS, UM-DAS, FDMAS and UM-FDMAS are shown in Fig. 6.14(b). UM is able to improve the LR at the -20 dB level for DAS and FDMAS. At $N = 5$ the LR at -20 dB for DAS and UM-DAS are 0.94 mm and 0.70 mm, while for FDMAS and UM-FDMAS they are 0.74 mm and 0.57 mm. The improvement with the proposed UM denoising method on the LR at -20 dB for DAS is 21.3% and for FDMAS it is 23%. As the number of compounding angles increases from $N = 5$ to $N = 25$, the LR at -20 dB for all investigated techniques does not show any significant change.

The PSLs in the lateral direction using DAS, UM-DAS, FDMAS and UM-FDMAS are shown in Fig. 6.14(c). The PSL is attenuated more when UM implemented with DAS and FDMAS. The PSL using UM combined with DAS and FDMAS are 19.2 dB and 19.3 dB with $N = 9$. As the number of compounding angles increases from $N = 9$ to $N = 25$, the PSLs for all beamfoming techniques don't show any significant change except for FDMAS. The beam profiles along the lateral direction at the 30 mm depth for all investigated techniques are shown in Fig. 6.12.

The experimental results for the anechoic cysts located at the depths of 15 mm and 45 mm with DAS and FDMAS ($N = 13$) and their UM counterparts are shown in Fig. 6.15. The ROI including all four cysts are highlighted with white dashed circles that are numbered from i to iv. Clutter noise is attenuated inside anechoic region ii when UM is combined with DAS and FDMAS as shown in Fig. 6.15(b) and (d). The lateral beam profiles at the depths of 15 mm and 45 mm for all investigated techniques are shown in Fig. 6.16.

A cyst with a 3.0 diameter at the 15 mm depth as marked by circle ii in Fig. 6.15(a) was chosen to measure the image CR and CNR. The B-mode images for the cyst formed using DAS, UM-DAS, FDMAS and UM-FDMAS are shown in Fig. 6.17. Clutter noise that is in the anechoic regions is attenuated more using UM-DAS and

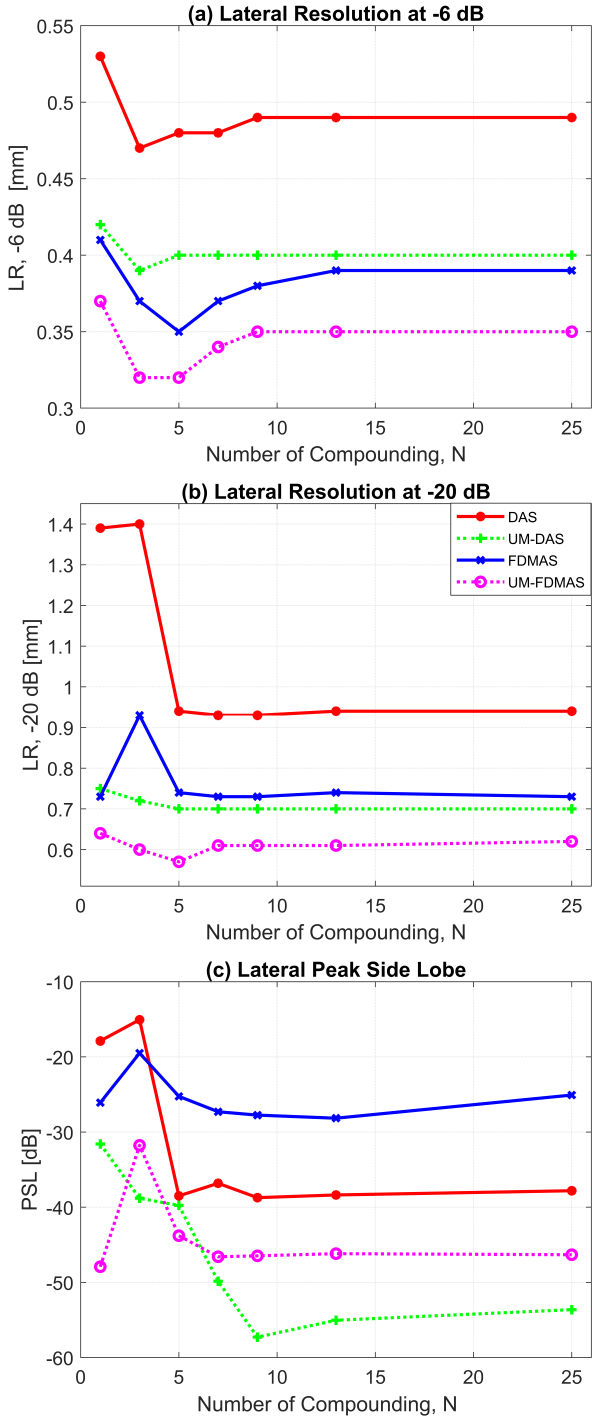

Figure 6.14: Results for LRs at a) −6 dB b) −20 dB and c) PSLs using DAS, UM-DAS, FDMAS and UM-FDMAS at the 30 mm depth.

UM-FDMAS, and this attenuation is more pronounced with the increasing number of steering angles. The reduction of clutter noise also improves the cyst edge. UM not only attenuates clutter noise that is inside the cyst, but also clutter noise outside of the cyst region. Since FDMAS already reduces clutter noise, black box regions (BBRs) are present when using UM-FDMAS. BBRs can be misclassified as small cysts. This will also reduce the image CNR due to the high fluctuation of the signals outside of the cyst.

The CRs for the 3.0 mm diameter cyst at the depth of 15 mm are given in Fig. 6.20(a). The CRs for all investigated techniques keep improving as the number of compounding angles increases. The UM techniques implemented on DAS and FDMAS are able to provide the improved CRs. For $N = 9$, UM is able to improve the CR by 7.94 dB and 6.39 dB when combined with DAS and FDMAS. At $N = 25$, the UM-DAS performed better than UM-FDMAS in improving the image CR.

The CNRs for the 3.0 mm diameter cyst at the 15 mm depth are given in Fig. 6.20(b). As opposed to all other performance indexes, the CNR tends to decrease when the UM is implemented on DAS and FDMAS. For $N = 9$, the reduction caused by UM on DAS and FDMAS are 3.88 dB and 3.67 dB. This reduction is due to the reduction of clutter noise outside of the cyst regions, producing higher signal variations. As a result, this will produce coarse B-mode images which need to be smoothened by despeckeing techniques.

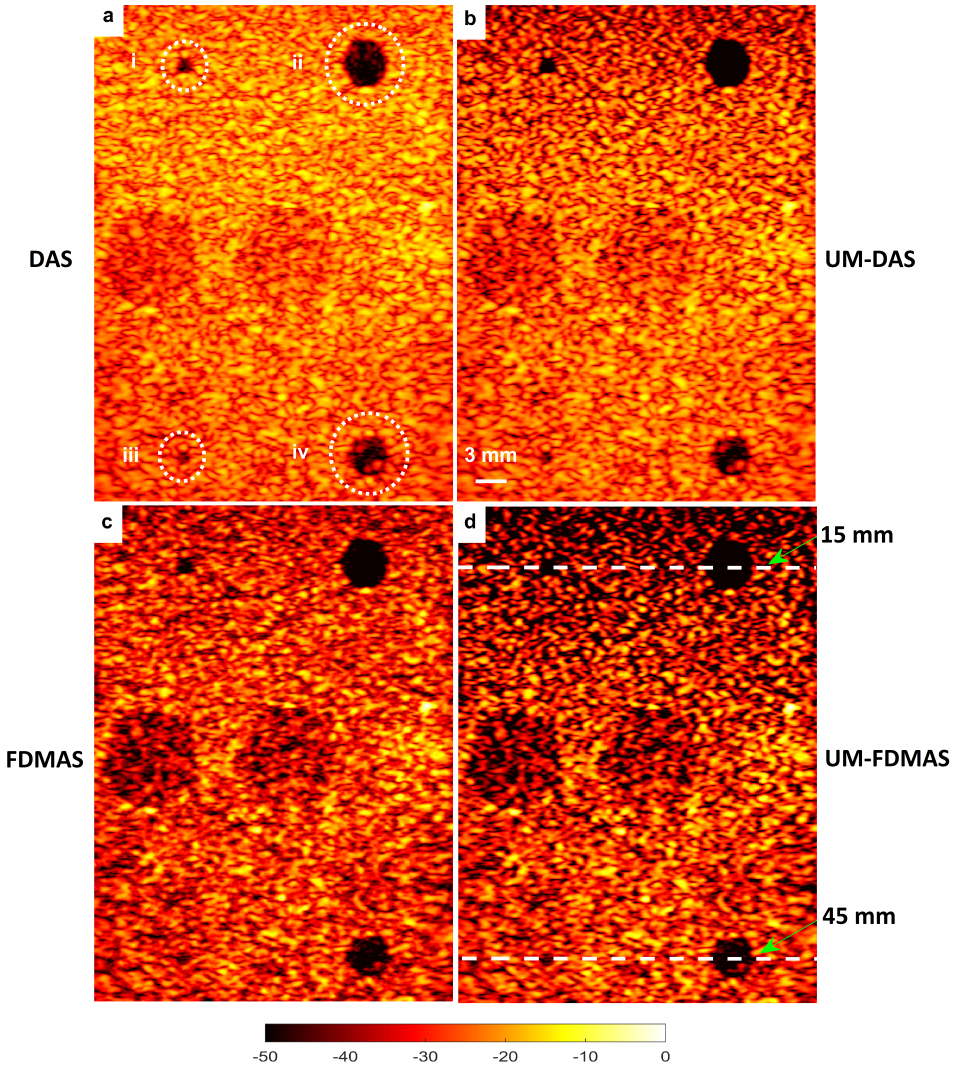

Figure 6.15: The cyst B-mode images beamformed with a) DAS, b) UM-DAS, c) FD-MAS and d) UM-FDMAS with $N = 13$.

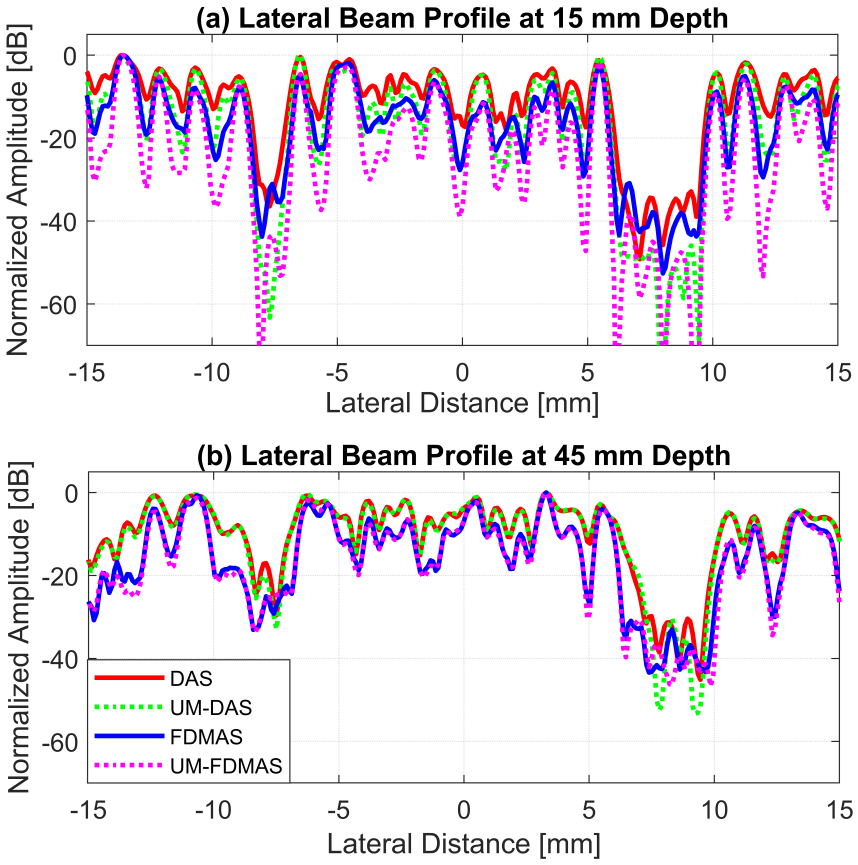

Figure 6.16: The lateral beam profiles for DAS, UM-DAS, FDMAS and UM-FDMAS at the depths of a) 15 mm and b) 45 mm.

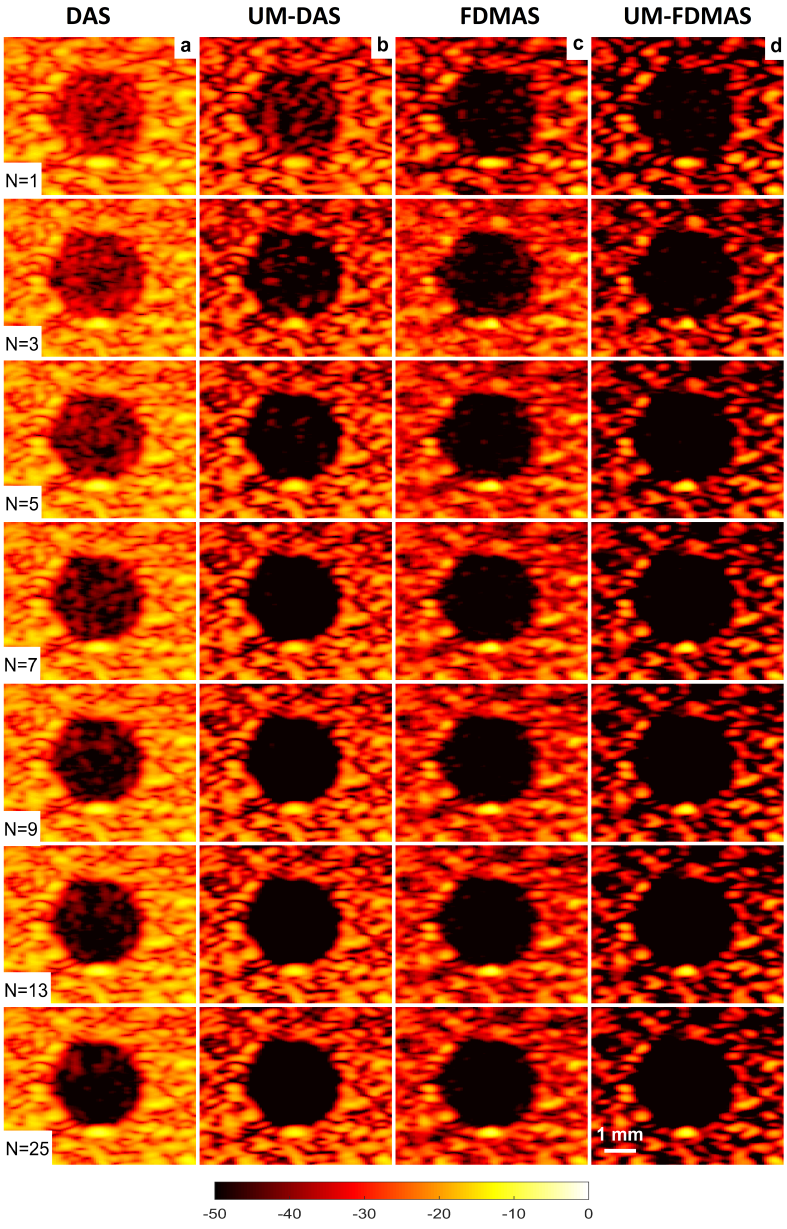

Figure 6.17: The B-mode images ($N = 1$ to $N = 25$) for the 3.0 mm diameter cyst at the 15.0 mm depth. The results are presented using a) DAS, b) UM-DAS, c) FDMAS and d) UM-FDMAS.

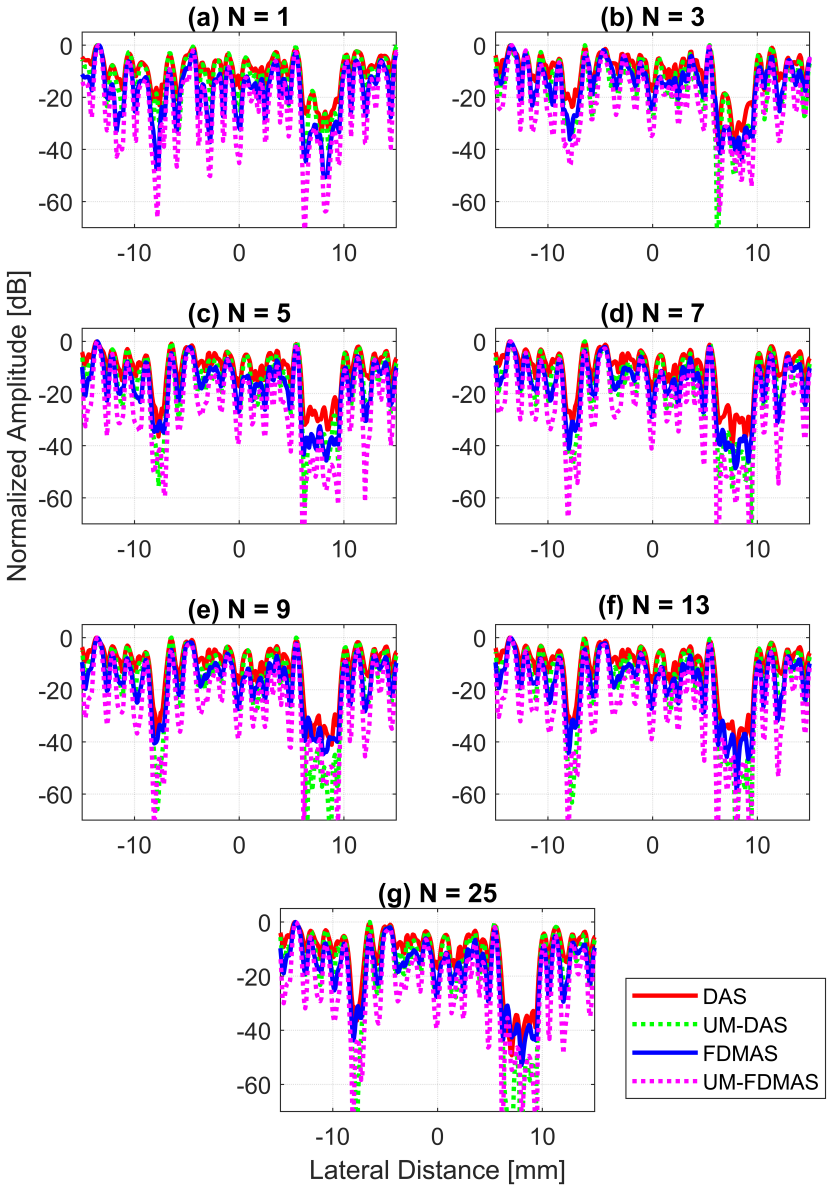

Figure 6.18: The lateral beam profiles for the 1.3 mm and 3.0 mm diameter cysts at the depth of 15 mm with a) $N = 1$, b) $N = 3$, c) $N = 5$, d) $N = 7$, e) $N = 9$, f) $N = 13$ and g) $N = 25$ using DAS, UM-DAS, FDMAS and UM-FDMAS.

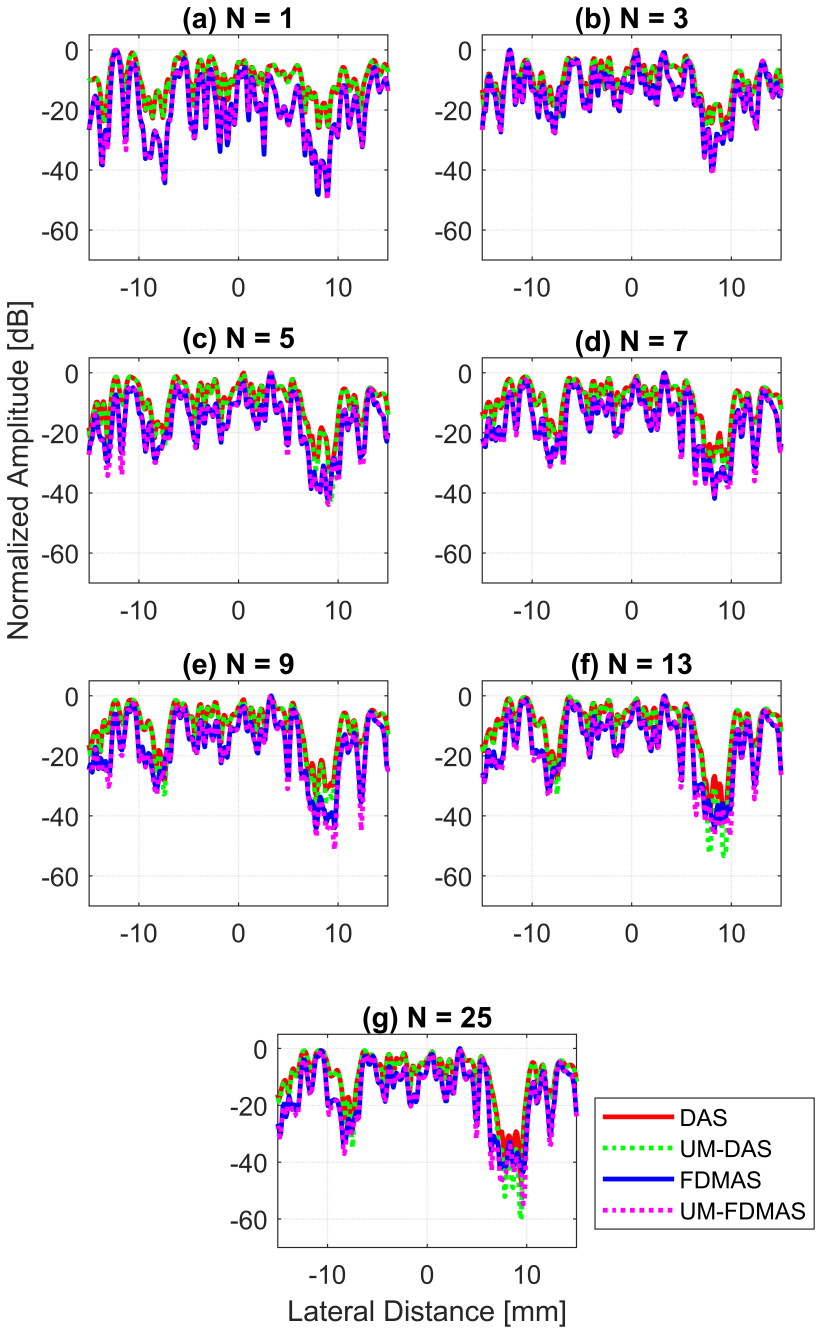

Figure 6.19: The lateral beam profiles for the 1.3 mm and 3.0 mm diameter cysts at the depth of 45 mm with a) $N = 1$, b) $N = 3$, c) $N = 5$, d) $N = 7$, e) $N = 9$, f) $N = 13$ and g) $N = 25$ using DAS, UM-DAS, FDMAS and UM-FDMAS.

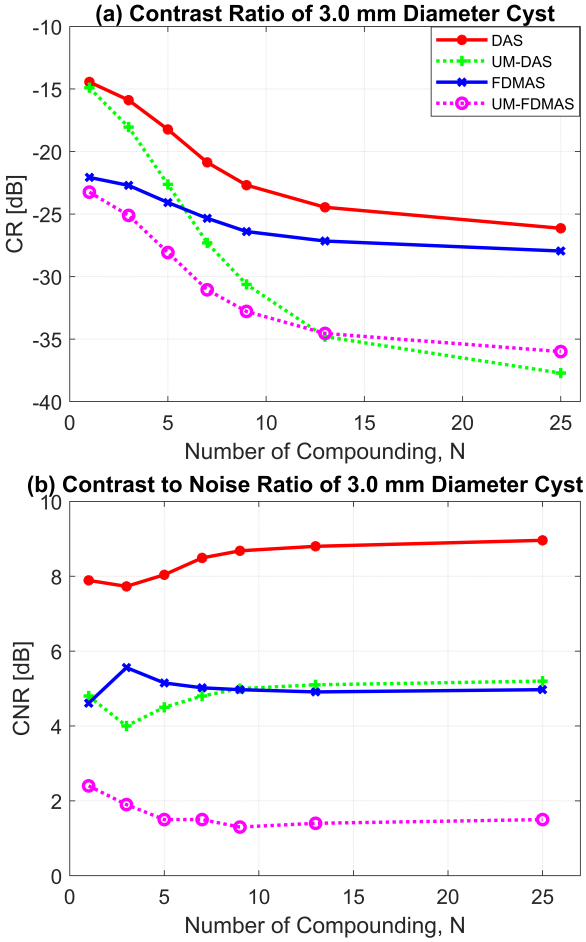

Figure 6.20: a) CRs and b) CNRs for DAS, UM-DAS, FDMAS and UM-FDMAS for the 3.0 mm diameter cyst at the 15 mm depth.

The *in-vivo* B-mode images obtained from DAS, UM-DAS, FDMAS and UM-FDMAS are presented in Fig. 6.21. All the images are shown with a 50 dB dynamic range. Clutter noise reduction can be seen on the B-mode images starting from $N = 3$ when UM applied to DAS and FDMAS. As the number of compounding angles increases to $N = 25$, the common carotid artery and the near field regions are free of clutter noise with UM-FDMAS.

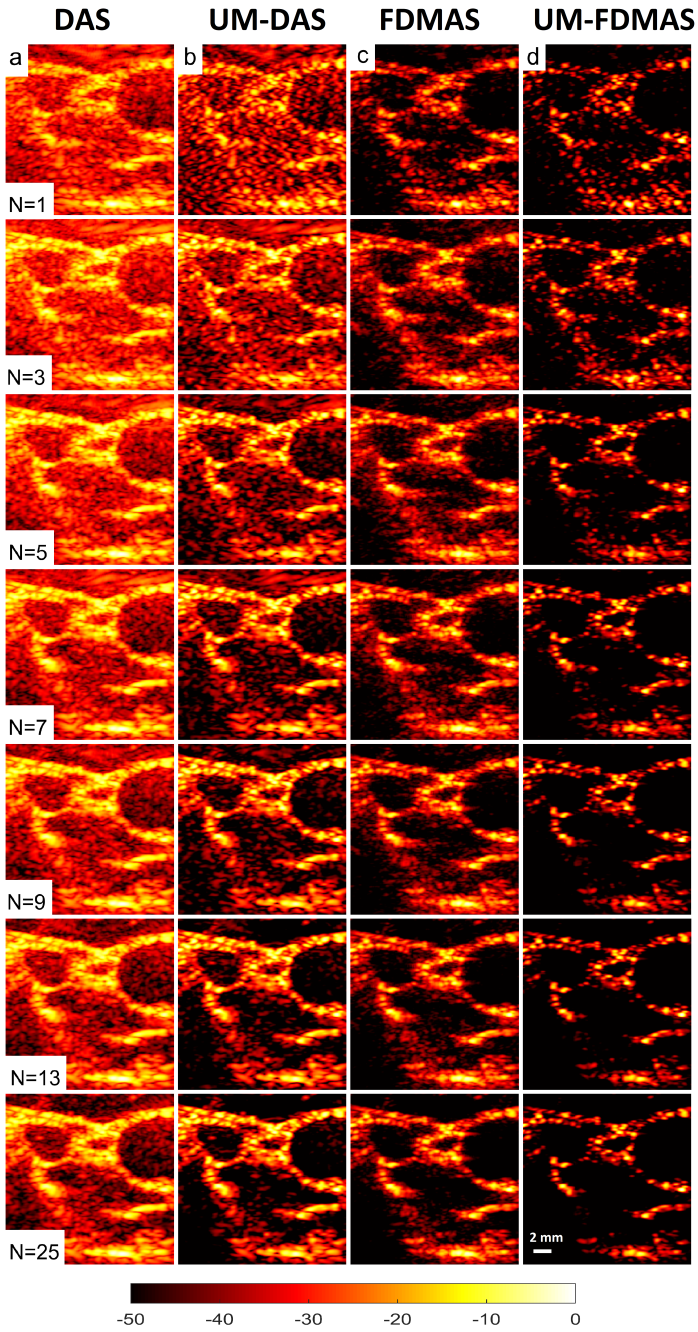

Figure 6.21: The B-mode images ($N = 1$ to $N = 25$) for the carotid artery. The results are obtained using a) DAS, b) UM-DAS, c) FDMAS and d) UM-FDMAS displayed within 50 dB dynamic range.

6.7 Conclusion

The measured key performance indexes on the B-mode images show that the new UM technique is able to improve the image contrast and spatial resolution. Both beamforming techniques, DAS and FDMAS show improvement in the image contrast and spatial resolution with UM. The ability of the UM technique to reduce clutter noise helps to define the border and visualize the cyst regions. The limitations in image spatial and contrast imposed by the beamforming technique DAS has been compensated by FDMAS. But clutter noise is still present with FDMAS. This shows that each method has a certain number of limitations. Thus, the UM method has been introduced to handle the limitation imposed by FDMAS. UM is able to improve the results with both DAS and FDMAS. While UM also has its own limitation on lowering the B-mode image CNR. For compensating the UM limitations, despeckeling techniques could be used to improve the image CNR. By manipulating the two weightage scales, the end users have the flexibilities to reduce clutter noise and improve the image resolution. UM is not suitable to be implemented on FDMAS. This is because the FDMAS itself has efficiently reduced clutter noise that is present inside the B-mode image. Further application of UM to FMDAS will reduced speckle noise outside the cyst region. This will lower the CNR value thus introduce the BBR.

Chapter 7

Despeckling and Segmentation of CPWI B-mode images

In this chapter, various despeckling and segmentation techniques were implemented on the compound plane wave imaging (CPWI) B-mode images. This was to evaluate the effect of despeckling and segmentation after denoising with the proposed UM technique. Results were presented for the cyst phantom and *in-vivo* carotid artery. Finally, based on the qualitative and quantitative analysis, the best despeckling and segmentation techniques were suggested.

7.1 Introduction

Ultrasound B-mode images are vulnerable to speckle and clutter noise. Despeckling is one of the easiest methods used to tackle the speckle problem in ultrasound imaging. The main function of despeckling techniques is to reduce the variation among constructive and destructive regions Loizou *et al.* (2005). In medical imaging, the selection of the right despeckling technique is important so that the diagnosis process can be carried out accurately. Choosing the unsuitable despeckling techniques can cause the edges and lines on the image over smoothened which will negatively affect the available anatomical information Jabarulla & Lee (2018). In more severe cases, the important features can be faded or lost during despeckling Baselice (2017); Roy *et al.* (2017). This can reduce the diagnostic value of imaging and lead to the wrong treatment. The size of the kernel or the window used for the despeckling process can affect the final results. If a large

window size is used for despeckling, it will over smoothen speckle together with other regions containing important features. The important property of the despeckling filter is that it should reduce speckle noise while preserve edges in order to pave the path for better segmentation.

7.1.1 Speckle Noise

Speckle noise is a granular pattern in ultrasonic images that reduces the detectability of a small anechoic structure, degrades the image contrast and its resolution Michailovich & Tannenbaum (2006); Tay *et al.* (2010). Speckle is formed by sub-resolution scatters located close enough to interact with each other. This interaction produces constructive or destructive interference which is represent in the B-mode image as dark (destructive) or bright (constructive) regions Wagner *et al.* (1983). The detectability of lesions in ultrasound imaging is significantly lower when compared to MRI and X-Ray due to the presence of speckle Bamber & Daft (1986). A high speckle noise level leads to misdiagnosis Tay *et al.* (2010). Not like white Gaussian noise, averaging the speckle pattern obtained with the same condition will not reduce it Michailovich & Tannenbaum (2006). The formation of speckle is independent of imaging techniques Jespersen *et al.* (1998); Montaldo *et al.* (2009). In ultrafast imaging, non-coherent CPWI and frequency compounding techniques have been used to reduce speckle noise but with loss in spatial resolution Michailovich & Tannenbaum (2006); Toulemonde *et al.* (2015). To retain the spatial resolution especially in the lateral direction and reduce speckle noise at the same time, coherent CPWI has been used widely in ultrasound imaging Alomari *et al.* (2014); Jespersen *et al.* (1998); Montaldo *et al.* (2009). More detailed descriptions of the statistics of ultrasound speckle can be found in Wagner *et al.* (1988).

To illustrate the formation of speckle, a Field II simulation was performed with four scattering points. The simulation setup is given in Table 2.2. The axial FWHM was 0.35 mm which was almost the same as the half (0.3 mm) length of the excitation signal ($2 \times \lambda = 0.6$ mm). The lateral FWHM was 0.4 mm. Fig. 7.1 shows the arrangement of the four points where (a) axial separation, $\Delta x = 12 \times$ FWHM, lateral separation, $\Delta z = 10 \times$ FWHM, (d) axial separation, $\Delta x = 4 \times$ FWHM, lateral separation, $\Delta z = 5 \times$ FWHM, (g) axial separation, $\Delta x = 2 \times$ FWHM, lateral separation, $\Delta z = 2.5 \times$ FWHM. In the last two images (d) and (g), the complex interference between all the four points becomes more visible where the constructive and destructive

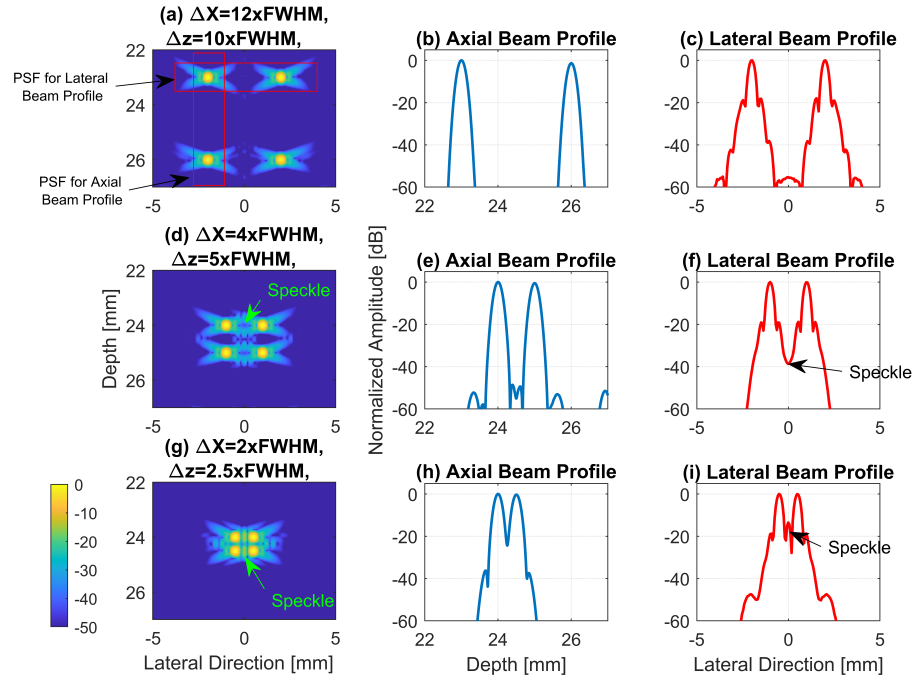

Figure 7.1: Speckle noise occurs when the scattering points are located close to each other in both the axial and lateral directions. (a) Axial separation, $\Delta x = 12 \times$ FWHM; lateral separation, $\Delta z = 10 \times$ FWHM, (d) Axial separation, $\Delta x = 4 \times$ FWHM, lateral separation, $\Delta z = 5 \times$ FWHM, (g) Axial separation, $\Delta x = 2 \times$ FWHM, lateral separation, $\Delta z = 2.5 \times$ FWHM. The blue and red lines are the beam profiles for the first two points in the axial and lateral directions, respectively.

regions start to emerge. Whereas the other two images on the side of the B-mode images in Fig. 7.1 are representing the axial and lateral beam profiles for the first two points in axial and lateral directions. For CPWI, the most common solution to reduce speckle noise is by applying the compounding techniques Jespersen *et al.* (1998); Montaldo *et al.* (2009). Less variation of the speckle pattern gives uniform and smooth B-mode images where the image contrast ratio can be increased.

7.1.2 Despeckling with 2-D Gaussian Filter

The Gaussian filter is the most basic despeckling filter applied to the ultrasound B-mode images to reduce speckle noise Cao *et al.* (2011). The selection of the 2-D window size and the Gaussian filter standard deviation σ will influence the despeckling outcome.

More details regarding the 2-D Gaussian filter equation and the window size selection is given in Ueng *et al.* (2014). The final image produced with the 2-D Gaussian despeckling is given by:

$$u_{\mathrm{g}}[a,b] = G[a,b] * h[a,b] \tag{7.1}$$

where a is the distance from the origin in the horizontal axis (columns), and b is the distance from the origin in the vertical direction (rows). $h[a,b]$ is the original digital B-mode image before despeckling, and $G[a,b]$ is the 2-D Gaussian filter as given by Cao *et al.* (2011); Ueng *et al.* (2014):

$$G[a,b] = \frac{1}{2\pi\sigma^2} e^{-\frac{a^2+b^2}{2\sigma^2}} \tag{7.2}$$

where σ is the standard deviation of the Gaussian pixel intensity distribution. The Gaussian filter is not the best option for despeckling as it does not take boundaries into consideration Izquierdo & Ghanbari (1999).

7.1.3 Despekling with 2-D Adaptive Weiner Filter

The adaptive filter has been used as an alternative to Gaussian despeckling in ultrasound imaging since its capabilities to update filter coefficients according to the noise level in particular regions. The conventional Weiner filter with the low pass characteristic is known to blur the image lines and edges Westin *et al.* (2000). This is because a fixed standard deviation has been used throughout the entire image Jin *et al.* (2003). Thus, Lee (1980) has derived a new noise-adaptive Weiner filter and the estimated output image is given by:

$$u_{\mathrm{w}}[a,b] = \mu + \frac{\sigma^2}{\sigma^2 + v^2}(h[a,b] - \mu) \tag{7.3}$$

$$\mu = \frac{1}{K_{\mathrm{e}}} \sum_{a,b \in K_{\mathrm{e}}} h[a,b] \tag{7.4}$$

$$\sigma^2 = \frac{1}{K_{\mathrm{e}}} \sum_{a,b \in K_{\mathrm{e}}} h^2[a,b] - \mu^2 \tag{7.5}$$

where μ and σ^2 are the local mean and variance within the kernel, K_{e} and v^2 are the average values of all the local estimated variances. The smoothing of the adaptive

Weiner filter is performed only in the area having low intensity variances but not in the area with high variances (edges). This is to retain the image information as much as possible. The filter works well when noise is white additive noise, such as the Gaussian noise Michailovich & Tannenbaum (2006); Westin *et al.* (2000). However, in ultrasound B-mode imaging, speckle is multiplicative noise Tay *et al.* (2010). Unlike the Gaussian noise which appears randomly in the image, speckle noise is predictable and will keep appearing in the same spatial domains. Thus, this filter does not suite well ultrasound B-mode imaging. One of the solutions provided by Jain (1989) is to convert the speckle multiplicative noise into additive zero mean Gaussian noise by applying logarithmic transformation before applying the Weiner filter. This however is an oversimplified approximation and Michailovich & Tannenbaum (2006) proved that considering the log transformed noise in the B-mode image as additive white Gaussian is wrong.

7.1.4 Despeckling with 2-D Median Filter

The median filter output depends on the ordering of the input values for the kernel. The median filter is known to effectively smoothen speckle and preserve the edges Huang *et al.* (1979); Kushwaha & Singh (2017). Not like the moving average filter which will average the values within the kernel, the median filter will replace the center of the pixel value with the median pixel value within the kernel (sliding window) Huang *et al.* (1979).

7.2 Segmentation of CPWI B-mode images

Manual image segmentation is subject to operator experience. The need of the high reproducibility motivates the development of computer-assisted semi-automated and automated segmentation techniques Bhushan (2009); Noble & Boukerroui (2006b). Segmenting ultrasound B-mode images brings new challenges due to the presence of speckle and clutter noise. In this work, the effect of denoising the CPWI B-mode images with the improved UM before despeckling and segmentation was investigated. Two different types of image segmentation methods were applied on the CPWI B-mode images, the Otsu thresholding and active contour balloon snake methods. Both segmentation techniques were implemented on the cyst phantom and *in-vivo* carotid artery after denoising with the new UM method.

7.2.1 Snake Active Contour

The Snake active contours (SAC) is one of the popular segmentation methods which was introduced by Kass in 1988 Kass *et al.* (1988); Shariat (2009). The SAC segmentation technique starts with the user defined boundary known as the contour around an object. Later the initial contour which is the internal energy of the SAC defined by the end user will evolve towards or away to locate the actual boundary of the object. The objective of the SAC is to minimize the combined energy of internal (shape of the contour) and the external (the image gradient) by continuously moving itself under a certain number of iterations. The overall snake energy is given as follows:

$$E(V(s)) = E_{\text{int}}(V(s)) + E_{\text{ext}}(V(s)) \tag{7.6}$$

where $V(s)$ is snake contour, E_{int} and E_{ext} are the internal and external energy of the snake.

The external energy attracts the snake to the edges and this can be represented by the following equation:

$$E_{\text{ext}}(V(s) = - \|\nabla[G[a,b] * h[a,b]\|^2 \tag{7.7}$$

where $G[a,b]$ is a Gaussian smoothing filter and $h[a,b]$ is the image. Note that the expression has a negative sign associated with it. The reason for this is that the internal energy of the contour needs to coincide with the external energy represented by the gradient. During each of the iterations, the overall SAC energy is computed so that it is always the minimum.

In the original SAC segmentation method proposed by Kass *et al.* (1988), the initial contour defined by users has to be drawn very near to the real or desired final boundary. If it fails to do so, the SAC will not settle at the desired structure boundary. Thus, Cohen (1991); Rebouças Filho *et al.* (2014) has proposed a solution for this problem by introducing a new internal pressure force. This pressure pushes the defined contour toward the edges, making the initialization process of defining the contour much simpler. The proposed method known as balloon snake active contour (BSAC) and can be defined as:

$$E_{\text{ext}}(V(s) = k_1 \boldsymbol{n}(s) - k\frac{\nabla P_s}{\|\nabla P_s\|} \tag{7.8}$$

$$\nabla P_s = \frac{\delta E_{\text{ext}} V(s)}{\delta s} \tag{7.9}$$

where $\boldsymbol{n}(s)$ is the normal vector to the curve at point $V(s)$ and k_1 is the amplitude of that force. The normal vector is always perpendicular to the tangent at the point $V(s)$, which means that the sign of k_1 can be set so that all of the $k_1\boldsymbol{n}(s)$ vectors are pointing outwards or inwards. This will make the internal curve expand towards the desired boundary from the inside or outside of the object. ∇P_s acts as a very strong stooping point to trap the incoming contour so that it can settle down at the edges.

7.2.2 Otsu's

The Otsu's method gains its popularity due to its simplicity. The Otsu's is an unsupervised automatic global thresholding algorithm Otsu (1979). The algorithm will determine the thresholding value (a gray scale intensity level) through minimizing the inter-class variance, defined as a weighted sum of the variance of two histogram classes. This is done by assuming the image histogram bimodal. The original gray scale image later will be converted into binary scale. If the gray image intensity is larger than the threshold, then it will be set to 1's. Otherwise, it will be set to 0's.

Even though the Otsu's method is able to differentiate the object from the background, the constructive speckle regions outside of the cyst still resemble the same intensity as that inside the cyst regions. Thus, with the Otsu's method, it will still classify the speckle destructive region as the background (0's). When segmentation is applied to the ROI, only the cyst region will be marked or delineated. In this thesis, few post-processing has been carried out on the conventional Otsu's method where only the largest region will be selected according to the total number of pixels. With this modified version of Otsu's, only the cyst region is marked with 0's and other portions of the ROI will be marks as 1's.

7.3 Experimental Setup

An experiment was carried out to find the influence of the despekling techniques on the CPWI B-mode images. The data from the CIRS phantom was collected with parameters as explained in Section 4.1.1. The received RF signals were beamformed with the DAS technique with $N = 9$. Three different despekling techniques used here

were the 2-D Gaussian, 2-D Adaptive Weiner and 2-D Median filters. For the Gaussian filler, three different standard deviations, $\sigma = 7$, 13 and 19, were chosen. For the Weiner and Median filters, three different windows sizes, K_e of $[7 \times 7]$, $[13 \times 13]$ and $[19 \times 19]$, were chosen. The B-mode images were converted to unsigned integer 8-bits, digital image formats before all the despekling techniques applied. The digital image terms referring to dB scales file saved as '.png' formats. The results were compared to the original B-mode image with no despekling. The best among those three despekling techniques were chosen for implementing the segmentation process.

Two different experiments were carried out to find the influence of the despekling techniques on the segmentation process. The experimental setup to collect data for the 3.0 mm cyst and the carotid artery were same to those used in Section 4.1.1. The cyst and carotid artery data were beamformed using DAS, UM-DAS, FDMAS and UM-FDMAS from $N = 1$ to $N = 25$. Later the images were despekled with the 2-D median filter with different kernel sizes, $[7 \times 7]$, $[13 \times 13]$ and $[19 \times 19]$. Both segmentation techniques, Otsu's and BSAC, were implemented on the same cyst and carotid artery B-mode images for comparison.

7.4 Results and Discussion

Several important features, the cyst boundary and point target on the B-mode image are shown in Fig. 7.2. The white and green boxes at the 15 and 45 mm depths were used to highlight the cysts with the diameter of 1.3 and 3.0 mm, respectively. The blue box was used to mark the point target located at approximately the depth of 30 mm. All the results are shown in Fig. 7.2 with the photopic imaging technique. Photopic-mode uses color-coding to gain contrast on the B-mode image without increasing the noise level Lin *et al.* (2003).

The results obtained from the 2-D Gaussian filter are shown in Fig. 7.2, column i. Even though the filter is able to smoothen the speckle regions, it is far from being an optimal despekling technique. The use of Gaussian filtering is to over smoothen the image details. It cannot differentiate any sharp transitions on the image such as the edges. This can cause problems in interpreting the medical images accurately. The small cyst with the 1.3 mm diameter located at the 45 mm depth also starts to disappear as the standard deviation σ increases from 7 to 19. This can be seen in

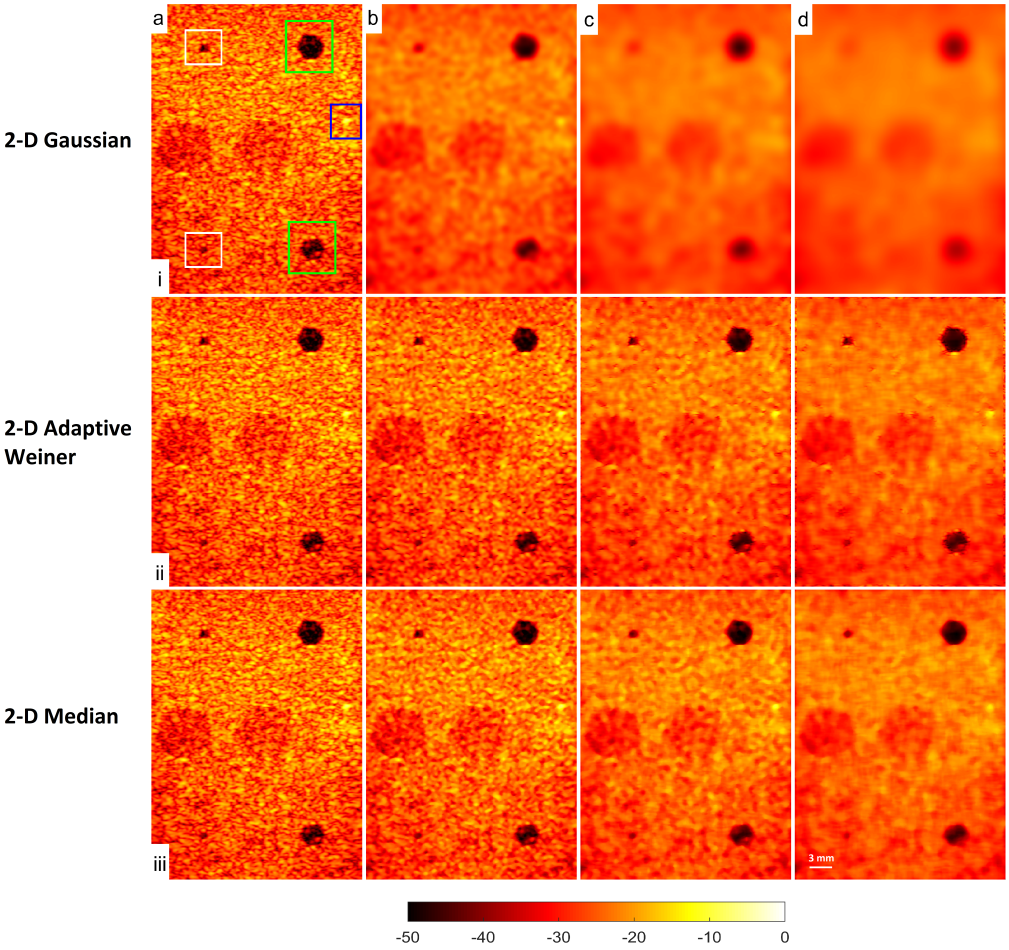

Figure 7.2: Despeckling was performed using DAS with $N = 9$ by the 2-D Gaussian, 2-D Adaptive Weiner and 2-D Median filters as shown in row i, ii and iii. The 2-D Gaussian filter standard deviations are b) 7, c) 13 and d) 19. The kernel sizes for the adaptive Weiner and the median filter were set to b) [7 × 7], c) [13 × 13] and d) [19 × 19]. No despeckling was applied to images in column a.

Fig. 7.2 row i, (b) to (d). The main reason for this is that the same standard deviation has been applied through the entire despeckling process regardless of the noise level on that particular kernel. The lateral beam profile of the wire target after despeckling with the 2-D Gaussian filter is given in Fig. 7.3 row i, (b) to (d). The results show that as the standard deviation in the 2-D Gaussian filter increases from 7 to 19, the wire

target beam profile is over smoothened. This leads to the loss of information about the wire target as shown in Fig. 7.2.

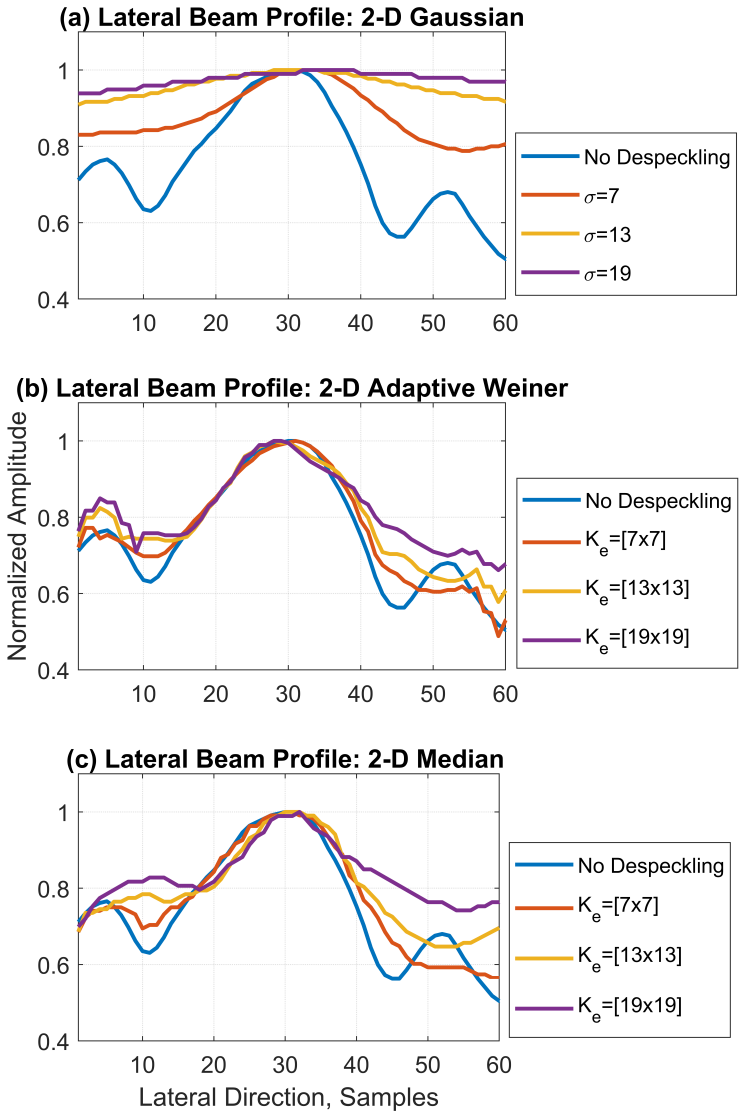

Figure 7.3: The lateral profile of the wire target as shown in Fig. 7.2 after despeckling using a) Gaussian, b) Adaptive-Weiner and c) Median filters.

The results obtained from the 2-D adaptive Weiner filter are shown in Fig. 7.2,

column ii. The filter starts to reduce speckle noise gradually as the size of the kernel increases from [7 × 7] to [19 × 19]. All the important features of the B-mode image have been retained. However, the main disadvantage of the 2-D Adaptive-Weiner filter is that it tends to ignore speckle noise in the areas close to the edges and lines Hiremath *et al.* (2013). This can be seen in Fig. 7.2, column ii, where both the cysts are not smoothened. The lateral beam profile of the wire target after despeckling with the 2-D adaptive Weiner filter is given in Fig. 7.3, row ii. The results show that as the kernel size increases from [7 × 7] to [19 × 19], the point target maintains its beam pattern. Few sharp transitions are noticeable on both the beams with the kernel size of [19×19]. This is the nature of this filter since every kernel does not have the same standard deviation. Thus, it will produce discontinuity whenever there are very different standard deviation values between the kernels.

Finally, the results obtained from the 2-D median filter are shown in Fig. 7.2, column iii. The filter reduces speckle noise as the size of the kernel increases from [7 × 7] to [19 × 19]. As the speckle noise has been reduced, the border or the cyst edges also have been smoothened without losing important features. This is one of the advantages of the median filter.

Based on the results, it was found that despeckling using the 2-D median filter produced better results in smoothing the speckle regions and retaining edges. Thus, the filter has been chosen as the despekling tool for both segmentation methods, Otsu's and BSAC.

The modification on the Otsu's thresholding method was performed in this work in order to segment the ROI. The complete steps involved in modifying the Otsu's are illustrated in Fig. 7.6. First, the B-mode image which has been mapped into the grey scale in the dB scale is converted into unsigned integer formats from 0 to 255 levels by saving it as a '.png' file. This '.png' file format is known as the digital B-mode image. By applying the Otsu's thresholding method, a binary image is created from the unsigned integer image by replacing all values above the threshold into 1's and others into 0's. Later the binary image 1's and 0's are inverted. This is to find and label the pixel group size. The regions are sorted from the smallest to the largest according to the total number of pixels. The biggest region is extracted and the 1's and 0's of the image are inverted back as it was prior to the sorting process. The perimeter or

border of the remaining binary image regions are computed and assigned to the original unsigned integer image as the cyst edge.

In BSAC the three different parameters that can be controlled by the end user are the number of iterations, the initial contour size and placement location. It is expected that within 100 iterations the initial contour will deform to the final settlement on the intended border. However, this is not valid all the time. If the initial contour is drawn smaller in size and placed further from the intended border, more iterations may be needed. The speckle and clutter noise also directly affect the number of iterations in BSAC. If the noise level is high, it can be detected as false edges. Thus, applying despeckeling and denoising on the B-mode image will be beneficial to reduce the number of iterations in BSAC and improve the overall segmentation process by increasing the accuracy on defining the ROI contour. Fig. 7.4 shows the effect of the initial contour size and iteration in BSAC. In column i, a smaller initial contour is placed at the center of the 3.0 mm diameter cyst. While in column ii, a bigger-size contour is placed at the center of the 3.0 mm diameter cyst. The two BSAC segmentation processes are performed in steps with 50, 100 and 200 iterations. With only 50 iterations, the bigger initial contour has been almost settled to the intended cyst border, while for the small initial contour, 200 iterations are needed for the initial contour to settle on the cyst border.

One of the advantage in BSAC segmentation is its ability to expand or compress the initial contour to the intended border Khadidos *et al.* (2014). If the object that is going to be segmented is solid and surrounded by low-level intensities, placing a bigger initial contour outside of the object is desired. While for the object that has lower intensities such as a cyst, placing the initial contour inside the anechoic region and letting it expand to the final contour is desired. Two different scenarios of placing the initial contour inside and outside of the cyst is shown in Fig. 7.5. But by placing the initial contour outside of the cyst, many undesired segmentations are also produced. This is due to the nature of BSAC that can break into many different smaller segmentation regions to minimize the overall energy Jumaat *et al.* (2014). Speckle produces sharp transitions that can be misclassified as edges. Thus, smoothing or despekling can reduce the false segmentation.

In this work BSAC segmentation was implemented within 100 iterations and the initial contour was placed as close as possible to the cyst edge.

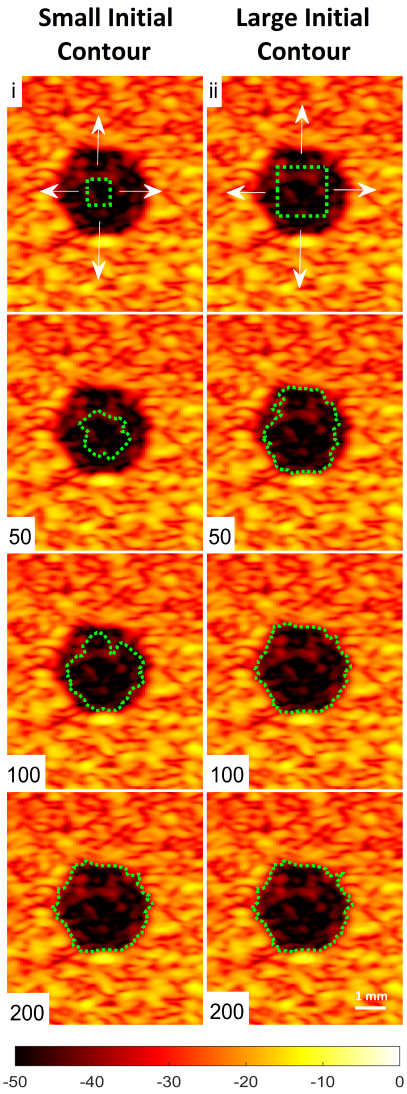

Figure 7.4: Column i and ii show the placement of the initial contour at the centre of the 3.0 mm diameter cyst and its deformation with different numbers of iterations. The arrows in i and ii indicate both initial contours expanding towards the cyst border. The B-mode images are obtained with DAS, $N = 9$ and despeckled with the 2-D median filter with the kernel size of $[7 \times 7]$.

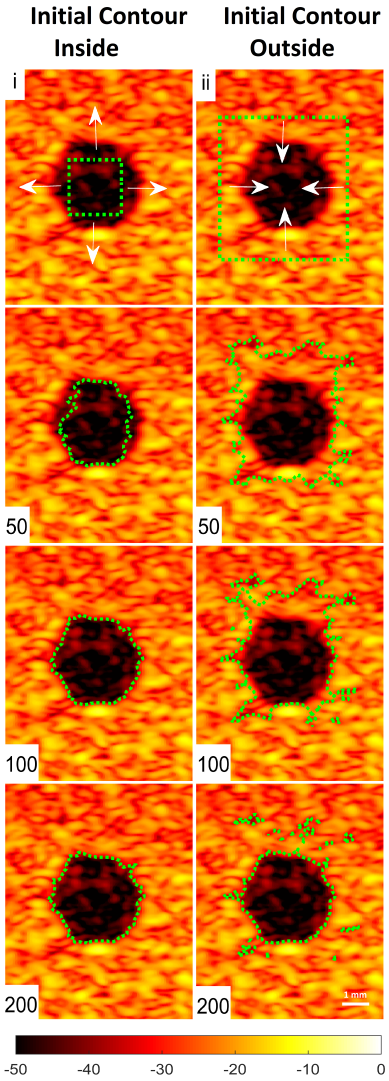

Figure 7.5: Column i and ii shows the placement of initial contour inform of rectangular at the centre of 3.0 mm diameter cyst and its deformation as the number of iterations increased in steps from 50 to 200. The arrows on i and ii indicates both initial contours expanding towards the cyst border. The B-mode obtained with DAS, $N = 9$ and despeckled with 2-D adaptive median with kernel size, K_e of $[7 \times 7]$.

The results obtained for implementing the Otsu's and BSAC on the 3.0 mm diameter cyst with DAS, UM-DAS, FDMAS and UM-FDMAS are presented in Fig. 7.7, 7.8, 7.9 and 7.10. The 2-D adaptive wiener filter with the kernel sizes of [7 × 7], [13 × 13] and [19 × 19] were used. In column (a) for all the B-mode images in Fig. 7.7, 7.8, 7.9 and 7.10, despeckling was not applied. In common, the ability of both Otsu's and BSAC to segment the cyst boundary with DAS, UM-DAS and FDMAS keeps improving as the number of despeckling kernel size increases from [7 × 7] to [19 × 19] and the compounding angles increases from $N = 1$ to $N = 25$. Both despeckling and compounding techniques in common reduce the speckle and clutter noise levels in the B-mode image. Increasing the kernel window size improves the B-mode image CNR. The results for CNR measured on the 3.0 mm diameter cyst at the 15 mm depth for DAS, UM-DAS, FDMAS and UM-FDMAS are given in Fig. 7.11.

The modified Otsu's method is able to segment the cyst boundary better than BSAC with a low number of compounding angles (from $N = 1$ to $N = 5$) with DAS. This is shown in shown in Fig. 7.7. As the number of compounding angles increases from $N = 7$ to $N = 25$ and the kernel size increases from [7 × 7] to [19 × 19], both Otsu's and BSAC produce almost the same contour pattern around the cyst boundary. The advantage of the modified Otsu's method is its reliance on identifying the biggest group. This however is not the case when UM denoising takes place on the B-mode image. The performance of the modified Otsu's method decreases compared to BSAC especially for a lower number of compounding and a smaller kernel size of [7 × 7]. This happened when UM was applied to DAS and FDMAS. The main reason for this is that when clutter noise is reduced on DAS and FDMAS with UM, high speckle variations are created outside of the cyst regions. Applying a larger kernel size of [19 × 19] is able to solve this problem on UM-DAS but not on UM-FDMAS.

The performance of the BSAC and Otsu's methods with the *in-vivo* data was evaluated on the right carotid artery. Both the segmentation processes were implemented on B-mode images beamformed with DAS and FDMAS. Parameters for despeckling and segmentation were identical to those for *in-vitro* measurements. The internal carotid artery (ICA) and the ROI are shown in Fig. 7.12. The performance of segmentation keeps improving as the number of compounding angles increases from $N = 1$ to $N = 25$ and as the 2-D median filter kernel size increases from [7 × 7] to [19 × 19]. With the Otsu's method, the ICA boundary is segmented well with DAS and UM-DAS starting

from $N = 5$ and $K_e = [13 \times 13]$. This is shown in Fig. 7.13 for DAS and in Fig. 7.14 for UM-DAS. While BSAC implemented with DAS has been affected by the presence of clutter noise inside the anechoic ICA region. Clutter noise becomes an obstacle for the initial contour expansion towards the ICA boundary. Reducing clutter noise inside the ICA by applying UM is able to improve the BSAC segmentation by increasing the initial contour expansion towards the ICA boundary.

The Otsu's segmentation method performed poor compare to BSAC implemented with FDMAS and UM-FDMAS. This is shown in Fig. 7.15 for FDMAS and in Fig. 7.16 for UM-FDMAS. The Otsu's failed to recognize the ICA as a single object with FDMAS and UM-FDMAS. Whereas BSAC is able to segment the ICA boundary with FDMAS and UM-FDMAS and the results are better than those with DAS and UM-DAS. This is due to the absence of clutter noise inside the ICA anechoic region makes the initial contour expand from the center of the ICA with less resistance.

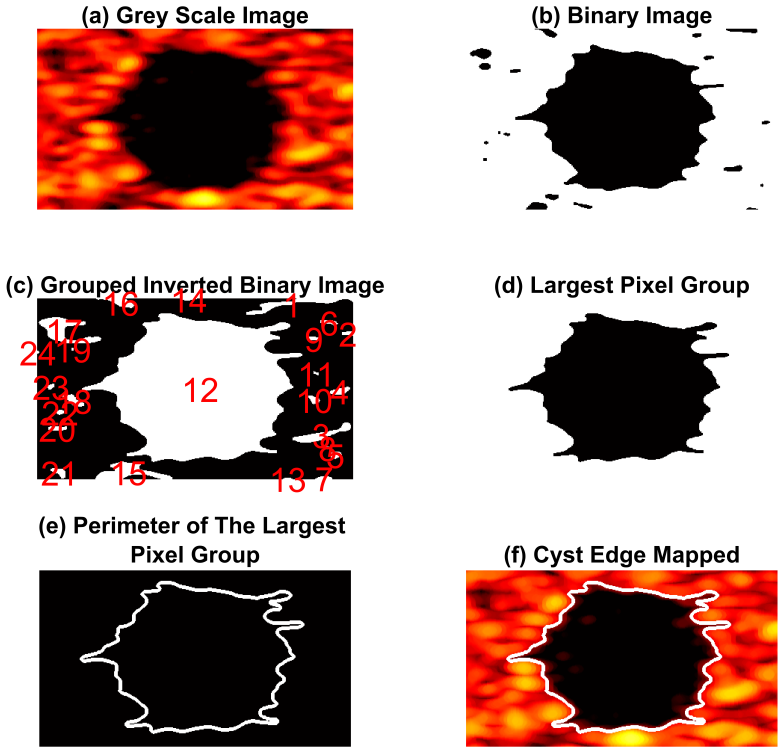

Figure 7.6: a) The grey scale image of the 3.0 mm diameter cyst at the 15 mm depth in digital formats, b) the grey scale image is converted into the binary image 0's and 1's based on the Otsu's thresholding technique, c) the binary image is inverted and mapped according to the pixel group size (from smallest to largest), d) the largest pixel group regions are extracted and the 0's and 1s are inverted back, e) the perimeter of the extracted largest pixel group region, f) the perimeter mapped to the grey scale image as the cyst edge. The example shows the segmented B-mode image with FDMAS, $N = 13$ and despekling with the 2-D adaptive Weiner filter ($[7 \times 7]$).

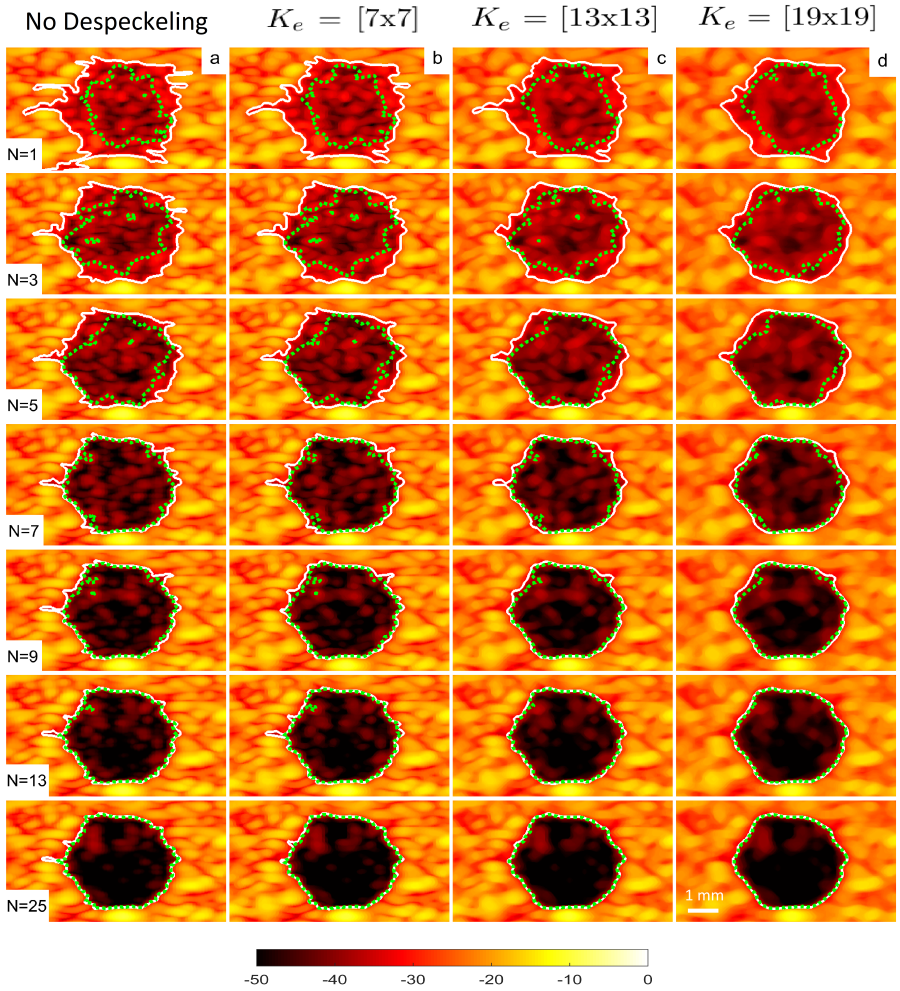

Figure 7.7: The B-mode images compounded from $N = 1$ to $N = 25$ beamformed with DAS despeckled with the 2-D adaptive median filter with the kernel size, b) $K_e = [7 \times 7]$, c) $K_e = [13 \times 13]$ and d) $K_e = [19 \times 19]$.

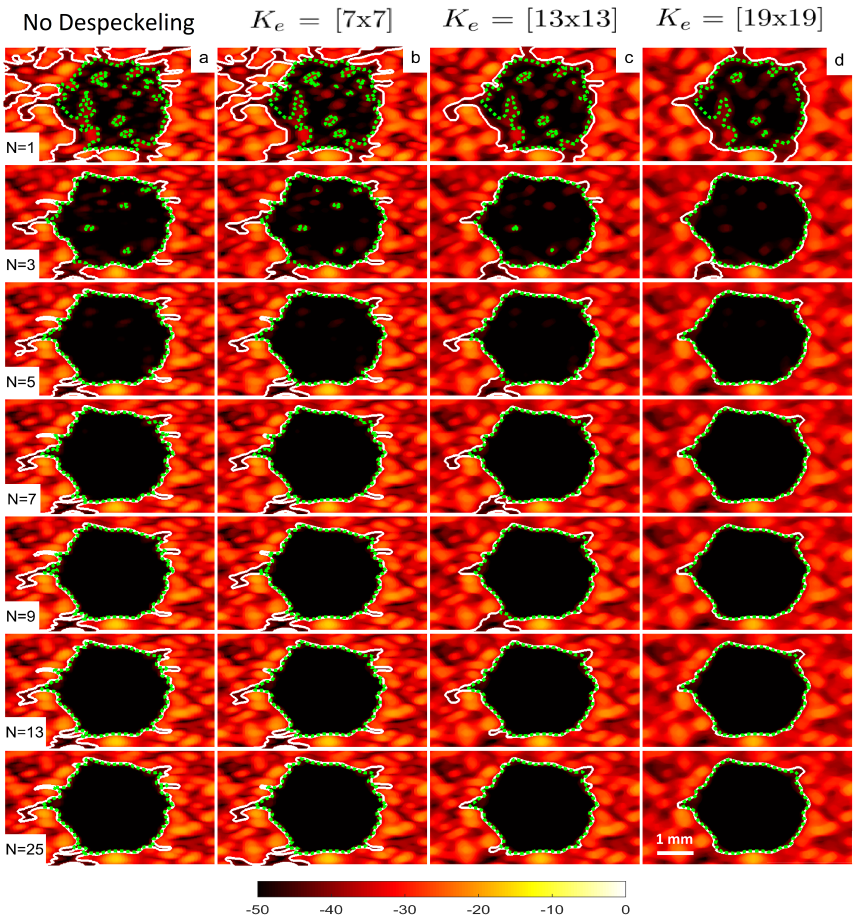

Figure 7.8: The B-mode images compounded from $N = 1$ to $N = 25$ beamformed with DAS, denoised with UM, despeckled with the 2-D adaptive median filter with the kernel size, b) $K_e = [7 \times 7]$, c) $K_e = [13 \times 13]$ and d) $K_e = [19 \times 19]$.

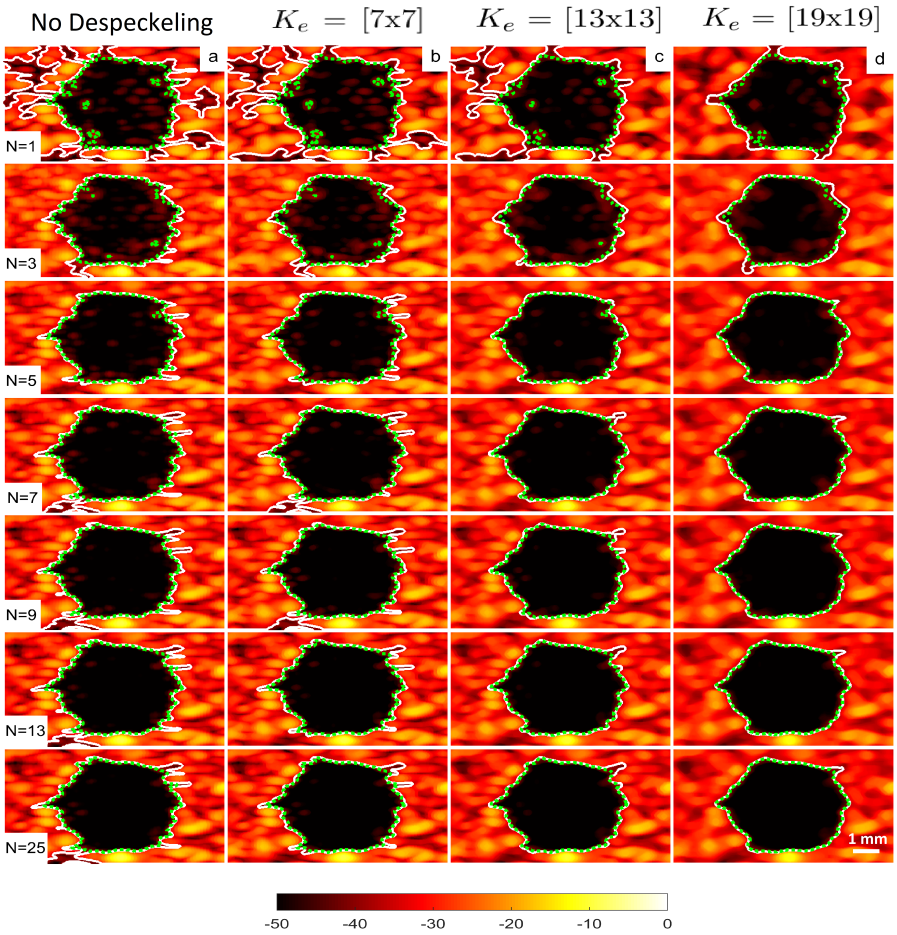

Figure 7.9: The B-mode images compounded from $N = 1$ to $N = 25$ beamformed with FDMAS despeckled with the 2-D adaptive median filter with the kernel size, b) $K_e = [7 \times 7]$, c) $K_e = [13 \times 13]$ and d) $K_e = [19 \times 19]$.

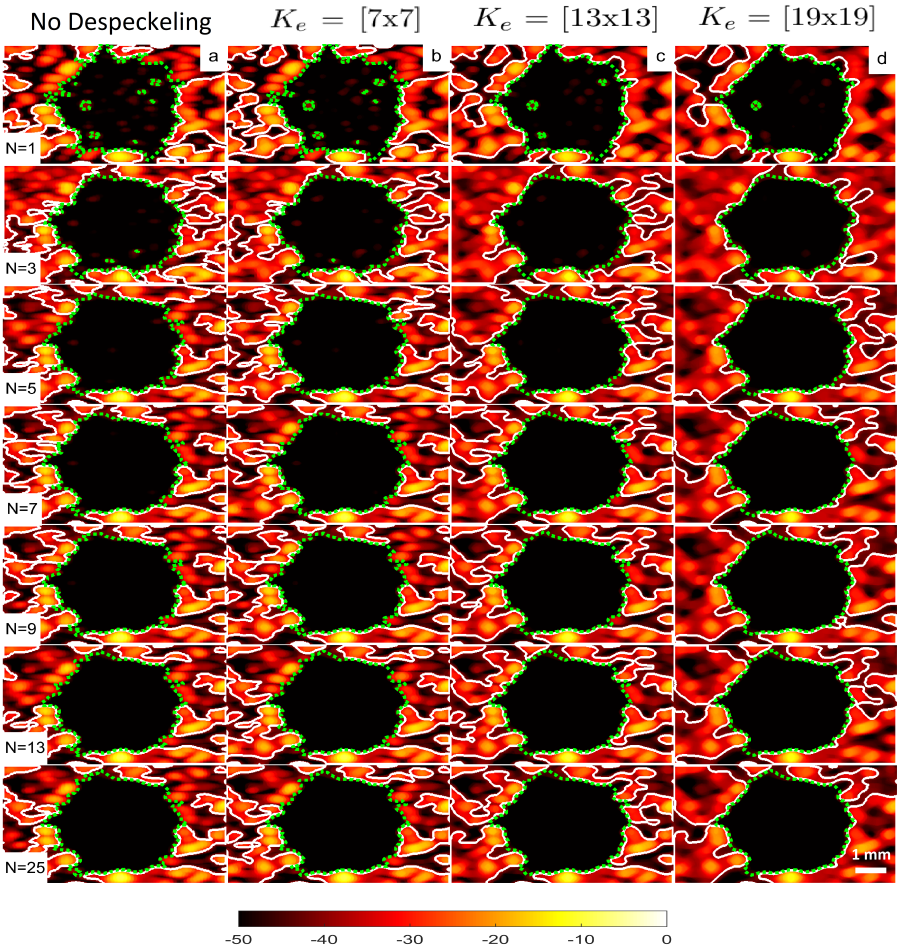

Figure 7.10: The B-mode images compounded from $N = 1$ to $N = 25$ beamformed with FDMAS, denoised with UM, despeckled with the 2-D adaptive median filter with the kernel size, b) $K_e = [7 \times 7]$, c) $K_e = [13 \times 13]$ and d) $K_e = [19 \times 19]$.

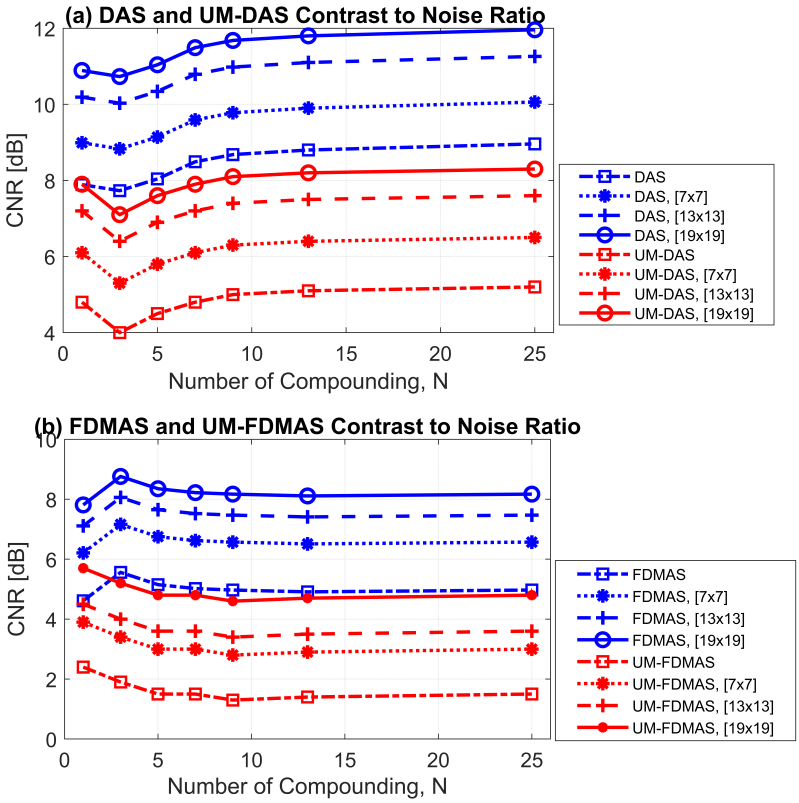

Figure 7.11: The CNR measured on the 3.0 mm diameter cyst with a) DAS and UM-DAS and b) FDMAS and UM-FDMAS after despeckled with 2-D adaptive median filter with $K_e = [7 \times 7]$, $[13 \times 13]$ and $[19 \times 19]$.

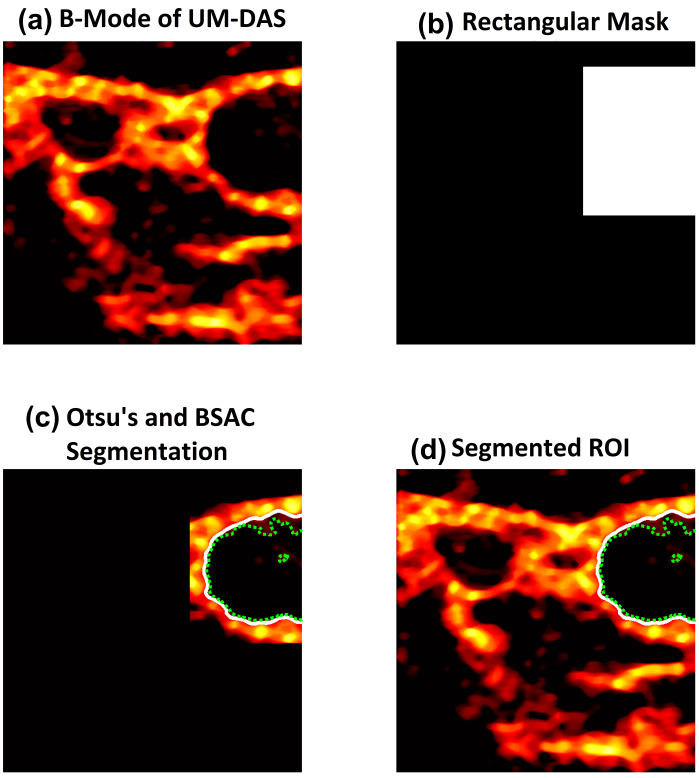

Figure 7.12: a) The UM-DAS compound B-mode images with $N = 25$ have been despeckled with the 2-D Median filter ($k_e = [19 \times 19]$). b) A rectangular mask has been applied on the CCA as ROI for initializing segmentation process. c) Otsu's (white colour line) and BSAC (Green dashed colour line) segmentation have been applied to the ROI. d) The segmented ROI has been concatenated back to the original image.

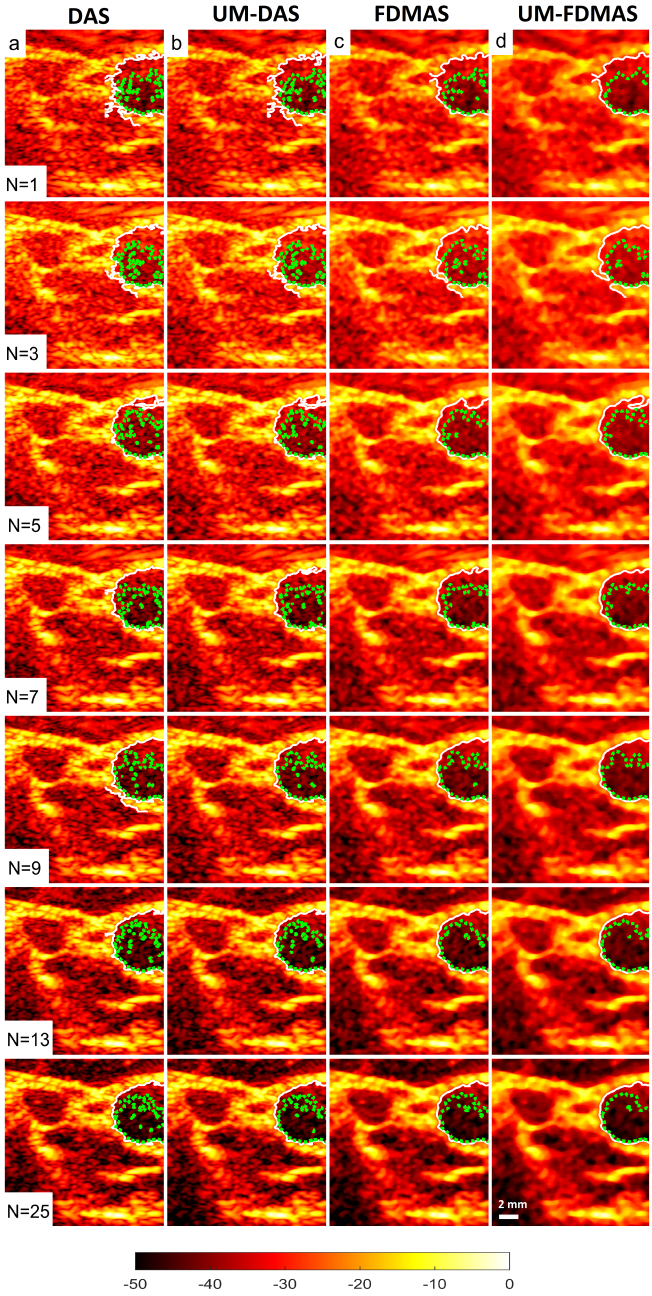

Figure 7.13: The CCA B-mode compound images ($N = 1$ to $N = 25$) beamformed with DAS and despeckled with the 2-D adaptive median filter with the kernel size, b) $K_e = [7 \times 7]$, c) $K_e = [13 \times 13]$ and d) $K_e = [19 \times 19]$. Otsu's (white colour line) and BSAC (Green dashed colour line) segmentation have been applied to the ROI.

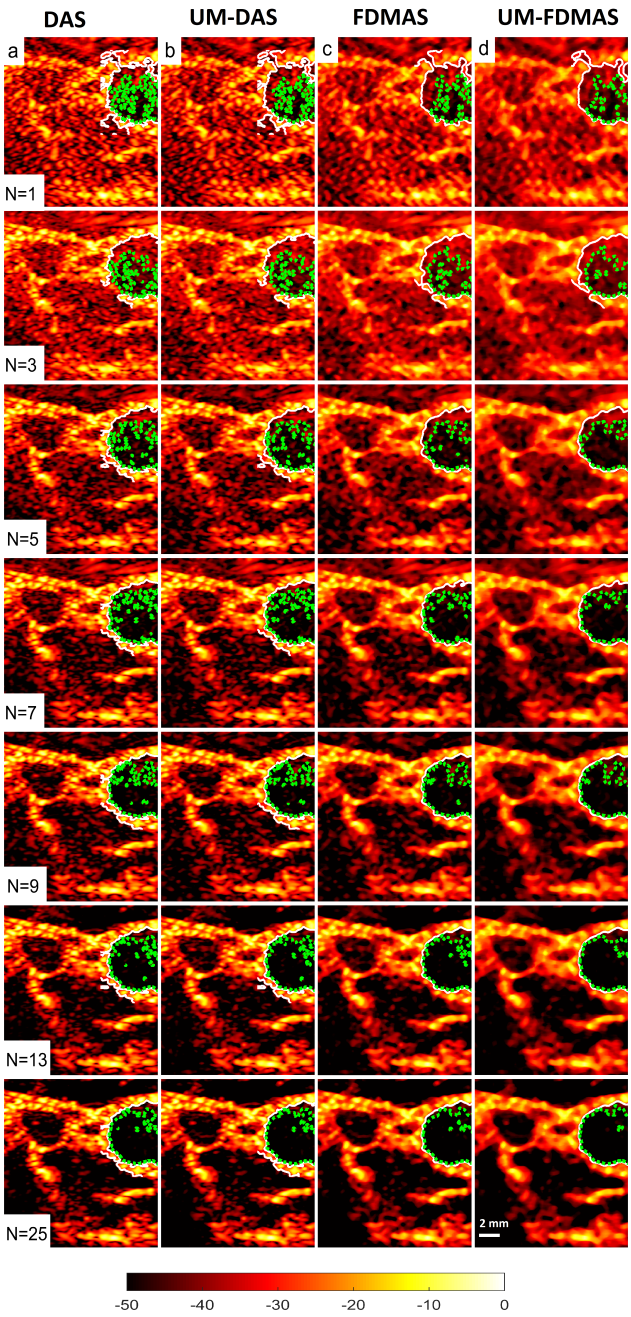

Figure 7.14: The CCA B-mode compound images ($N = 1$ to $N = 25$) beamformed with DAS, denoised with UM and despeckled with the 2-D adaptive median filter with the kernel size, b) $K_e = [7 \times 7]$, c) $K_e = [13 \times 13]$ and d) $K_e = [19 \times 19]$. Otsu's (white colour line) and BSAC (Green dashed colour line) segmentation have been applied to the ROI.

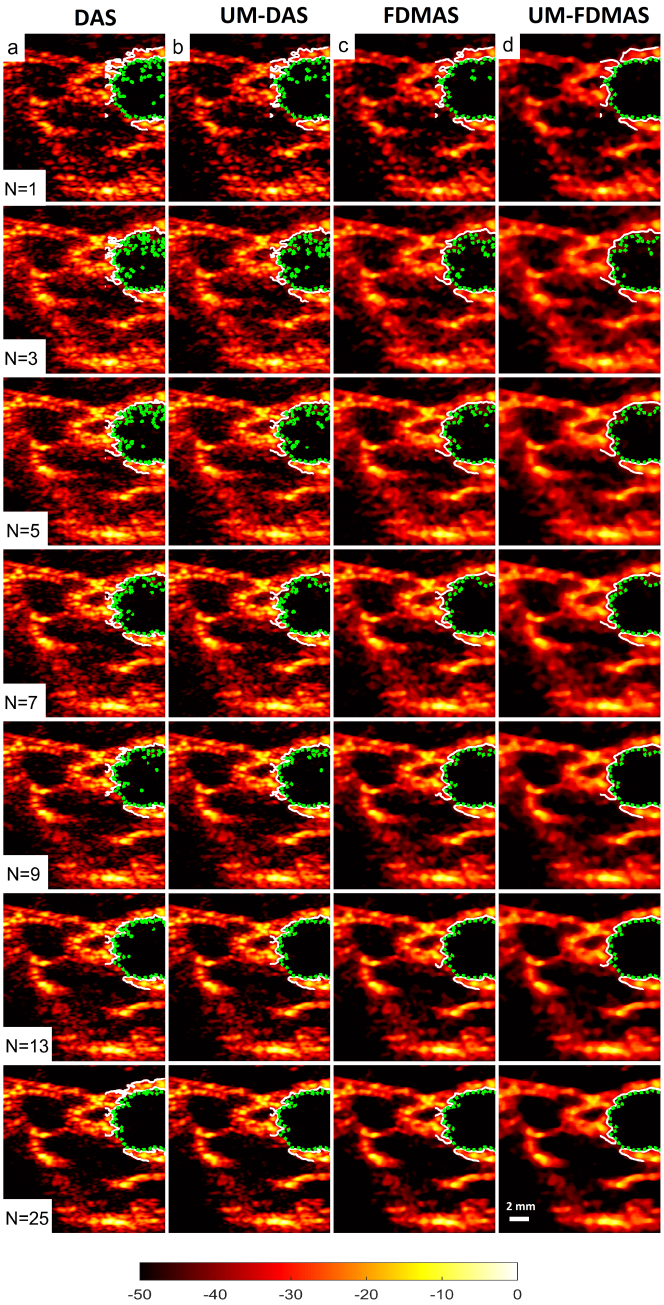

Figure 7.15: The CCA B-mode compound images ($N = 1$ to $N = 25$) beamformed with FDMAS and despeckled with the 2-D adaptive median filter with the kernel size, b) $K_e = [7 \times 7]$, c) $K_e = [13 \times 13]$ and d) $K_e = [19 \times 19]$. Otsu's (white colour line) and BSAC (Green dashed colour line) segmentation have been applied to the ROI.

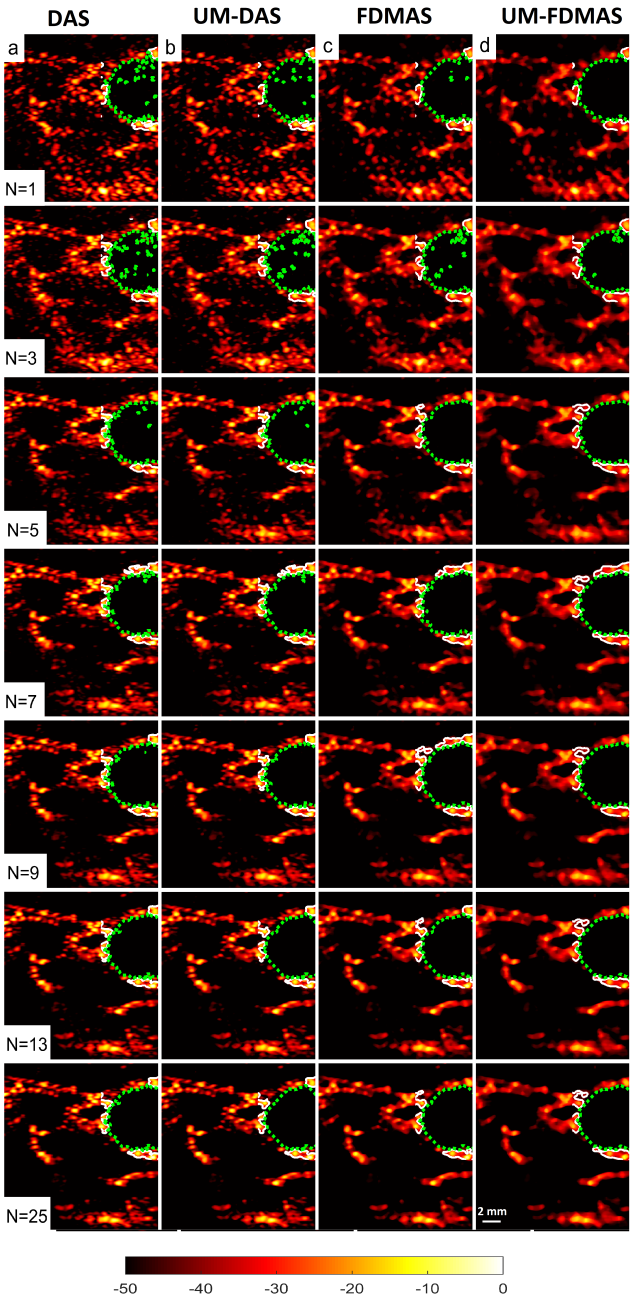

Figure 7.16: The CCA B-mode compound images ($N = 1$ to $N = 25$) beamformed with FDMAS, denoised with UM and despeckled with the 2-D adaptive median filter with the kernel size, b) $K_e = [7 \times 7]$, c) $K_e = [13 \times 13]$ and d) $K_e = [19 \times 19]$. Otsu's (white colour line) and BSAC (Green dashed colour line) segmentation have been applied to the ROI.

7.5 Conclusion

In this chapter, the performance of two different segmentation methods, Otsu's and BSAC were evaluated on compounded DAS and FDMAS B-mode images. UM denoising and despeckling with the 2-D median filter were used. Reducing both speckle and clutter noise with compounding and despeckling improve the Otsu's and BSAC segmentation processes in general. However, Otsu's can only segment the cyst and ICA if the boundary of the object is intact. This however is not the case for BSAC. The discontinuity of the cyst and ICA boundary will not affect the segmentation process. The main obstacle for BSAC is clutter noise inside the ICA region. Reducing clutter noise inside the anechoic region with UM improves the BSAC based segmentation. Applying a higher despeckling kernel size such as $[21 \times 21]$, may reduce the existing clutter noise inside the anechoic regions and eliminate the false segmentation.

Chapter 8

Measurement of the Intima Media Thickness

In this chapter, the improved unsharp masking (UM) was evaluated on ultrasound B-mode medical images by quantitatively measuring the intima-media thickness (IMT) on the common carotid artery. The B-mode images were segmented with balloon snake active contour (BSAC) with different iterations after denoising with UM and despeckling with the 2-D adaptive median filter. The time needed for BSAC segmentation settled on the intima-media layers with and without UM was measured with different iterations. The IMT thickness obtained from BSAC segmentation was compared with manual measurements.

8.1 Introduction

The measurement of IMT on common carotid artery is a common clinical practice which has been used to determine the extent of plaque buildup on the walls of the arteries Hobbs *et al.* (2016); Hurst *et al.* (2007). This clinical procedure has been used by the physicians to assess risk factors or as an earlier indicator of cardiovascular diseases (CVDs) such as heart attack and stroke. This is because there is a strong link between the IMT and cardiovascular events. Thus, continuously monitoring the characteristic changes of the artery wall is crucial. According to the European Guidelines on cardiovascular disease presentation in clinical practice 2016, an IMT superior to 0.9 mm was considered to be abnormal and needs further medical attention immediately Hobbs

et al. (2016). The probability of having CVDs is more than 94% if the IMT is greater than 1.15 mm Hurst *et al.* (2007). Ultrasound B-mode imaging has been used widely to estimate the IMT due to its simplicity and non-invasive nature Xu & Cao (2013).

The most common techniques used to measure the IMT on the B-mode image is segmenting the intima-media borders manually, semi automated or automated border segmentation Loizou (2014); Loizou *et al.* (2005). The thickness between the two boundaries is computed at all points (pixels) along the arterial far wall to obtain the IMT values. The intima-media layers located on the far wall is shown in Fig. 8.1. The measurement of the IMT takes place at the far wall due to strong acoustic shadowing at the near wall. The most popular techniques used for segmentation process are manual delineation of the borders or semi-automated methods such as edge detection, snake active contours (SAC), level sets and Hough transform Loizou (2014); Loizou *et al.* (2005). The manual process of determining the borders is known to vulnerable and prone to human errors. Large variability on the IMT reading with manual techniques is subject to different experts and different equipment. The main advantage of semi-automated segmentation techniques is its accuracy in defining the seeding boundary compared to the manual and complete automated segmentation methods.

The patient will be recommended for more medical attention if the IMT is thicker by 0.1 mm Xu & Cao (2013). Thus, the precise IMT measurement is crucial especially for follow-up patients with high risks. Increasing the B-mode image contrast and spatial resolution could be beneficial for measuring the anatomical structure more accurately. By applying the proposed UM method on CPWI, it is expected the B-mode image contrast and spatial resolution will be improved for better IMT measurements. In the proposed UM technique discussed in detail in the previous chapter, the improvement in the spatial resolution only takes place in the lateral direction. However, reducing clutter noise in the lateral direction will also influence the results in the axial direction. The measurement of the IMT takes place in the axial direction. Thus, when clutter noise is reduced, better image segmentation with more precise and fast measurements could be available.

Reducing the side lobes and clutter noise inside the anechoic regions will improve the B-mode image contrast ratio and improve the semi-automated BSAC segmentation process. In order to measure the IMT, intima-media regions need to be segmented first. The segmentation process is based on identifying the edge or the boundary of the

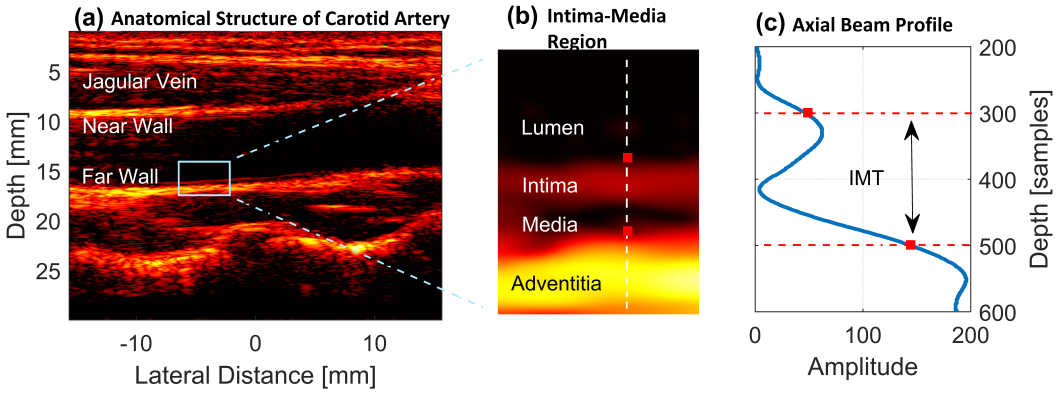

Figure 8.1: a) The anatomical structure of the CCA. b) Detailed regions showing the lumen, intima, media and adventitia layers in the far wall of the CCA. The two red points highlight the intima-media layers. c) The axial beam profile corresponding to the white dashed line in b). The IMT measured between the intima-media layers is also shown on the beam profile.

intima-media walls. If any noise is present between those walls, more iterations may be needed for the initial contour to reach the intended boundary in the BSAC segmentation process. At the same time, there is also a chance for false border detections. The semi-automated method relies on the quick and simple interactive initialization of BSAC aiming to increase the overall robustness to reduce errors that may be introduced by complete automatic techniques Zahnd *et al.* (2014). For the semi-automated BSAC, the contour is initialized by the user near to those walls. This is to reduce errors where the snake (referring to the initial contour) fails to converge or diverge to the intended borders Loizou *et al.* (2015). Common lengths of the intima-media layers in the lateral direction are between 3 mm to 10 mm Zahnd *et al.* (2014).

Thus in this chapter, the improved UM technique was implemented to reduce clutter noise on the B-mode image before the IMT measurement. It is expected that the reduction of clutter noise in the B-mode image will fasten the segmentation process with a lower number of iterations. The accuracy of measurements is also expected to improve since the boundaries of intima-media can be easily detected with less clutter noise.

8.2 Experimental Setup

The *in-vivo* data were collected from the cross section of the right CCA of a healthy volunteer as shown in Fig. 4.3. The protocol used in this study to measure the artery IMT was according to the clinical practice Casella *et al.* (2008); Garovic *et al.* (2017). The IMT measurements were obtained with the volunteer lying in the supine position. Three CCA samples were collected in sequence at the same posture classified as sample 1, 2 and 3. A 128-element linear array transducer (L11-4, Verasonics, Inc. United Stated of America) with a centre frequency of 7.55 MHz and a -6 dB bandwidth of 90.8% was used to collect all the data. A two-cycle sinusoidal excitation signal with a centre frequency of 7.55 MHz was digitised with the ultrasound array research platform II (University of Leeds, UK) Cowell & Freear (2008b); Cowell *et al.* (2016); Smith *et al.* (2012). A pulse sequence consisting of 13 angles was used with an increment of 2° within a $\pm 12°$ sector. The maximum imaging depth was set to 30 mm. The FR is 2 KHz. The received signals were sampled at 80 MHz before beamformed with DAS and FDMAS. The experimental parameters are provided in Table 8.1. To maximize the image resolution, no apodization was applied to the elements along the lateral direction during transmission and reception.

8.3 Methods

The received RF echoes were beamformed with DAS and FDMAS before denoised with UM. The beamformed and denoised B-mode images were despeckled with the 2-D adaptive median filter with the kernel size of [19 $\times$ 19] to smoothen speckle and reduce clutter noise that is present in the B-mode image. A ROI with a size of 2 mm $\times$ 5 mm (width $\times$ length) was selected from the far wall of the common carotid artery to start segmentation before the IMT measurement. Two separate initial contours with the rectangular shape have been set on top and bottom of the intima later as the initial contour A and contour B as shown in Fig. 8.2. This is to speed up the BSAC segmentation process in identifying the intima-media layers. The initial contour A will expand to locate the intima layer, while the initial contour B will shrink to locate the adventitia layer. Both the initial contours were drawn in a square shape as near as possible to the intended borders to reduce the number of iterations. The IMT thickness is computed between the two boundaries, intima-media, at all points

Table 8.1: Experiment parameters.

Properties	Equations	Values
Transducer		Verasonics L11-4
Speed of Sound		1540 m/s
Number of Elements	-	128
Transducer Centre Frequency	-	7.55 MHz
Transducer Bandwidth (−6 dB)	-	90.8%
Transducer Element Pitch, p	1.5*λ	0.30 mm
Transducer Element Kerf	$p/20$	15.0 μm
Transducer Element Width	Pitch-Kerf	285.0 μm
Transducer Element Height	-	6 mm
Transducer Elevation Focus	-	20 mm
Sampling Frequency for Tx/Rx	-	160/80 MHz
Rx Sampling Time, T_s	$1/f_s$	12.5 ns
Excitation Signal	-	2-Cycle Sinusoid
Excitation Signal Window	-	Tukey ($\alpha = 0.5$)
Excitation Signal Centre Frequency, f_o	-	7.55 MHz
Imaging Point Step, x	$\lambda/3$	0.1016 mm
Imaging Point Step, z	$c * Ts/2$	9.625 μm
Spatial Apodization	-	-

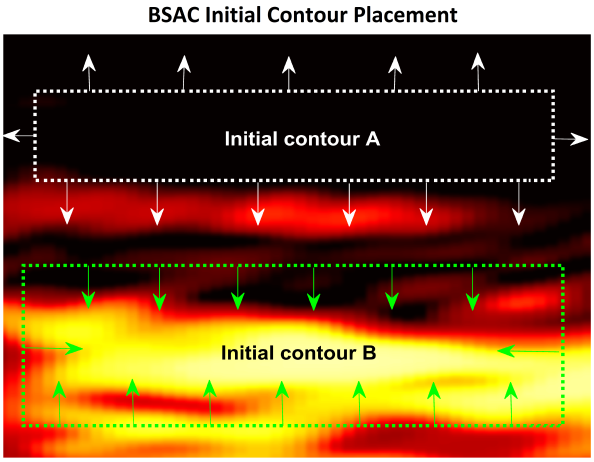

Figure 8.2: Two different BSAC segmentations are initiated simultaneously in order to locate the initma and adventitia layers. The first and second BSAC initial contour, A and B are drawn above and below the intima layer. The fist initial contour A will expand to locate at the intima layer while the second initial contour will shrink to locate at the adventitia layer.

along the far arterial wall in the lateral direction segmented by BSAC. As for manual dilation, a Matlab function was used to trace the intima-media boundaries on the ROI with the help of a computer mouse. The difference between the upper (intima) and lower (media) pixel values was converted into values in mm.

8.4 Results and Discussion

The results for IMT measurements and the iterations with BSAC using different iterations in three ROIs are presented in Fig. 8.4. In CCA sample 1, the IMT_{mean} value for DAS increases from 0.4002 mm to 0.6315 mm when the iterations change from 50 to 200. There is a 57.8% increment in IMT_{mean}. This shows that the BSAC internal contour keeps deforming and has not reached the final minimum energy yet. The reason for this is clutter noise that tends to stop the internal contour from deforming by providing false edges. Denoising clutter noise with UM and applying despeckeling will make the initial contour to expand faster to the global edge. As shown in Fig. 8.3(d), with 50 iterations, the BSAC initial contour approaches the adventitia border much closer by combining UM and DAS. Whereas with DAS alone, as shown in Fig. 8.3(c),

Table 8.2: Differences of IMT_{mean} with different BSAC iterations for sample 1.

	50-100		100-200		50-200	
	mm	%	mm	%	mm	%
DAS	0.1164	29.1	0.1149	22.2	0.2313	57.8
UM-DAS	0.0968	18.5	0.0016	0.25	0.0984	18.8
FDMAS	0.0983	18.5	0.0006	0.09	0.0989	18.6
UM-FDMAS	0.076	13.5	0.0009	0.14	0.078	13.7

the BSAC initial contour stops at the region of clutter noise rather than on the adventitia border. Although when combining UM and DAS the contour reaches closer to adventitia border, the final border is not reached due to a low number of iterations of 50. This can be seen in Fig. 8.3(d) as highlighted by the arrow. The difference for the IMT_{mean} from the 50 to 200 iterations using UM-DAS is only 18.8%. This is much lower when compared to the difference of 57.8% in IMT_{mean} using DAS. FDMAS and UM-FDMAS show 18.6% and 13.7% differences in IMT_{mean} measurements with 50 to 200 iterations. The same pattern of differences in IMT_{mean} with 50 to 200 iterations can be seen for samples 2 and 3. DAS shows higher differences while other investigated techniques show smaller differences in for the same change of iterations. With only 100 iterations, the segmentation process with all techniques except DAS have reached the final border (minimum energy), and when the iteration is increased to 200, the changes of the IMT_{mean} between 100 and 200 iteration are small. In sample 1, the IMT_{mean} measured with UM-DAS shows the difference of 0.0016 mm or 0.25%, while DAS shows 0.1149 mm or 22.2% difference between 100 and 200 iterations. Results for IMT_{mean} differences between 50-100, 100-200 and 50-200 for all samples are shown in Table 8.2, 8.3 and 8.4. In Table 8.3 it can be seen that from 100-200 iterations, the IMT_{mean} values decrease for UM-DAS and UM-FDMAS. This indicates that the BSAC has reached the minimum energy level within 100 iterations, and from 100 to 200 iterations the initial contour keeps oscillating between initial and final intended borders. The BSAC will not reach the final intended border if the initial contour defined by the user is far from the final border with a low number of iterations Gadermayr *et al.* (2013). On the other hand, if a very large initial contour is drawn with a large number of iterations, the initial contour will keep oscillating between the initial contour and the intended final border as happened in sample 2 for UM-DAS and UM-FDMAS.

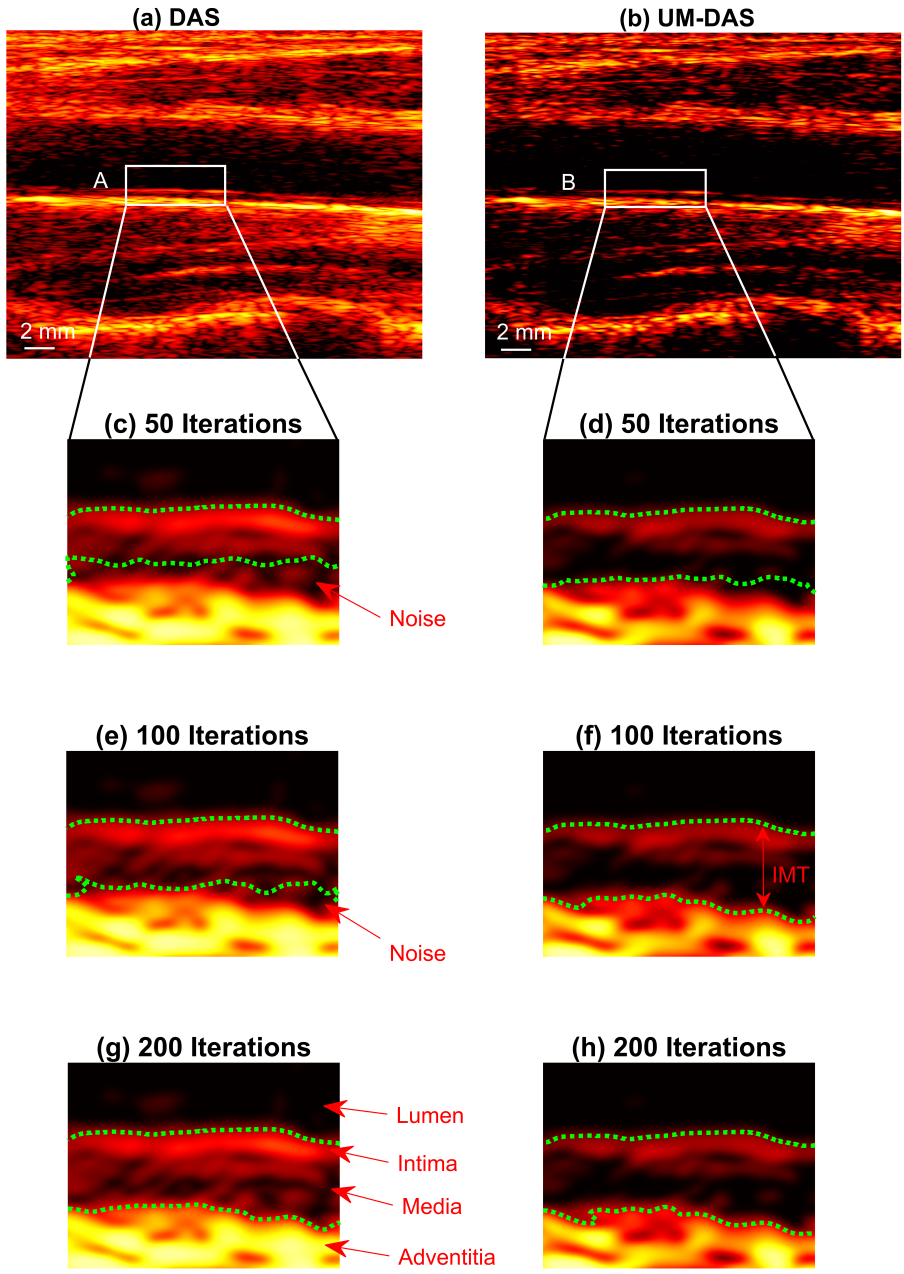

Figure 8.3: The CCA beamformed with a) DAS and denoised with b) UM-DAS. The BSAC contour (green line) implemented within the ROI (white box, A (DAS) and B (UM-DAS)) after 50 iterations (c and d), 100 iterations (e and f) and 200 iterations (g and h). The SAC contour settles on the media border within 100 iterations for UM-DAS while it needs 200 iterations for DAS.

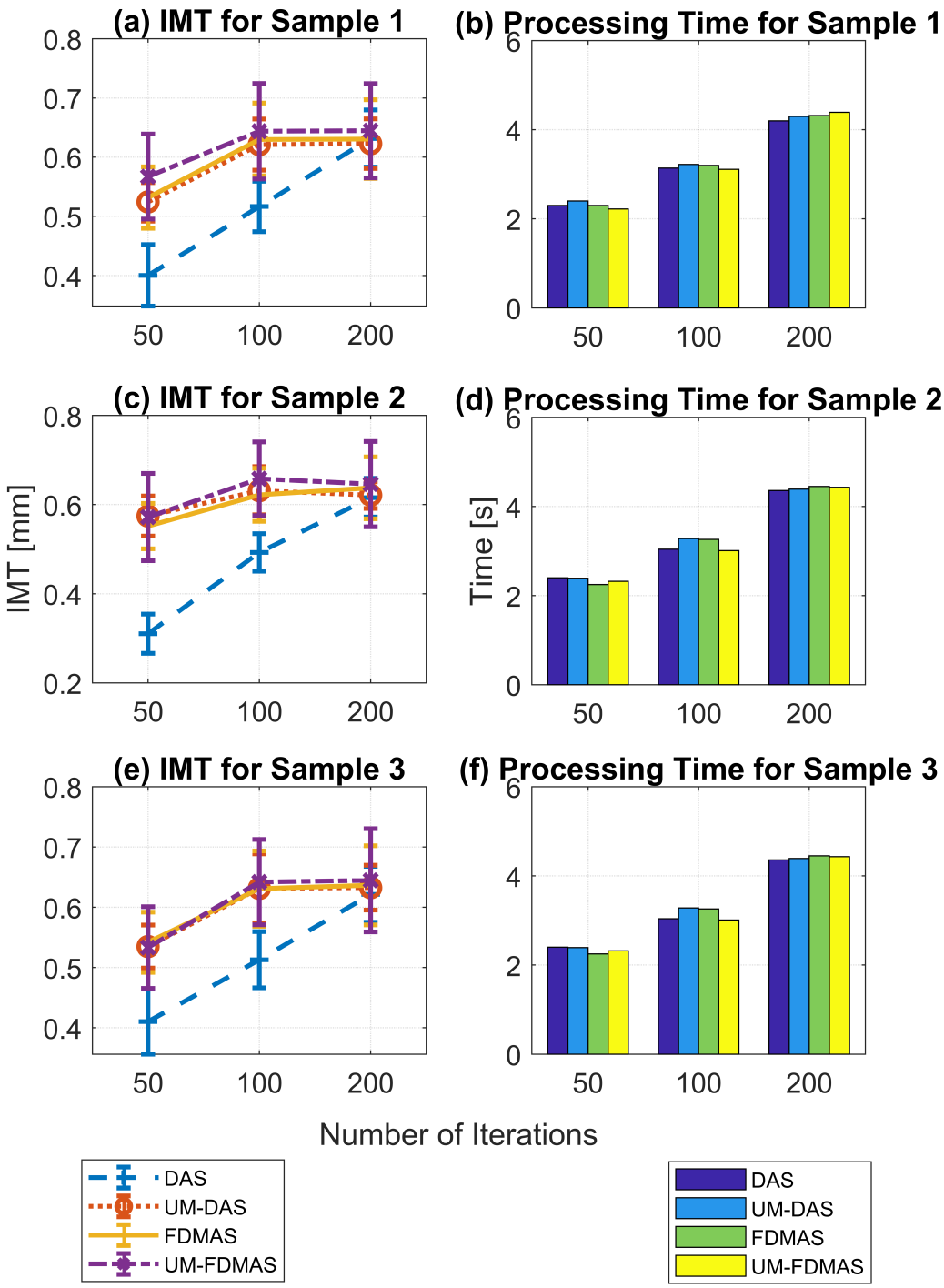

Figure 8.4: The IMT_{mean} with standard deviations and time needed for sample 1 (a and b), sample 2 (c and d) and sample 3 (e and f) with 50, 100 and 200 iterations are provided when using DAS, UM-DAS, FDMAS and UM-FDMAS.

Table 8.3: Differences of IMT_{mean} with different BSAC iterations for sample 2.

	50-100		100-200		50-200	
	mm	%	mm	%	mm	%
DAS	0.1825	58.8	0.1228	24.9	0.3053	98.4
UM-DAS	0.0568	9.88	−0.01	−1.6	0.0468	8.1
FDMAS	0.0702	12.7	0.0156	2.5	0.0858	15.5
UM-FDMAS	0.086	15	−0.012	−1.8	0.074	12.9

Table 8.4: Differences of IMT_{mean} with different BSAC iterations for sample 3.

	50-100		100-200		50-200	
	mm	%	mm	%	mm	%
DAS	0.1027	25	0.1086	21.2	0.2113	51.5
UM-DAS	0.0965	18	0.0012	0.19	0.0977	18.3
FDMAS	0.089	16.4	0.0056	0.9	0.0946	17.5
UM-FDMAS	0.1086	20	0.003	0.45	0.1115	21

The processing time for SAC segmentation is not affected by the techniques investigated but dependent on the total number of iterations. The average processing time for 50, 100 and 200 iterations are 2.3 s, 3.2 s and 4.2 s for all samples and all techniques. The computer operating system used to calculate the processing time is Windows 7 enterprise 64-bit. The computer specification is as follows: CPU (CORE i5-4460, Intel Corporation Co., Ltd., Santa Clara, CA, USA), 3.20-GHz clock speed, 4 cores and 16-GB DDR3 RAM. The number of iterations is set according to the initial contour size Yu *et al.* (2013). The definition of the initial contour is dependent on the object shape and in general drawn as near as possible to the intended border to reduce the number of iterations. The typical time needed to measure the IMT with SAC was between 15 to 45 seconds Ceccarelli *et al.* (2007).

The IMT_{mean} values which were measured manually are compared with BSAC (200 iterations) for all three samples and all techniques as shown in Fig. 8.5. The B-mode images for sample 1 are shown in Fig. 8.6. The main objective of applying semi-automated segmentation process (BSAC) on measuring the IMT is to obtain the same or better results from manual delineation which is prone to human error and time consuming. A study in Polak *et al.* (2011) where 26 IMTs were measured manually by

5 different experts shows significant differences in the final evaluation between them. This is known as inter-observer differences. As a final outcome, the author concluded that the inter-observer differences can affect the correct evaluation of the cardiovascular risk. The differences in IMT_{mean} measured manually and with BSAC segmentation for samples 1, 2 and 3 were calculated according to equation 8.1 Loizou *et al.* (2015):

$$Err = \frac{1}{P}|\sum_{e=1}^{P} \text{Manual}_e - \text{BSAC}_e| \tag{8.1}$$

where P is the total number of B-mode images, Manual_e and BSAC_e are IMT_{mean} measured manually and with BSAC segmentation. Table 8.6 presents the errors between the two measurements.

The best or optimal imaging results for IMT measurement can be achieved when the carotid artery was perpendicular to the face of the transducer Cronenwett & Johnston (2014). This is because the echogenity of the intima-media complex is comparable low to the carotid wall. Thus, only the maximum amount of energy transferred to the IMT is able to produce a high echo for IMT measurement. In the segmentation technique proposed by Ilea *et al.* (2013), a low contrast value on the B-mode image has been mentioned as one of the main obstacles in measurements of IMT. Thus, reducing clutter noise and increasing the image CR will assist with the segmentation process and measurement of IMT. According to a study conducted by Loizou *et al.* (2015), there is no significant deference on the measurement of IMT on the right or left side carotid artery wall. Thus, experiments were conducted only for the right CCA in this work. A clinical study conducted by Gaarder & Seierstad (2015) on 313 participants shows that the dynamic range (DR) may influence the IMT measurements. It was found that the relative changes in IMT were largest between 40 and 55 dB (6.7%) and smallest between 70 and 85 dB (2.6%). The main outcomes from the study were suggestions to set the same DR for the same patient during the follow-up measurements. The standard deviation of the IMT measurements can predict the plaque formation on the intima layers. The uneven shape of plaque formation on the intima layers gives high IMT standard deviation values indicating the plaque composition at certain parts of the measured intima-media layer.

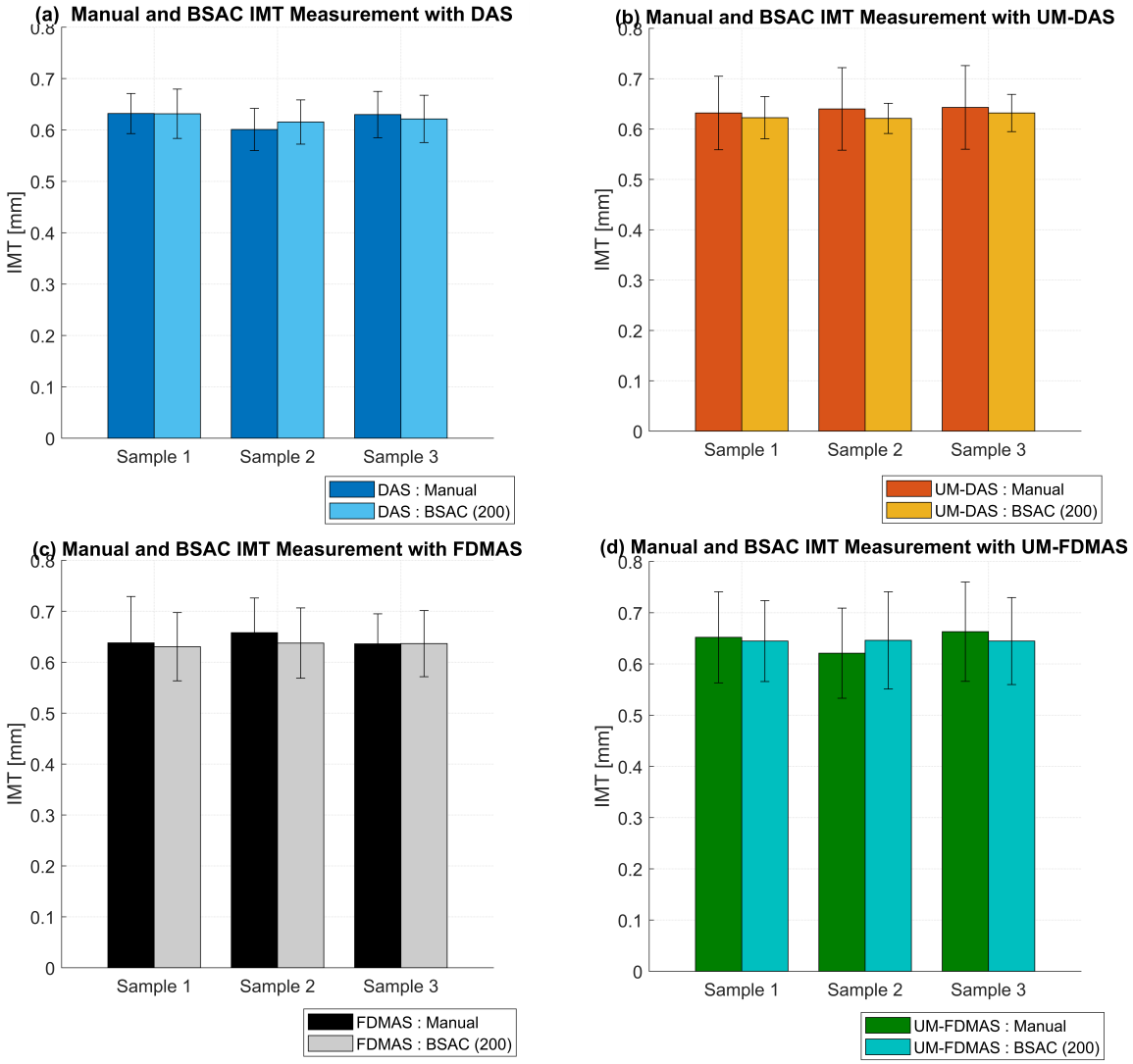

Figure 8.5: The measurements of IMT measured manually have been compared with BSAC (200 iterations) for all three samples.

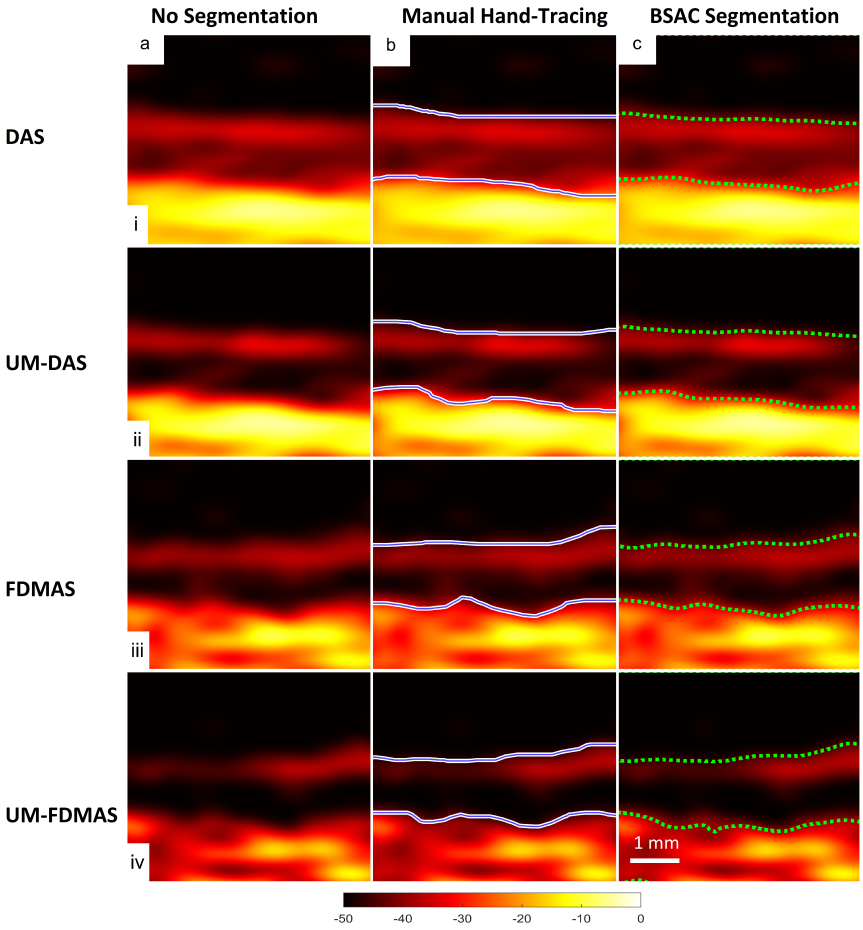

Figure 8.6: The IMT layers on the ROI obtained from sample 1 without any segmentation shown in column a), segmented by hand tracing shown in column (b) and segmented with BASC shown in column (c). The images obtained using i) DAS, ii) UM-DAS, iii) FDMAS and iv) UM-FDMAS.

Table 8.5: Processing Time for Manual and BSAC (200 iterations)

	Sample 1		Sample 2		Sample 3	
	Manual	BSAC	Manual	BSAC	Manual	BSAC
DAS	4.2	20.2	4.4	19.8	4.36	19.7
UM-DAS	4.3	18	4.49	20.1	4.39	19.8
FDMAS	4.32	19.5	4.45	18.8	4.45	19.3
UM-FDMAS	4.39	18.8	4.44	19	4.43	19.7

Table 8.6: Differences Between Manual Measurement and BSAC (200 iterations) in IMT_{mean}

Techniques	mm	%
DAS	0.011	1.72
UM-DAS	0.017	2.6
FDMAS	0.009	1.45
UM-FDMAS	0.02	3.1

8.5 Conclusion

The proposed UM as a denoising tool for DAS is able to reduce clutter noise in between the intima-media layers and improve the IMT measurement. The number of iterations needed for BSAC to settle on the final border is less with UM (100 iterations) compared to that without the denoising technique. The implementation of UM with FDMAS does not affect the IMT measurement significantly. This is because the CR with FDMAS is already good when compared to that using DAS. The implementation of UM with FDMAS may cause the intima layers to diminish and nonvisible in the worst case. Although all the three CCA samples used for IMT measurements show the intima layers, but it is always a challenge to find the best B-mode images for IMT with UM-FDMAS. Thus, it is not recommended to use UM-FDMAS for IMT measurements. Both UM-DAS and FDMAS techniques are able to provide better results with less time in measuring the IMT compared to that using DAS. One of the challenges during the IMT measurement on the B-mode image with BSAC is the placement of the initial contours. The manual placement of the initial contour should be as near as possible to the intima and adventitia borders in the ROI.

Chapter 9

Summary

Ultrasound B-mode imaging is one of the most important modalities in medical imaging. It can provide real-time diagnosis results, and the nonionizing and noninvasive properties make it safer to be used compared to x-ray and MRI. Recently, ultrafast imaging gained its popularity due to its capabilities to provide thousands of frames in a second. This has opened many avenues for new applications such as measuring the transient mechanical wave speed for elastography and higher contrast-enhanced imaging without bursting the microbubbles. Plane wave imaging (PWI) is commonly used to achieve high FRs as it uses the single unfocused plane wave for a single transmit. This causes low contrast and poor resolution due to the lack of focusing. Although spatial compounding has been used to overcome the low signal-to-noise ratio problem in PWI but it comes at the cost of reducing FRs. The commonly used DAS beamforming technique to form the B-mode image is unable to further improve the PWI performance. Thus in this thesis, we have proposed and investigated several methods to reduce clutter noise which is with PWI. In general, reducing clutter noise in PWI is able to improve the B-mode image quality by increasing its contrast ratio and spatial resolution.

Filtered delay multiply and sum (FDMAS) is a new beamforming technique which has been adopted from radar microwave imaging and it is able to increase the B-mode image contrast by reducing the side lobes and improve the resolution by narrowing the main lobes in the lateral direction. In this thesis, a detailed study on the effect of varying the imaging point steps in the lateral direction was evaluated. This is because the fundamental of FDMAS algorithm is based on a process similar to autocorrelation.

Thus, varying the lateral steps generally affect the final FDMAS results. An optimized lateral step of $\lambda/3$ has been suggested for FDMAS after considering the trade-off between the computational complexity (CC) and improvements in CR and spatial resolution. It is also found that by reducing the lateral step to $\lambda/3$, a low number of steering angles $N = 9$ can be used to produce better image quality compared to that with a high number of compounding angles $N = 25$ using a larger lateral step of $\lambda/2$.

A new compounding method was proposed in this thesis, inspired by the FDMAS beamforming technique. Although FDMAS is able to improve the B-mode image quality compared to DAS but the CC is higher than that using DAS. The new compounding technique is based on the process similar to autocorrelation to reduce the CC without sacrificing the B-mode image quality. The new technique named as filtered multiply and sum (FMAS) was implemented with DAS and it provide better image quality with the processing time as required using DAS. DAS-FMAS provides improvements of 14.1 dB and 7.29 dB in contrast ratio (CR) than DAS and FDMAS with $N = 3$. The peak side lobe (PSL) in the axial direction is attenuated by 33 dB and 48 dB more with DAS-FMAS when compared to DAS and FDMAS for $N = 3$. The lateral resolution (LR) for DAS-FMAS is improved by 36% and 19% compared to DAS and FDMAS with $N = 3$. The simulations and experiments performed on point targets, cysts and *in-vivo* carotid artery showed promising results. The most advantage gained by FMAS is its ability to improve the image spatial resolution in the axial direction. Conventionally, spatial compounding can only improve the lateral resolution since the steering operation takes place in that direction. However, in this work it is found that there is a small phase shift among the steered beams in the axial direction. The existence of this phase shift between the steered beams was proven with experimental and simulation work. The simulated pressure fields at different steering angles also showed this phase shift. Although the phase shift is small but when the process similar to autocorrelation takes place with the RF signals from the steered angles, the final outcome significantly affects the formation of the axial beam profiles. At $N = 3$, the axial resolution (AR) with DAS-FMAS is improved by 43% and 12.5% compared to DAS and FDMAS, respectively.

Unsharp masking (UM) is an image sharpening tool which has been used excessively in conventional digital image processing in order to improve the image quality by enhancing the image edges. The UM technique has been adopted in a few medical

imaging modalities such as x-ray and mammogram. The conventional UM is not a famous tool for increasing the B-mode image contrast and spatial resolution. This is because the flaws that are present in the equation which is dependent on the single weightage scheme and the design of the low pass filter (LPF). Thus, in this work, a new UM denoising method dedicated to compound plane wave imaging (CPWI) was proposed. The proposed UM has an iterative process with two different weightage schemes and non-coherent compound plane wave imaging is used as its LPF. The new UM method can improve the B-mode image contrast and enhance the lateral resolution for DAS and FDMAS. The best LRs using DAS and UM-DAS are 0.47 mm and 0.39 mm with $N = 3$, and a 17% of improvement is achieved with UM. UM is able to improve the CR by 7.94 dB and 6.39 dB when combined with DAS and FDMAS for $N = 9$. The PSL is attenuated more when UM implemented with DAS and FDMAS. The PSLs using UM combined with DAS and FDMAS are 19.2 dB and 19.3 dB with $N = 9$. The potential of the proposed UM method needs further exploration. This is because the manipulation of the weightage scheme gives opportunities to the end user to change the final results as wanted. Using specific parameters in the weightage scheme gives the flexibility to improve the spatial resolution and the image contrast. Although the proposed UM method shows improvement in B-mode imaging using delay and sum (DAS) but it is not the case for FDMAS. Since in FDMAS the CR is higher than DAS, applying the proposed UM method for denoising with FDMAS attenuates more signal and produces anechoic spots or black box regions which are undesirable for B-mode imaging.

Conventionally, the despeckling techniques are applied to the ultrasound B-mode images without considering the presence of clutter noise. Although the main priority of despeckling is to smooth the speckle region in the B-mode image, the presence of clutter noise especially in the cyst regions impacts the final result. Despeckling redistributes clutter noise to larger regions. Thus, denoising the B-mode image with the new UM method before despeckling showed improvement in segmentation. The balloon snake active contour (BSAC) performed better in delineating the intended cyst region when combining the new UM technique with DAS. Only 100 instead of 200 iterations are needed for segmenting the cyst region when UM applied to reduce the clutter noise in DAS.

The intima-media thickness (IMT) is one of the most important indicators for detecting cardiovascular deceases. This manual delineation process somehow is not the best option since it is time consuming and dependent on individual experience. Semi-automated IMT measurement methods gain the popularity for more reproducible measurements. The BSAC segmentation method is one of the popular techniques used to measure the IMT. Since clutter noise that is present in between intima-media layers imposes restrictions for segmentation, reducing clutter noise first with the new UM method before segmentation could fasten and improve the IMT measurement accuracy. The time taken for the snake contour formation around the intima-media layer with different iterations was less when the proposed UM denosing method was used. Both UM-DAS and FDMAS techniques are able to provide better results with less time in measuring the IMT compared to that using DAS. The differences in IMT measured between 100 to 200 iterations for DAS and UM-DAS were 21.2% and 0.19%, respectively.

The semi-automated BSAC also showed very similar results for IMT measurements with manual delineation. The preliminary results show that improving the CR will be beneficial for the segmentation process with BSAC. This can be the step stone for further studies in detail with the proposed UM method to reduce clutter noise in more medical applications using ultrasound imaging. The new proposed compounding technique, FMAS is expected to produce narrower intima layers since its ability to improve the axial resolution.

References

Ahmed, H.S. & Nordin, M.J. (2011). Improving diagnostic viewing of medical images using enhancement algorithms. *Journal of Computer Science*, **7**, 1831. 5

Akbay, C. (2015). *Application of Image Enhancement Algorithms to Improve Visibility and Classification of Microcalcifications in Mammograms*. Ph.D. thesis, Middle East Technical University. 5, 119

Akram, M.U., Atzaz, A., Aneeque, S.F. & Khan, S.A. (2009). Blood vessel enhancement and segmentation using wavelet transform. In *2009 International Conference on Digital Image Processing*, 34–38. 5

Ali, M., Magee, D. & Dasgupta, U. (2008). Signal processing overview of ultrasound systems for medical imaging. *SPRAB12, Texas Instruments, Texas*. 21

Aliabadi, S., Wang, Y., Yu, J., Zhao, J., Guo, W. & Zhang, S. (2016). Eigenspace-based beamformer using oblique signal subspace projection for ultrasound plane-wave imaging. *Biomedical Engineering Online*, **15**, 127. 116

Alomari, Z., Harput, S., Hyder, S. & Freear, S. (2014). Selecting the number and values of the cpwi steering angles and the effect of that on imaging quality. In *Ultrasonics Symposium (IUS), 2014 IEEE International*, 1191–1194, IEEE. 14, 18, 68, 150

Azhari, H. (2010). Appendix a: typical acoustic properties of tissues. *Basics of Biomedical Ultrasound for Engineers*, 313–314. 54

Bamber, J. & Daft, C. (1986). Adaptive filtering for reduction of speckle in ultrasonic pulse-echo images. *Ultrasonics*, **24**, 41 – 44. 150

Baselice, F. (2017). Ultrasound image despeckling based on statistical similarity. *Ultrasound in Medicine & Biology*, **43**, 2065 – 2078. 149

Bercoff, J. (2011). Ultrafast ultrasound imaging. In *Ultrasound Imaging-Medical Applications*, InTech. 1, 2

Bhateja, V., Misra, M. & Urooj, S. (2017). Human visual system based unsharp masking for enhancement of mammographic images. *Journal of Computational Science*, **21**, 387 – 393. 5, 119

Bhushan, C. (2009). Ultrasound image segmentation. *Basics on Image*. 153

Bradley, W.G. (2008). History of medical imaging. *Proceedings of the American Philosophical Society*, **152**, 349–361. 1

Burckhardt, C.B. (1978). Speckle in ultrasound b-mode scans. *IEEE Transactions on Sonics and Ultrasonics*, **25**, 1–6. 16

Cao, G., Zhao, Y., Ni, R. & Kot, A.C. (2011). Unsharp masking sharpening detection via overshoot artifacts analysis. *IEEE Signal Processing Letters*, **18**, 603. 7, 118, 151, 152

Casella, I.B., Presti, C., Porta, R.M.P., Sabbag, C.R.D., Bosch, M.A. & Yamazaki, Y. (2008). A practical protocol to measure common carotid artery intima-media thickness. *Clinics*, **63**, 515–520. 180

Ceccarelli, M., Luca, N.D. & Morganella, A. (2007). Automatic measurement of the intima-media thickness with active contour based image segmentation. In *2007 IEEE International Workshop on Medical Measurement and Applications*, 1–5. 186

Chen, J., Hayden, K.H.S. & Alfred, C. (2013). Towards establishing a design rule for aperture parameters in minimum-variance beamforming. In *2013 IEEE International Ultrasonics Symposium (IUS)*, 589–592, IEEE. 3

Chen, J., Chen, J. & Min, H. (2017). Design and evaluation of medical ultrasonic adaptive beamforming algorithm implementation on heterogeneous embedded computing platform. *EURASIP Journal on Embedded Systems*, **2017**, 19. 3

Chun, G.C., Chiang, H.J., Lin, K.H., Li, C.M., Chen, P.J. & Chen, T. (2015). Ultrasound elasticity imaging system with chirp-coded excitation for assessing biomechanical properties of elasticity phantom. *Materials*, **8**, 8392–8413. 51

Cohen, L.D. (1991). On active contour models and balloons. *CVGIP: Image understanding*, **53**, 211–218. 154

Cooley, C.R. & Robinson, B.S. (1994). Synthetic focus imaging using partial datasets. In *1994 Proceedings of IEEE Ultrasonics Symposium*, vol. 3, 1539–1542 vol.3. 14

Cowell, D. & Freear, S. (2008a). Quinary excitation method for pulse compression ultrasound measurements. *Ultrasonics*, **48**, 98 – 108. 36, 48, 51

Cowell, D. & Freear, S. (2008b). Quinary excitation method for pulse compression ultrasound measurements. *Ultrasonics*, **48**, 98–108. 47, 60, 180

Cowell, D.M.J., Carpenter, T., Smith, P., Adams, C., Harput, S. & Freear, S. (2016). Performance of switched mode arbitrary excitation using harmonic reduction pulse width modulation (hrpwm) in array imaging applications. In *2016 IEEE International Ultrasonics Symposium (IUS)*, 1–4. 60, 180

Cronenwett, J.L. & Johnston, K.W. (2014). *Rutherford's Vascular Surgery E-Book*. Elsevier Health Sciences. 187

Cruz, C.F.d. *et al.* (2012). Automatic analysis of mammography images: enhancement and segmentation techniques. 5, 119

Dahl, J.J., Hyun, D., Lediju, M. & Trahey, G.E. (2011). Lesion detectability in diagnostic ultrasound with short-lag spatial coherence imaging. *Ultrasonic imaging*, **33**, 119–133. 4

De Jong, N., Bom, N., Souquet, J. & Faber, G. (1985). Vibration modes, matching layers and grating lobes. *Ultrasonics*, **23**, 176–182. 25

Deylami, A.M. & Asl, B.M. (2018). Iterative minimum variance beamformer with low complexity for medical ultrasound imaging. *Ultrasound in medicine & biology*, **44**, 1882–1890. 3

Dutt, V. & Greenleaf, J.F. (1996). Adaptive speckle reduction filter for log-compressed b-scan images. *IEEE Transactions on Medical Imaging*, **15**, 802–813. 4, 7, 120

Fear, E.C., Li, X., Hagness, S.C. & Stuchly, M.A. (2002). Confocal microwave imaging for breast cancer detection: localization of tumors in three dimensions. *IEEE Transactions on Biomedical Engineering*, **49**, 812–822. 4

Fowlkes, J.B. (2008). American institute of ultrasound in medicine consensus report on potential bioeffects of diagnostic ultrasound: executive summary. *Journal of ultrasound in medicine: official journal of the American Institute of Ultrasound in Medicine*, **27**, 503–515. 53, 54

Gaarder, M. & Seierstad, T. (2015). Measurements of carotid intima media thickness in non-invasive high-frequency ultrasound images: the effect of dynamic range setting. *Cardiovascular ultrasound*, **13**, 5. 2, 187

Gadermayr, M., Maier, A. & Uhl, A. (2013). Active contours methods with respect to vickers indentations. *Machine Vision and Applications*, **24**, 1183–1196. 183

Garovic, V.D., Milic, N.M., Weissgerber, T.L., Mielke, M.M., Bailey, K.R., Lahr, B., Jayachandran, M., White, W.M., Hodis, H.N. & Miller, V.M. (2017). Carotid artery intima-media thickness and subclinical atherosclerosis in women with remote histories of preeclampsia: Results from a rochester epidemiology project-based study and meta-analysis. *Mayo Clinic Proceedings*, **92**, 1328 – 1340. 180

Guo, W., Wang, Y., Wu, G. & Yu, J. (2018). Sidelobe reduction for plane wave compounding with a limited frame number. *Biomedical Engineering Online*, **17**, 94. 2

Hansen, J. & Jensen, J. (2012). *Synthetic Aperture Compound Imaging*. Ph.D. thesis. 36

Harput, S., Arif, M., Mclaughlan, J., Cowell, D.M.J. & Freear, S. (2013). The effect of amplitude modulation on subharmonic imaging with chirp excitation. *IEEE Transactions on Ultrasonics, Ferroelectrics, and Frequency Control*, **60**, 2532–2544. 51

Harput, S., McLaughlan, J., Cowell, D.M.J. & Freear, S. (2014). New performance metrics for ultrasound pulse compression systems. In *2014 IEEE International Ultrasonics Symposium*, 440–443. 63

Harput, S., McLaughlan, J., Cowell, D.M. & Freear, S. (2015). Contrast-enhanced ultrasound imaging with chirps: Signal processing and pulse compression. In *Ultrasonics Symposium (IUS), 2015 IEEE International*, 1–4, IEEE. 58

Harrington, J. & Cassidy, S. (2012). *Techniques in speech acoustics*, vol. 8. Springer Science & Business Media. 71, 73

Hemmsen, M.C., Kortbek, J., Nikolov, S.I. & Jensen, J.A. (2010). Simulation of high quality ultrasound imaging. In *2010 IEEE International Ultrasonics Symposium*, 1739–1742. 36

Hiremath, P., Akkasaligar, P.T. & Badiger, S. (2013). Speckle noise reduction in medical ultrasound images. In *Advancements and Breakthroughs in Ultrasound Imaging*, InTech. 159

Hobbs, F., Piepoli, M., Hoes, A., Agewall, S., Albus, C., Brotons, C., Catapano, A., Cooney, M., Corra, U., Cosyns, B. *et al.* (2016). 2016 european guidelines on cardiovascular disease prevention in clinical practice. *European heart journal*, **37**, 2315–2381. 177

Holfort, I.K., Austeng, A., Synnevåg, J.F., Holm, S., Gran, F. & Jensen, J.A. (2009). Adaptive receive and transmit apodization for synthetic aperture ultrasound imaging. In *2009 IEEE International Ultrasonics Symposium*, 1–4. 3, 4

Hoskins, P.R., Martin, K. & Thrush, A. (2010). *Diagnostic Ultrasound: Physics and Equipment*. Cambridge University Press. 28

Huang, T., Yang, G. & Tang, G. (1979). A fast two-dimensional median filtering algorithm. *IEEE Transactions on Acoustics, Speech, and Signal Processing*, **27**, 13–18. 153

Hurst, R.T., Ng, D.W., Kendall, C. & Khandheria, B. (2007). Clinical use of carotid intima-media thickness: review of the literature. *Journal of the American Society of Echocardiography*, **20**, 907–914. 177, 178

Ilea, D.E., Duffy, C., Kavanagh, L., Stanton, A. & Whelan, P.F. (2013). Fully automated segmentation and tracking of the intima media thickness in ultrasound video sequences of the common carotid artery. *IEEE Transactions on Ultrasonics, Ferroelectrics, and Frequency Control*, **60**, 158–177. 187

Izquierdo, E. & Ghanbari, M. (1999). Nonlinear gaussian filtering approach for object segmentation. *IEE Proceedings-Vision, Image and Signal Processing*, **146**, 137–143. 152

Jabarulla, M.Y. & Lee, H.N. (2018). Speckle reduction on ultrasound liver images based on a sparse representation over a learned dictionary. *Applied Sciences*, **8**. 149

Jain, A.K. (1989). *Fundamentals of digital image processing*. Prentice-Hall, Inc., Upper Saddle River, NJ, USA. 153

Jensen, J., Stuart, M.B. & Jensen, J.A. (2015). Increased frame rate for plane wave imaging without loss of image quality. In *2015 IEEE International Ultrasonics Symposium (IUS)*, 1–4. 25, 26

Jensen, J., Stuart, M.B. & Jensen, J.A. (2016a). Optimized plane wave imaging for fast and high-quality ultrasound imaging. *IEEE Transactions on Ultrasonics, Ferroelectrics, and Frequency Control*, **63**, 1922–1934. xvi, 62

Jensen, J., Stuart, M.B. & Jensen, J.A. (2016b). Optimized plane wave imaging for fast and high-quality ultrasound imaging. *IEEE Transactions on Ultrasonics, Ferroelectrics, and Frequency Control*, **63**, 1922–1934. 6, 64, 68

Jensen, J.A. (1991). A model for the propagation and scattering of ultrasound in tissue. *The Journal of the Acoustical Society of America*, **89**, 182–190. 51

Jespersen, S.K., Wilhjelm, J.E. & Sillesen, H. (1998). Multi-angle compound imaging. *Ultrasonic Imaging*, **20**, 81–102. 16, 19, 150, 151

Jin, F., Fieguth, P., Winger, L. & Jernigan, E. (2003). Adaptive wiener filtering of noisy images and image sequences. In *Proceedings 2003 International Conference on Image Processing (Cat. No.03CH37429)*, vol. 3, III–349–52 vol.2. 152

Joshi, G.D. & Sivaswamy, J. (2008). Colour retinal image enhancement based on domain knowledge. In *2008 Sixth Indian Conference on Computer Vision, Graphics Image Processing*, 591–598. 5

Jumaat, A.K., Yasiran, S.S., Malek, A.A., Rahman, W.E.Z.W.A., Badrin, N., Osman, S.H., Rafiee, S.R. & Mahmud, R. (2014). Performance comparison of canny and sobel edge detectors on balloon snake in segmenting masses. In *2014 International Conference on Computer and Information Sciences (ICCOINS)*, 1–5. 5, 160

Kanai, H., Koiwa, Y. & Zhang, J. (1999). Real-time measurements of local myocardium motion and arterial wall thickening. *IEEE Transactions on Ultrasonics, Ferroelectrics, and Frequency Control*, **46**, 1229–1241. 28

Karaman, M., Atalar, A., Koymen, H. & O'Donnell, M. (1993). A phase aberration correction method for ultrasound imaging. *IEEE Transactions on Ultrasonics, Ferroelectrics, and Frequency Control*, **40**, 275–282. 36

Karunakaran, C.P. & Oelze, M.L. (2013). Amplitude modulated chirp excitation to reduce grating lobes and maintain ultrasound intensity at the focus of an array. *Ultrasonics*, **53**, 1293–1303. 25

Kass, M., Witkin, A. & Terzopoulos, D. (1988). Snakes: Active contour models. *International journal of computer vision*, **1**, 321–331. 154

Khadidos, A., Sanchez, V. & Li, C.T. (2014). Active contours based on weighted gradient vector flow and balloon forces for medical image segmentation. In *2014 IEEE International Conference on Image Processing (ICIP)*, 902–906. 7, 8, 10, 83, 160

Klemm, M., Craddock, I., Leendertz, J., Preece, A. & Benjamin, R. (2008). Improved delay-and-sum beamforming algorithm for breast cancer detection. *International Journal of Antennas and Propagation*, **2008**. 4

Klemm, M., Leendertz, J.A., Gibbins, D., Craddock, I.J., Preece, A. & Benjamin, R. (2009). Microwave radar-based breast cancer detection: Imaging in inhomogeneous breast phantoms. *IEEE Antennas and Wireless Propagation Letters*, **8**, 1349–1352. 4

Korukonda, S. (2012). *Application of Synthetic Aperture Imaging to Non-Invasive Vascular Elastography*. Ph.D. thesis, University of Rochester. 18

Kumar, J.R.H., Seelamantula, C.S., Narayan, N.S. & Marziliano, P. (2016). Automatic segmentation of common carotid artery in transverse mode ultrasound images. In *2016 IEEE International Conference on Image Processing (ICIP)*, 389–393. 83

Kumar, V., Webb, J.M., Gregory, A., Denis, M., Meixner, D.D., Bayat, M., Whaley, D.H., Fatemi, M. & Alizad, A. (2018). Automated and real-time segmentation of suspicious breast masses using convolutional neural network. *PloS one*, **13**, e0195816. 8

Kuo, J.W., Wang, Y., Aristizábal, O., Ketterling, J.A. & Mamou, J. (2013). Automatic mouse embryo brain ventricle segmentation from 3d 40-mhz ultrasound data. In *2013 IEEE International Ultrasonics Symposium (IUS)*, 1781–1784. 6

Kushwaha, S. & Singh, R.K. (2017). Performance comparison of different despeckled filters for ultrasound images. *Biomedical and Pharmacology Journal*, **10**, 837–845. 153

Kwok, N., Shi, H., Fang, G. & Ha, Q. (2013). Adaptive scale adjustment design of unsharp masking filters for image contrast enhancement. In *2013 International Conference on Machine Learning and Cybernetics*, vol. 02, 884–889. 119

Laugier, P. & Haïat, G. (2011). Introduction to the physics of ultrasound. In *Bone quantitative ultrasound*, 29–45, Springer. 53

Lawrence, J.P. (2007). Physics and instrumentation of ultrasound. *Critical care medicine*, **35**, S314–S322. 80

Lazebnik, M., McCartney, L., Popovic, D., Watkins, C.B., Lindstrom, M.J., Harter, J., Sewall, S., Magliocco, A., Booske, J.H., Okoniewski, M. *et al.* (2007). A large-scale study of the ultrawideband microwave dielectric properties of normal breast tissue obtained from reduction surgeries. *Physics in Medicine and Biology*, **52**, 2637. 4

Lediju, M.A., Pihl, M.J., Dahl, J.J. & Trahey, G.E. (2008). Quantitative assessment of the magnitude, impact and spatial extent of ultrasonic clutter. *Ultrasonic Imaging*, **30**, 151–168. 2, 3, 9, 23

Lee, J.S. (1980). Digital image enhancement and noise filtering by use of local statistics. *IEEE Transactions on Pattern Analysis and Machine Intelligence*, **PAMI-2**, 165–168. 5, 152

Lim, H.B., Nhung, N.T.T., Li, E.P. & Thang, N.D. (2008). Confocal microwave imaging for breast cancer detection: Delay-multiply-and-sum image reconstruction algorithm. *IEEE Transactions on Biomedical Engineering*, **55**, 1697–1704. 4

Lin, D., Sofka, C., Rybak, L. & Adler, R. (2003). Advantages of photopic imaging in sonography of low contrast musculoskeletal lesions and structures in the foot. *Ultrasound in Medicine & Biology*, **29**, S27–S28. 23, 156

Lin, D.C., Nazarian, L.N., O'Kane, P.L., McShane, J.M., Parker, L. & Merritt, C.R. (2002). Advantages of real-time spatial compound sonography of the musculoskeletal system versus conventional sonography. *American Journal of Roentgenology*, **179**, 1629–1631. 14

Loizou, C.P. (2014). A review of ultrasound common carotid artery image and video segmentation techniques. *Medical & Biological Engineering & Computing*, **52**, 1073–1093. 178

Loizou, C.P., Pattichis, C.S., Christodoulou, C.I., Istepanian, R.S., Pantziaris, M. & Nicolaides, A. (2005). Comparative evaluation of despeckle filtering in ultrasound imaging of the carotid artery. *IEEE transactions on ultrasonics, ferroelectrics, and frequency control*, **52**, 1653–1669. 5, 149, 178

Loizou, C.P., Nicolaides, A., Kyriacou, E., Georghiou, N., Griffin, M. & Pattichis, C.S. (2015). A comparison of ultrasound intima-media thickness measurements of the left and right common carotid artery. *IEEE Journal of Translational Engineering in Health and Medicine*, **3**, 1–10. 179, 187

Magnin, P.A., von Ramm, O.T. & Thurstone, F.L. (1982). Frequency compounding for speckle contrast reduction in phased array images. *Ultrasonic Imaging*, **4**, 267–281. 16

Mahmood, N.H., Razif, M. & Gany, M. (2011). Comparison between median, unsharp and wiener filter and its effect on ultrasound stomach tissue image segmentation for pyloric stenosis. *Inte J Appl Sci Technol*, **1**. 5

Mahmoudzadeh, A.P. & Kashou, N.H. (2013). Evaluation of interpolation effects on upsampling and accuracy of cost functions-based optimized automatic image registration. *Journal of Biomedical Imaging*, **2013**, 16. 42

Matrone, G., Savoia, A.S., Caliano, G. & Magenes, G. (2015). The delay multiply and sum beamforming algorithm in ultrasound b-mode medical imaging. *IEEE Transactions on Medical Imaging*, **34**, 940–949. 4, 59, 63, 80

Matrone, G., Savoia, A.S., Caliano, G. & Magenes, G. (2016). Ultrasound plane-wave imaging with delay multiply and sum beamforming and coherent compounding. In *2016 38th Annual International Conference of the IEEE Engineering in Medicine and Biology Society (EMBC)*, 3223–3226. 2, 4

Matrone, G., Ramalli, A., Savoia, A.S., Tortoli, P. & Magenes, G. (2017a). High frame-rate, high resolution ultrasound imaging with multi-line transmission and filtered-delay multiply and sum beamforming. *IEEE Transactions on Medical Imaging*, **36**, 478–486. 4

Matrone, G., Savoia, A.S., Caliano, G. & Magenes, G. (2017b). Depth-of-field enhancement in filtered-delay multiply and sum beamformed images using synthetic aperture focusing. *Ultrasonics*, **75**, 216–225. 4

Mccowan, I. (2018). Microphone arrays : A tutorial. 72

Michailovich, O.V. & Tannenbaum, A. (2006). Despeckling of medical ultrasound images. *IEEE Transactions on Ultrasonics, Ferroelectrics, and Frequency Control*, **53**, 64–78. 5, 51, 150, 153

Misaridis, T. & Jensen, J.A. (2005). Use of modulated excitation signals in medical ultrasound. part iii: high frame rate imaging. *IEEE Transactions on Ultrasonics, Ferroelectrics, and Frequency Control*, **52**, 208–219. 80

Montaldo, G., Tanter, M., Bercoff, J., Benech, N. & Fink, M. (2009). Coherent plane-wave compounding for very high frame rate ultrasonography and transient elastography. *IEEE Transactions on Ultrasonics, Ferroelectrics, and Frequency Control*, **56**, 489–506. 1, 2, 9, 14, 17, 18, 23, 68, 90, 150, 151

Moubark, A.M., Harput, S., Cowell, D.M.J. & Freear, S. (2016). Clutter noise reduction in b-mode image through mapping and clustering signal energy for better cyst classification. In *2016 IEEE International Ultrasonics Symposium (IUS)*, 1–4. 3

Nelson, T.R., Fowlkes, J.B., Abramowicz, J.S. & Church, C.C. (2009). Ultrasound biosafety considerations for the practicing sonographer and sonologist. *Journal of Ultrasound in Medicine*, **28**, 139–150. 53

Nightingale, K.R., Church, C.C., Harris, G., Wear, K.A., Bailey, M.R., Carson, P.L., Jiang, H., Sandstrom, K.L., Szabo, T.L. & Ziskin, M.C. (2015). Conditionally increased acoustic pressures in nonfetal diagnostic ultrasound examinations without contrast agents: A preliminary assessment. *Journal of Ultrasound in Medicine*, **34**, 1–41. 54

Nikolic, M., Tuba, E. & Tuba, M. (2016). Edge detection in medical ultrasound images using adjusted canny edge detection algorithm. In *2016 24th Telecommunications Forum (TELFOR)*, 1–4. 7

Noble, J.A. & Boukerroui, D. (2006a). Ultrasound image segmentation: a survey. *IEEE Transactions on Medical Imaging*, **25**, 987–1010. 6

Noble, J.A. & Boukerroui, D. (2006b). Ultrasound image segmentation: a survey. *IEEE Transactions on Medical Imaging*, **25**, 987–1010. 153

Nock, L., Trahey, G.E. & Smith, S.W. (1989). Phase aberration correction in medical ultrasound using speckle brightness as a quality factor. *The Journal of the Acoustical Society of America*, **85**, 1819–1833. 36

Otsu, N. (1979). A threshold selection method from gray-level histograms. *IEEE Transactions on Systems, Man, and Cybernetics*, **9**, 62–66. 155

Øvland, R. (2012). *Coherent Plane-Wave Compounding in Medical Ultrasound Imaging: Quality Investigation of 2D B-mode Images of Stationary and Moving Objects.*. Master's thesis, Institutt for fysikk. 29

Papadacci, C., Pernot, M., Couade, M., Fink, M. & Tanter, M. (2014). High-contrast ultrafast imaging of the heart. *IEEE Transactions on Ultrasonics, Ferroelectrics, and Frequency Control*, **61**, 288–301. 24

Polak, J.F., Funk, L.C. & O'Leary, D.H. (2011). Inter-reader differences in common carotid artery intima-media thickness: implications for cardiovascular risk assessment and vascular age determination. *Journal of Ultrasound in Medicine*, **30**, 915–920. 186

Polesel, A., Ramponi, G. & Mathews, V.J. (2000). Image enhancement via adaptive unsharp masking. *IEEE Transactions on Image Processing*, **9**, 505–510. 7

Ponnle, A., Hasegawa, H. & Kanai, H. (2013). Suppression of grating lobe artifacts in ultrasound images formed from diverging transmitting beams by modulation of receiving beams. *Ultrasound in Medicine & Biology*, **39**, 681–691. 25, 72

Rebouças Filho, P.P., Cortez, P.C., da Silva Barros, A.C. & De Albuquerque, V.H.C. (2014). Novel adaptive balloon active contour method based on internal force for image segmentation–a systematic evaluation on synthetic and real images. *Expert Systems with Applications*, **41**, 7707–7721. 154

Rodriguez-Molares, A., Avdal, J., Torp, H. & Løvstakken, L. (2016a). Axial lobes in coherent plane-wave compounding. In *2016 IEEE International Ultrasonics Symposium (IUS)*, 1–4. 26

Rodriguez-Molares, A., Avdal, J., Torp, H. & Løvstakken, L. (2016b). Axial lobes in coherent plane-wave compounding. In *2016 IEEE International Ultrasonics Symposium (IUS)*, 1–4. 31

Rodriguez-Molares, H.A., Lovstakken, L. & Denarie, B. (2015). Busting the ghost in coherent planewave imaging. In *IEEE Int Ultrason Symp. Taipei, Taiwan*. 26

Roy, R., Ghosh, S., Cho, S.B. & Ghosh, A. (2017). Despeckling with structure preservation in clinical ultrasound images using historical edge information weighted regularizer. In *International Conference on Mining Intelligence and Knowledge Exploration*, 144–155, Springer. 149

Ruchkin, D. (1965). Error of correlation coefficient estimates from polarity coincidences (corresp.). *IEEE Transactions on Information Theory*, **11**, 296–297. 71

Sakhaei, S.M. (2015). A decimated minimum variance beamformer applied to ultrasound imaging. *Ultrasonics*, **59**, 119 – 127. 3

Sanchez, J.R. & Oelze, M.L. (2009). An ultrasonic imaging speckle-suppression and contrast-enhancement technique by means of frequency compounding and coded excitation. *IEEE Transactions on Ultrasonics, Ferroelectrics, and Frequency Control*, **56**. 16

Schafer, R.W. (2011). What is a savitzky-golay filter?[lecture notes]. *IEEE Signal Processing Magazine*, **28**, 111–117. 125

Schwiegerling, J. (2004). Field guide to visual and ophthalmic optics. SPIE. 23

Shariat, F. (2009). Object segmentation using active contours: A level set approach. 154

Slabaugh, G., Unal, G., Wels, M., Fang, T. & Rao, B. (2009). Statistical region-based segmentation of ultrasound images. *Ultrasound in Medicine & Biology*, **35**, 781–795. 8, 24, 83

Smith, P.R., Cowell, D.M.J., Raiton, B., Ky, C.V. & Freear, S. (2012). Ultrasound array transmitter architecture with high timing resolution using embedded phase-locked loops. *IEEE Transactions on Ultrasonics, Ferroelectrics, and Frequency Control*, **59**, 40–49. 47, 60, 180

Smith, P.R., Cowell, D.M. & Freear, S. (2013). Width-modulated square-wave pulses for ultrasound applications. *IEEE Transactions on Ultrasonics, Ferroelectrics, and Frequency Control*, **60**, 2244–2256. 48

Song, T.K. & Chang, J.H. (2004). Synthetic aperture focusing method for ultrasound imaging based on planar waves. US Patent 6,736,780. 17

Tanter, M. & Fink, M. (2014). Ultrafast imaging in biomedical ultrasound. *IEEE Transactions on Ultrasonics, Ferroelectrics, and Frequency Control*, **61**, 102–119. 1, 2, 17

Tanter, M., Bercoff, J., Sandrin, L. & Fink, M. (2002). Ultrafast compound imaging for 2-d motion vector estimation: Application to transient elastography. *IEEE Transactions on Ultrasonics, Ferroelectrics, and Frequency Control*, **49**, 1363–1374. 17

Taxt, T. (1995). Restoration of medical ultrasound images using two-dimensional homomorphic deconvolution. *IEEE Transactions on Ultrasonics, Ferroelectrics, and Frequency Control*, **42**, 543–554. 51

Tay, P.C., Garson, C.D., Acton, S.T. & Hossack, J.A. (2010). Ultrasound despeckling for contrast enhancement. *IEEE Transactions on Image Processing*, **19**, 1847–1860. 150, 153

Tegeler, C.H., Ratanakorn, D. & Kim, J. (2005). Advances in carotid ultrasound. *Seminars in Cerebrovascular Diseases and Stroke*, **5**, 74 – 82. xvi, 62

Ter Haar, G. (2011). Ultrasonic imaging: safety considerations. *Interface focus*, rsfs20110029. 53

Tole, N.M., Ostensen, H., Organization, W.H. *et al.* (2005). Basic physics of ultrasonic imaging. 58

Toulemonde, M., Basset, O., Tortoli, P. & Cachard, C. (2015). Thomson's multitaper approach combined with coherent plane-wave compounding to reduce speckle in ultrasound imaging. *Ultrasonics*, **56**, 390–398. 14, 16, 68, 90, 150

Trahey, G., Zhao, D., Miglin, J.A. & Smith, S.W. (1990). Experimental results with a real-time adaptive ultrasonic imaging system for viewing through distorting media. *IEEE Transactions on Ultrasonics, Ferroelectrics, and Frequency Control*, **37**, 418–427. 36

Tranquart, F., Grenier, N., Eder, V. & Pourcelot, L. (1999). Clinical use of ultrasound tissue harmonic imaging. *Ultrasound in Medicine & Biology*, **25**, 889–894. 2, 9, 23

Ueng, S.K., Yen, C.L. & Chen, G.Z. (2014). Ultrasound image enhancement using structure-based filtering. *Computational and Mathematical Methods in Medicine*, **2014**. 119, 152

Ullom, J.S., Oelze, M.L. & Sanchez, J.R. (2012). Speckle reduction for ultrasonic imaging using frequency compounding and despeckling filters along with coded excitation and pulse compression. *Advances in Acoustics and Vibration*, **2012**. 14, 16, 63

Wagner, R., Smith, S., Sandrik, J. & Lopez, H. (1983). Statistics of speckle in ultrasound b-scans. *IEEE Transactions on Sonics and Ultrasonics*, **30**, 156–163. 150

Wagner, R.F., Insana, M.F. & Smith, S.W. (1988). Fundamental correlation lengths of coherent speckle in medical ultrasonic images. *IEEE Transactions on Ultrasonics, Ferroelectrics, and Frequency Control*, **35**, 34–44. 150

Westin, H.K., Kikinis, R. & Knutsson, H. (2000). Adaptive image filtering. *Handbook of medical imaging*. 5, 152, 153

Wilkinson, L., Thomas, V. & Sharma, N. (2016). Microcalcification on mammography: approaches to interpretation and biopsy. *The British journal of radiology*, **90**, 20160594. 5

Xu, J. & Cao, Y. (2013). Radiation-induced carotid artery stenosis: a comprehensive review of the literature. *Interventional Neurology*, **2**, 183–192. 178

Yaqub, M., Mahon, P., Javaid, M., Cooper, C. & Noble, J. (2010). Weighted voting in 3d random forest segmentation. *Proc. Medical Image Understanding and Analysis, Warwick, UK*, 261–266. 8

Yeom, E., Nam, K.H., Jin, C., Paeng, D.G. & joon Lee, S. (2014). 3d reconstruction of a carotid bifurcation from 2d transversal ultrasound images. *Ultrasonics*, **54 8**, 2184–92. 85

Yoon, C., Kim, G.D., Yoo, Y., Song, T.K. & Chang, J.H. (2013). Frequency equalized compounding for effective speckle reduction in medical ultrasound imaging. *Biomedical Signal Processing and Control*, **8**, 876–887. 14

Yu, C.Y., Zhang, W.S., Yu, Y.Y. & Li, Y. (2013). A novel active contour model for image segmentation using distance regularization term. *Computers & Mathematics with Applications*, **65**, 1746–1759. 186

Zahnd, G., Orkisz, M., Sérusclat, A., Moulin, P. & Vray, D. (2014). Simultaneous extraction of carotid artery intima-media interfaces in ultrasound images: assessment of wall thickness temporal variation during the cardiac cycle. *International Journal of Computer Assisted Radiology and Surgery*, **9**, 645–658. 179

Zeng, X., Wang, Y., Yu, J. & Guo, Y. (2013). Correspondence-beam-domain eigenspace-based minimum variance beamformer for medical ultrasound imaging. *IEEE Transactions on Ultrasonics, Ferroelectrics, and Frequency Control*, **60**, 2670–2676. 2, 116

Zhang, H.K., Cheng, A., Bottenus, N., Guo, X., Trahey, G.E. & Boctor, E.M. (2016). Synthetic tracked aperture ultrasound imaging: design, simulation, and experimental evaluation. *Journal of Medical Imaging*, **3**, 027001. 3

Zhang, Y., Guo, Y. & Lee, W.N. (2018). Ultrafast ultrasound imaging using combined transmissions with cross-coherence-based reconstruction. *IEEE Transactions on Medical Imaging*, **37**, 337–348. 26

Zhao, J., Wang, Y., Yu, J., Guo, W., Zhang, S. & Aliabadi, S. (2017). Short-lag spatial coherence ultrasound imaging with adaptive synthetic transmit aperture focusing. *Ultrasonic Imaging*, **39**, 224–239, pMID: 28068874. 3

Zheng, Y., Zhou, Y., Zhou, H. & Gong, X. (2015). Ultrasound image edge detection based on a novel multiplicative gradient and canny operator. *Ultrasonic Imaging*, **37**, 238–250, pMID: 25315657. 7

Zhou, T., Li, Q.L., Chen, X., Wang, T.F. & Chen, S.P. (2013). Forward-backward minimum variance beamforming combined with coherence weighting applied to ultrasound imaging. In *World Congress on Medical Physics and Biomedical Engineering May 26-31, 2012, Beijing, China*, 1092–1096, Springer. 3

Zhu, G., Zhang, S., Zeng, Q. & Wang, C. (2010). Gradient vector flow active contours with prior directional information. *Pattern Recognition Letters*, **31**, 845–856. 8, 83